University of Alberta

Multilevel Signaling for Increasing the Capacity of High-Speed Optical Communication Systems

By

Sheldon Samuel Walklin ©

A thesis submitted to the Faculty of Graduate Studies and Research in partial fulfillment of the requirements for the degree of **Doctor of Philosophy**

Department of Electrical and Computer Engineering

Edmonton, Alberta

Fall 1997

National Library
of Canada

Acquisitions and
Bibliographic Services

395 Wellington Street
Ottawa ON K1A 0N4
Canada

Bibliothèque nationale
du Canada

Acquisitions et
services bibliographiques

395, rue Wellington
Ottawa ON K1A 0N4
Canada

Your file Votre référence

Our file Notre référence

The author has granted a non-exclusive licence allowing the National Library of Canada to reproduce, loan, distribute or sell copies of this thesis in microform, paper or electronic formats.

The author retains ownership of the copyright in this thesis. Neither the thesis nor substantial extracts from it may be printed or otherwise reproduced without the author's permission.

L'auteur a accordé une licence non exclusive permettant à la Bibliothèque nationale du Canada de reproduire, prêter, distribuer ou vendre des copies de cette thèse sous la forme de microfiche/film, de reproduction sur papier ou sur format électronique.

L'auteur conserve la propriété du droit d'auteur qui protège cette thèse. Ni la thèse ni des extraits substantiels de celle-ci ne doivent être imprimés ou autrement reproduits sans son autorisation.

0-612-23088-0

Canadä

University of Alberta

Library Release Form

Name of Author: **Sheldon Samuel Walklin**

Title of Thesis: **Multilevel Signaling for Increasing the Capacity of High-Speed Optical Communication Systems**

Degree: **Doctor of Philosophy**

Year this Degree Granted: **1997**

Permission is hereby granted to the University of Alberta Library to reproduce single copies of this thesis and to lend or sell such copies for private, scholarly, or scientific research purposes only.

The author reserves all other publication and other rights in association with the copyright in the thesis, and except as hereinbefore provided, neither the thesis nor any substantial portion thereof may be printed or otherwise reproduced in any material form whatever without the author's prior written permission.

Sheldon Samuel Walklin

40 Alderwood Blvd.
St. Albert, Alberta
Canada T8N 3Z6

Date: Aug. 12, 1997

University of Alberta

Faculty of Graduate Studies and Research

The undersigned certify that they have read, and recommend to the Faculty of Graduate Studies and Research for acceptance, a thesis entitled **Multilevel Signaling for Increasing the Capacity of High-Speed Optical Communication Systems** submitted by **Sheldon Samuel Walklin** in partial fulfillment of the requirements for the degree of **Doctor of Philosophy**.

J. Conradi

Dr. J. Conradi, Supervisor

J. N. McMullin

Dr. J. McMullin

ZJ Koles

Dr. Z. Koles

Dr. W. Grover

Dr. J. Cartledge, External

Date: July 31/97

To my wife, Michelle and my son, Ryan

Abstract

This thesis investigates the potential of M-ary ASK, polybinary, polyquaternary, and AM-PSK polybinary signaling schemes operating at 10 Gb/s for increasing the capacity of digital, lightwave communication systems. The premise for exploring these signals was that, because spectral components closer to the carrier experience a lower phase distortion than those components farther away, a dispersion improvement should be offered for signals in which the spectrum is more concentrated about the optical carrier. All signaling methods were investigated through theoretical considerations and computer simulation. The experimental phase of this work focussed on M-ary ASK, where the complete design, construction and testing of a 4-ary ASK lightwave system operating at a bit rate of 10 Gb/s was carried out.

It was found that, of all the polybinary signaling schemes investigated, only the duobinary signal offers an improvement in dispersion immunity, and that no improvement is offered for higher-level polybinary signals because they do not permit the required transmission bandwidth to be further reduced. Hence, it is the spectral occupancy, and not the shape of the power spectrum, that is the important parameter for assessing the dispersion tolerance of polybinary signals. Duobinary signaling allows the dispersion-limited distance to be extended to ~200 km, which is an improvement of two to three times over a conventional binary signal.

Transmission at 10 Gb/s using 4-ary ASK was experimentally demonstrated over 225 km of standard fiber, and simulations indicate that the dispersion-limited distance

can be extended to ~350 km using this signaling scheme; however, it is believed that 4-ary ASK signaling does not offer a practical solution to chromatic dispersion because of the inherently large power penalty of 7 to 9 dB over a binary signal, which results because of the strong signal dependence of noise. Moreover, a 4-ary ASK signal requires a laser with a linewidth less than 1 MHz to avoid a substantial RIN-induced power penalty from PM-to-AM noise conversion.

Acknowledgements

First and foremost, I thank my supervisor Dr. Jan Conradi for serving as my mentor and providing me with an exceptional environment to develop my professional skills, and to grow intellectually. Dr. Conradi has developed an internationally prominent research program of which I am especially privileged to have been a part of.

I also thank David Clegg for sharing his wealth of knowledge on practical design, and for helping me with many of the laboratory tasks. Jason Lamont is also acknowledged for his assistance with much of the laboratory work.

I wish to thank Ping Wan and Ben Chan for their many stimulating discussions on noise modeling, and Greg May for his assistance and advice during the earlier stages of this work. I also thank Mike Sieben for participating in some of the laboratory work, and Sing Cheng for his enlightening discussions on nonlinear fiber modeling. Alan Hnatiw and David Boertjes are also acknowledged for proofreading portions of this thesis, and for their many stimulating discussions on various topics in photonics. Tom Young, Stephen Lai, Dave Moore, Craig Unick, Ray DeCorby, Geoffrey Hayward and Rohit Sharma are all acknowledged for their many useful discussions on a variety of subjects in communications.

For their assistance with computer-related matters, I wish to thank Dean Michaels and Luke Chong.

I thank all the staff and students at TRLabs for making the TRLabs experience truly enjoyable and fulfilling. As I leave TRLabs, the strongest impression I am left with is the integrity with which the staff and students conduct their daily business. I will always remember the excellence of TRLabs and what the organization has done for me.

Nortel Technologies is also acknowledged for providing equipment that was essential to the success of experimental work.

My gratitude is especially extended to Dr. George Cormack for providing me with the initial opportunity, through a summer work term, to enter the field of communications.

Finally, for their financial support, I wish to thank the National Science and Engineering Research Council of Canada, the University of Alberta and TRLabs. Without their support, this work would not have been possible.

Table of Contents

1 INTRODUCTION **1**

1.1 Evolution of Fiber-Optic Communication Systems *1*

1.1.1 First Generation Systems 2

1.1.2 Second Generation Systems 3

1.1.3 Third Generation Systems 4

1.2 Limitations in a High-Speed, Fiber-Optic Communication System *5*

1.3 Increasing the Capacity of a High-Speed, Fiber-Optic Communication System *7*

1.3.1 Optical Methods 7

1.3.1.1 Optical Time-Division Multiplexing 7

1.3.1.2 Wavelength-Division Multiplexing 11

1.3.1.3 Polarization-Division Multiplexing 13

1.3.1.4 Soliton Transmission 13

1.3.1.5 Mid-Span Spectral Inversion (MSSI) 14

1.3.1.6 Dispersion Compensating Fiber and Chirped Bragg Gratings 14

1.3.2 Transmission Format Methods 15

1.3.2.1 Dispersion Supported Transmission 15

1.3.2.2 Partial-Response Signaling 15

1.3.2.3 Multilevel Signaling (M-ary ASK) 16

1.4 Thesis Organization *20*

2 SIGNALING SCHEMES **21**

2.1 Power Spectral Density *21*

2.2 Binary ASK *22*

2.2.1 PSD of an NRZ Binary Signal 23

2.3 M-ary ASK *24*

2.3.1 Generating an M-ary Signal 24

2.3.2 PSD of an M-ary NRZ Signal 25

2.4 Polybinary ASK *25*

2.4.1 Generating a Polybinary Signal 25
2.4.2 Precoding and Decoding 26
2.4.3 PSD of a Polybinary Signal 28
2.5 Polyquaternary ASK *29*
2.5.1 Precoding and Decoding 30
2.5.2 PSD of a Polyquaternary Signal 30
2.6 AM-PSK Duobinary *30*
2.6.1 Generating an Optical AM-PSK Duobinary Signal 31
2.6.2 PSD of an AM-PSK Duobinary Signal 32
2.7 AM-PSK Polybinary *32*
2.8 Summary *32*
3 FIBER-OPTIC SYSTEM RESPONSE AND PERFORMANCE MEASURES 33
3.1 Determining System Response *33*
3.1.1 LED with Multimode Fiber 33
3.1.2 LED with Singlemode Fiber 35
3.1.3 Laser Diode with Singlemode Fiber 37
3.1.3.1 Lowpass-Equivalent Modeling of a Bandpass System 38
3.2 Measuring Performance *39*
3.2.1 Eye Diagrams and ISI 39
3.2.1.1 Realizable Filters that Minimize ISI 41
3.2.2 BER and Receiver Sensitivity 45
3.3 Summary *46*
4 NOISE MODELING AND RELATED TOPICS 47
4.1 Noise Sources *48*
4.1.1 Receiver Thermal Noise 48
4.1.2 Noise from Amplified Spontaneous Emission in Optical Amplifiers 50
4.1.3 Shot Noise 51
4.1.4 Relative Intensity Noise 52

4.2 Static Noise Model *53*

4.2.1 Calculating BER and Receiver Sensitivity 54

4.2.2 Optimal Level Spacing 57

4.2.3 Power Penalty for M-ary Signaling 62

4.3 Dynamic Noise Model *64*

4.4 PM-to-AM Relative Intensity Noise *68*

4.4.1 PM-to-AM Conversion in a Dispersive Medium 68

4.4.2 Spectral Density of PM-to-AM RIN 72

4.4.3 RIN-Induced BER Floor 74

4.4.4 RIN in a Dynamic Noise model 77

4.5 Summary *78*

5 COMPONENT MODELING AND RELATED TOPICS 79

5.1 Electrical Devices *79*

5.2 Mach-Zehnder External Modulators and Frequency Chirping *79*

5.2.1 Structure of a Mach-Zehnder Optical Modulator 80

5.2.2 Transfer Characteristic 81

5.2.3 Frequency Chirping 83

5.2.4 Optical Pulse Compression 85

5.2.5 Chirp Parameter 86

5.2.6 Optical Extinction Ratio and Residual Chirp 90

5.2.7 Multiple Quantum Well InP/InGaAsP Mach-Zehnder Modulator 93

5.3 Fiber Transfer Function for Singlemode Fiber *94*

5.3.1 Modeling Chromatic Dispersion in the Power Domain 99

5.4 Erbium-Doped Fiber Amplifiers *101*

5.5 Summary *103*

6 COMPONENT CHARACTERIZATION 104

6.1 Laser Measurements *104*

6.1.1 Wavelength 104

6.1.2 Linewidth 104
6.1.3 RIN 105
6.1.4 Laser Chirp 107
6.2 Frequency Response of Electrical Components *108*
6.3 Frequency Response of Modulators and Photodetectors *110*
6.4 Modulator RF Switching Voltage *111*
6.5 Transfer Characteristic of Multiple Quantum Well InP/InGaAsP Mach-Zehnder Modulator *113*
6.6 EDFAs *115*
6.7 Optical Bandpass Filters *118*
6.8 Photodetector Responsivity *120*
6.9 Transimpedance Gain of Nortel PIN-Preamp Module *120*
6.10 RF Amplifier Noise Figure *121*
6.11 GaAs Logic Devices *122*
6.12 Summary *124*
7 SYSTEM SIMULATION AND DISCUSSION **125**
7.1 Fiber Optic Communication System Simulator (FOCSS) *125*
7.2 Ideal Simulations Based on a Static Noise Model *127*
7.2.1 Effect of Optical Filter Bandwidth and Spontaneous Emission Factor 127
7.2.2 Power Penalty for M-ary ASK 128
7.2.3 Effect of Optical Preamplifier Gain on Receiver Sensitivity 129
7.2.4 Power Penalty from a Non-Zero Laser Linewidth 130
7.2.5 Quantum-Limited Receiver Sensitivity 131
7.3 Ideal Simulations Based on a Dynamic Noise Model *132*
7.3.1 Dispersion Immunity of Signaling Schemes 135
7.3.1.1 Binary 135
7.3.1.2 Duobinary 137
7.3.1.3 Polybinary 142

7.3.1.4 M-ary ASK 146
7.3.1.5 Optical AM-PSK Duobinary 148
7.3.2 Residual Chirp from a Finite Optical Extinction Ratio 149
7.3.3 Transmission with Controlled Frequency Chirping 152
7.3.4 Relationship between Filter Response and Chromatic Dispersion in Duobinary Optical Communication Systems 155
7.3.5 Optimal Level Spacing and ISI 160
7.3.6 Overview of Expected Reach for Signaling Schemes 161
7.3.7 Power Penalty from a Non-Zero Laser Linewidth 163
7.3.8 Optical Inline Amplifiers and ASE Accumulation 164
7.4 Realistic System Simulation *167*
7.4.1 Effect of Component Frequency Response 168
7.4.2 Bias and Drive Conditions for an InP/InGaAsP Mach-Zehnder Modulator .. 171
7.5 Summary *173*
8 EXPERIMENTAL RESULTS **174**
8.1 Noise Measurements *174*
8.2 10 Gb/s Binary Transmission Experiments *179*
8.2.1 Experimental Setup 179
8.2.2 Experimental Results 184
8.3 10 Gb/s 4-Level ASK Transmission Experiments *188*
8.3.1 Experimental Setup 188
8.3.2 Experimental Results 195
8.4 Summary *200*
9 SUMMARY AND CONCLUSIONS **201**
10 REFERENCES **210**
11 APPENDIXES **221**
11.1 Appendix A: Computer Simulation of Analog Linear Systems *222*
11.1.1 Discrete Time Records of Continuous-Time Signals 222

11.1.2 Convolution and the Fourier Transform 223

11.1.3 The Discrete Fourier Transform 225

11.1.4 Periodicity 226

11.1.5 System Response to an Energy (aperiodic) Signal 227

11.1.6 System Response to a Power (periodic) Signal 230

11.1.7 Power Spectral Density and Spectral Resolution 231

11.1.8 Summary 232

11.2 Appendix B: MATLAB Programs Based on a Static Noise Model *233*

11.3 Appendix C: Optical Component Data *249*

11.3.1 Active Components 249

11.3.1.1 Lasers 249

11.3.1.2 Mach-Zehnder Modulators 251

11.3.1.3 Erbium-Doped Fiber Amplifiers 253

11.3.1.4 Photodiode Responsivity 255

11.3.2 Passive Components 256

11.3.2.1 Loss Measurements 256

11.3.2.2 Optical Filter Bandwidths 257

11.4 Appendix D: Electrical Component Data *259*

11.4.1 Electrical Amplifier Specifications 259

11.4.2 VM10LA-155 Limiting Amplifier 260

11.4.3 VM10CMD-320 Differential Pulse Amplifier 261

11.4.4 Frequency Response Measurements 262

11.5 Appendix E: GaAs IC Power Supply *269*

11.5.1 Description 269

11.5.2 Front Panel Controls and Connectors 269

11.5.2.1 Supply Voltage Outputs 269

11.5.2.2 Variable Voltage Outputs 269

11.5.2.3 Built-in Voltmeter 270

11.5.3 Rear Panel Controls and Connectors.. 270
  11.5.3.1 Power Supply Terminals 270
  11.5.3.2 Voltmeter Range Selector 271
11.5.4 Internal Components 271
11.5.5 Bias Circuit for Variable Outputs.. 273
11.5.6 Handling and Care of GaAs Logic ICs.. 274

List of Tables

Table C.1 Measured laser parameters. 249

Table C.2 Parameters for Mach-Zehnder external modulators. 251

Table C.3 DC responsivity measurements and maximum average powers for photodiodes. 255

Table C.4 Loss measurements for passive optical components. 256

Table C.5 Optical filter bandwidth measurements at 1557 nm. 257

Table D.1 Specifications for electrical amplifiers. 259

List of Figures

Figure 1.1 Cross section of a multimode optical fiber (left); refraction index profiles for step and radially-graded fibers (right)........ 3

Figure 1.2 Wavelength dependence of transit delay in silica optical fibers. The minimum occurs at about 1.3 μm for standard fiber........ 4

Figure 1.3 Two-channel OTDM system using separate laser sources for each channel (after G. Eisenstein et al. [13])........ 8

Figure 1.4 OTDM system using a single laser (after G. Eisenstein et al. [14])........ 9

Figure 1.5 OTDM system using an integrated-optic chip and continuous wave light source (after Djupsjöbacka [16])........ 10

Figure 1.6 Block diagram of a WDM communication system........ 11

Figure 1.7 Multilevel transmitter using a single 2.5 Gb/s source to simulate four 2.5 Gb/s tributaries transmitted by a 10 Gb/s four-level signal........ 17

Figure 1.8 Drive voltage levels required to obtain evenly spaced optical intensity levels in a $LiNbO_3$ Mach-Zehnder optical switch 19

Figure 1.9 Multilevel receiver; the four 2.5 Gb/s tributaries are recovered from the received four-level signal........ 19

Figure 2.1 PSD of a binary NRZ Signal........ 23

Figure 2.2 Constructing a 4-level signal from 2 binary signals........ 24

Figure 2.3 Filter for generating a polybinary signal........ 26

Figure 2.4 Power transmission response of a polybinary filter........ 28

Figure 2.5 PSDs of NRZ polybinary signals........ 29

Figure 2.6 Mach-Zehnder drive condition to obtain a conventional binary, intensity-modulated signal (left) and an optical AM-PSK duobinary signal (right)........ 31

Figure 3.1 Optical communication system using a directly-modulated LED and multimode fiber: (a) block diagram; (b) equivalent model. 34

Figure 3.2 Magnitude response of singlemode fiber when using an LED. 36

Figure 3.3 Nonlinear model for a communication system that uses an external modulator and laser. 37

Figure 3.4 (a) Ideal NRZ binary signal; (b) Filtered NRZ binary signal. 40

Figure 3.5 (a) Eye diagram for an ideal NRZ binary signal; (b) Eye diagram for a filtered NRZ binary signal. 40

Figure 3.6 Pole locations for a realizable second-order filter. 41

Figure 3.7 Eye diagrams for a raised-cosine response with β=0 (top left) and β=1 (top right), and a ninth-order, all-pole filter (bottem left). Impulse response for the all-pole filter (bottom right). 43

Figure 3.8 Eye diagram for response of a 7-pole filter with four finite zeros from [85] (left), and an all-pole, 7-pole filter (right). 44

Figure 3.9 Eye diagrams for an ideal binary NRZ signal filtered by: third-order Butterworth filter with a cutoff frequency at 4.5 GHz (top left), 5.5 GHz (top right) 6.5 GHz (bottom left); 6 GHz, fifth-order Bessel filter (bottom right). 45

Figure 4.1 Calculating receiver noise in an electrical amplifier. 49

Figure 4.2 Optical front end of a receiver. 50

Figure 4.3 Gaussian PDFs for a **0** and a **1**. 55

Figure 4.4 Gaussian PDFs for a **0**, **1**, **2** and **3** in a 4-ary signal. 57

Figure 4.5 Optimal level weights versus extinction ratio for a signal dominated by RIN. 60

Figure 4.6 Optimal level weights versus extinction ratio for a signal dominated by stationary noise (left), or dominated by noise that is proportional to received optical power (right). 60

Figure 4.7 Optimal level weights versus optical preamplifer gain for a system where all noise sources are present. 61

Figure 4.8 Expected value of signal passed to decision circuit for which the noise power varies continuously with time........ 64

Figure 4.9 Relationship between the received optical power $s^2(t)$, receiver impulse response $h_r(t)$, and summation indices k and l........ 67

Figure 4.10 Phase modulation at the input is converted to amplitude modulation at the output of a dispersive fiber. 69

Figure 4.11 PM-to-AM conversion of an optical carrier that is phase modulated by a sinusoid. 70

Figure 4.12 PM-to-AM conversion versus: (a) frequency; (b) fiber length. 70

Figure 4.13 Detector photocurrent for various frequencies of the phase modulation corresponding to Figure 4.12a. 71

Figure 4.14 PSD of transmitted optical field referenced to the optical carrier (top left), and of the detected photocurrent at various frequencies corresponding to Figure 4.12a. 72

Figure 4.15 PM-to-AM RIN spectral density at 100 km (left) and 300 km (right)... 74

Figure 4.16 PM-to-AM RIN-induced SNR versus fiber length for different receiver bandwidths. 75

Figure 4.17 PM-to-AM RIN-induced SNR versus receiver bandwidth for different fiber lengths. 75

Figure 4.18 Linewidth that will produce a 10^{-14} BER floor for 10 Gb/s transmission. 77

Figure 5.1 Basic structure of a Mach-Zehnder optical modulator. 80

Figure 5.2 Chirping performance of a $LiNbO_3$ Mach-Zehnder modulator driven with a 5 GHz sinusoidal electrical drive: Optical power pulse (top); phase of output optical electric field (middle); instantaneous shift in optical carrier frequency in Hz (bottom). 85

Figure 5.3 Group delay per unit distance versus wavelength for standard fiber. 85

Figure 5.4 a) Optical electric field versus time for a chirped pulse; b) Optical electric field versus space for a chirped pulse. 86

Figure 5.5 Time dependence of the chirp parameter for different modulation indices. 89

Figure 5.6 Power transfer characteristic versus normalized differential voltage for a $LiNbO_3$ Mach-Zehnder modulator: "O" and "X" denote bias points. 90

Figure 5.7 Phasor diagram showing residual phase in the output field of a Mach-Zehnder modulator. 92

Figure 5. 8 Cross section of rib waveguide structure in a MQW InP/InGaAsP MZ Modulator (after [112]). 93

Figure 5.9 Transfer characteristic for a III-V MZ Modulator. 94

Figure 5.10 Fiber with length L and transfer function $H(f)$. 94

Figure 5.11 Transforming a bandpass transfer function to a lowpass equivalent. 96

Figure 5.12 Signal distortion of a 5 GHz intensity-modulated tone after 30 km. 100

Figure 5.13 Parts of an erbium-doped fiber amplifier. 101

Figure 5.14 Gain curve for an EDFA with G_o=30 dB and P_{sat}=+15 dBm. 102

Figure 6.1 Setup for delayed self-homodyne linewidth measurement (after [118]). 104

Figure 6.2 DSH linewidth measurements for two lasers. 105

Figure 6.3 Setup for measuring average laser RIN. 106

Figure 6.4 Frequency response of two wideband amplifiers having the same model number. 109

Figure 6.5 Eye diagrams: (top left) 5 Gb/s binary tributary input to multilevel symbol generator; (top right) 5 Gbaud signal output from symbol generator; (bottom left) output from amplifier **A**; (bottom right) output from amplifier **B** 110

Figure 6.6 Setup for measuring the frequency response of an external modulator and photodetector. 110

Figure 6.7 DC transfer characteristic for Lucent $LiNbO_3$ MZ. 112

Figure 6.8 Phasor diagram showing calculation of phase. 114

Figure 6.9 Meausred amplitude (left) and phase (right) for a III-V MZ................. 115

Figure 6.10 III-V MZ transfer characteristic; (left) modeled using curve fits for amplitude and phase; (right) measured. 115

Figure 6.11 Setup for measuring external EDFA parameters. 116

Figure 6.12 Measured gain curve for an EDFA operating at 1533 nm and 1557 nm. 117

Figure 6.13 Monochrometer scan of ASE spectral density. 118

Figure 6.14 Setup for measuring optical filter bandwidth. 119

Figure 6.15 Transmission response for a Fabry-Perot optical bandpass filter. 119

Figure 6.16 Setup used for measuring transimpedance gain of Nortel PIN-preamp module. 120

Figure 6.17 GaAS D-FF logic module. 122

Figure 6.18 Output waveform of a GaAs logic device operating at 5 Gb/s. 123

Figure 6.19 S_{11} magnitude response of D-FF input. 123

Figure 7.1 Menu structure of FOCSS. 126

Figure 7.2 Block diagram and system parameters used for simulations based on a static noise model. 127

Figure 7.3 Receiver sensitivity versus optical filter bandwidth (left), and spontaneous emission factor (right) for binary and 4-ary ASK signals. 127

Figure 7.4 Receiver sensitivity versus optical preamplifier gain. 129

Figure 7.5 BER versus received power for a binary system in which various BER floors are present. 130

Figure 7.6 Power penalty versus source linewidth for binary and 4-ary ASK signals. 131

Figure 7.7 Block diagram of optical communication system simulated in FOCSS.133

Figure 7.8 Receiver sensitivity versus distance for RZ and NRZ binary signals. ... 136

Figure 7.9 Optical signals input to fiber: (left) RZ pulse shapes; (right) Filtered NRZ optical signal. 136

Figure 7.10 Eye diagrams of received filtered NRZ binary signal at 0, 75 and 125 km. 137

Figure 7.11 Two methods for implementing a duobinary filter: (a) delay-and-add filter followed by an optional band-limiting filter; (b) lowpass filter will a cutoff at about ¼ the bit rate. 138

Figure 7.12 Receiver sensitivity versus distance for systems employing a duobinary filter at the transmitter or receiver. 139

Figure 7.13 Eye diagrams of received filtered duobinary signal at 0, 100 and 175 km. 140

Figure 7.14 Eye diagrams for an optical back-to-back system: (top left) optical power incident on photodetector; all other eye diagrams are for the received electrical signal filtered by a fifth-order Bessel filter with the indicated 3 dB cutoff. 141

Figure 7.15 Eye diagrams versus distance: (top) received optical power; (bottom) filtered electrical signal after being passed through a duobinary filter. 142

Figure 7.16 Receiver sensitivity versus distance for 5-level and 7-level polybinary signals. 143

Figure 7.17 Eye diagrams of 5-level (top) and 7-level (bottom) polybinary signals. 143

Figure 7.18 Minimum bandwidth channels for a binary signal (top) and a duobinary signal(bottom). 144

Figure 7.19 Eye diagram after 0 km and 150 km for a 5-level polybinary signal that has been bandlimited to 10 GHz. 146

Figure 7.20 Receiver sensitivity versus distance for 4-ary ASK, 8-ary ASK and polyquaternary (7 levels) signals. 147

Figure 7.21 Eye diagrams at various distances for 4-ary ASK (top) and 8-ary ASK (bottom). 147

Figure 7.22 Receiver sensitivity versus distance for AM-PSK polybinary signals using various duobinary filters at the transmitter. 148

Figure 7.23 Eye diagrams of the received optical intensity (top) and the filtered electrical signal (directly below) for an AM-PSK signal. 149

Figure 7.24 Polarity of residual chirp alternates in an AM-PSK duobianry signal. 151

Figure 7.25 Effect of residual chirp from a finite DC optical extinction ratio on various signaling schemes. 151

Figure 7.26 Receiver sensitivity versus chirp parameter for a binary system using an external modulator with various DC extinction ratios and residual chirp polarity. 153

Figure 7.27 Receiver sensitivity versus chirp parameter for a 4-ary ASK system using an external modulator with an ideal and 20 dB DC exticntion ratio. 154

Figure 7.28 receiver sensitivity versus chirp parameter for an optical AM-PSK duobinary signal. 154

Figure 7.29 The effect of various electrical transmitter filter structures on receiver sensitivity versus distance for 10 Gb/s binary, duobinary and AM-PSK duobinary systems. 156

Figure 7.30 PSD of the optical electric field (top) and corresponding filtered receiver eye diagrams (bottom) after transmission over 200 km. 158

Figure 7.31 Eye diagrams of a 4-ary ASK signal using optimal level weights....... 160

Figure 7.32 receiver sensitivity versus distance for various level weights of the electrical signal applied at the modulator... 161

Figure 7.33 Receiver sensitivity versus distance for various signaling schemes. ... 162

Figure 7.34 Receiver sensitivity versus source linewidth: (left) binary and duobinary systems; (right) M-ary ASK systems.. 163

Figure 7.35 Ratio of optical signal power to ASE power at each amplifier stage for 40 km and 80 km amplifier spacings. 166

Figure 7.36 BER versus launched optical power for 4ary ASK and 8-ary ASK signals.. 167

Figure 7.37 Trace and eye diagram for a signal output from a GaAs 4:1 Multiplexer operating at 10 Gb/s. 168

Figure 7.38 Trace and eye diagram of a 10 Gb/s 4-ary ASK electrical signal used at the transmitter.. 168

Figure 7.39 Small-signal magnitude and phase response of overall system: (left) using UTP modulator and BT&D photodetector; (right) using Nortel MZ with Nortel PIN photodetector. 169

Figure 7.40 Eye diagrams of 10 Gb/s binary received signal for a system using the frequency responses from Figure 7.39. 170

Figure 7.41 Eye diagrams of 4-ary ASK 10 Gb/s received signal for a system using the frequency responses from Figure 7.39.. 170

Figure 7.42 Receiver sensitivity versus laser linewidth for a 4-ary ASK system using acquired data for modeling components. 171

Figure 7.43 Intensity envelope and frequency chirp for a binary signal (left) and a 4-ary ASK signal (right) using optimized drive conditions for a III-V MZ. 172

Figure 8.1 Setup for measuring noise in an optically-preamplified system. 174

Figure 8.2 Measured and calculated noise for an optically-preamplified receiver with residual pump power. 175

Figure 8.3 Measured and calculated noise for a receiver using an EDFA preamplifier. 176

Figure 8.4 Measured and calculated noise for a system using an optical postamplifer, 100 km of fiber (or optical attenuator), and an optically-preamplified receiver. 176

Figure 8.5 Measured and calculated noise for a system using an optical postamplifer, 100 km of fiber, and an optically-preamplified receiver. 177

Figure 8.6 Defining noise-equivalent bandwidth for a component with a practical frequency response. 178

Figure 8.7 Optical setup used in 10 Gb/s transmission experiments.......... 179

Figure 8.8 Eletrical transmitter setup for 10 Gb/s binary experiments. 180

Figure 8.9 10 GHz clock generating circuit. 181

Figure 8.10 Eletrical receiver setup for 10 Gb/s binary experiments. 182

Figure 8.11 Magnitude (left) and phase (right) response of system for 10 Gb/s binary experiments. 182

Figure 8.12 Clock recovery circuit used in 10 Gb/s binary transmission experiments. 183

Figure 8.13 Experimental and simulated BER curves for 10 Gb/s binary transmission experiments. 184

Figure 8.14 Simulated and experimental eye diagrams for 10 Gb/s binary transmissions. 185

Figure 8.15 Plot of square error calculation versus temporal drift. 187

Figure 8.16 10 Gb/s binary eye diagrams before and after correction for temporal drift. 187

Figure 8.17 Optical link used for 10 Gb/s 4-ary transmission experiments over 225 km. 188

Figure 8.18 EDFA operating conditions for transmission over 225 km: (left) small-signal gain and operating gain of each amplifier; (middle) optical power output from each amplifier; (right) ratio of signal power to ASE power at the output of each amplifier. 189

Figure 8.19 Electrical transmitter for 10 Gb/s 4-ary ASK experiments. 189

Figure 8.20 Electrical receiver used in 10 Gb/s 4-ary ASK experiments. 191

Figure 8.21 System frequency response for 10 Gb/s 4-ary ASK experiments: (a) frequency response using the Nortel III-V MZ module; (b) frequency response using the Lucent $LiNbO_3$ MZ. 191

Figure 8.22 Multilevel decoder used in 10 Gb/s 4-ary ASK experiments. 192

Figure 8.23 Clock recovery circuit used in 10 Gb/s 4-ary ASK experiments. 193

Figure 8.24 PSD of electrical 4-ary ASK signal at the receiver. 194

Figure 8.25 BER versus received optical power for 4-ary experiments using the Nortel III-V MZ module. 195

Figure 8.26 EDFA using a reflecting loop mirror to obtain a double-pass gain. 196

Figure 8.27 BER versus received optical power for 4-ary experiments using the Nortel III-V MZ module, and two EDFAs in cascade as an optical preamp. 197

Figure 8.28 Experimental and simulated eye diagrams for a 4-ary ASK signal transmitted over 170 km. 198

Figure 8.29 Experimental and simulted eye diagrams for 10 Gb/s 4-ary ASK experiments using the Nortel III-V MZ module. 198

Figure 8.30 BER versus received optical power for experiments using a dual-drive $LiNbO_3$ MZ and a narrow-linewidth laser. 199

Figure 8.31 Experimental and simulted eye diagrams for 10 Gb/s 4-ary ASK experiments using the Lucent $LiNbO_3$ MZ modulator. 200

Figure A.1 Sampling an analog signal and constructing a discrete time record...... 222

Figure A.2 Visualizing the convolution of an input signal $s(t)$ with the impulse response $h(t)$ of a linear system to produce the output response $y(t)$. 223

Figure A.3 Relationship between the discrete time record $u(n\Delta t)$ and the discrete frequency record $U(m\Delta f)$. 227

Figure A.4 (a) resulting output $y(t)$ when time record is not extended with zero padding; (b) resulting output $y(t)$ when time record is extended with zero padding. 230

Figure C.1 Spectrum analyzer scans for laser linewidth measurements using DSH method. 250

Figure C.2 Power transfer characteristic for left and right arm of III-V MZ. 252

Figure C.3 Power Transfer characteristic for left and right arm of Lucent $LiNbO_3$ MZ for a positive (top) and negative (bottom) DC bias. 252

Figure C.4 Meausred gain curves and parameters for EDFAs operating at 1533 nm. 253

Figure C.5 Meausred gain curves and parameters for EDFAs operating at 1541 nm. 253

Figure C.6 Meausred gain curves and parameters for EDFAs operating at 1552 nm. 254

Figure C.7 Meausred gain curves and parameters for EDFAs operating at 1557 nm. 254

Figure C.8 Spontaneous emission factor and small-signal gain versus pump current for EDFA1. 255

Figure C.9 Transmission response for tunable FFP BPFs. 258

Figure D.1 Input sensiivity (top) and output swing versus control voltage (bottom) for the VM10LA-155 limiting amplifier. 260

Figure D.2 Transfer curves (top) and output bias offset versus applied voltage (bottom) for the VM10CMD-320 differential pulse amplifier. 261

Figure D.3 Small-signal frequency response of Nortel III-V MZ and Nortel PIN-preamp module. 262

Figure D.4 Small-signal frequency response of Lucent MZ and Nortel PIN-preamp module. 262

Figure D.5 Small-signal frequency response of UTP MZ and Nortel PIN-preamp module. 263

Figure D.6 Frequency response of SHF90P 15 GHz amplifier. 263

Figure D.7 Frequency response of Veritech VMA3k10C-232 10 GHz amplifier. 263

Figure D.8 Frequency response of MITEQ JS4-00102600-30 26 GHz amplifier. 264

Figure D.9 Frequency response of Veritech VMPPA-438 high-power pulse amplifier. 264

Figure D.10 Frequency response of Veritech 10CMD-320 differential driver amplifier, J1 to J2. 264

Figure D.11 Frequency response of Veritech 10CMD-320 differential driver amplifier, J2 to J4. 265

Figure D.12 Frequency response of B&H AC26011H24ELL9P1 (6235) 26 GHz amplifier. 265

Figure D.13 Frequency response of B&H AC26011H24ELL9P1 (7693) 26 GHz amplifier. 265

Figure D.14 Frequency response of PSPL 5575A Bias Tee. 266

Figure D.15 Frequency response of PSPL 5500 DC blocking capactior. 266

Figure D.16 Frequency response of PSPL 5315 differential pulse splitter, input to non-inverting output. 266

Figure D.17 Frequency response of PSPL 5315 differential pulse splitter, input to inverting output. 267

Figure D.18 Frequency response of HP 8494B and 8495B variable attenuators is cascade. 267

Figure D.19 Frequency response of K&L 5.8 GHz, 3-rd order Butterworth lowpass filter. 267

Figure D.20 Frequency response of PSPL 5575A bias tee and two PSPL 5330A 6-dB resistive splitters in cascade. This represents the response of the 1-to-4 power splitter and bias tee used in the multilevel decoder. 268

Figure E.1 Front panel of GaAs IC power supply. 269

Figure E.2 Rear panel of GaAs IC Power Supply. 270

Figure E.3 Internal components and wiring of the GaAs IC power supply. 272

Figure E.4 Scanned image of the finished GaAs IC power supply; (top) internal components; (bottom) front panel. 272

Figure E.5 Bias circuit for reference voltage provided to ICs. 273

Figure E.6 IC Reference voltage, V_{ref}, versus linear sweep on potentiometer. 273

Figure E.7 Bias voltage, V_{bias}, versus linear sweep on potentiometer. 274

List of Acronyms and Abbreviations

APD	Avalanche Photodiode
ASE	Amplified Spontaneous Emission
ASK	Amplitude Shift Keying
BDI	Birth-Death-Immigration
BER	Bit-Error Ratio
BERT	Bit-Error Ratio Tester
CW	Continuous Wave
DCF	Dispersion Compensating Fiber
DEMUX	Demultiplexer
DFB	Distributed Feedback
D-FF	D-Type Flip Flop
DSF	Dispersion-Shifted Fiber
DSH	Delayed Self-Homodyne
DST	Dispersion Supported Transmission
EDFA	Erbium-Doped Fiber Amplifier
FOCSS	Fiber Optic Communication System Simulator
FOM	Figure of Merit
GPIB	General Purpose Interface Bus
GUI	Graphical User Interface
IM-DD	Intensity Modulation with Direct Detection
ISI	Intersymbol Interference
LED	Light Emitting Diode
MGF	Moment Generating Function
MMF	Multimode Fiber
MSSI	Mid-Span Spectral Inversion
MUX	Multiplexer
MZ	Mach Zehnder
NEB	Noise-Equivalent Bandwidth
NRZ	Non-Return-to-Zero
OADM	Optical Add and Drop Multiplexer
OC-48	Optical Carrier at 2.48832 Gb/s

OC-96	Optical Carrier at 4.97664 Gb/s
OC-192	Optical Carrier at 9.95328 Gb/s
OPC	Optical Phase Conjugation
OTDM	Optical Time-Division Multiplexing
OXC	Optical Cross-Connect
PDF	Probability Density Function
PDM	Polarization-Division Multiplexing
PIN	Positive-Intrinsic-Negative
PM-to-AM	Phase Modulation to Amplitude Modulation
PN	Pseudonoise
PolSK-DD	Polarization Shift Keying with Direct Detection
PRBS	Pseudorandom Bit Sequence
PRS	Partial-Response Signaling
PSK	Phase Shift Keying
RIN	Relative Intensity Noise
RZ	Return-to-Zero
SBS	Stimulated Brillouin Scattering
SNR	Signal-to-Noise Ratio
SOP	State of Polarization
SPM	Self-Phase Modulation
WDM	Wavelength-Division Multiplexing
WDM-AON	Wavelength-Division Multiplexed, All-Optical Network
XOR	Exclusive OR
XPM	Cross-Phase Modulation

1 Introduction

In response to increasing societal needs for improved and faster communications, fiber-optic communication systems have been developed over the years with great success. Fiber-optic communication offers reliable transmission rates of many Gigabits per second (Gb/s) over a single fiber, with the capacity to carry 100,000 or more simultaneous voice signals. If multiple wavelengths are used, a fiber's carrying capacity can be increased further by about two orders of magnitude where capacity exceeding 1 Tb/s (1000 Gb/s) is possible over a single fiber [1], [2]. The large capacity of fiber-optic communication is due to the nature of the signal and transmission channel (fiber). The optical carrier frequency of about 200 THz is much higher than for other communication systems by several orders of magnitude and, therefore, has a significantly larger information-carrying capacity. In a properly designed system, optical signals can be transmitted over thousands of kilometers with a minimum amount of distortion and noise. Present efforts are directed toward the optimization of fiber-optic communication systems by configuring them in a way that exploits the desired properties of system components while avoiding or mitigating inherent limitations. With an increasing demand for high-bandwidth, multimedia content and the pervasion of the Internet, the deployment of high-capacity communication systems is imperative.

This introductory chapter starts with a discussion about the evolution of fiber-optic communication systems—in other words, what has been done in the past leading up to the state of the art. Then, some of the major limitations in a high-capacity system are described, followed by a discussion on methods for extending the capacity of a fiber-optic communication system. Finally, a description is given of the signaling schemes investigated in this thesis, along with details for a multilevel, fiber-optic communication system prototype that was built and tested as part of the experimental work.

1.1 Evolution of Fiber-Optic Communication Systems

Advances that have been made in optical communication systems include fiber geometry and composition, transmitter and detection devices, and the recent development of new optoelectronic waveguide devices and optical amplifiers. Following is a chronological overview of the advances made in optical communications for which the evolution of fiber-optic communications can be divided into three generations. First generation systems operate at a wavelength near

0.85 μm, second generation systems operate near 1.3 μm, and third generation systems operate near 1.55 μm.

1.1.1 First Generation Systems

The first commercial fiber-optic systems operated at a wavelength of 0.85 μm and used multimode silica fiber. AlGaAs lasers and light-emitting diodes (LEDs) were used as sources while silicon based PIN (positive-intrinsic-negative) photodiodes and avalanche photodiodes (APDs) were used as photodetectors. The laser has the advantage of coupling more power into the fiber than an LED and produces light over a narrower spectrum, which helps mitigate dispersion problems, i.e., pulse spreading. The laser can also be modulated at a much higher rate (at Gb/s rates). However, a laser is typically more expensive and less rugged than an LED. An LED is well suited for short distance communication links where its limited coupled power and wide emission spectrum can be tolerated. Using an APD as the detector provides the advantage of a better receiver sensitivity because of its inherent internal gain, which reduces the impact of receiver noise. Unfortunately, an APD requires a much higher supply voltage and is more temperature sensitive than a PIN.

Multimode fiber does not have the low dispersion properties of singlemode fiber used in later generation systems; however, it does have the advantage of a much larger core diameter (50 μm compared to 8 μm for singlemode fiber), which makes connecting and splicing much easier. The first multimode fibers were of the step-index type where the core has a uniform index of refraction that is slightly higher than that of the cladding. The cladding surrounds the core and serves as the boundary where the light undergoes total internal reflection. Because the refractive index is uniform throughout the core, light travels at a constant speed everywhere within the core. Using a ray model of light, light rays traversing different paths will reach the detector at different times, resulting in a spreading or dispersing of the transmitted pulse when it reaches the receiver. To circumvent this problem, fibers were developed with a radially-graded refractive index within the core. These refractive index profiles are typically near parabolic [3], [4] with the center of the core having the highest index of refraction. Figure 1.1 shows the cross section of a multimode fiber along with the refractive index profile for step and radially-graded fibers. The graded-index multimode fiber offers a significant reduction in pulse spreading. Light that travels down the center of the fiber sees the highest refractive index and, therefore, travels at the lowest speed. Light that deviates from the center of the core sees a lower refractive index and, therefore, travels at a faster speed, but also a farther distance.

The net effect is that all light rays arrive at the receiver with a smaller spread in time than for a step-index multimode fiber, thereby reducing the amount of dispersion.

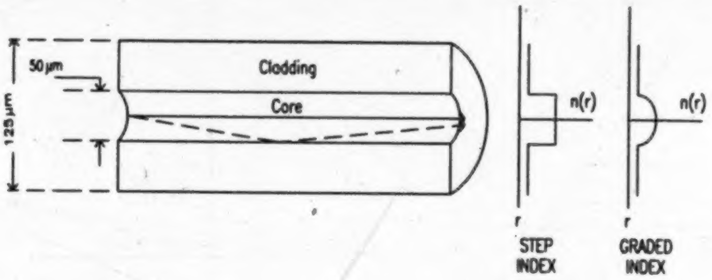

Figure 1.1 Cross section of a multimode optical fiber (left); refraction index profiles for step and radially-graded fibers (right).

1.1.2 Second Generation Systems

The development of optoelectronic devices using InGaAsP and Ge as the materials for the optical source and detector, respectively, marked the beginning of second generation fiber-optic communication systems. These devices are well suited to operate at a wavelength of about 1.3 µm. The main advantage of using this longer wavelength rather than 0.85 µm is that loss-limited transmission distances are improved by 5 to 10 times [3]. Optical signals are attenuated as they propagate down the fiber because of Rayleigh scattering and vibrational absorption in silica. However, there is an attenuation minimum "window" at wavelengths of about 1.3 and 1.5 µm. An additional and more important feature in second generation systems is the introduction of singlemode fibers which provide lower loss and much improved dispersion properties over multimode fibers.

A simple singlemode fiber has a step-indexed profile and a core diameter of about 8 µm. Multimode dispersion is eliminated because, at the 1.3 µm wavelength, the narrow waveguiding core allows propagation of a single mode only. However, singlemode fibers still experience dispersion problems due to chromatic dispersion, which is caused by the wavelength dependence of the refractive index in fused silica [5] and wavelength-dependent waveguide dispersion within this one remaining mode. In other words, the group velocity of the light in a singlemode fiber depends on the wavelength of the transmitted light, as shown in Figure 1.2. The important thing here is that, for standard silica fiber, the transit delay time is a minimum near 1.3 µm. This implies that, if the transmitted signal is centered about 1.3 µm, then the received pulse will essentially be undistorted, provided the frequency content of the signal does not deviate significantly from 1.3 μm. A useful parameter for characterizing dispersion in a singlemode fiber is the linear dispersion coefficient, *D*, which is defined as the slope of the delay versus wavelength in Figure 1.2 per unit distance, i.e., ps/(km·nm).

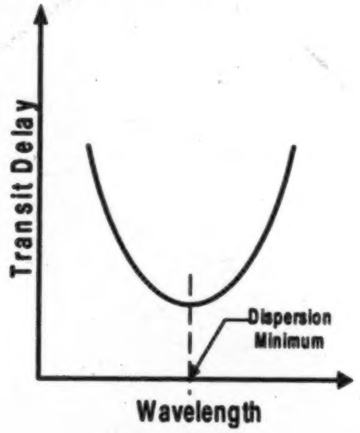

Figure 1.2 Wavelength dependence of transit delay in silica optical fibers. The minimum occurs at about 1.3 μm for standard fiber.

1.1.3 Third Generation Systems

Third generation systems are the state of the art. The arrival of erbium-doped fiber amplifiers[1] (EDFAs) and integrated-optic devices on lithium niobate ($LiNbO_3$) have invited many new possibilities in optical communications.

An EDFA is used to amplify light signals in the optical domain while introducing minimal distortion and noise [6]. The principal advantage of optical amplifiers is that signals can be amplified as they travel through the fiber without having to convert the signal to the electrical domain. Moreover, EDFAs can be used over a relatively large range of wavelengths, about 1530-1560 nm, making them well suited for wavelength-division multiplexing (WDM). EDFAs provide a solution to fiber attenuation problems and facilitate the use of optical switches and other devices that have an inherent insertion loss. One of the principal limitations of EDFAs is that they operate at about 1550 nm where chromatic dispersion is quite high in conventional (standard) silica fiber. This is not critical for newly installed systems where the use of dispersion-shifted fiber is possible; however, new technologies must be compatible, at least in part, with the present fiber-optic infrastructure. For this reason, dispersion compensation of systems operating at 1550 nm over standard fiber has been a very active area of research in resent years.

---

[1] An EDFA may be more appropriately classified as a fourth-generation component. For the purpose of brevity, however, it will be discussed in the context of third generation systems.

Integrated-optic technology on a $LiNbO_3$ substrate [7], [8] has allowed the production of optical components such as switches/modulators, frequency shifters, filters, polarization controllers and multiplexers. The introduction of these devices can help avoid the transmission rate bottleneck due to speed limitations in electronic devices. The fabrication of optoelectronic waveguide devices on $LiNbO_3$ involves the sputtering or evaporation of thin titanium films (roughly 50-150 nm thick) onto the $LiNbO_3$ substrate followed by photolithography and in-diffusion of the Ti to create a Ti doped region (waveguide) where the Ti increases the refractive index.

1.2 Limitations in a High-Speed, Fiber-Optic Communication System

There are many attributes of an optical communication system that can lead to degraded system performance: spectral broadening in light sources due to chirping; mode partition noise; pulse broadening from chromatic dispersion and/or polarization dispersion within the fiber; attenuation from inherent losses in the transmission channel or the insertion loss accompanying the use of optical devices; noise from spontaneous emission in optical amplifiers; nonlinear behavior of fiber, optoelectronic devices and electrical components; non-ideal frequency response of components. All of these attributes will affect system performance in some way. One of the main objectives of this research is to avoid these impairments by choosing a system architecture that minimizes their influence. A brief description of some of these limiting factors is given below.

Light Sources - Laser light sources do not emit perfectly monochromatic light. The continuous-wave (CW) spectrum of lasers contains a continuum of frequencies about some center frequency, resulting in a non-zero linewidth. In addition, there are smaller side lobes of narrow spectra, each spaced about 1 nm apart, that are present at lower and higher frequencies from the main lobe. When the laser is modulated, its central wavelength can shift (called frequency chirping) making the signal much more dispersive. In addition, the side lobes can possess much larger magnitudes compared to CW operation resulting in a broadened laser spectrum. Also, the relative intensity of side lobes can vary from one pulse to the next resulting in an additional uncertainty in the pulse shape known as mode partition noise. In high-speed systems, frequency chirping of a directly modulated laser is a significant problem because it broadens the spectral content of the transmitted signal well beyond the intrinsic bandwidth of the modulating signal, resulting in a signal that is much more dispersive. To overcome this limitation, most high-speed transmission schemes use some form of external modulation.

Attenuation - Attenuation of the light signal occurs from losses in the fiber, the use of fiber connectors, fiber splicing, and the insertion of optical or optoelectronic devices in the system. However, the availability of optical amplifiers like EDFAs has provided a means of circumventing attenuation limitations. Optical amplifiers will certainly be a necessary component in many optical systems.

Chromatic dispersion - Fiber dispersion has proven to be a difficult problem to address in a practical way. With the introduction of EDFAs, there is good reason to design around their operating wavelength near 1.55 μm. However, there has been a great capital outlay in fiber with a minimum dispersion near 1.3 μm (called standard fiber), which is highly dispersive at 1.55 μm. For this reason, much effort has gone into devising ways to reduce the dispersion penalty inherent at the longer 1.55 μm wavelength of operation. The best suited dispersion-compensating scheme will likely be application specific and will depend on the relative importance of factors such as complexity, cost, reliability, ruggedness, maintainability, compatibility with other systems, etc. Section 1.3 discusses some of the more successful anti-dispersion techniques.

Polarization Dispersion - It was previously mentioned that a singlemode fiber is not free from pulse broadening because of chromatic dispersion. Actually, there is yet another dispersion mechanism due to modal birefringence that exists in practical singlemode fibers. A "real" singlemode fiber [9] will have core deformities due to manufacturing tolerances, bending and stress. These deviations from the ideal allow for variations in the propagation of orthogonally polarized, but identical modes, whereby the orthogonal modes experience different refractive indexes, resulting in different group velocities for the same frequency of light. This dependence of refractive index on the state of polarization (SOP) is called modal birefringence. A singlemode fiber with an ideal circular core is free from this effect because the orthogonally-polarized modes are completely degenerate. Tsubokawa & Sasaki [10] demonstrated a pulse broadening of 17 ps through 100 km of fiber due to polarization dispersion. Their results indicate that 10 Gb/s transmission rates may be limited to about 150 km for some conventional singlemode fibers. C.D. Poole et al.

demonstrated a significant ambient temperature sensitivity of polarization dispersion [11].

Component Frequency Response - The frequency response of components used in high-speed communication systems is generally non-ideal. For example, wideband microwave amplifiers typically have a ripple within the passband of about ±1.5 dB. Lowpass filters with a cutoff in the GHz range can also exhibit ripple of ±1 dB or more, especially in the rolloff region. External modulators and photodetectors can have a frequency response that fluctuates considerably within the passband or in the rolloff region. The cumulative effect of the non-ideal frequency response of all components in the system can result in a substantial power penalty. In some cases, the system may even be inoperable because of the non-ideal response of components.

1.3 Increasing the Capacity of a High-Speed, Fiber-Optic Communication System

The following is a description of methods for increasing the capacity of an optical communication system, some of which have been investigated at TRLabs in the past. Increasing the capacity involves increasing the bit rate and/or increasing the transmission distance. For this reason, a system's capacity is often expressed as a bit rate-distance product. Optical-based methods for increasing system capacity will be described first. Then, transmission format-based methods will be described, which are the methods explored in this research.

1.3.1 Optical Methods

1.3.1.1 Optical Time-Division Multiplexing

The first high-speed experiments conducted at TRLabs used Optical Time-Division Multiplexing (OTDM). The principle of OTDM has been understood for many years, but was initially difficult because the required technology was not available. With the development of optoelectronic devices on $LiNbO_3$, the fabrication of optical switches/modulators, multiplexers and integrated optics was made possible. This led to much interest in OTDM starting in about the mid-eighties, and research in this field remains active today.

OTDM is an extension of time-division multiplexing in the electrical domain to the optical domain. It involves the interleaving of symbols (light pulses) in separate time slots to increase the transmission rate. The main advantage of OTDM is that it avoids some of the bottlenecks set by speed limitations in electronic components. Practical OTDM systems only require the electronics to operate at the transmission rate of individual tributaries rather than at the rate of the multiplexed signal. Complications in OTDM include attenuation from the insertion loss of added components such as optical switches, fiber dispersion and a more complex system architecture. Attenuation can be successfully addressed with the use of optical amplifiers, such as EDFAs. It may be difficult, however, to provide a simple dispersion-compensating technique for OTDM systems that is easily adaptable to arbitrary fiber types and lengths. Some of the earlier OTDM work was done by R.S. Tucker et al. in 1987 [12] where they reported 16 Gb/s OTDM transmission over 8 km of fiber with a BER less than 10^{-9}. The basic structure of their OTDM system is similar to that shown in Figure 1.3.

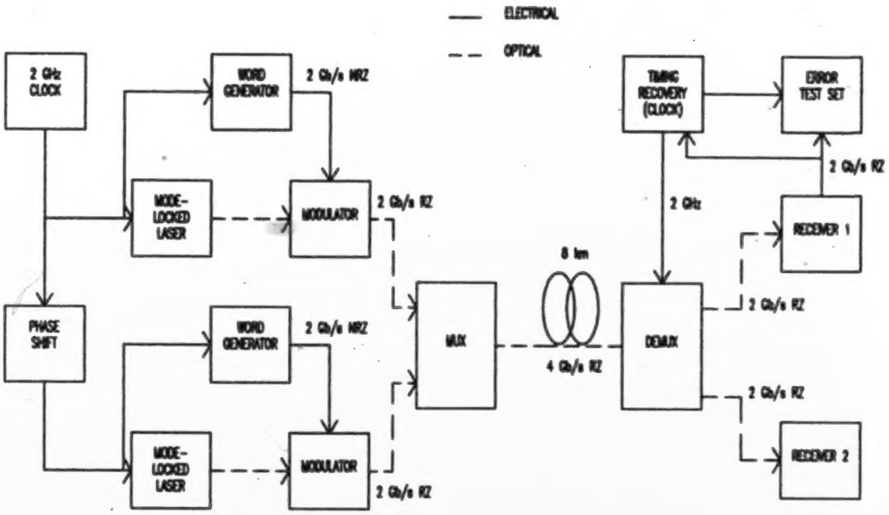
ELECTRICAL
OPTICAL
2 GHz CLOCK
WORD GENERATOR
2 Gb/s NRZ
MODE-LOCKED LASER
MODULATOR
2 Gb/s RZ
PHASE SHIFT
WORD GENERATOR
2 Gb/s NRZ
MODE-LOCKED LASER
MODULATOR
2 Gb/s RZ
MUX
8 km
4 Gb/s RZ
DEMUX
TIMING RECOVERY (CLOCK)
ERROR TEST SET
2 Gb/s RZ
2 GHz
RECEIVER 1
2 Gb/s RZ
2 Gb/s RZ
RECEIVER 2

Figure 1.3 Two-channel OTDM system using separate laser sources for each channel (after G. Eisenstein et al. [13]).

The 16 Gb/s transmission rate was accomplished by optically time-division multiplexing four 4 Gb/s channels. Note that Figure 1.3 shows the multiplexing of two 2 Gb/s channels; however, four channel multiplexing can be achieved by replicating (in parallel) the appropriate components in the architecture. The multiplexer in Figure 1.3 can be passive or active. A passive multiplexer could consist of a simple optical coupler, whereas an active multiplexer could use optical switching.

In Figure 1.3 a clock is used to drive two pulse generating circuits. In the Tucker et al. experiment these were 1.3 μm mode-locked semiconductor lasers that produced pulses about 15 ps wide. The clock signal is delayed before input to the second laser so that it produces pulses at times between the pulses produced by the first laser. The pulse stream from each laser is then modulated by the non-return-to-zero (NRZ) information provided by the word generator. Ti:LiNbO$_3$ optical switches were used as modulators in the Tucker et al. experiment. The modulated pulses from each channel are combined in the multiplexer to produce the multiplexed optical signal which, after transmission, is demultiplexed at the receiver where each individual channel is detected. Demultiplexing is done through the use of optical switches. Note that in Figure 1.3, the electronics are only required to operate at the rate of individual channels. In addition, the timing information at the receiver is extracted from a single demultiplexed channel where, again, the electronics speed is minimized.

An alternative to the OTDM system of Figure 1.3 is shown in Figure 1.4 where a single laser is used as the optical source for all channels.

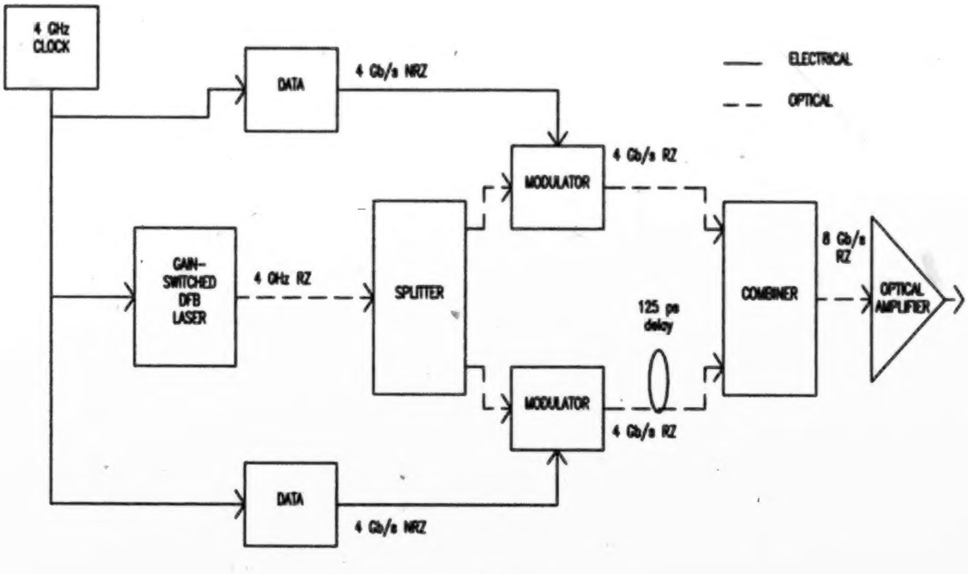
4 GHz CLOCK
DATA
4 Gb/s NRZ
ELECTRICAL
OPTICAL
MODULATOR
4 Gb/s RZ
GAIN-SWITCHED DFB LASER
4 GHz RZ
SPLITTER
125 ps delay
COMBINER
8 Gb/s RZ
OPTICAL AMPLIFIER
MODULATOR
4 Gb/s RZ
DATA
4 Gb/s NRZ

Figure 1.4 OTDM system using a single laser (after G. Eisenstein et al. [14]).

In Figure 1.4 a single gain-switched distributed feedback (DFB) laser produces a narrow-width pulse train at 4 GHz. The pulse train is split by a 3 dB fiber coupler and routed to two Ti:LiNbO$_3$ waveguide modulators where the pulses are intensity modulated by 4 Gb/s NRZ data streams. The multiplexing is achieved by delaying one of the modulated channels as shown in Figure 1.4. The signals are then combined in an active or passive combiner to obtain an 8 Gb/s return-to-zero (RZ) signal. In 1989, Eisenstein et al. used an OTDM system similar to that in Figure 1.4 to transmit an 8 Gb/s RZ (4 Gb/s x 2) signal over 57 km of singlemode fiber [14]. The receiver for their system is essentially the same as that in Figure 1.3. In 1991, G.E. Wickens et al. [15] also used an OTDM system similar to Fig. 1.4 to transmit 20 Gb/s (5 Gb/s x 4) over 205 km of dispersion-shifted fiber.

A disadvantage of the system in Figure 1.3 is that the lasers must be closely matched to avoid different propagation speeds in the multiplexed signals. A disadvantage of the system in Figure 1.4 is that a single laser can couple only a limited amount of power into the system necessitating optical amplification and the accompanying noise. However, each multiplexed channel contains the same source wavelength of light, which reduces pulse overlapping.

A third possibility for OTDM [16] is shown in Fig. 1.5 where a CW light source is used.

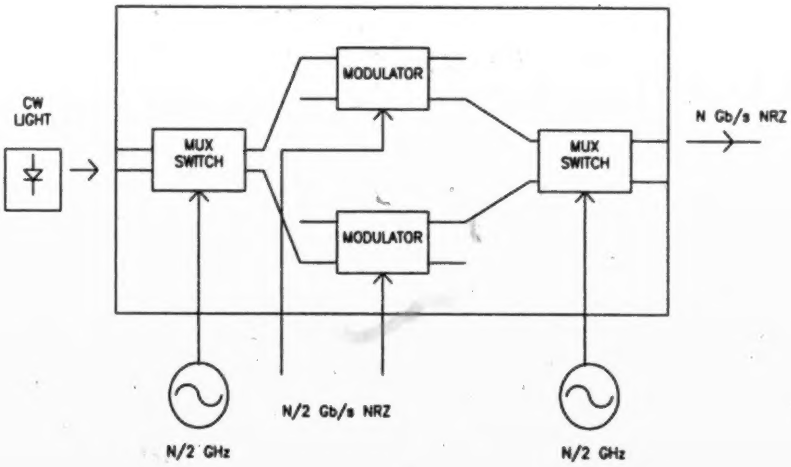

Figure 1.5 OTDM system using an integrated-optic chip and continuous wave light source (after Djupsjöbacka [16]).

In Figure 1.5 a CW laser is used as the source and an optical switch driven at N/2 GHz is used to divide the light into two pulse streams. The pulse streams are then modulated by N/2 Gb/s NRZ data with additional optical switches. Finally, the resulting modulated pulses are multiplexed with a fourth optical switch to produce the N Gb/s NRZ signal. The advantage of the OTDM system in Figure 1.5 is that a CW light source is used, which provides a very narrow linewidth carrier without the chirp and mode partitioning noise associated with pulsed lasers. The disadvantage of this system is that coherent addition of light occurs at the input to the second multiplexer during switching [16]. The coherence, resulting from the use of a single laser, causes a reduced eye opening in the output signal because of random fluctuations in the optical intensity. The jitter also makes timing extraction more difficult, which can further degrade the eye opening. A solution to this problem is to use an RZ coded data format or to use differing optical path lengths between the two multiplexers that are several times the laser light coherence length.

Because many successful OTDM demonstrations have taken place to date, it is likely to play a significant role in future optical communication systems, especially in soliton-based systems. Three possible OTDM architectures were described above; however, there are many possible variations that might lead to improved performance. It is also expected that the number of channels and aggregate bit rate will increase as OTDM technologies are refined. For example, OTDM transmission of forty 10 Gb/s tributaries (400 Gb/s) over 40 km was reported in [17].

1.3.1.2 Wavelength-Division Multiplexing

Wavelength-Division Multiplexing (WDM) is by far the most active research area in optical communication systems today. This technology promises to exploit the full bandwidth of an optical fiber by transmitting many wavelengths simultaneously over a single fiber. Figure 1.6 shows a simplified block diagram of a WDM lightwave system.

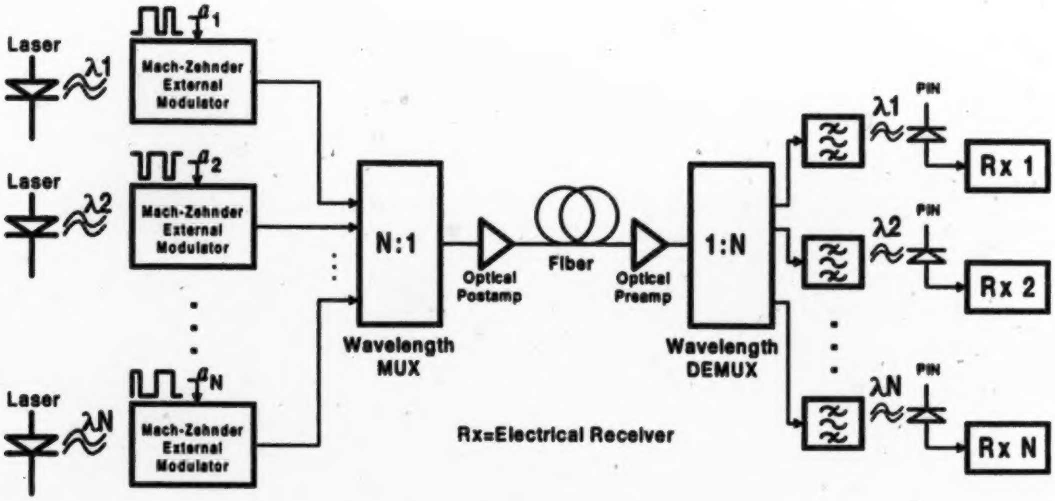
Laser
λ1
f_1
Mach-Zehnder External Modulator
Laser
λ2
f_2
Mach-Zehnder External Modulator
Laser
λN
f_N
Mach-Zehnder External Modulator
N:1
Wavelength MUX
Optical Postamp
Fiber
Optical Preamp
1:N
Wavelength DEMUX
λ1
PIN
Rx 1
λ2
PIN
Rx 2
λN
PIN
Rx N
Rx=Electrical Receiver

Figure 1.6 Block diagram of a WDM communication system.

Multiple laser sources, each at a unique wavelength, are externally modulated by the electrical tributaries a_1 through a_N. The modulated optical carriers are then combined using a wavelength multiplexer (MUX), after which the combined carriers are amplified and transmitted over a single fiber. At the receiver, an optical demultiplexer (DEMUX) is used to separate the individual wavelengths, which are then routed to individual receivers. Additional optical filtering may be used for each demultiplexed wavelength to ensure minimal crosstalk, and one or more optical amplifiers may be present at the receiver to overcome splitting losses and/or improve the receiver's sensitivity.

The achievements in WDM have progressed at a phenomenal rate. For example, 20 Gb/s transmission was achieved in [18] by transmitting two wavelengths, each at 10 Gb/s, over 360 km of standard fiber. In [19] 160 Gb/s transmission was achieved by transmitting eight 20 Gb/s channels over 232 km of conventional fiber. The first WDM experiments to reach 1 Tb/s were reported at OFC'96 where 1 Tb/s (50x20 Gb/s) was demonstrated over 50 km [20] and 1.1 Tb/s (55x20 Gb/s) was demonstrated over 150 km [21]. Only months later a new world record was set at ECOC'96 where transmission at 2.6 Tb/s (132x20 Gb/s) over 120 km of fiber was demonstrated [1].

There is much research presently under way aimed at improving the components that make up a WDM system. For example, it is essential that each wavelength experiences the same gain as it passes through an optical amplifier. Conventional silica-based EDFAs, however, have a strong wavelength dependence, making them unsuitable for broadband amplification of many WDM channels, especially when amplifiers are cascaded. Therefore, methods for improving the gain flatness are actively being pursued, including gain equalization using grating filters [22], or using fluoride-based EDFAs [23], [24], [25]. It is also desirable to obtain gain over the widest bandwidth possible, and recent advances have been made using tellurite-based EDFAs [26] where a small-signal gain exceeding 20 dB has been demonstrated over an 80 nm bandwidth from 1530 nm to 1610 nm. The feasibility of WDM all-optical networks (WDM-AONs) is also being actively pursued [27], [28], [29]. There are many limiting factors that must be addressed in WDM-AONs, including signal attenuation, crosstalk, signal distortion, noise accumulation and scalability [30]. Moreover, new and/or improved technologies are required [31] for the practical implementation of WDM-AONs, such as optical add-drop multiplexers (OADMs), stable laser sources, flat-gain EDFAs, optical cross-connects (OXCs), and wavelength converters [32]. The activity in WDM-AONs is likely to be very active for many years to come.

1.3.1.3 Polarization-Division Multiplexing

A singlemode fiber is not really "single mode" in that it supports the transmission of two orthogonally polarized modes. These orthogonal modes can be used to simultaneously carry two independent channels, thereby doubling the information throughput. Some of the earlier demonstrations were done by P. M. Hill et al. where a polarization-division multiplexing (PDM) system was used to transmit 4 Gb/s over 45 km [33], and 8 Gb/s over 36 km [34]. A similar scheme to PDM is Polarization Shift Keying-Direct Detection (PolSK-DD). In this scheme, the orthogonal polarization states are alternated to transmit a MARK or SPACE. Fukuchi et al. [35] demonstrated a single and dual channel 5 Gb/s PolSK-DD system over 1000 km of dispersion-shifted fiber (DSF) using nine EDFAs. They conclude that PolSK-DD suppresses the nonlinear effects of self-phase modulation (SPM) and cross-phase modulation (XPM), and that the signaling scheme, therefore, may be useful in WDM systems. Indeed, the WDM demonstration at 1.28 Tb/s in [2] used polarization interleave multiplexing to improve system performance.

1.3.1.4 Soliton Transmission

In a WDM system it is important to limit the optical power to avoid deleterious effects from fiber nonlinearities, such as SPM and XPM. Soliton systems use narrow RZ pulses (typically 10 to 50 ps) of sufficiently high power to exploit fiber nonlinearities by balancing phase changes induced by fiber nonlinearities with the fiber's dispersion [36]. Thus, solitons may be useful for long-haul transmission. A major limitation in soliton systems is Gordon-Haus jitter: a temporal jitter manifested at the receiver due to the random shift in soliton frequency resulting from the nonlinear interaction between noise and signal [37]. Narrow inline filters were proposed to reduce Gordon-Haus jitter, but result in an exponential increase in noise around the signal wavelength. The noise accumulation, however, can be greatly reduced by sliding (slightly shifting) the filter's center frequency at each amplifier stage along the fiber—a nonlinear soliton is able to follow the filters, whereas linear amplifier noise is not. Although short spacing between optical amplifiers was once a concern for soliton systems, recent demonstrations indicate that this is no longer a limitation [38]. For example, in [39] a 200 Gb/s (10x20 Gb/s) soliton WDM system was demonstrated with 100 km amplifier spacing over 1000 km of standard fiber with dispersion compensation and pre-chirping. Indeed, the potential capacity of soliton WDM systems is impressive. For example, 100 Gb/s (5x20 Gb/s) soliton WDM transmission has been demonstrated [40] over 10,000 km, which is a capacity of 1000 Tb/s·km. Research in this area will likely continue to be very active for some time to come.

1.3.1.5 Mid-Span Spectral Inversion (MSSI)

Mid-span spectral inversion (MSSI), also known as nonlinear optical phase conjugation (OPC), uses four-wave mixing between the signal and a high power pump to obtain an optical signal with a conjugated phase [41], [42], [43], [44]. The nonlinear element used can be dispersion-shifted fiber or a semiconductor amplifier. In this scheme, signals at frequencies ω_1 and ω_2 are input to a phase conjugator, placed at mid span, which generates new signals at $2\omega_1-\omega_2$ and $2\omega_2-\omega_1$ with a conjugated phase. The signal with a conjugated phase is then extracted using an optical bandpass filter and transmitted through the second half of the fiber span. Because the phase is conjugated at mid span, transmission through the second half of the fiber reverses the pulse broadening imparted by the first half. Using this technique, it is predicted that 10 Gb/s transmission over 6000 km is possible [45].

1.3.1.6 Dispersion Compensating Fiber and Chirped Bragg Gratings

Dispersion compensating fiber (DCF) is one of the most practical means of dispersion compensation at present [41], [49]. It is fiber designed with a dispersion opposite to that in conventional singlemode fiber, which can be achieved by specially designed refractive index profiles. Because these index profiles are achieved by adding germania to the core and/or adding fluorine to the cladding, DCFs are quite lossy, typically 0.32 to 0.5 dB/km. It is desired to obtain as large a negative dispersion as possible in these fibers without introducing excessive loss. At present, dispersion of -80 to -100 ps/(nm·km) is typical for commercial DCFs. Therefore, 1 km of DCF is required for every 4 to 6 km of standard fiber and, therefore, has the disadvantage of being bulky with a high insertion loss. In addition, the core diameters of DCFs are typically less than 4 µm, making them susceptible to nonlinear effects. An advantage of DCFs is that they are simple passive devices that can be used over a very broad bandwidth. In order to maintain compatibility with future WDM systems, DCFs are also designed with a negative second-order dispersion slope ($dD / d\lambda$) of about -0.2 ps/(nm^2·km) to offset the ~+0.07 ps/(nm^2·km) dispersion slope present in conventional fiber. A figure of merit (FOM) for DCFs is the ratio of dispersion to loss, expressed as an absolute value. Commercial DCFs have FOMs in the range 150 to 250 ps/(nm·dB).

An alternative optical equalization technique uses chirped fiber Bragg gratings [50], [51], [52]. With these devices, a chirped grating (grating period changes with length) is written into the fiber so that the time delay is wavelength dependent. A principle advantage of these devices is that they do not suffer from the nonlinear problems of DCFs. Chirped fiber Bragg gratings can be made with high negative dispersion and a small bandwidth, or lower dispersion and a larger bandwidth, although recent demonstrations have shown chirped fiber gratings with bandwidths of 4 nm [53] and 10 nm [54] for compensating ~100 km of fiber.

1.3.2 Transmission Format Methods

1.3.2.1 Dispersion Supported Transmission

Dispersion Supported Transmission (DST) [46] uses the frequency-chirping properties of a directly-modulated laser to obtain a frequency modulated signal input to the fiber. MARKS and SPACES, each represented by a unique frequency at the fiber input, are converted to amplitude modulation at the fiber output because of group velocity dispersion. The receiver then interprets the resulting intensity fluctuations at the receiver as MARKS and SPACES using conventional threshold detection. This method was used to transmit a 10 Gb/s signal over 204 km [47] and a 20 Gb/s signal over 53 km [48] of standard fiber.

1.3.2.2 Partial-Response Signaling

Partial-response signaling (PRS) can be used to reshape the signal's spectrum such that it is more compatible with the transmission channel [55]. This is done by introducing correlation, that spans two or more bits in the original binary sequence, into a transmitted symbol. Standard singlemode fiber operating at 1550 nm imparts pure phase distortion on the optical field's spectrum for which the dispersive part of the fiber transfer function is of the form $\exp(jkf^2)$ where k is a constant and f is measured relative to f_o, the optical carrier frequency. Because of the square dependence on frequency, this phase distortion will impart a larger phase shift on frequency components farther away from the optical carrier. For this reason, it was felt that signaling schemes that concentrate a greater amount of power closer to the carrier may be more immune to fiber dispersion. Adam Lender describes a class of correlative-level codes called polybinary that achieve this [56], [57]. Much of the research presented in this thesis evaluates the potential of polybinary signaling. It should be noted that a previous project at TRLabs evaluated the potential of duobinary signaling, which is a special case of polybinary, as described in Chapter 2. That work focused on binary transmission with a duobinary filter placed at the receiver [58], and successful duobinary reception of a 10 Gb/s binary signal over

160 km was demonstrated [59]. Other results in the literature demonstrated an improvement in dispersion immunity when three optical intensity levels are transmitted [60], [61]. Moreover, the use of AM-PSK (amplitude modulation with phase-shift keying) duobinary signaling in optical systems [62], [63], [64], [65], [66], [67] is beginning to receive much attention for reasons discussed in Chapters 2 and 7. In fact, this signaling scheme, in conjunction with WDM, was used to achieve the recent record capacities of 1.28 Tb/s [2] and 2.6 Tb/s [1] over a single fiber. An Optical AM-PSK duobinary signal has been demonstrated to reduce the impact of fiber nonlinearities [68], and to improve the reach of systems using chirped fiber Bragg gratings [69]. Much of the research in this thesis is on optical AM-PSK duobinary signaling. A description is given in Chapter 2 of the partial-response signaling schemes investigated.

1.3.2.3 Multilevel Signaling (M-ary ASK)

This transmission scheme is the emphasis of this research, especially the experimental phase. Multilevel signaling may serve as a means for increasing the bit rate in a digital, fiber-optic communication system. For example, if two *B* Gb/s binary signals are mapped into a four-level signal, then 2*B* Gb/s transmission is possible at a symbol rate of *B* GHz using 4-ary amplitude-shift keying (ASK). The penalty in multilevel signaling is eye closure due to more closely spaced levels. A four-level signal requires three times the transmitted optical power of a binary signal to obtain the same separation between received levels. Fortunately, optical amplifiers are presently available making multilevel signaling a viable alternative. Although the concept of multilevel signaling is not new, to our knowledge it has never been demonstrated experimentally (until recently [70]) in a high-speed, fiber-optic communication system. In [70], a 4-level signal was used to frequency modulate a laser in a 20 Gb/s DST system. Another recent demonstration of optical multilevel signaling was presented in [71] where the outputs from two binary, intensity-modulated lasers were power combined to obtain a 4-ary ASK optical signal at 1.244 Gb/s. In that work, the multilevel signal was shown to be more dispersion tolerant than a binary signal after transmission over 600 m of multimode fiber (MMF). Some other theoretical and simulation work has been done [72], [73], [74], but makes many simplifying assumptions about the multilevel system. Moreover, prior to [70], no simple scheme had been presented for generating a multilevel signal at GHz rates from two or more binary signals. Multilevel signaling requires a method for generating multilevel optical intensities at the transmitter and a way to convert the received multilevel signal back to the binary tributaries. A single, externally-modulated laser is desired for the light source to minimize cost and spectral broadening due to laser chirp. This precludes multilevel generation by optical power combining because of the inherent coherency properties accompanying the use of a single laser in singlemode systems [16], [75]. An alternative is to use a multilevel modulator drive voltage. There is no way to generate a multilevel electrical signal using GaAs logic directly because outputs produce only one of two voltage levels; however, very broadband Wilkinson power dividers are available, as well as resistive splitters, which may be used as power combiners to generate a multilevel electrical drive signal by combining two binary signals of unequal weights. This simple approach, which was conceptualized at the outset of this research, was recently used in [70].

The following is a simplified description of the fiber-optic communication system using four-level transmission that was demonstrated in the experimental phase of this work. The scheme used for four-level detection and decoding is also presented. The entire system was constructed using commercially available components and was experimentally demonstrated at 10 Gb/s as a part of this research.

Multilevel Transmitter

Shown in Figure 1.7 is the four-level transmitter.

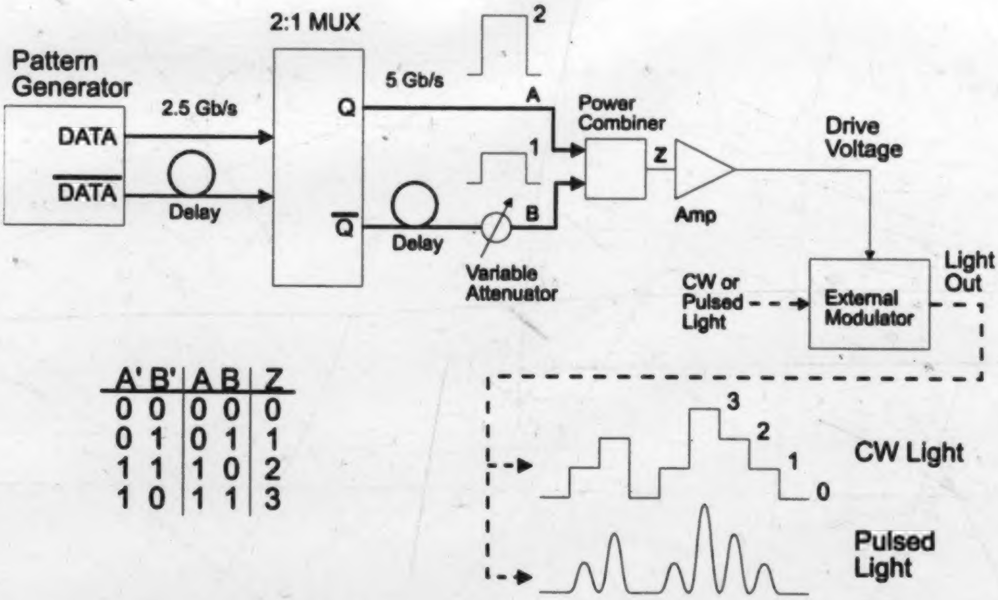

2:1 MUX
Pattern Generator
2.5 Gb/s
DATA
$\overline{\text{DATA}}$
Delay
Q
$\overline{\text{Q}}$
5 Gb/s
2
A
1
B
Delay
Variable Attenuator
Power Combiner
Z
Amp
Drive Voltage
CW or Pulsed Light
External Modulator
Light Out
3
2
1
0
CW Light
Pulsed Light

A'	B'	A	B	Z
0	0	0	0	0
0	1	0	1	1
1	1	1	0	2
1	0	1	1	3

Figure 1.7 Multilevel transmitter using a single 2.5 Gb/s source to simulate four 2.5 Gb/s tributaries transmitted by a 10 Gb/s four-level signal.

The bit-error-ratio tester (BERT) residing at TRLabs is not able to generate data above 3 Gb/s. Therefore, a 2:1 selector (NEL part NLG4115) was used as a 2:1 time-division multiplexer to produce the desired 5 Gb/s data. To simulate two separate 2.5 Gb/s tributaries, one of the signals output from the BERT is delayed by an integer number of bit periods with respect to the other output. Similarly, one of the outputs from the 2:1 selector is delayed by an integer number of bit periods to simulate two different 5 Gb/s data sequences. The two 5 Gb/s data sources are then used to generate a four-level signal at a rate of 5 GHz. This is done by attenuating the 5 Gb/s signals such that one has roughly twice the amplitude of the other, and then combining them with a broadband Wilkinson power divider/combiner or resistive splitter. The variable attenuators following the 5 Gb/s binary signals give a great deal of flexibility when adjusting the relative amplitudes of the multilevel signal. If channel **A** has a normalized amplitude of 2 and channel **B** has a normalized amplitude of 1, then an equally-spaced, four-level signal will result with levels 0,1,2,3. Figure 1.7 shows the resulting four-level signal denoted by Z in the form of a truth table. In practice, the original 5 Gb/s signals **A'B'** should be mapped into **AB** as shown in the truth table of Figure 1.7 (called Gray encoding). This should be done because the most likely error to occur is between two adjacent levels in the received multilevel signal. This precoding step would force only one bit to be in error when decision errors are made between adjacent levels. A laboratory demonstration would not require this precoding stage because, at any given time, only one of the channels is recovered for input to the BERT. However, the desired Gray encoding and decoding could be accomplished by performing the Exclusive-OR operation $\mathbf{B}-\mathbf{B}\oplus\mathbf{A}$ at the transmitter and receiver.

The desired four-level optical signal can be obtained by driving an external optical modulator with the four-level electrical signal. The desired ratio of amplitudes for binary signals **A** and **B** in Figure 1.7 would depend on the transfer characteristic of the external modulator. For example, if evenly spaced levels are desired at the receiver, then for a square-law detector the received optical intensity levels should also be evenly spaced. For a modulator with a $\sin^2(x)$ transfer characteristic, such as a Mach-Zehnder $LiNbO_3$ optical switch, the required drive voltage levels are as shown in Figure 1.8. The input light to the modulator may be continuous wave for NRZ transmission, or be a sequence of pulses with the resulting output as shown in Figure 1.7.

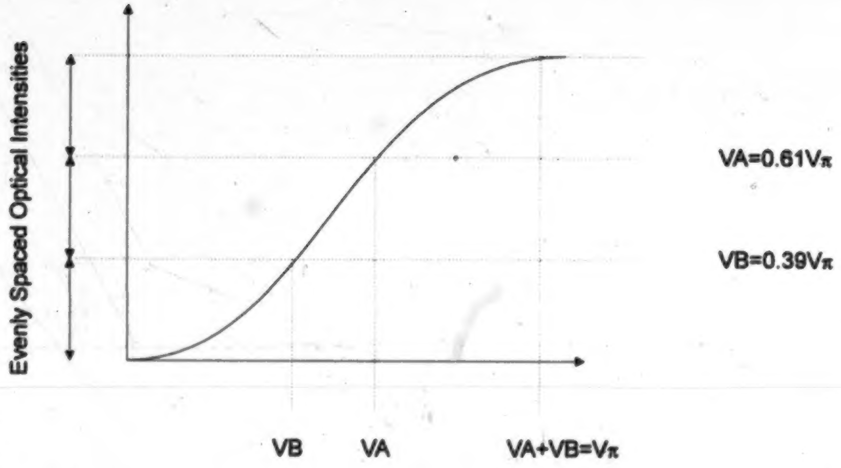

Figure 1.8 Drive voltage levels required to obtain evenly spaced optical intensity levels in a $LiNbO_3$ Mach-Zehnder optical switch .

Multilevel Receiver

A four-level receiver is shown in Figure 1.9.

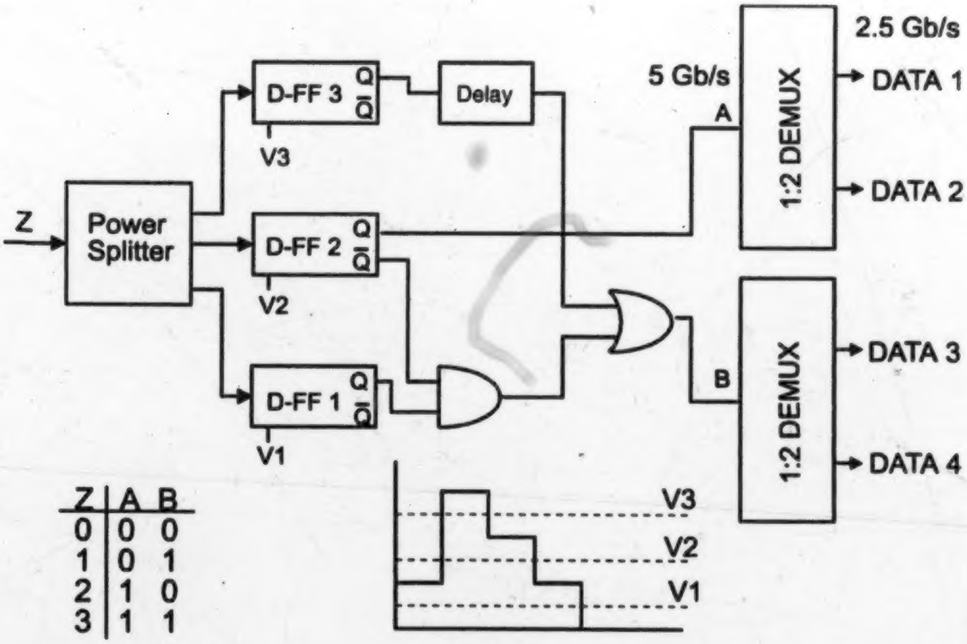
2.5 Gb/s
5 Gb/s
D-FF 3
Q
Q̄
Delay
V3
A
1:2 DEMUX
DATA 1
DATA 2
Z
Power Splitter
D-FF 2
Q
Q̄
V2
D-FF 1
Q
Q̄
V1
B
1:2 DEMUX
DATA 3
DATA 4
V3
V2
V1

Z	A	B
0	0	0
1	0	1
2	1	0
3	1	1

Figure 1.9 Multilevel receiver; the four 2.5 Gb/s tributaries are recovered from the received four-level signal.

After photodetection, the received signal is power divided into three D flip-flops (part NLG4104) that serve as three independent decision circuits. The reference voltage on each flip-flop is set at the decision levels V1, V2 and V3, respectively. From the truth table in Figure 1.9, the 5 Gb/s binary data for channel **A** is obtained directly from the output of the second flip-flop. An OR gate (NLG4101) and AND gate (NLG 4119) are required to extract the binary data for channel **B**, as given by the truth table in Figure 1.9. A delay element at the output of D-FF3 is required to compensate for the propagation delay through the AND gate. Finally, each 5 Gb/s binary signal is routed to a 1:2 DEMUX (NLG4122) to recover the 2.5 Gb/s tributaries.

Higher-level M-ary systems are possible by weighting and combining additional binary tributaries—simulation work is presented in Chapter 7 for an 8-level ASK system. Although the description provided here of a multilevel system is conceptually simple, there are many issues to deal with in making this system actually work at Gb/s rates: impact of inline optical amplifiers; frequency chirping of the transmitted signal; laser source linewidth; component and noise modeling; component characterization; software development for realistic system simulation; accounting for non-ideal frequency response of system components, etc.. All of these issues will be thoroughly treated in the following chapters.

1.4 Thesis Organization

The thesis is organized into nine chapters in an order that reflects the chronology of research activities. Chapter 1 provides some basic background on fiber-optic communications. Limitations in a high-speed optical communication system are discussed along with methods for overcoming them. This research specifically focuses on signaling schemes for increasing the capacity of an optical communication system; the experimental stage focuses on 4-level ASK. A basic description of the signaling schemes explored is given in Chapter 2. Chapter 3 describes the nonlinear nature of the system being considered and explains the methods commonly used for measuring system performance. Noise modeling and component modeling are discussed in Chapters 4 and 5, respectively. Methods for characterizing system components are described in Chapter 6. Simulation results are presented in Chapter 7 for all signaling schemes investigated, and Chapter 8 presents the experimental results of this work, along with details about the setups used. Finally, a summary and conclusions are given in Chapter 9.

2 Signaling Schemes

This chapter describes each of the signaling schemes explored. It explains the fundamental differences among them including PSD (power spectral density), precoding and decoding, and potential advantages and/or limitations. Because of the nonlinear nature of the communication system being considered, the merits of one signaling scheme over another are not immediately obvious; however, the rationale for investigating each of them will be given. The chapter starts with a description of a generalized method for calculating PSDs, followed by a description of each signaling scheme. For the purpose of this discussion, it is assumed that all modulated signals can be represented by

$$s(t) = a(t)\cos(2\pi f_o t) \tag{2.1}$$

where f_o is the optical carrier frequency and $a(t)$ is the baseband modulating signal, which may contain a DC component. Note that, for now, any phase modulation of the carrier is ignored . For optical communication systems, f_o is typically around 200 THz, whereas the frequency content of the baseband signal $a(t)$ is, at most, a few tens of GHz. Therefore, $s(t)$ is a bandpass signal and its spectrum is simply that of $a(t)$ shifted up in frequency by an amount equal to f_o. For this reason, the following discussion focuses on the PSD of the baseband signal $a(t)$.

2.1 Power Spectral Density

Consider a digital baseband information signal $a(t)$ represented by a superposition of identically-shaped, randomly-weighted pulses, through

$$a(t) = \sum_n I_n g(t - nT) \tag{2.2}$$

Here, T is the time between pulses (symbol period), $g(t)$ is the pulse shape, and $\{I_n\}$ is the information sequence of discrete values. The PSD of $a(t)$ can be calculated from [76]

$$S_a(f) = \frac{1}{T}|G(f)|^2 S_i(f) \tag{2.3}$$

where $G(f)$ is the Fourier transform of $g(t)$, and $S_i(f)$ is the PSD of the information sequence given by

$$S_i(f) = \sum_{k=-\infty}^{\infty} \Phi_i(k) \exp(-j2\pi fkT) \tag{2.4}$$

where $\Phi_i(k)$ is the autocorrelation sequence, defined as

$$\Phi_i(k) = E[I_n I_{n+k}] \tag{2.5}$$

for which $E[\ ]$ denotes the expected value and $\{I_n\}$ is assumed to be a real-valued sequence. When the information symbols are uncorrelated, it is possible to cast (2.3) into a more useful form [76], given by

$$S_a(f) = \frac{\sigma_i^2}{T}|G(f)|^2 + \frac{\mu_i^2}{T^2}\sum_{k=-\infty}^{\infty}\left|G\left(\frac{k}{T}\right)\right|^2 \delta\left(f - \frac{k}{T}\right) \tag{2.6}$$

where μ_i and σ_i^2 represent the mean and variance, respectively, of an information symbol, and $\delta(x)$ is the delta function. From (2.6) it can be seen that the PSD consists of a continuous spectrum, given by the first term, and discrete line spectra, given by the second term. Note that when an information symbol has zero mean, there are no discrete line spectra in the PSD. Finally, if the information signal $a(t)$ is passed through a linear system having a transfer function $H(f)$, the PSD $S_r(f)$ of the output signal can be obtained from

$$S_r(f) = S_a(f)|H(f)|^2 \tag{2.7}$$

Equations (2.6) and (2.7) can be used to calculate the PSD for any of the following signaling schemes.

2.2 Binary ASK

Binary signaling uses amplitude-shift keying (ASK) of the optical carrier, i.e., $a(t)$ is switched between two states to represent MARKS (logical ONES) and SPACES (logical ZEROS). It is the simplest of the modulation formats considered and allows for viable operation even when the signal is relatively noisy and distorted. In high-speed optical communication systems, the frequency response of ultra-wideband electrical and optoelectronic components is often far from ideal. Conventional high-speed systems use binary ASK because it can accommodate a wide variation in device behavior, and provides good performance when the received optical power is low.

2.2.1 PSD of an NRZ Binary Signal

Non-return-to-zero (NRZ) binary signaling is achieved by directly modulating a laser or external modulator with an NRZ information signal. Here, the elements of the information sequence $\{I_n\}$ are either 0 or 1, are independent of one another, and occur with equal probability. If the NRZ rectangular pulse shape $g(t)$ has an amplitude equal to A during the interval T, and is otherwise 0, the PSD can be obtained from (2.6) as

$$S_a(f) = \frac{A^2T}{4}\text{sinc}^2(fT) + \frac{A^2}{4}\delta(f) \tag{2.8}$$

where $\text{sinc}(x) = \sin(\pi x)/(\pi x)$. A plot of (2.8) is shown in Figure 2.1.

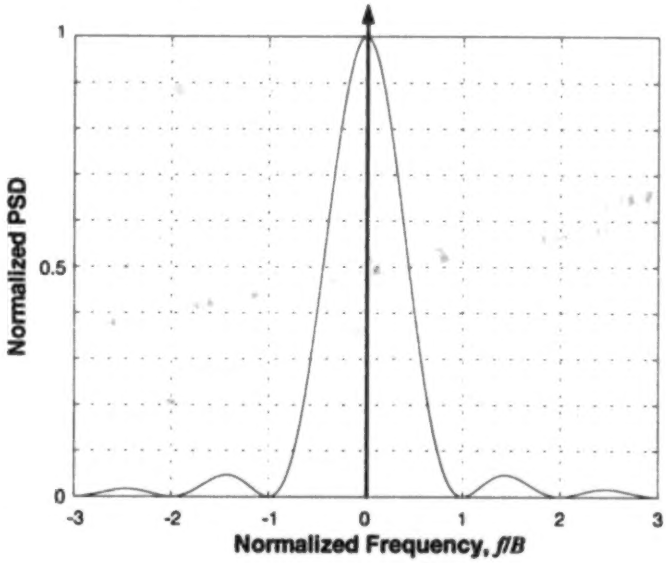

Figure 2.1 PSD of a binary NRZ Signal.

Note that the first nulls occur at $\pm 1/T = \pm B$ where B is the bit rate, and that ~90 % of the power that makes up the continuous part of the spectrum is contained in the main lobe. This signal can be successfully transmitted in a bandwidth of roughly $\pm B$ about the carrier. Hence, the transmission bandwidth required for this signal is ~$2B$. Note that for return-to-zero (RZ) signaling, the PSD is modified through the form of $G(f)$. In that case, nulls in the spectrum of $G(f)$ will not necessarily coincide with the line spectra; therefore, the PSD will generally possess additional line spectra at frequencies other than zero.

2.3 M-ary ASK

With multilevel ASK (M-ary ASK), the amplitude of the carrier $a(t)$ is switched between multiple levels where each level represents two or more bits of information. If q is the number of bits represented by each symbol, then the number of levels required for each symbol is $M=2^q$. A multilevel signal is more sensitive to noise and distortion than a binary signal and, therefore, requires higher-quality components and a larger optical power at the receiver. However, with the advent of EDFAs, concern has shifted from available optical power to fiber dispersion limitations. Fiber dispersion is related to the transmission bandwidth of the signal and, because a multilevel signal requires a narrower transmission bandwidth than a binary signal, it may be more immune to fiber dispersion. In addition, logic devices operate at a lower bit rate when using multilevel signaling, and the bandwidth requirement of electrical components is reduced.

2.3.1 Generating an M-ary Signal

An M-ary signal can be generated by weighting the binary tributaries and then summing the result. To obtain evenly-spaced levels for the multilevel signal, the binary tributaries should be weighted according to a geometric sequence with a common ratio of 2, i.e., {1, 2, 4, 8...}. Figure 2.2 shows a 4-level signal generated from two binary tributaries, **A** and **B**.

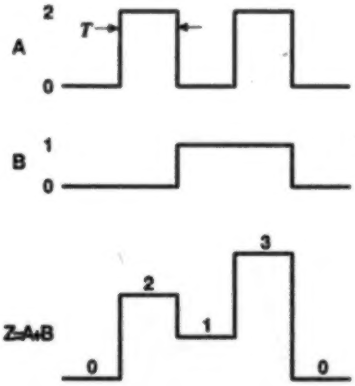

Figure 2.2 Constructing a 4-level signal from 2 binary signals.

Note that the symbol period T for a multilevel signal is the same as for a single tributary.

2.3.2 PSD of an M-ary NRZ Signal

Consider an M-ary signal having M evenly-spaced levels with amplitudes {0, 1, 2,...M-1} where each level is equally likely with probability 1/M. Assuming the binary tributaries are independent, the generalized PSD for this signal can be obtained from (2.6) as

$$S_a(f)=\frac{\left(M^2-1\right)}{12T}\left|G(f)\right|^2+\frac{(M-1)^2}{4T^2}\sum_{k=-\infty}^{\infty}\left|G\left(\frac{k}{T}\right)\right|^2\delta\left(f-\frac{k}{T}\right) \tag{2.9}$$

If the same NRZ pulse shape is used as in (2.8), then (2.9) becomes

$$S_a(f)=\frac{\left(M^2-1\right)A^2T}{12}\operatorname{sinc}^2(fT)+\frac{(M-1)^2A^2}{4}\delta(f) \tag{2.10}$$

Note that the PSD of an M-ary signal has the same form as the binary signal in (2.8). Also, just as with a binary signal, the M-ary signal requires a transmission bandwidth of ≈2/T about the carrier; however, each symbol now carries $\mathrm{Log}_2(M)$ bits of information. Therefore, the transmission bandwidth required for an M-ary signal is reduced by a factor of $\mathrm{Log}_2(M)$ in comparison to that for a binary signal operating at the same bit rate. When an RZ pulse shape is used, the M-ary PSD will be modified in the same way as described for the binary case.

2.4 Polybinary ASK

Polybinary signals are multilevel signals obtained by introducing correlation among bits in a binary sequence. This process is referred to as correlative-level coding [56], [57] or partial-response signaling [55]. The interesting property of polybinary signals is that power is redistributed such that there is more relative power at lower frequencies (frequencies closer to the carrier in the modulated signal). Because the phase distortion of the electric field's spectrum increases for frequencies farther away from the carrier when transmitting over dispersive fiber, it was felt that polybinary signals may be more immune to dispersion.

2.4.1 Generating a Polybinary Signal

A polybinary signal is obtained by passing a binary signal through the filter shown in Figure 2.3.

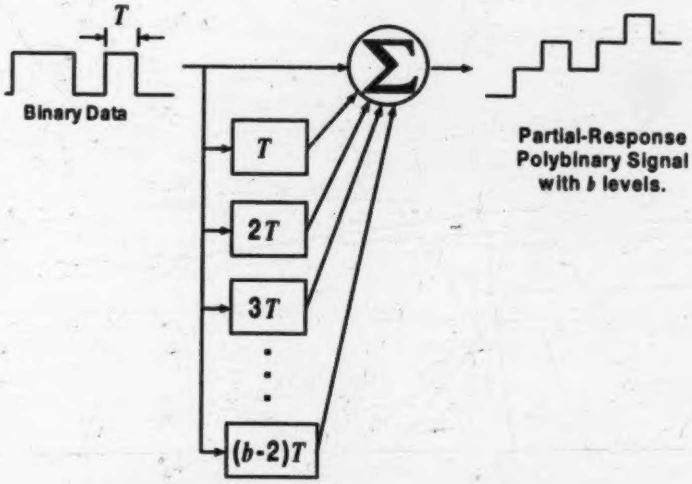

Figure 2.3 Filter for generating a polybinary signal.

If the input binary sequence consists of levels 0 and 1, then the signal output from the polybinary filter will contain *b* levels when there are (*b*-2) delay elements. In other words, correlation introduced among (*b*-1) binary symbols results in a partial-response signal containing *b* levels. Note that a duobinary signal is a polybinary signal with $b=3$. It is important to note the difference between a multilevel polybinary signal and the M-ary signal described earlier. Although both have a symbol duration equal to *T*, each symbol in a polybinary signal carries only one bit of information, regardless of the number of levels. In other words, for an aggregate bit rate *B*, the symbol period for a polybinary signal is always $1/B$, whereas for an M-ary signal with *M* levels the symbol period is $\log_2(M)/B$. Also, a polybinary signal can only make transitions between adjacent levels. Finally, for a polybinary signal, the probability of a given level occurring decreases for levels farther from the middle level. For *b* levels spaced at {0, 1, 2,...(*b*-1)}, the probability of the m^{th} level occurring can be shown to be

$$P(m) = \frac{\binom{(b-1)}{m}}{2^{b-1}} \tag{2.11}$$

where $\binom{x}{y}$ is the binomial coefficient.

2.4.2 Precoding and Decoding

Because correlation is introduced among symbols in the original binary sequence, it would appear that recovering a binary symbol requires an observation of the detected polybinary symbols over more than one symbol period. This also suggests that an error in a given polybinary symbol could produce additional errors in the decoded binary sequence, i.e., errors could propagate. However, it is possible to decode the binary sequence from decisions made on individual polybinary symbols, independent of one another, if a form of precoding is used. Consider the case when $b=3$. Let $\{a_k\}$ represent the original binary sequence and $\{b_k\}$ be a binary sequence obtained by applying a coding rule to $\{a_k\}$. Finally, let $\{c_k\}$ represent the polybinary signal. The elements of $\{a_k\}$ can be recovered from independent decisions on $\{c_k\}$ if the following relationships are used

$$\begin{aligned} a_k &= (b_k + b_{k-1}) \mod 2 \qquad (2.12) \\ c_k &= b_k + b_{k-1} \end{aligned}$$

where $(x \pm y) \bmod 2$ is the modulus of the remainder of $(x \pm y)/2$. Therefore, from (2.12) the precoded sequence $\{b_k\}$ is obtained from

$$b_k = (a_k - b_{k-1}) \mod 2 \qquad (2.13)$$

For binary numbers, modulo-2 subtraction is equivalent to modulo-2 addition, which is equivalent to an Exclusive-OR operation. Hence, (2.13) could also be written $b_k = a_k \oplus b_{k-1}$. For larger values of b, the generalized precoding rule becomes [56]

$$b_k = a_k \oplus b_{k-1} \oplus b_{k-2} \ldots \oplus b_{k-(b-2)} \qquad (2.14)$$

When the above precoding rule is applied, the original data sequence can be recovered by independent decisions on $\{c_k\}$, through

$$a_k = c_k \mod 2 \qquad (2.15)$$

From (2.15) it can be seen that *even* levels in $\{c_k\}$ represent a SPACE, whereas *odd* levels represent a MARK. This pattern can be inverted by simply replacing a_k in (2.14) with its complement. Note, too, that it is possible to detect errors in the received polybinary signal by monitoring pattern violations [57]. For example, consider the properties of a duobinary signal ($b=3$). A transition from the highest to lowest level (MARK to MARK) should never occur, but should be separated by an odd number of SPACES. Also, if two MARKS represented by the same level are separated by SPACES, the number of intervening SPACES must be even. Note that, although error detection is possible, error correction is not because the time location of the error that causes a pattern violation is not known. Nonetheless, error monitoring can be used as a measure of channel quality.

2.4.3 PSD of a Polybinary Signal

We could use the statistics of the correlated symbols output from the filter in Figure 2.3 along with (2.3) through (2.5) to calculate the PSD. An alternative approach is to use the uncorrelated statistics of the binary sequence so that we may apply (2.6). Then, the partial-response filter of Figure 2.3 can be accounted for using (2.7). The filter in Figure 2.3 has a periodic transmission response (in frequency) with period 1/*T*, and has nulls that are spaced 2/((*b*-1)*T*) apart. Figure 2.4 shows the power transmission response, normalized to unity gain at dc, of a polybinary filter for *b*=3, 5 and 7.

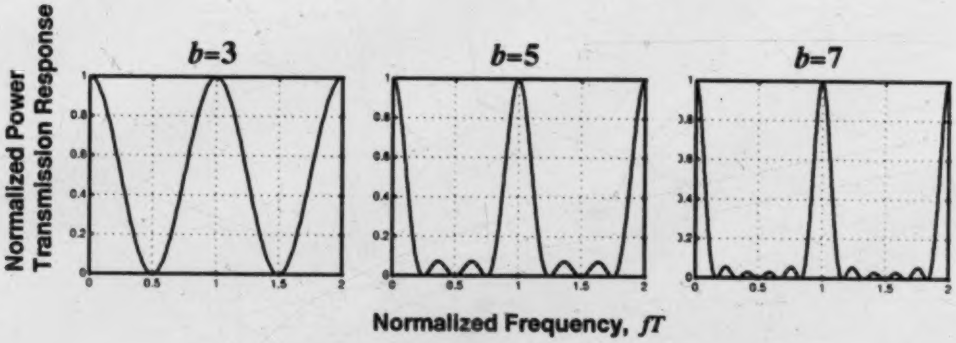

Figure 2.4 Power transmission response of a polybinary filter.

Obviously, the polybinary filter will produce nulls in the PSD at the same places they occur in the filter response. When an ideal NRZ binary sequence with amplitude *A* is input to the polybinary filter, an ideal NRZ polybinary signal will result at the output, for which the continuous part of the PSD can be written as [57]

$$S_r(f) = \frac{(b-1)^2 A^2 T}{4} \operatorname{sinc}^2\{(b-1)fT\} \tag{2.16}$$

The normalized PSD of (2.16) is shown in Figure 2.5 for b=2, 3, 5 and 7. It is evident that the first null in the PSD is lowered in frequency by a factor of 1/(*b*-1) in comparison to a binary signal. Note, too, the functional similarity of (2.16) with the continuous part of the PSD given in (2.8), which is obtained by setting *b*=2 in (2.16).

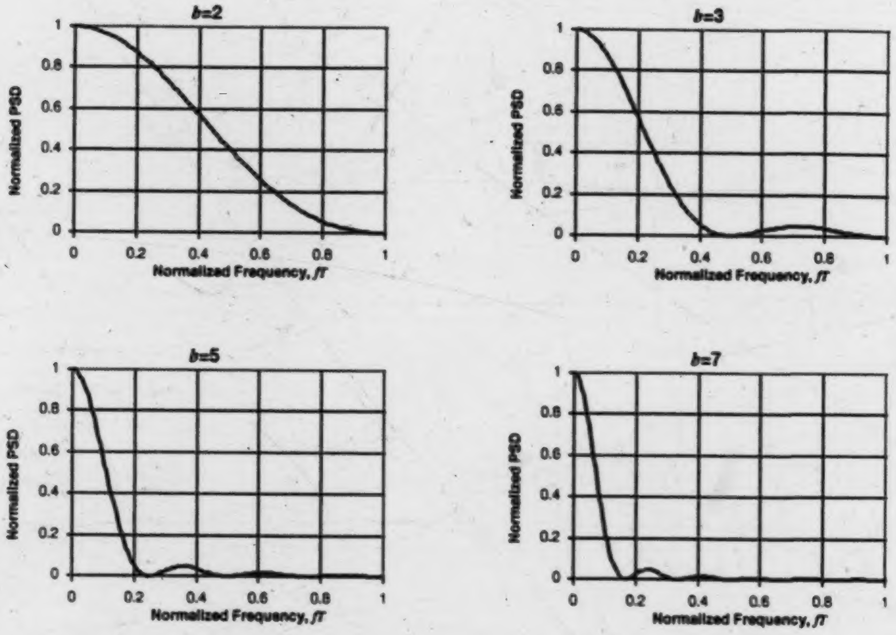

Figure 2.5 PSDs of NRZ polybinary signals.

As with a binary signal, ~90% of the power is contained in the main lobe, regardless of the value of *b*. It was mentioned that a binary signal can be transmitted in a bandwidth bounded by the nulls of the main lobe. However, this is not true for a polybinary signal. This is easy to see when one considers the polybinary signal in the time domain for which the symbol period is equal to *T*, regardless of the number of levels *b*, as illustrated in Figure 7.18 in Chapter 7. Different weights for a transmitted symbol do not change the pulse response requirements of the channel to obtain zero ISI. Hence, Nyquist's criterion for zero ISI must still be satisfied, which relates the required transmission bandwidth to the symbol period, not the value of *b*.

2.5 Polyquaternary ASK

It is possible to extend the ideas of polybinary signaling to M-ary input sequences [77]. For example, consider a 4-level (quaternary) signal where each symbol represents two bits of information. This signal can be filtered by a delay-and-add circuit to produce a partial-response signal with 7 levels, with a corresponding redistribution of power in the PSD. Of course, each symbol in the polyquaternary signal still carries only two bits of information.

2.5.1 Precoding and Decoding

Precoding and decoding is done in a similar manner to polybinary, except mod 2 operations are replaced by mod 4. Also, unlike for binary signals, modulo addition is not equivalent to modulo subtraction. For example, consider the precoding for a polyquaternary signal correlated over two symbols. The precoded 4-level sequence $\{b_k\}$ is obtained from

$$b_k = (a_k - b_{k-1}) \quad \text{mod } 4 \tag{2.17}$$

where $\{a_k\}$ is the original 4-level sequence. The polyquaternary signal is then obtained from $c_k=b_k+b_{k-1}$. Finally, the 4-level sequence is obtained from independent decisions on each polyquaternary symbol, through

$$a_k = c_k \quad \text{mod } 4 \tag{2.18}$$

Note that the mod Q operator can be applied to positive or negative numbers. For positive numbers, it is simply the remainder when dividing the number by Q. For negative numbers, you must first add a multiple of Q that makes the number ≥0. For example, 3 mod 4=3, 6 mod 4=2, and -5 mod 4=3.

2.5.2 PSD of a Polyquaternary Signal

Because the M-ary signal is subjected to the same partial-response filter of Figure 2.3, its PSD will be altered in the same way as for a polybinary signal. For an ideal NRZ M-ary signal with equally-spaced levels, each separated in amplitude by an amount *A*, the continuous part of the PSD can be expressed as

$$S_r(f) = \frac{5(b-1)^2 A^2 T}{4} \text{sinc}^2((b-1)fT) \tag{2.19}$$

where, here, *b* is the number of levels that would be produced in response to a binary signal, i.e., the partial-response filter has *b*-2 delay elements.

2.6 AM-PSK Duobinary

Consider the case when the baseband duobinary signal $a(t)$ has no dc component so that its levels are [-1 0 1]. When it modulates the carrier as in (2.1), the PSD about the carrier will be that of a duobinary signal with a suppressed carrier. Now, recall that the states of the duobinary signal [-1 0 1] represent the encoded binary symbols [1 0 1]. Hence, the two duobinary MARK states result in a carrier with equal amplitude, but with a π radians phase shift with respect to one another, and a SPACE is represented by the absence of carrier. The intriguing thing here is that an envelope detector will properly recover the binary data. Therefore, a receiver that directly detects intensity (power) will properly decode the signal. This type of signaling is appropriately called AM-PSK (amplitude modulation with phase-shift keying) duobinary [56], [57].

2.6.1 Generating an Optical AM-PSK Duobinary Signal

Generation of an optical AM-PSK duobinary signal can be accomplished by biasing a Mach-Zehnder (MZ) external modulator at maximum extinction and applying a baseband duobinary signal, as shown in Figure 2.6. Also shown in Figure 2.6 is the conventional way of biasing a MZ external modulator to produce a binary, intensity-modulated signal.

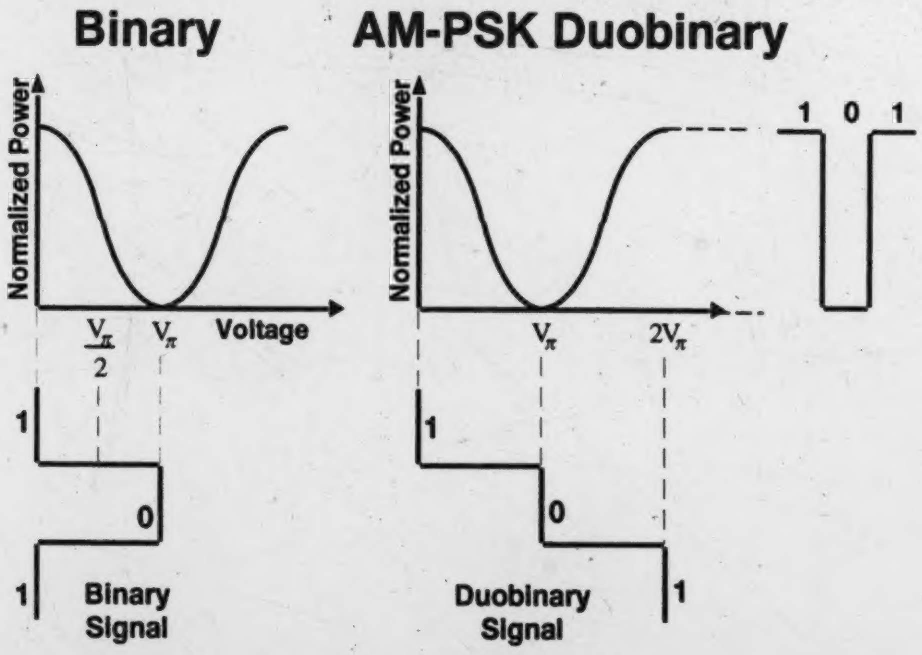
Binary
AM-PSK Duobinary
Normalized Power
Normalized Power
1 0 1
$\frac{V_\pi}{2}$
V_π
Voltage
V_π
$2V_\pi$
1
0
1
Binary Signal
1
0
1
Duobinary Signal

Figure 2.6 Mach-Zehnder drive condition to obtain a conventional binary, intensity-modulated signal (left) and an optical AM-PSK duobinary signal (right).

As the electrical signal passes through the point of maximum extinction, the phase of the optical carrier is reversed, providing the desired phase-shift keying. Details about the MZ's transfer characteristic are given in Chapter 5.

The optical AM-PSK signaling scheme is beginning to receive much attention because of its many desirable properties, including the fact that it

- is less susceptible to dispersion because of a reduced transmission bandwidth [65]
- can be used with a conventional binary receiver, with no inherent degradation in the receiver's sensitivity
- reduces the bandwidth requirement of transmitter electronics
- can greatly increase the dispersion-limited distance when used with chirped Bragg gratings [69]
- reduces fiber nonlinear effects because of the suppressed carrier, and allows for closer channel spacing in WDM applications [1], [68]

2.6.2 PSD of an AM-PSK Duobinary Signal

In accordance with (2.1), the PSD of the bandpass signal is simply that of $a(t)$ centered about the carrier. Because $a(t)$ is a duobinary signal, the spectrum about the carrier must be that of a duobinary signal.

2.7 AM-PSK Polybinary

It is also possible to use AM-PSK signaling with higher-level polybinary signals. For example, the external modulator of Figure 2.6 could be modulated by a polybinary signal having 5 levels to produce three transmitted intensity levels. As with AM-PSK duobinary signaling, the signal's spectrum is simply that of the polybinary baseband signal shifted up in frequency by an amount equal to the carrier frequency.

2.8 Summary

This chapter gave a basic description of the signaling schemes explored as a part of this research. These include conventional binary, M-ary ASK, polybinary ASK, polyquaternary ASK, and AM-PSK polybinary. Calculating the PSD for these signals was explained. The motive for exploring these signalling schemes is that the power in the transmitted signal is more concentrated about the carrier where phase distortion of the optical field's spectrum is reduced.

3 Fiber-Optic System Response and Performance Measures

This Chapter explains the mathematical model used for calculating the system's response to an input information signal. Methods for evaluating performance are also explained including eye diagrams, bit-error ratio, and receiver sensitivity. Topics on realizable filters that minimize intersymbol interference are also discussed. For contrast, communication systems that can be modeled as linear in optical power are described first—these use an LED with multimode or singlemode fiber. Then, a description is given of the nonlinear model required for the system considered in this research, which uses an external modulator, semiconductor laser, and singlemode fiber. The parameter that determines whether or not a system can be modeled as linear in the power domain is the source's spectral width. When an LED is used, the source width is many THz, which is much larger than the bandwidth of the modulating signal. Hence, the spectral width of the optical signal is set by the source width, and does not depend on the bandwidth of the modulating signal. The fiber dispersion then acts on the randomly changing electric field of the source, with an overall averaging effect that allows the fiber to be treated as a linear filter acting on the optical intensity. When a laser is used at Gb/s data rates, the source linewidth—typically a few tens of MHz—is much narrower than the bandwidth of the modulating signal, in which case the spectrum of the modulated carrier is determined by the modulating signal. In this case, to accurately predict the intensity envelope at the fiber's output, it is necessary to account for the phase shift of spectral components in the electric field domain resulting from fiber dispersion.

3.1 Determining System Response

Described below are appropriate models for calculating the system's response for three different system types: LED with multimode fiber; LED with singlemode fiber; laser diode with singlemode fiber. The system considered throughout this thesis uses a laser diode with singlemode fiber. However, to illustrate how it differs from other system types, models of systems using an LED are described first.

3.1.1 LED with Multimode Fiber

Consider a directly-modulated LED operating over multimode fiber, as shown in Figure 3.1.

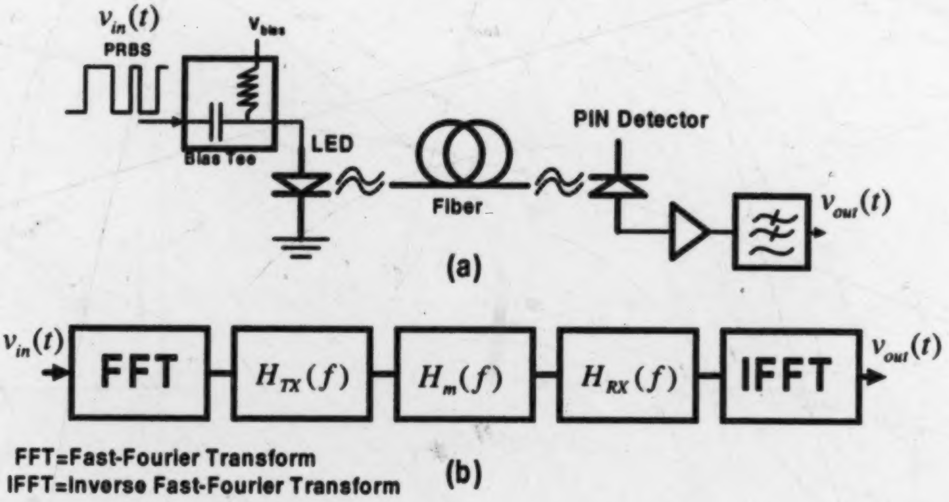

Figure 3.1 Optical communication system using a directly-modulated LED and multimode fiber: (a) block diagram; (b) equivalent model.

Here, $H_{TX}(f)$ represents the frequency response of all transmitter components, including the LED, and $H_{RX}(f)$ represents the frequency response of all receiver components, including the photodetector. The fiber is modeled as a linear filter $H_m(f)$ that acts on the optical intensity (power). Note that the optical intensity at the fiber input is linearly proportional to the applied information signal, and that the received electrical signal is linearly proportional to the optical intensity incident on the photodetector. Hence, the entire system is treated as a linear channel from electrical input to electrical output. The multimode fiber transfer function can be written as [78]

$$H_m(f) = \exp\left(-\sigma_m^2 2(\pi f)^2 - j2\pi f t_d\right) \tag{3.1}$$

where t_d is the bulk time delay through the fiber and σ_m is the rms pulse spreading from intermodal dispersion. The second term in the exponential of (3.1) simply represents the linear phase shift associated with t_d and, therefore, does not distort the pulse. The fiber transfer function acts as a lowpass filter on the optical intensity for which the 3-dB cutoff frequency can be obtained as

$$f_{3dB} = \frac{\sqrt{\ln(2)}}{2\pi\sigma_m} \approx \frac{1}{8\sigma_m} \tag{3.2}$$

For step-index multimode fiber, an approximation for the rms pulse spreading is [4]

$$\sigma_m \approx \frac{Ln_1\Delta}{2\sqrt{3}c} \qquad \text{(step index)} \qquad (3.3)$$

where L is the fiber length, n_1 is the core's index of refraction, c is the free-space speed of light, and $\Delta=(n_1-n_2)/n_1$ is the refractive index difference between the core and cladding (n_2 is the index of refraction for the cladding). If graded-index multimode fiber is used that has a near-parabolic index profile, the rms pulse spreading can be greatly reduced to [4]

$$\sigma_m = \frac{Ln_1\Delta^2}{20\sqrt{3}c} \qquad \text{(graded index)} \qquad (3.4)$$

The capacity of the fiber channel is often expressed as a bandwidth-length product. For a conventional system that uses binary intensity modulation, the required bandwidth is roughly equal to the bit rate B, so that a bit rate-length product can also be obtained. Using (3.2) and (3.3), and typical values of $\Delta=0.01$ and $n_1=1.5$, the capacity of step-index multimode fiber is about 10 (Mb/s)·km. By using graded-index fiber, (3.4) suggests that the capacity can be increased by a factor of ≈1000. However, this is not true in practice because of variations in the graded-index profile over the fiber's length. Also, the effect of intramodal dispersion (waveguide and material dispersion) becomes significant in multimode fiber—hence, the spectral width of the source becomes important. Realistic capacities for graded-index fiber are roughly 100 (Mb/s)·km and 1 (Gb/s)·km when using an LED or semiconductor laser, respectively.

3.1.2 LED with Singlemode Fiber

For this case, too, the fiber can be modeled as a linear filter acting on the optical intensity. If the LED is assumed to have a Gaussian-intensity distribution about its mean wavelength, and an rms spectral width σ_D, the fiber transfer function can be written as [79]

$$H(f) = \left(1 + j2\pi fL\sigma_D^2 \frac{d^2\tau}{d\lambda^2}\right)^{-1/2} \exp\left[\frac{-2(\pi fL\sigma_D)^2\left(\dfrac{d\tau}{d\lambda}\right)^2}{\left(1 + j2\pi fL\sigma_D^2 \dfrac{d^2\tau}{d\lambda^2}\right)}\right] \qquad (3.5)$$

where τ is the group delay per unit distance. For a depressed-cladding singlemode fiber having a dispersion minimum at 1310 nm, τ can be expressed by [79]

$$\tau(\lambda) = a + b\lambda^2 + c\lambda^{-2} \tag{3.6}$$

where for the fiber in [79] a=34.74 ns/km, b=10.11 ns/(km·μm^2) and c=29.83 ns·μm^2/km. The fiber transfer function of (3.5) behaves as a lowpass filter with a bandwidth determined by the fiber length L, source spectral width σ_D, and the fiber material dispersion through $d\tau/d\lambda$ (first-order dispersion) and $d^2\tau/d\lambda^2$ (second-order dispersion). Figure 3.2 shows the fiber's magnitude response at various distances when operating at 1500 nm with an LED having a spectral width of 50 nm.

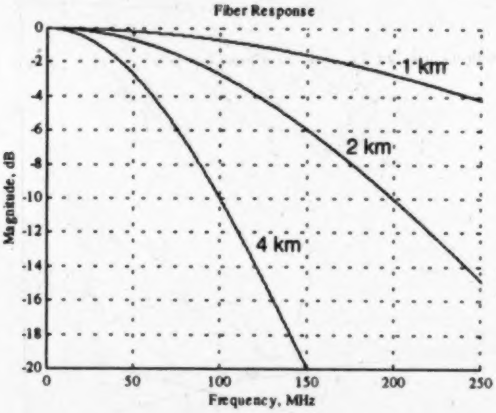

Figure 3.2 Magnitude response of singlemode fiber when using an LED.

In Figure 3.2, the response at 1 km has a 3-dB cutoff at ~210 MHz. Assuming that the maximum bit rate is about 1 to 2 times the bandwidth, this corresponds to a fiber capacity of about 200-400 (Mb/s)·km. The fiber's capacity can also be estimated using the rms pulsewidth of its impulse response, given by [79]

$$\sigma_f = L\sigma_D\left[\left(\frac{d\tau}{d\lambda}\right)^2 + \frac{1}{2}\sigma_D^2\left(\frac{d^2\tau}{d\lambda^2}\right)^2\right]^{\frac{1}{2}} \tag{3.7}$$

Assuming σ_f can be as large as $T/4$ where T is the bit period, the maximum bit rate is $B \approx 1/4\sigma_f$, and a BL product can be obtained. For standard singlemode fiber operating at 1500 nm, the first-order dispersion $d\tau/d\lambda$ will dominate and, assuming an LED source width of 50 nm, the system capacity would be ~300 (Mb/s)·km, which agrees with the result obtained from Figure 3.2.

3.1.3 Laser Diode with Singlemode Fiber

As mentioned in the introduction, this research focuses on transmission at ~1550 nm over standard singlemode fiber. Here, first-order dispersion is dominant and is usually expressed by a dispersion coefficient $D=d\tau/d\lambda$ that is typically 15 to 20 ps/(km·nm). In a similar manner to systems using singlemode fiber with an LED, an approximation of system capacity may be obtained, except that the spectral width of the source is now determined by the width of the modulating signal's spectrum. In this case, the spectral width $\Delta\lambda$ becomes linearly proportional to the bit rate B. The dispersion is $\sigma=DL\Delta\lambda$, which, using $\Delta\lambda=\Delta f\lambda^2/c$, can be written $\sigma=DL\Delta f\lambda^2/c$ where c is the free-space speed of light. Now, assuming that the dispersion can be some fraction k of the bit period $T=1/B$, the system capacity can be arrived at as $B^2L=kc/(D\lambda^2)$, so that the system capacity is expressed as a B^2L product rather than a BL product. For a dispersion between 0.25 and 0.5 times the bit period and a dispersion coefficient of D=17 ps/(km·nm), the system's capacity can be calculated to be between 3700 and 7400 $(\mathrm{Gb/s})^2\cdot\mathrm{km}$. However, the fiber can no longer be modeled as a linear filter acting on the optical power. Instead, it can be modeled as a linear filter acting on the optical electric field. The relationship between the optical field and the electrical signals at the transmitter and receiver is, however, nonlinear, as shown in the system model of Figure 3.3.

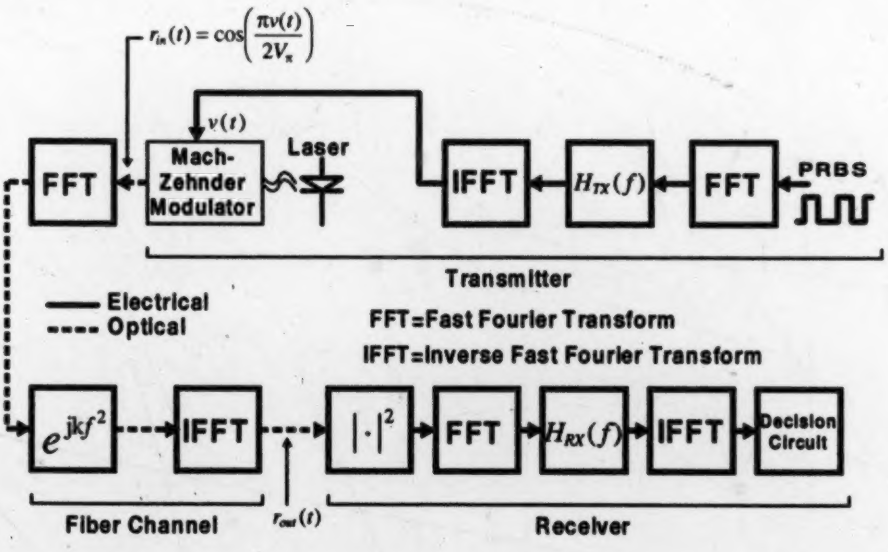
$r_{in}(t)=\cos\left(\frac{\pi v(t)}{2V_\pi}\right)$
$v(t)$
FFT
Mach-Zehnder Modulator
Laser
IFFT
$H_{TX}(f)$
FFT
PRBS
Transmitter
Electrical
Optical
FFT=Fast Fourier Transform
IFFT=Inverse Fast Fourier Transform
e^{jkf^2}
IFFT
$|\cdot|^2$
FFT
$H_{RX}(f)$
IFFT
Decision Circuit
Fiber Channel
$r_{out}(t)$
Receiver

Figure 3.3 Nonlinear model for a communication system that uses an external modulator and laser.

As can be seen from Figure 3.3, the input optical field $r_{in}(t)$ is a nonlinear function of the modulating voltage $v(t)$. Similarly, the received electrical signal is a nonlinear function of the received optical field $r_{out}(t)$ because the photodetector produces a signal proportional to the received optical power, which varies as the square of the field amplitude. The transfer characteristic for the external modulator would, generally, also impart phase modulation on the optical carrier. A detailed description of the fiber transfer function and a detailed model for the Mach-Zehnder external modulator are presented in Chapter 5.

3.1.3.1 Lowpass-Equivalent Modeling of a Bandpass System

A wavelength of 1500 nm corresponds to a carrier frequency of about 200 THz, whereas the width of the spectrum about the carrier is, at most, a few tens of GHz. Hence, the fiber channel is a bandpass system and can be appropriately treated with a lowpass equivalent model [78]. Indeed, this is necessary if a discrete-time analysis is to be used, i.e., the sampling interval is then determined by the spectral width of the modulating signal rather than the optical carrier frequency. The bandpass signals at the fiber input and output have the general forms

$$\begin{aligned} s_{in}(t) &= a_{in}(t)\cos\left(2\pi f_o t + \varphi_{in}(t)\right) \\ s_{out}(t) &= a_{out}(t)\cos\left(2\pi f_o t + \varphi_{out}(t)\right) \end{aligned} \tag{3.8}$$

for which the lowpass-equivalent (complex envelope) signals are

$$\begin{aligned} r_{in}(t) &= a_{in}(t)\exp\left(j\varphi_{in}(t)\right) \\ r_{out}(t) &= a_{out}(t)\exp\left(j\varphi_{out}(t)\right) \end{aligned} \tag{3.9}$$

The output field is obtained by multiplying the spectrum (FFT) of $r_{in}(t)$ with the lowpass-equivalent, electric-field transfer function for the fiber, which, as explained in section 5.3, has the form $\exp(jkf^2)$ where k is a constant. The IFFT is then computed on the result to obtain the optical signal $r_{out}(t)$ at the fiber output. The modulus squared is then taken of $r_{out}(t)$, which gives the intensity envelope at the receiver, to obtain the baseband electrical signal at the receiver, as provided by an ideal photodetector. Any linear filtering at the receiver is then applied to obtain the signal input to the decision circuit. Receiver filtering would normally include the frequency response of the photodetector, electrical amplifiers and a lowpass filter. Details about using the FFT/IFFT for linear system analyses are given in Appendix A. Note that the fiber transfer function imparts pure phase distortion on the electric field's spectrum—there is no significant band limiting of the optical spectrum. It is important that the lowpass-equivalent transfer function is not confused with that for a lowpass filter. The impulse response of a lowpass filter is real-valued and is convolved with a real-valued input signal. In a lowpass-equivalent system, such as we have here, the impulse responses of a lowpass-equivalent filter and the input and output signals, are, in general, complex-valued. The actual bandpass system, of course, operates on real-valued signals.

In summary, the electrical part of the transmitter and receiver are treated as linear systems in which filtering can be carried out in the frequency domain. Similarly, the fiber channel is treated as a lowpass-equivalent linear system operating on the optical field's complex envelope. Nonlinear transformations occur when mapping the electrical signal at the transmitter to the optical field input to the fiber, and when mapping the optical field at the fiber's output to the detected electrical signal. This model is sufficiently accurate provided the optical power launched into the fiber does not exceed about +10 dBm for fiber lengths up to about 200-300 km. Above these powers and/or fiber lengths, fiber nonlinearities become significant for which the fiber channel can no longer be treated as a linear filter acting on the optical field. The model in Figure 3.3 is used throughout this thesis.

3.2 Measuring Performance

Eye diagrams, bit-error ratio (BER) and receiver sensitivity are the three means often used to measure the quality of an optical communication system. These are described below.

3.2.1 Eye Diagrams and ISI

Eye diagrams are used to determine the quality of a system's response to a digital signal. For example, consider a system using binary on-off keying where hard decisions are made on each symbol passed to the decision circuit. Ideally, all MARKS would have the same signal level. Similarly, all SPACES would have the same signal level, which is different from the MARKS, as shown Figure 3.4a. The decision circuit's threshold would be set in-between the two levels and would output a MARK when the signal is above the threshold, and a SPACE when the signal is below the threshold. Of course, decisions would be made at the information symbol rate, and at points in time somewhere in-between the transitions between MARKS and SPACES. In a real communication system, the binary signal will be bandlimited by various components in the system, including a receiver filter to minimize noise. This band limiting, generally, results in MARKS (or SPACES) that no longer all have the same signal level at the decision time within each bit, as shown in Figure 3.4b.

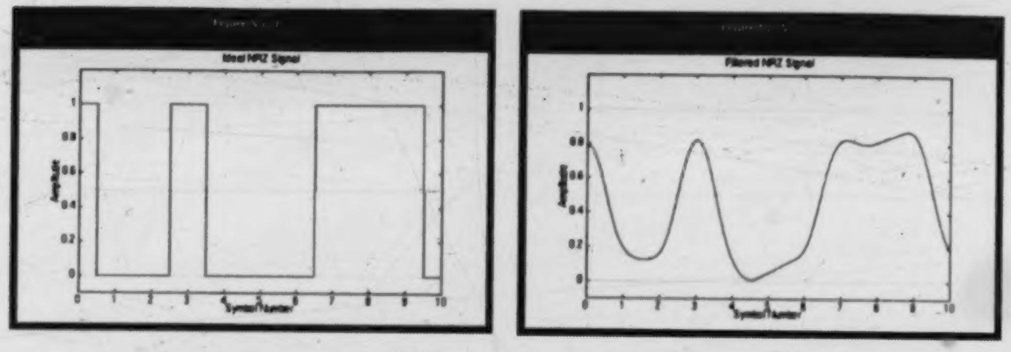

(a) **(b)**

Figure 3.4 (a) Ideal NRZ binary signal; (b) Filtered NRZ binary signal.

An eye diagram is obtained by superposing traces of the signal, each shifted by a different integer number of bit periods. Figure 3.5 shows eye diagrams of the signals in Figure 3.4.

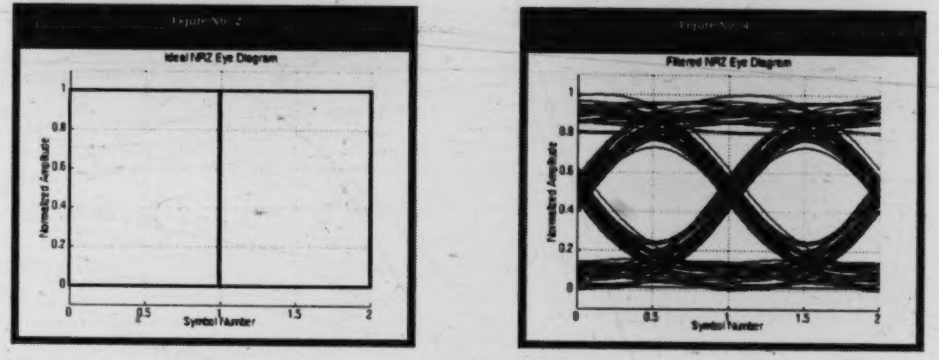

(a) **(b)**

Figure 3.5 (a) Eye diagram for an ideal NRZ binary signal; (b) Eye diagram for a filtered NRZ binary signal.

Eye diagrams clearly show symbols that have traces closer to the decision threshold. Note that these traces are more likely to cause an error. If the signal distortion is severe, the trace for a particular symbol may even occur on the wrong side of the decision threshold. This "smearing" of MARKS and SPACES is called intersymbol interference (ISI) and is undesirable because it degrades system performance. One of the goals of a good system design is to specify filters at the transmitter and/or receiver that will minimize ISI while concurrently limiting the amount of noise present in the received signal. Nyquist has shown that any filter (often called a Nyquist filter) with a linear phase response and vestigial symmetry about $B/2$ will produce zero ISI. A class of zero-ISI filters often referenced in the literature have a raised-cosine response, given by [78]

$$H(f)=\begin{cases}1, & |f|\le\frac{B}{2}(1-\beta)\\ \cos^2\left[\frac{\pi}{2\beta B}\left(|f|-\frac{B}{2}(1-\beta)\right)\right], & \frac{B}{2}(1-\beta)<|f|\le\frac{B}{2}(1+\beta)\\ 0, & |f|>\frac{B}{2}(1+\beta)\end{cases}\tag{3.10}$$

where β is a rolloff factor for which $0\le\beta\le1$. When $\beta=0$ the raised-cosine filter is an ideal brick-wall lowpass filter with a cutoff at $B/2$. For $\beta=1$ the filter has a cosine-shaped monotonic decreasing magnitude response for frequencies up to B, and is zero otherwise. A raised-cosine filter will produce an output signal with zero ISI when the input signal is a series of impulses at a signaling rate B. Hence, it represents a design objective for the output pulse shapes of the system. It should be noted that the impulse response of a raised-cosine filter is noncausal and, therefore, is not realizable. The objective, then, is to specify a filter response that minimizes ISI, maximizes signal-to-noise ratio (called matched filtering), and is realizable.

3.2.1.1 Realizable Filters that Minimize ISI

Consider a generalized all-pole, second-order lowpass filter for which the poles are complex conjugates and located in the left-hand side of the s plane, as shown in Figure 3.6.

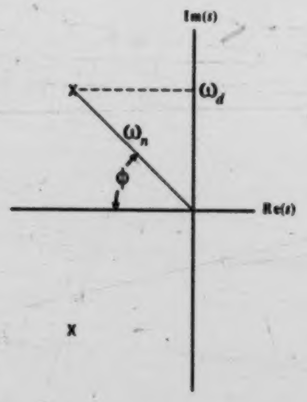

Figure 3.6 Pole locations for a realizable second-order filter.

The Laplace transfer function for this filter is

$$H(s) = \frac{\omega_n^2}{s^2 + 2\zeta\omega_n s + \omega_n^2} \qquad (3.11)$$

where $\zeta = \cos(\phi)$. By taking the inverse-Laplace transform, the impulse response is obtained as

$$h(t) = \frac{\omega_n}{\sqrt{1-\zeta^2}} \exp(-\zeta\omega_n t)\sin(\omega_d t) \qquad (3.12)$$

where $\omega_d = \omega_n\sqrt{1-\zeta^2}$ is the damped oscillation frequency. In order to obtain zero ISI in the output signal, the filter's response must have zero crossings spaced T apart where T is the symbol period. From (3.12) this occurs when $\omega_d = k\pi/T$ where k is a positive integer, and to minimize the bandwidth and overshoot of the filter, $k=1$ should be chosen. Therefore, a zero-ISI filter is obtained by fixing the imaginary part of the poles at $\pm\pi/T$. In other words, the damped frequency $f_d = \omega_d/2\pi$ should be related to the signaling rate B through $f_d = B/2$. By solving (3.11) for $|H(s = j2\pi f)| = 1/\sqrt{2}$, the 3 dB cutoff frequency of the filter can be arrived at, as

$$f_{3dB} = \frac{\omega_n}{2\pi}\left[1 - 2\zeta^2 + \sqrt{2 - 4\zeta^2(1-\zeta^2)}\right] \qquad (3.13)$$

For example, consider a second-order Butterworth filter for which $\zeta = 1/\sqrt{2}$. Using $f_d = B/2$, (3.13) can be used to arrive at the simple result $f_{3dB} = B/\sqrt{2}$.

The response of (3.12) is realizable and produces zero crossings that eliminate ISI when $\omega_d = \pm\pi/T$. However, the peak response does not coincide with the nulls and, therefore, the filter does not represent a good design objective. Additionally, a slow rolloff in the filter response is not necessarily desirable because electrical amplifiers tend to rolloff very rapidly beyond their band edge, which can "clip" the rolloff in the response. It was found, however, that if additional poles are added, with the imaginary part of complex poles constrained to $\pm\pi/T$ in accordance with the above discussion, that higher-order filters could be obtained with little ISI and with a peak response that coincides with the nulls. Figure 3.7 shows eye diagrams for a raised-cosine filter with a rolloff factor of 0 and 1, and for a ninth-order, all-pole filter that contains three identical complex-pole pairs and one real pole. The impulse response of the all-pole filter is also shown.

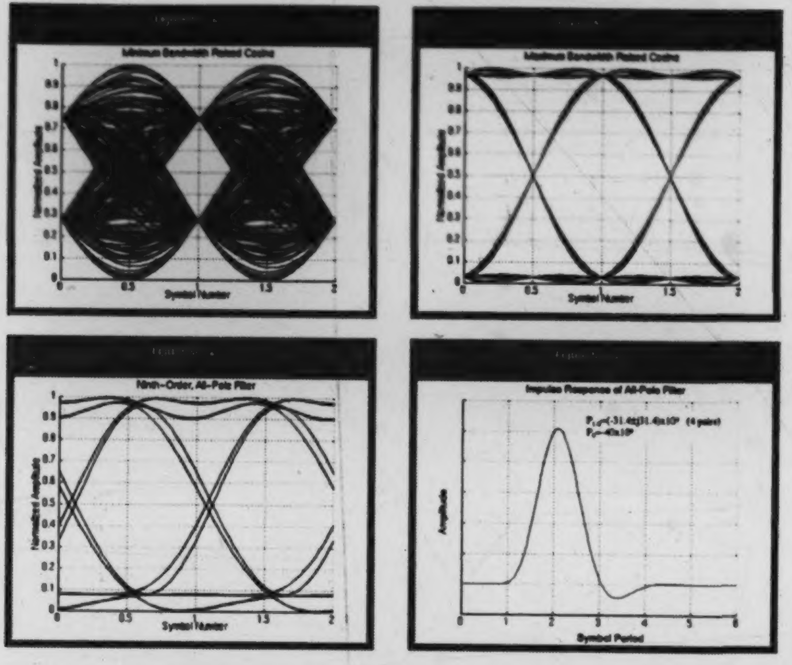

Figure 3.7 Eye diagrams for a raised-cosine response with $\beta=0$ (top left) and $\beta=1$ (top right), and a ninth-order, all-pole filter (bottom left). Impulse response for the all-pole filter (bottom right).

A more general approach to filter design is to approximate the magnitude response of a Nyquist filter, followed by an all-pass filter that equalizes any phase distortion [80]. Yet another approach, done entirely in the time domain, is to specify an ISI square error, and then solve for the pole locations of the filter [81], [82], [83], [84]. This analysis can also be extended to filters with finite transmission zeros [85], [86], [87]. It should be noted that these procedures seek to minimize ISI, but do not address the temporal width of the resulting eye , which is extremely important in high-speed communication systems.

At the beginning of this research, filters were obtained on a somewhat trial-and-error bases, as described above, and the resulting eye diagram and noise-equivalent bandwidth (NEB) were observed to determine the quality of the filter. Figure 3.8 shows eye diagrams for a 4-level signal using an optimized filter with 7 poles and 4 finite zeros according to [85], and for an all-pole, 7-pole filter that was arrived at through trial-and-error with the imaginary part of complex poles constrained to $\pm\pi/T$. The NEBs for these filters are 4.4 GHz and 4.5 GHz, respectively, and the symbol period is 100 ps (20 Gb/s multilevel). Although the filter from [85] gives good ISI results, it would clearly be much more sensitive to decision-time errors.

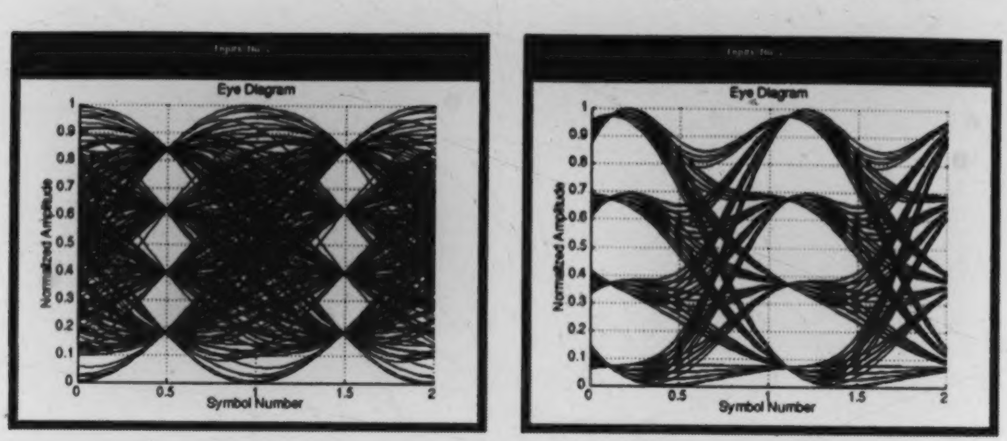

Figure 3.8 Eye diagram for response of a 7-pole filter with four finite zeros from [85] (left), and an all-pole, 7-pole filter (right).

The above discussion deals with optimizing the overall system response for which the input is a series of impulses at the signaling rate. A more realistic input might be an NRZ signal where each symbol occupies an entire symbol period. Of course, any of the filters mentioned above could be divided by the Fourier transform of a square pulse to achieve a filter with good ISI performance when the input is an ideal NRZ signal. Alternatively, the receiver filter is often specified as a third-order Butterworth response with a 3-dB point at ~$0.65B$ because it produces a small amount of ISI in response to an ideal NRZ signal. Bessel filters, too, are often used because they have a relatively linear phase response and produce a minimum amount of overshoot. For comparison, eye diagrams are shown in Figure 3.9 for an ideal NRZ signal that has been filtered by Butterworth and Bessel responses. To illustrate the impact of varying the cutoff frequency, results are shown for different cuttoff frequencies in the Butterworth response.

It should be noted that the above approaches to filter optimization assume a linear system, i.e., that superposition holds. Because the system in Figure 3.3 is nonlinear, filter optimization is difficult to quantify because the overall response is affected by many factors, including filtering at the transmitter, chirp on the transmitted optical signal, fiber dispersion, and receiver filtering. Regardless, computer simulation can always be used to evaluate a system design that is based on ideal components, or on real components. Chapter 7 shows simulation results for ideal and non-ideal systems employing a variety of filter responses at the transmitter and/or receiver.

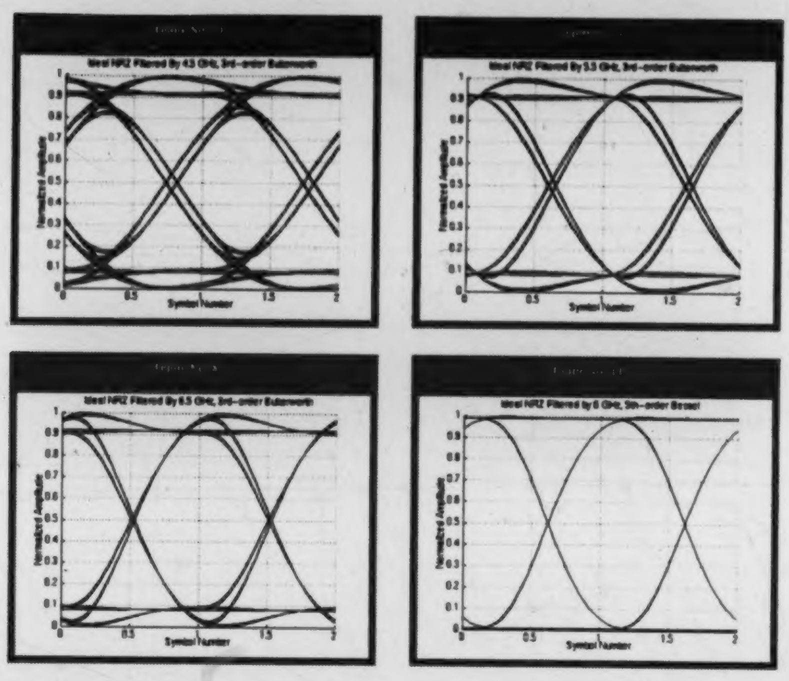

Figure 3.9 Eye diagrams for an ideal binary NRZ signal filtered by: third-order Butterworth filter with a cutoff frequency at 4.5 GHz (top left), 5.5 GHz (top right) 6.5 GHz (bottom left); 6 GHz, fifth-order Bessel filter (bottom right).

3.2.2 BER and Receiver Sensitivity

The bit-error ratio (BER) is the average ratio of bits in error to the total number of bits received and, in optical systems, is usually plotted as a function of received optical power. *Receiver sensitivity* is the average optical power required at the receiver to produce a target BER, which, for optical systems, is often taken as 10^{-9}, 10^{-12} or 10^{-14}.

Bit errors can be caused by a number of system impairments. For example, consider a 2^7-1 pseudorandom bit sequence (PRBS) that is absent of noise, but with one of the 127 symbols having a trace that is on the wrong side of the decision threshold, due to signal distortion. One of the 127 bits received will always be in error and the other bits error-free, resulting in a BER floor (i.e., is independent of received optical power) of 7.87×10^{-3}. In this case, the low BER required for a well-designed optical system could never be achieved. If the corresponding trace for all symbols is on the correct side of the decision threshold, the theoretical BER, in the absence of noise, is zero. However, noise will always be present, which, when added to the signal, can produce a signal level that falls on the wrong side of the decision threshold, resulting in an error.

3.3 Summary

This chapter explained a model that can be used for calculating system response in an optical communication system that uses a laser diode with singlemode fiber. It was shown how it differs from other system models using an LED in which the fiber is treated as a linear filter acting on the optical intensity. Specifically, it was explained that the fiber can be treated as a bandpass system that operates on the optical electric field and, therefore, can be modeled using a lowpass-equivalent representation. The nonlinear nature of the system from electrical input to electrical output was also explained. Also, it was shown how to estimate the system capacity for the various system types considered.

Methods for measuring performance were explained including BER, receiver sensitivity and eye diagrams. Topics about realizable filters that minimize ISI were also discussed.

4 Noise Modeling and Related Topics

To predict the receiver sensitivity of an optical communication system, it must be possible to calculate the BER from the received optical power. Precise BER calculations require a knowledge of all noise sources and their associated statistics. Often, this starts with a physical description of components that are characterized by counting statistics involving photons and/or electrons. For example, the relationship between the number of photons at the input and output of an optical amplifier can be modeled as a birth-death-immigration (BDI) process [88], which accounts for stimulated emission (birth), absorption (death) and spontaneous emission (immigration) within the amplifying medium. In general, the number of photons at the input or output is not deterministic, but must be described in terms of probabilities. Similarly, the number of charge carriers produced in the photodetector is a random variable that is influenced by the statistics of the incident photons. Eventually, all noise sources must be reflected in the statistical description of the signal passed to the decision circuit.

Various approaches and approximations can be used in arriving at a noise model. One approach is to use the counting statistics of photons at the output of the optical preamplifier [89], or to expand the optical field in a series with random coefficients [90], [91], [92], [93] to arrive at the characteristic function or moment generating function (MGF) for the signal passed to the decision circuit. Then, if an integrate-and-dump receiver is assumed, a closed form expression for the probability density function (PDF) of a symbol's amplitude can be obtained in the absence of receiver noise [91], or approximated in the presence of receiver noise [92]. Using a series expansion of the field, it is also possible to obtain a generalized MGF that accounts for an arbitrary receiver response [90]. Once the MGF is known, upper bounds on the BER can be obtained, or it can be approximated by assuming Gaussian statistics. Numerical methods can also be employed as described in [89] that use the MGF and inverse fast-Fourier transform to arrive at a discrete version of the exact PDF which, then, can be integrated numerically to arrive at the probability of error.

A useful noise model should provide good predictions about the receiver's sensitivity, without being too computationally intensive. Also, to perform realistic system simulations, the noise model should allow for an arbitrary time dependence of the received optical power and receiver's response. In [89], [90], [91], [92] it has been shown that a Gaussian approximation can lead to significant errors in the optimal decision threshold, or predict BERs that are inaccurate by up to an order of magnitude. However, the predicted receiver sensitivity is very close to that obtained from exact statistics. Therefore, because it makes good predictions about receiver sensitivity and reduces computation time, a Gaussian approximation will be used.

Two noise models were employed in this research, referred to as *static* and *dynamic*, and are described in this chapter. The simplest of the two is the static noise model. It is based on [94], [95] and is useful for doing rapid calculations of BER and/or receiver sensitivity. It assumes a fixed optical power level for each symbol and only requires a knowledge of the receiver's NEB. This model is useful for obtaining a "ball park" estimation of BER or receiver sensitivity in the absence of ISI. The dynamic noise model is based on [96] and allows for an arbitrary time dependence of the received optical power and receiver's impulse response. It is completely compatible with the model in Figure 3.3 and, therefore, accounts for ISI from all system impairments. The dynamic model is more computationally intensive, but is still sufficiently simple that calculations of a receiver's sensitivity can be obtained within a few minutes, depending on simulation size and computer speed, of course. Lastly, it is assumed that the power in the fiber is sufficiently low that nonlinear effects such as stimulated Brillioun scattering (SBS) and SPM are insignificant. Also, it is assumed that optical amplifiers contain isolators so that there is no significant accumulation of double Rayleigh backscattered noise.

4.1 Noise Sources

There are many sources of noise in a communication system employing an optical preamplifier. Each noise source is described below.

4.1.1 Receiver Thermal Noise

Although the total charge within a resistor is neutral, the spatial distribution of charge at any instant in time, due to thermal agitation, can produce a non-zero voltage between the terminals. The one-sided PSD of this noise [97] is given by $4kT$ where k is Boltzmann's constant and T is the absolute temperature. Normally, the resistor is terminated in a load resistor such as the input of an amplifier. The amplifier, in addition to amplifying the resistor's noise, produces additional noise from the resistors and active components that it contains. This additional noise is characterized by a noise factor F (usually called noise figure when expressed in dB) for the amplifier. The noise introduced by all electrical components at the receiver is called *receiver noise* or *receiver thermal noise*. Figure 4.1 shows a model for calculating the amount of receiver noise.

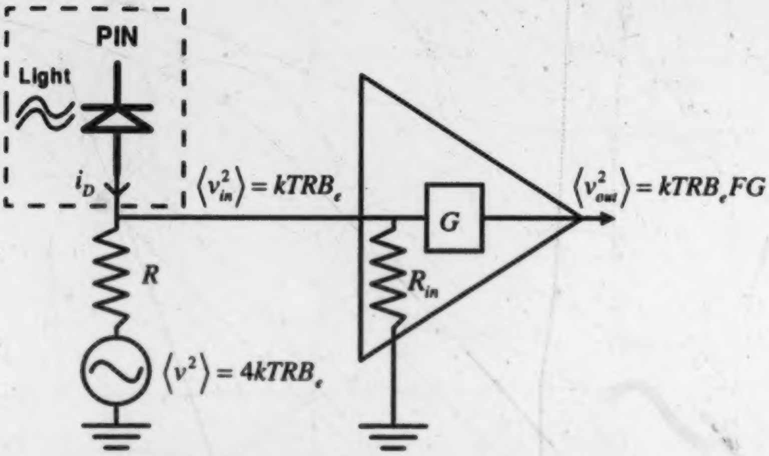
PIN
Light
i_D
$\langle v_{in}^2 \rangle = kTRB_e$
G
$\langle v_{out}^2 \rangle = kTRB_eFG$
R
R_{in}
$\langle v^2 \rangle = 4kTRB_e$

Figure 4.1 Calculating receiver noise in an electrical amplifier.

The noise figure for an amplifier is normally specified under matched conditions, i.e., $R=R_{in}$ in Figure 4.1. Under these conditions, R and R_{in} act as a voltage divider on the open-circuit noise voltage of resistor R, reducing it by a factor of two (noise power is reduced by a factor of four) at the input to the amplifier. Other noise sources that are not introduced by the electrical receiver are already present in the photodiode current i_D. These, along with the signal current, could be converted to voltages at the output of the amplifier. However, it is more convenient to model the receiver noise by an equivalent noise current, along with the other noise currents, present in the total current, i_D, through the photodiode. Then, all noise sources are referenced to the current flowing through the photodetector. When $R=R_{in}$, it is straightforward to show that the equivalent thermal noise current is

$$\langle i_{th}^2 \rangle = \frac{4kTFB_e}{R} \tag{4.1}$$

where B_e is the receiver's noise-equivalent bandwidth. It is often the case that more than one electrical amplifier is needed to provide the required gain at the receiver. If the first amplifier in a cascade has a power gain G_1 and a noise factor F_1, the second amplifier a power gain G_2 and a noise factor F_2, etc., then the equivalent noise factor F_{eq} for the cascade of amplifiers is given by [97]

$$F_{eq} = F_1 + \frac{F_2 - 1}{G_1} + \frac{F_3 - 1}{G_1 G_2} + \dots \tag{4.2}$$

Hence, the equivalent noise factor is essentially determined by the first amplifier in the cascade. For example, for a cascade of five identical amplifiers, each having a noise figure of 7 dB and a gain of 10 dB, the equivalent noise figure for the cascade would be 7.37 dB.

4.1.2 Noise from Amplified Spontaneous Emission in Optical Amplifiers

Consider the optical front end of a receiver shown in Figure 4.2

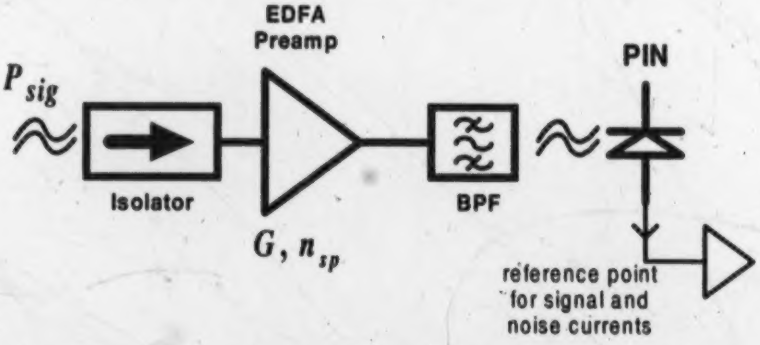

Figure 4.2 Optical front end of a receiver.

where P_{sig} is the received optical signal power and G is the power gain of the EDFA preamp. Some of the excited atoms in an optical amplifier undergo a spontaneous transition and produce a spontaneously-emitted photon. This photon can then stimulate further emissions from other atoms which amplifies the spontaneous emission. This process is a source of noise and is appropriately called amplified spontaneous emission (ASE). The amount of ASE is characterized by a parameter called the spontaneous emission factor, n_{sp}, and the total ASE power incident on the photodetector in Figure 4.2 can be obtained from [98]

$$P_{ASE} = m_t n_{sp} h\upsilon (G-1) B_o \eta_o \tag{4.3}$$

where m_t is the number of orthogonal modes, $h\upsilon$ is the photon energy, B_o is the bandwidth of the optical bandpass filter, and η_o is the output coupling efficiency, which accounts for all losses between the output of the optical amplifier and the photodetector. Normally, m_t would be 2 because there are two degenerate fields orthogonal to one another in singlemode fiber. However, if a polarization demultiplexer is placed at the output of the optical preamp, only the signal along one of the polarization axes would be passed to the photodetector, for which case m_t=1.

ASE is usually modeled as a random field that, upon square-law detection, can beat with itself or with the received optical signal. When it beats with itself it is called spontaneous-spontaneous beat noise and produces a noise current given by [94]

$$\left\langle i_{sp-sp}^2 \right\rangle = (\Re P_{ASE})^2 \frac{B_e(2B_o - B_e)}{B_o^2} \tag{4.4}$$

where $\langle \cdot \rangle$ denotes expected value, B_e is the one-sided bandwidth of the electrical receiver, and $\Re$ (Amps/Watt) is the photodetector's responsivity. When ASE beats with the signal it is called signal-spontaneous beat noise and produces a noise current given by [94]

$$\left\langle i_{sig-sp}^2 \right\rangle = 4P_{sig} P_{ASE} \Re^2 \eta_i G \eta_o \frac{B_e}{B_o} \tag{4.5}$$

where η_i is the input coupling efficiency, which accounts for all losses between the received signal power and the input of the EDFA preamp. Equations (4.4) and (4.5) are valid for $B_o \geq B_e$, a condition that would usually be satisfied in a practical system.

4.1.3 Shot Noise

Shot noise is due to the quantum nature of light (photons) incident on a photodetector and of charge carriers that traverse a semiconductor junction. For example, the arrival of photons is a Poisson process for coherent light, i.e., the number of photons that arrive over a given time interval is a Poisson-distributed random variable. The photon arrivals produce current impulses that are filtered by the receiver response to produce a noise voltage (current), which is now a continuous random variable—this is called a filtered Poisson process [99]. For a non-coherent sources such as ASE, the statistics of the photon arrivals is not Poisson; however, for simplicity, it will be modeled as a shot-noise process. Three sources of shot noise are then considered that arise from the signal, dark current and ASE. Shot noise from the signal has a noise current given by

$$\left\langle i_{shot\_sig}^2 \right\rangle = 2qP_{sig} \eta_i G \eta_o \Re B_e \tag{4.6}$$

where q is the charge of an electron. Shot noise from ASE has a noise current given by

$$\left\langle i_{shot\_ASE}^2 \right\rangle = 2qP_{ASE} \Re B_e \tag{4.7}$$

A small current, called dark current, also occurs in photodiodes due to stray light and/or thermal agitation. This dark current, I_{dark}, produces a shot noise given by

$$\left\langle i_{shot\_dark}^2 \right\rangle = 2qI_{dark}B_e \tag{4.8}$$

Because the shot noises are independent, they can be added to produce a total shot noise given by

$$\left\langle i_{shot}^2 \right\rangle = \left\langle i_{shot\_sig}^2 \right\rangle + \left\langle i_{shot\_ASE}^2 \right\rangle + \left\langle i_{shot\_dark}^2 \right\rangle \tag{4.9}$$

4.1.4 Relative Intensity Noise

Relative intensity noise (RIN) refers to the random fluctuations of intensity in a light source. For lasers, it is believed to result from spontaneous emission and from back reflections into the active medium [4]. RIN relates the mean-square power fluctuation in a 1 Hz bandwidth to the square of the average power, through

$$RIN = \frac{\left\langle \delta P^2 \right\rangle}{\left\langle P \right\rangle^2} = \frac{\left\langle i_{RIN}^2 \right\rangle}{\left\langle i \right\rangle^2} \tag{4.10}$$

and is usually expressed in units dB/Hz, i.e., ten times the log of (4.10). Note that, because current is directly proportional to received power in a receiver using square-law detection, RIN can also be expressed in terms of currents, as in (4.10). RIN is, generally, a function of frequency so that (4.10) would have to be integrated over the bandwidth of the receiver to obtain the total RIN. Alternatively, an average RIN value could be defined that, when integrated over the receiver's bandwidth, gives the total RIN. For lasers, RIN values are typically between –130 and –160 dB/Hz. Assuming an average RIN value (dB/Hz) over the bandwidth of the receiver, the total RIN current can be expressed in terms of the received optical power (i.e., incident on the optical preamplifier), through

$$\left\langle i_{RIN}^2 \right\rangle = \left(P_{sig} \eta_i G \eta_o \Re \right)^2 10^{\frac{RIN}{10}} B_e \tag{4.11}$$

Another source of RIN occurs when the light from a laser with a finite linewidth is transmitted over a dispersive medium. For this noise, phase fluctuations in the optical field are converted to amplitude fluctuations at the receiver because of the dispersion. This process is called PM-to-AM (phase modulation to amplitude modulation) conversion [100]. The one-sided PM-to-AM RIN spectral density, which is arrived at in Section 4.4, can be written as

$$RIN_{PM\_AM}(f) = \frac{2\Delta\upsilon}{\pi f^2}\left[1 - \cos\left(8\pi^2 F_D f^2\right)\right] \tag{4.12}$$

where $\Delta\upsilon$ is the source linewidth and F_D is a parameter that characterizes the fiber dispersion, by

$$F_D = \frac{\lambda^2}{4\pi c} DL \tag{4.13}$$

Where λ is the carrier wavelength, c is the free-space speed of light, D is the fiber dispersion coefficient (ps/(km·nm)), and L is the fiber length. Normally, (4.12) would be integrated over the receiver's bandwidth to obtain the total RIN from PM-to-AM conversion. For a receiver with an ideal (brick-wall) lowpass response and bandwidth B_e, the total PM-to-AM RIN can be obtained as (see section 4.4)

$$RIN_{PM.AM} = \frac{2\Delta\upsilon}{\pi B_e}\left[\cos\left(8\pi^2 F_D B_e^2\right) + 4\pi^{3/2} B_e \sqrt{F_D}\,\mathrm{FresnelS}\left(4B_e\sqrt{\pi F_D}\right) - 1\right] \tag{4.14}$$

where FresnelS(·) is the Fresnel sine function, defined as

$$\mathrm{FresnelS}(x) = \int_0^x \sin\left(\frac{\pi}{2}t^2\right)dt \tag{4.15}$$

The total RIN current from PM-to-AM conversion can be obtained by using (4.14) in (4.11), provided (4.14) is first converted to an equivalent average RIN in dB/Hz by

$$RIN_{PM.AM,dB/Hz} = 10\log\left(\frac{1}{B_e} RIN_{PM.AM}\right) \tag{4.16}$$

An important property of RIN is that it places a bound on the achievable signal-to-noise ratio (SNR), i.e., it will produce a BER floor. In a system design, the BER floor associated with RIN must be lower than the target BER. For long-haul systems operating over dispersive fiber, PM-to-AM RIN can be the dominant noise and produce BER floors much worse than those typical of high-quality fiber links. A detailed description of PM-to-AM RIN is given in Section 4.4.

4.2 Static Noise Model

For this model, all SPACES (0s) are assumed to be of an identical power level, and similarly for all MARKS (1s). Also, each level has associated with it a Gaussian PDF that is identically-distributed for levels of the same logical value. For example, for a binary communication system, the signal currents for a **1** and **0**, referenced to the photodetector, take on the following forms

$$i_0 = kP_0 + n_0 \qquad \text{(SPACE)} \tag{4.17}$$

$$i_1 = kP_1 + n_1 \qquad \text{(MARK)}$$

where P_0 is the received optical power in a **0**, P_1 is the optical power in a **1**, k is a constant, and n_0 and n_1 are zero-mean Gaussian noise currents for which the variance (noise power) takes on one of two values corresponding to a **0** or **1**, respectively. Because the currents have the same mean and variance for all symbols of the same logical level, this model will be referred to as *static*. Using the results from the previous section, the mean-square noise current for a **0** and **1** can be calculated from

$$\left\langle i^2 \right\rangle_0 = \left\langle i^2_{sig\_sp} \right\rangle_0 + \left\langle i^2_{shot} \right\rangle_0 + \left\langle i^2_{RIN} \right\rangle_0 + \left\langle i^2_{sp\_sp} \right\rangle + \left\langle i^2_{th} \right\rangle \qquad \text{(SPACE)} \tag{4.18}$$

$$\left\langle i^2 \right\rangle_1 = \left\langle i^2_{sig\_sp} \right\rangle_1 + \left\langle i^2_{shot} \right\rangle_1 + \left\langle i^2_{RIN} \right\rangle_1 + \left\langle i^2_{sp\_sp} \right\rangle + \left\langle i^2_{th} \right\rangle \qquad \text{(MARK)}$$

where the subscripts “0” and “1” denote noises that are dependent on the received optical signal power in a **0** and **1**, respectively. The expected (average) photocurrent for a **0** and a **1** can be obtained as

$$I_0 = P_0 \eta_i G \eta_o \Re + P_{ASE} \Re + I_{dark} \qquad \text{(SPACE)} \tag{4.19}$$

$$I_1 = P_1 \eta_i G \eta_o \Re + P_{ASE} \Re + I_{dark} \qquad \text{(MARK)}$$

A Gaussian PDF can now be associated with a **0** and a **1**, with a mean given by (4.19) and a variance given by (4.18).

4.2.1 Calculating BER and Receiver Sensitivity

BERs and the receiver’s sensitivity can now be calculated by considering Figure 4.3.

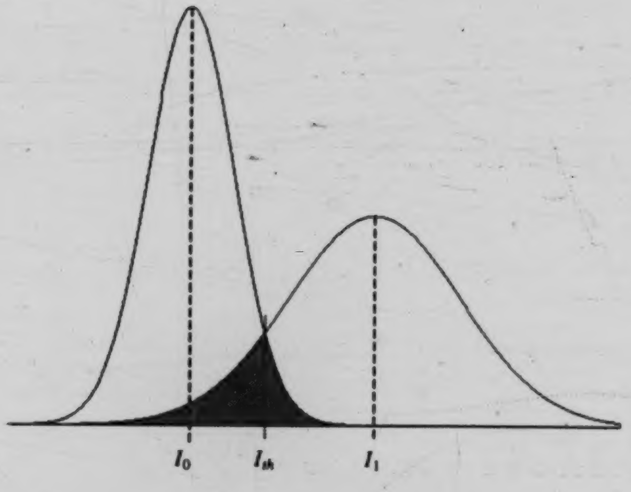

Figure 4.3 Gaussian PDFs for a **0** and a **1**.

Assuming **0**s and **1**s are equally likely, the optimum decision threshold, I_{th}, is where the PDFs intersect, i.e.,

$$\frac{1}{\sqrt{2\pi}\sigma_0}\exp\left(-\frac{(I_{th}-I_0)^2}{2\sigma_0^2}\right)=\frac{1}{\sqrt{2\pi}\sigma_1}\exp\left(-\frac{(I_1-I_{th})^2}{2\sigma_1^2}\right) \tag{4.20}$$

For BERs of practical interest, a very good approximation is obtained by equating the exponential terms, to get

$$I_{th}=\frac{I_1\sigma_0+I_0\sigma_1}{\sigma_0+\sigma_1} \tag{4.21}$$

Now, assuming **0**s and **1**s are equally likely, the BER can be obtained from the area in the tails of the PDFs in Figure 4.3, as

$$BER=\frac{1}{2}\int_{I_{th}}^{\infty}p_0(x)dx+\frac{1}{2}\int_{-\infty}^{I_{th}}p_1(x)dx \tag{4.22}$$

where $p_0(x)$ is a Gaussian PDF associated with a **0** and $p_1(x)$ is a Gaussian PDF associated with a **1**. It is convenient to express the BER in terms of the upper-tail probability of a Normal distribution, defined as

$$\mathrm{Q}(x)=\frac{1}{\sqrt{2\pi}}\int_{x}^{\infty}e^{-\frac{x^2}{2}}dx \tag{4.23}$$

or in terms of the complementary error function, which is related to Q(x) through

$$Q(x) = \frac{1}{2}\,\mathrm{erfc}\left(\frac{x}{\sqrt{2}}\right) \tag{4.24}$$

For x>>2, Q(x) can be approximated by [102]

$$Q(x) \approx \frac{1}{x\sqrt{2\pi}}\exp\left(-\frac{x^2}{2}\right) \tag{4.25}$$

which becomes more accurate as x increases. For example, when x=6, (4.25) is accurate to within about 2 %. It is interesting to note that I_{th} given by (4.21) is the same number of standard deviations away from a **1** as from a **0**, i.e.,

$$\frac{I_{th} - I_0}{\sigma_0} = \frac{I_1 - I_{th}}{\sigma_1} = \frac{I_1 - I_0}{\sigma_0 + \sigma_1} \tag{4.26}$$

Now, using (4.23) and (4.26), (4.22) can be written

$$BER = Q\left(\frac{I_1 - I_0}{\sigma_0 + \sigma_1}\right) \tag{4.27}$$

where I_0, I_1, σ_0 and σ_1 are determined by the received optical power through (4.19) and (4.18). After specifying a target BER, the receiver's sensitivity can be obtained by determining the required argument for the Q function, and then calculating the required average optical power to obtain this argument. For example, for BER=10^{-9} the argument of the Q function must be ≈ 6.

For a system using 4-ary ASK signaling, a mean and variance can be associated with a logical **0**, **1**, **2** and **3**, as shown in Figure 4.4

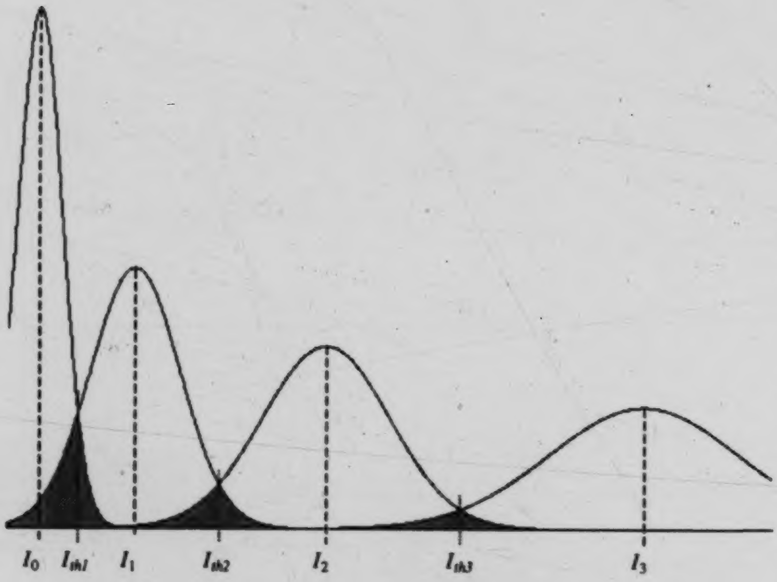

Figure 4.4 Gaussian PDFs for a 0, 1, 2 and 3 in a 4-ary signal.

In a similar manner to the binary case, the probability of error is obtained from the shaded area in the tails of the PDFs, and assuming all levels have an equal probability of occurrence, the BER[2] can be obtained as

$$BER = \frac{1}{2}\left\{Q\left(\frac{I_1 - I_0}{\sigma_1 + \sigma_0}\right) + Q\left(\frac{I_2 - I_1}{\sigma_2 + \sigma_1}\right) + Q\left(\frac{I_3 - I_2}{\sigma_3 + \sigma_2}\right)\right\} \tag{4.28}$$

Similar expressions can also be written for higher-level, M-ary signals.

4.2.2 Optimal Level Spacing

Clearly, the BER in (4.28), and the receiver's sensitivity, depend on the relative spacing of levels in a multilevel signal. Because the noise is signal dependent, it is expected that higher levels should be spaced farther apart than lower levels in an optimized system. There are practical issues that must be addressed when considering level spacing, as discussed in Chapter 7. Here, however, ideal (zero ISI) levels will be considered. As a starting point, it is postulated that the BER in (4.28) is minimized when the Q-function arguments are equal, i.e.,

---

[2] Strictly speaking, (4.28) gives the symbol-error ratio, which, depending on how the data is mapped into the M-ary signal, may or may not be equal to the BER of a decoded binary tributary. Regardless, when referring to M-ary signals, BER will be synonymous with symbol-error ratio.

$$\frac{I_1 - I_0}{\sigma_1 + \sigma_0} = \frac{I_2 - I_1}{\sigma_2 + \sigma_1} = \frac{I_3 - I_2}{\sigma_3 + \sigma_2} \tag{4.29}$$

This postulate will be used to obtain some analytical results, which, to test their validity, can then be compared to numerical minimization techniques. Let I_1 and I_2 be given by

$$\begin{aligned} I_1 &= I_0 + \varepsilon_1 (I_3 - I_0) \\ I_2 &= I_0 + \varepsilon_2 (I_3 - I_0) \end{aligned} \tag{4.30}$$

where $0 < \varepsilon_1, \varepsilon_2 < 1$. Hence, the task is to find the normalized level weights ε_1 and ε_2. Note that with this definition, I_0 has a normalized weight of zero, and I_3 has a normalized weight of unity. The noise powers for each level can be expressed as

$$\begin{aligned} \sigma_0^2 &= k_1 + k_2 I_0 + k_3 I_0^2 \\ \sigma_1^2 &= k_1 + k_2 I_1 + k_3 I_1^2 \\ \sigma_2^2 &= k_1 + k_2 I_2 + k_3 I_2^2 \\ \sigma_3^2 &= k_1 + k_2 I_3 + k_3 I_3^2 \end{aligned} \tag{4.31}$$

where the constants k_1, k_2 and k_3 are determined by system parameters. First, consider the case when stationary noise is dominant, i.e., $k_2 = k_3 = 0$. Using (4.31) in (4.29) implies that $I_3 - I_2 = I_2 - I_1 = I_1 - I_0$. In other words, the levels are equally spaced between I_0 and I_3, hence

$$\varepsilon_1 = \frac{1}{3} \qquad \text{(stationary noise)} \tag{4.32}$$

$$\varepsilon_2 = \frac{2}{3}$$

Next, consider the case when noise that is linearly proportional to signal current (i.e., linearly proportional to received optical power, P_{opt}) is dominant, for which $k_1 = k_3 = 0$. This would include signal-dependent shot noise or signal-spontaneous beat noise. If $I_0 = 0$, (4.29)-(4.31) can be solved to get

$$\varepsilon_1 = \frac{1}{9} \qquad (\text{noise} \propto P_{opt}) \tag{4.33}$$

$$\varepsilon_2 = \frac{4}{9}$$

In other words, if the M-ary signal has levels $m=\{0,1,2,3\}$, then the normalized weight of the m^{th} level is $\varepsilon_m = (1/9)m^2$. Finally, consider the case when noise proportional to the square of received optical power is dominant, such as RIN. In this case, $k_1=k_2=0$ and (4.31) implies that

$$\frac{\sigma_0}{I_0} = \frac{\sigma_1}{I_1} = \frac{\sigma_2}{I_2} = \frac{\sigma_3}{I_3} \tag{4.34}$$

which, when combined with (4.29), can be used to obtain

$$\frac{I_3}{I_2} = \frac{I_2}{I_1} = \frac{I_1}{I_0} \tag{4.35}$$

Therefore, the ratio of adjacent levels is the same for all levels when they are optimally spaced. Note, however, that (4.35) is undefined when $I_0=0$. This undefined condition is also visible in (4.28) where, if $I_0=0$ and I_3 is non-zero, I_1 and I_2 would tend toward zero to minimize the BER. This ill condition can be avoided, however, if $I_0 \neq 0$, i.e., the optical extinction ratio is finite. It might be expected, then, that the normalized levels, ε_1 and ε_2, approach zero as the optical extinction is allowed to increase without bound. With the optical extinction ratio defined as $\delta=P_{max}/P_{min}=I_3/I_0$, (4.30) and (4.35) can be used to arrive at

$$\varepsilon_1 = \frac{\delta^{1/3} - 1}{\delta - 1} \qquad (\text{noise} \propto P_{opt}^2) \tag{4.36}$$

$$\varepsilon_2 = \frac{\delta^{2/3} - 1}{\delta - 1}$$

where it is evident that ε_1 and ε_2 approach 0 as δ increases without bound. Also, it can be seen that ε_1 and ε_2 approach 1/3 and 2/3, respectively, as δ approaches 1. Figure 4.5 shows the optimal level weights versus extinction ratio when RIN is dominant.

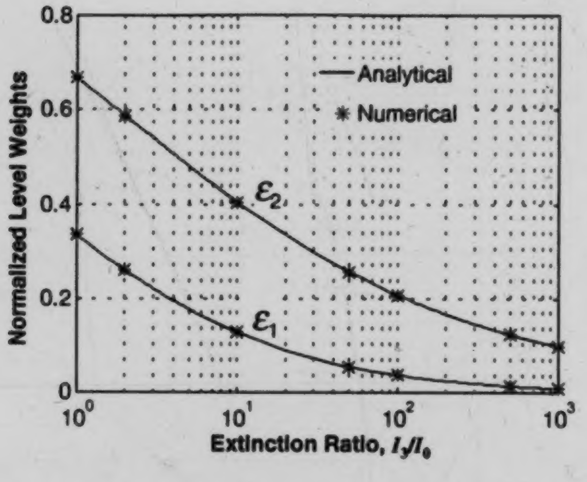

Figure 4.5 Optimal level weights versus extinction ratio for a signal dominated by RIN.

In Figure 4.5, the analytical curve was generated using (4.36). To test the validity of (4.36), optimal level weights were also calculated using a numerical minimization routine with the program in Appendix B. To test (4.32) and (4.33), Figure 4.6 shows the optimal weights versus extinction ratio, which were obtained numerically using the program in Appendix B.

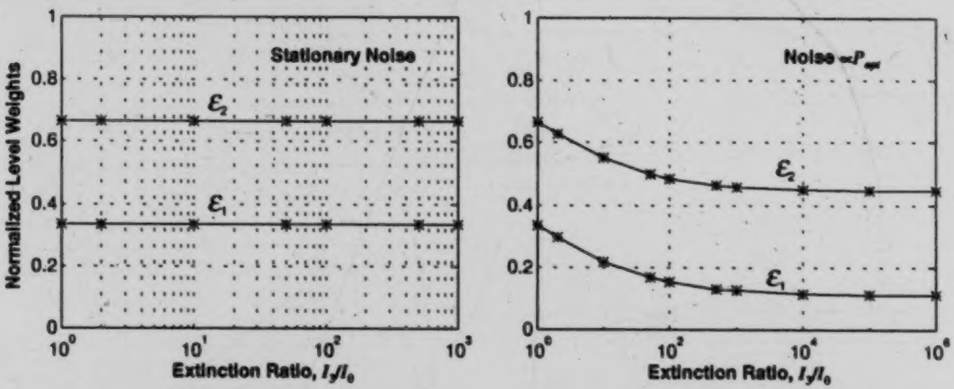

Figure 4.6 Optimal level weights versus extinction ratio for a signal dominated by stationary noise (left), or dominated by noise that is proportional to received optical power (right).

As expected, the optimal level weights for stationary noise are constant. For noise that varies linearly with received optical power, the optimal weights approach those for stationary noise as the extinction ratio approaches 1. However, when the extinction ratio becomes large, i.e., I_0 tends toward 0, the optimal level weights approach asymptotic limits of 1/9 and 4/9, as predicted by (4.33). At this point, it appears that bounds on optimal level weights are $0 < \varepsilon_1 < 1/3$ and $0 < \varepsilon_2 < 2/3$. In a practical system, all noise sources will be present, although one may dominate depending on system parameters and the particular level being considered. The target BER can also influence the optimal weights. For example, for a particular RIN value, RIN noise may be dominant for higher levels when the target BER is close to the BER floor associated with the RIN value. Regardless, numerical methods can always be used to determine the optimal level weights for a given system. For example, Figure 4.7 shows the optimal weights versus the gain of an optical preamp for BER=10^{-9} where the weights were obtained numerically using the program in Appendix B.

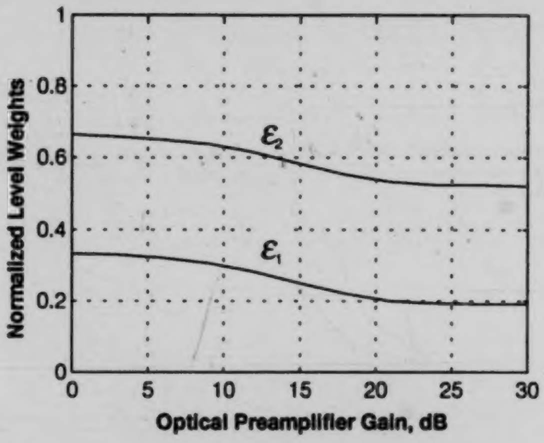

Figure 4.7 Optimal level weights versus optical preamplifer gain for a system where all noise sources are present.

When the gain of the optical preamp is unity, receiver noise (stationary) dominates and the levels are equally spaced. As the preamp gain increases, signal-spontaneous beat noise (noise proportional to received power) starts to dominate and the optimal level weights are lowered. For large gain, the asymptotes are slightly higher than given by (4.33) because of the small amount of power in a logical **0** (extinction ratio=20 dB) along with the presence of stationary noise. These factors tend to push the optimal weights slightly higher than (4.33). The RIN used in generating Figure 4.7 was small and did not significantly impact the level weights.

4.2.3 Power Penalty for M-ary Signaling

It is clear that an M-ary signal requires more power than a binary signal to achieve the same probability of error for a symbol. Therefore, it is useful to define a power penalty associated with an M-ary signal, given by

$$P_p = \frac{P_M}{P_2} \tag{4.37}$$

where P_M is the power for an M-ary signal and P_2 is the power for a binary signal operating at the same bit rate and BER. Although it *may* be feasible, a closed form solution for the general case, which would account for signal-dependent noise and optimally-spaced levels, will not be pursued here—simulation results will be presented in Chapter 7 for the general case. Instead, here we consider equally-spaced levels in the presence of white Gaussian noise.

Consider an ideal M-ary NRZ signal where the symbols take on amplitudes $\pm A$, $\pm 3A$, $\pm 5A$, …, $\pm(M\text{-}1)A$. Note that the levels in the M-ary signal are spaced the same distance apart as for the binary signal, i.e., $2A$, to obtain roughly the same probability of error for a symbol. Now, the power in a binary signal is P_2=A^2, whereas for an M-ary signal it is

$$P_M = \frac{2}{M}\left[A^2 + (3A)^2 + \ldots + ((M-1)A)^2\right] \tag{4.38}$$

$$= \frac{2A^2}{M}\sum_{k=0}^{\frac{M}{2}-1}(1+2k)^2 = \frac{A^2\left(M^2-1\right)}{3}$$

Dividing (4.38) by A^2, i.e., the power for a binary signal, gives the power penalty as

$$P_p = \frac{\left(M^2-1\right)}{3} \tag{4.39}$$

Hence, for M>>1, the additional power in an M-ary signal increases as M^2. Note, though, that each M-ary symbol contains $\log_2(M)$ bits of information, which allows the signal to be transmitted in a bandwidth scaled by a factor of $1/\log_2(M)$. Now, assuming white Gaussian noise, the noise power scales linearly with the transmission bandwidth. Therefore, to maintain the same probability of error, the required power in an M-ary signal, as given by (4.38), should also be scaled by a factor of $1/\log_2(M)$. Therefore, the power penalty for the M-ary signal becomes

$$P_p = \frac{(M^2 - 1)}{3\log_2(M)} \tag{4.40}$$

Although ideal NRZ pulses where considered here, the results obtained apply equally well to other pulse shapes.

Up to this point, only electrical powers have been considered. However, in an optical communication system it is the received optical power that is of concern. Recall that the electrical signal is linearly proportional to the received optical power in a receiver that directly detects the optical power. In this case, the received optical power for an M-ary signal will have symbols given by 0, A, $2A$,…, $(M-1)A$ where, here, A represents the optical power in a logical **1**. To obtain equally-spaced voltage levels, the optical power levels are equally spaced. In this case, the average received optical power for a binary signal is P_2=(1/2)A, whereas the average optical power in the M-ary signal is

$$P_M = \frac{1}{M}\left(0 + A + 2A + \ldots + (M-1)A\right) \tag{4.41}$$

$$= \frac{A}{M}\sum_{k=0}^{M-1} k = \frac{A}{2}(M-1)$$

Dividing (4.41) by P_2=(1/2)A gives the optical power penalty as

$$P_p = M - 1 \tag{4.42}$$

Therefore, for M>>1, the required optical power for an M-ary signal increases as M, not M^2, as with electrical power. Of course, (4.42) should be corrected for the required receiver bandwidth and associated reduction in noise power. Because the noise power is scaled by a factor 1/log$_2$(M), the noise voltage is scaled by a factor 1/(log$_2$(M))$^{1/2}$. Now, because voltage is linearly proportional to optical power, the required power in (4.41) should also be scaled by 1/(log$_2$(M))$^{1/2}$. Therefore, the *optical* power penalty for an M-ary signal becomes

$$P_p = \frac{M - 1}{\sqrt{\log_2(M)}} \tag{4.43}$$

4.3 Dynamic Noise Model

The static noise model described in section 4.2 is applicable to the analysis of an ideal NRZ (no ISI) intensity-modulated optical signal. In a real system, however, the signal passed to the decision circuit has a complicated time dependence for which there is no simple, closed-form expression. Furthermore, a significant amount of ISI is often present because of electrical filtering at the transmitter and/or receiver, or the nonlinear effect that chromatic dispersion has on the directly-detected intensity envelope. In addition, any frequency chirping of the transmitted optical signal will interact with the dispersive fiber and alter the shape of the received optical intensity in a nonlinear way. To account for these aspects of a real system, a dynamic noise model was employed. In this model, the received electrical signal is first determined through numerical simulation using the system model of Figure 3.3. This provides a sampled time record of the filtered received electrical signal in the absence of noise. In other words, it is the expected signal trace of a stochastic process. Then, a zero-mean noise current can be added to this trace that has a time-dependent variance, depicted by the length of the vertical lines in Figure 4.8.

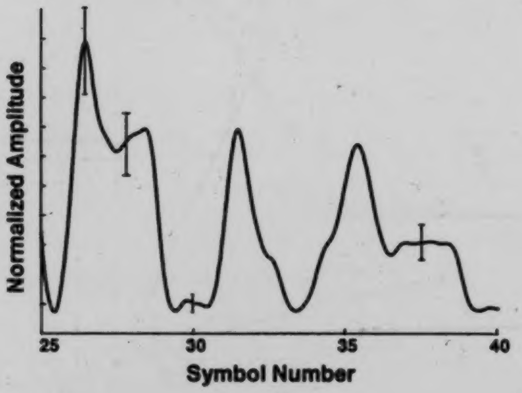

Figure 4.8 Expected value of signal passed to decision circuit for which the noise power varies continuously with time.

Because the variance is time dependent and can be different for symbols of the same logical value, this noise model will be called *dynamic*. A rigorous analysis would account for the exact statistics of the noise process. As stated earlier, however, accurate results for receiver sensitivity can be obtained using a Gaussian assumption. To proceed, the variance must be calculated at the decision time within each symbol of the sequence. In other words, if there are 512 symbols in a pseudonoise (PN) sequence, the variance must be calculated at 512 distinct points in time. The probability of error can then be calculated for each symbol, and the BER obtained by averaging the probability of error over all symbols. This is called the ***exhaustive*** method for determining the BER. Hence, if there are N symbols in the PN sequence, and I_k and σ_k^2 are the mean and variance, respectively, of the k^{th} symbol, then the BER can be obtained from

$$BER = \frac{1}{N}\sum_{k=1}^{N} Q\left(\frac{|I_k - I_{th}|}{\sigma_k}\right) \tag{4.44}$$

which, equivalently, can be expressed using the complementary error function, through

$$BER = \frac{1}{2N}\sum_{k=1}^{N} \mathrm{erfc}\left(\frac{|I_k - I_{th}|}{\sqrt{2}\sigma_k}\right) \tag{4.45}$$

where I_{th} is the decision threshold. The optimum threshold is that which minimizes the BER. For an M-ary signal, there are M-1 decision circuits and (4.45) can be generalized to

$$BER = \frac{1}{2N}\sum_{m=1}^{M-1}\sum_{k=1}^{N} \mathrm{erfc}\left(\frac{|I_k - I_{th,m}|}{\sqrt{2}\sigma_k}\right) \tag{4.46}$$

where $I_{th,m}$ is the decision threshold for the m^{th} decision circuit. Note that (4.46) also includes the area in the tails of PDFs belonging to symbols that are not adjacent to the threshold of a particular decision circuit. However, these contributions to the overall error probability would be very small and would have a negligible impact on the overall BER calculation.

Calculating the variance at the decision time within each symbol might be accomplished by assuming that the time dependence of noise follows exactly the time variation in the received optical power—in other words, allow the optical powers in the static noise model, which is based on Olsson's theory [94], to be time varying [103]. However, this assumes that the noise variance at some instant in time depends only on the optical power at that instant in time, and not on the history of the received optical power. Also, the time dependence of the receiver's impulse response is not taken into account. To explicitly account for the history of the received optical power and the time dependence of the receiver's impulse response, the theory in [96] can be used where the following expression was derived for the time-dependent variance.

$$
\begin{aligned}
\sigma^2(\tau) &= \Re q G \eta_i \eta_o \int s^2(t) h_r^2(\tau - t)dt + qI_{dark} \int h_r^2(t)dt + \ldots \\
&+ 2P_n \sum_k \sum_l \left[\Re q \eta_o \int_{(k+(l/M'))T}^{(k+((l+1)/M'))T} h_r^2(\tau - t)dt + 2P_n \left(\Re \eta_o \int_{(k+(l/M'))T}^{(k+((l+1)/M'))T} h_r(\tau - t)dt \right)^2 \right] + \ldots \\
&+ P_n \sum_k \sum_l \left[\begin{array}{l} \left(2\Re \sqrt{G\eta_i}\, \eta_o \displaystyle\int_{(k+(l/M'))T}^{(k+((l+1)/M'))T} s(t)\cos(\phi_s(t)) h_r(\tau - t)dt \right)^2 + \ldots \\ + \left(2\Re \sqrt{G\eta_i}\, \eta_o \displaystyle\int_{(k+(l/M'))T}^{(k+((l+1)/M'))T} s(t)\sin(\phi_s(t)) h_r(\tau - t)dt \right)^2 \end{array} \right]
\end{aligned}
\qquad (4.47)
$$

where $s(t)\exp(j\phi_s(t))$ is the complex envelope of the received optical field, $h_r(t)$ is the receiver's impulse response, $P_n = (G-1)h\upsilon n_{sp} B_o$ and T is the symbol period. Note that various noise terms are readily visible in (4.47): the first term is from signal-dependent shot noise, the second is due to shot noise from dark current, the third term represents shot noise from ASE (first integral in the double summation) and spontaneous-spontaneous beat noise (second integral in the double summation), and the last term gives the signal-spontaneous beat noise. In [96], (4.47) is used to calculate the variance of a **0** or **1** with a specified number of bits to the left and right of the symbol under consideration. The probability of error is then calculated for that particular bit pattern (truncated pulse train). This is done for all possible bit patterns, after which the error probabilities are averaged to obtain the BER. In (4.47), each bit period is divided into M' sub-intervals that are indexed from $l=0$ to $l=M'-1$, and k indexes a particular bit in the truncated pulse train. A constraint used in [96] in arriving at (4.47) is that the optical filter bandwidth B_o and sampling interval $\Delta t=T/M'$ are related by $B_o=1/\Delta t$. To facilitate the interpretation of (4.47), consider Figure 4.9 where it can be seen that k indexes the symbol number, and l indexes the sample interval within a given symbol.

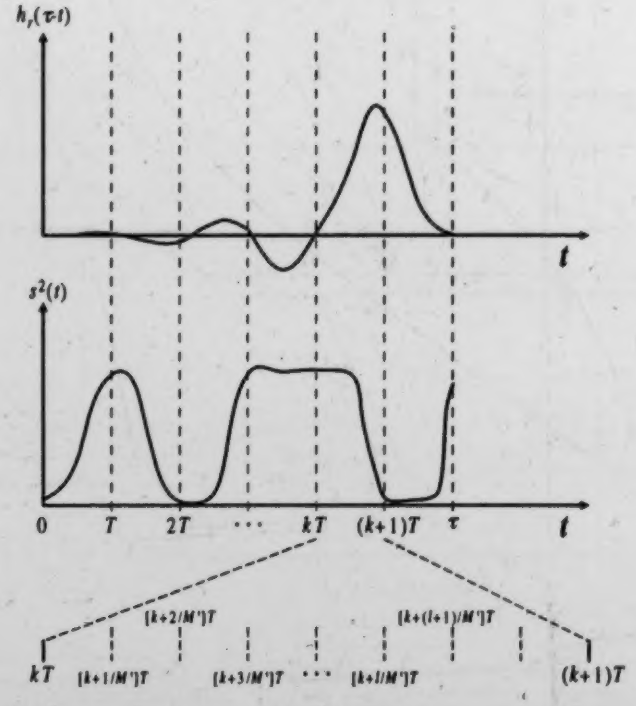

Figure 4.9 Relationship between the received optical power $s^2(t)$, receiver impulse response $h_r(t)$, and summation indices k and l.

Note that the integration limits in (4.47) are from $[k+l/M']T$ to $[k+(l+1)/M']T$, which is the duration of a sample interval. Using these observations, and with some algebraic simplification, (4.47) can be expressed in terms of a single index n and rewritten as

$$\begin{aligned}\sigma^2(\tau) &= \Re qG\eta_i\eta_o\sum_n s^2(n\Delta t)h_r^2(\tau - n\Delta t)\Delta t + qI_{dark}\sum_n h_r^2(n\Delta t)\Delta t + \ldots \\ &+ 2P_n\Re q\eta_o\sum_n h_r^2(\tau - n\Delta t)\Delta t + \left(2P_n\Re\eta_o\right)^2\Delta t\sum_n h_r^2(\tau - n\Delta t)\Delta t + \ldots \\ &+ 4P_n\Re^2 G\eta_i\eta_o^2\Delta t\sum_n s^2(n\Delta t)h_r^2(\tau - n\Delta t)\Delta t\end{aligned} \tag{4.48}$$

where the identity $\cos^2\phi_s(n\Delta t) + \sin^2\phi_s(n\Delta t) = 1$ was used. In (4.48), n indexes each sample within the time record of the received optical field, or within the receiver's impulse response. Again, each noise term is clearly identified in (4.48) where the first term represents signal-dependent shot noise, the second is shot noise from dark current, the third term is shot noise from ASE, the fourth term represents spontaneous-spontaneous beat noise, and the last term represents signal-spontaneous beat noise. Note that for the third and fourth noise terms, the parameter τ acts only to time shift the receiver's impulse response, but does not change the value of the summation. Hence, these noise terms, along with the second noise term, are stationary, as expected. With the noise terms now in the form of (4.48), it can be seen that signal-spontaneous beat noise and signal-dependent shot noise have the same time dependence. Also, if the summations in (4.48) are interpreted as discrete-time approximations to continuous integrals, and if any remaining terms of Δt are replaced by $\Delta t = 1/B_o$, the restriction that B_o is determined by the sampling interval is removed, provided B_o is now allowed to take on an arbitrary value. Analogous to the time-domain expression for signal-dependent shot noise, a similar expression could then be deduced for signal-spontaneous beat noise, as

$$\left\langle i^2_{sig-sp}(\tau)\right\rangle = \frac{4P_{ASE}\Re^2}{B_o}\int_{-\infty}^{\infty} P_{sig}(t)h_r^2(\tau - t)dt \qquad (4.49)$$

where, here, P_{sig} and P_{ASE} are, respectively, the optical signal and ASE power incident on the photodetector. Hence, at least in terms of calculating the time-dependent variance, signal-spontaneous beat noise may be modeled as a filtered Poisson shot noise process [99] with a time-dependent intensity function that is proportional to the product of ASE and signal power. It is interesting to note that under steady state conditions, i.e., constant received optical power, (4.48) reduces to the noise expressions presented in section 4.1. The only exception is that, for the spontaneous-spontaneous beat noise terms to be identical, the approximation $(2B_o - B_e) \approx 2B_o$ must be made in (4.4), i.e., it must be assumed that the optical filter bandwidth is much larger than the electrical receiver bandwidth.

4.4 PM-to-AM Relative Intensity Noise

This section gives details about PM-to-AM noise conversion in a dispersive medium. First, to gain insight into this phenomenon, PM-to-AM conversion of a deterministic, phase-modulated carrier will be described. Then, the case where the phase modulation is a random variable will be treated to arrive at expressions for the resulting RIN.

4.4.1 PM-to-AM Conversion in a Dispersive Medium

A model for PM-to-AM conversion is illustrated in Figure 4.10 where the input optical signal has a constant amplitude and a time-varying phase with respect to the carrier.

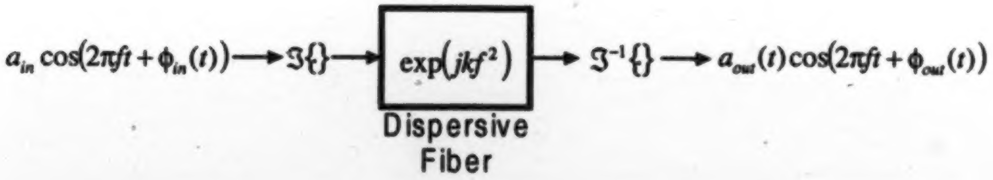
$a_{in}\cos(2\pi ft+\phi_{in}(t))$
$\Im\{\}$
$\exp(jkf^2)$
$\Im^{-1}\{\}$
$a_{out}(t)\cos(2\pi ft+\phi_{out}(t))$
Dispersive
Fiber

Figure 4.10 Phase modulation at the input is converted to amplitude modulation at the output of a dispersive fiber.

First, the Fourier transform is taken to obtain the frequency spectrum of the input signal. Then, each spectral component experiences a phase shift that is proportional to the square of frequency, which implies that the time delay is different for different spectral components. At the output of the fiber, the inverse-Fourier transform is taken of the output frequency spectrum to obtain the output signal, which will have a time-varying amplitude. Hence, phase modulation at the input is converted to amplitude modulation at the output. If the received signal is directly detected, the signal current at the receiver is given by the square of the received optical signal's amplitude. The extent of this PM-to-AM conversion depends on the modulation frequency, modulation depth, and the amount of dispersion, i.e., length of the dispersive fiber. For example, consider a phase-modulated input signal with a modulation depth of $\pi/2$ radians, given by

$$a_{in}\cos\left(2\pi ft+\frac{\pi}{2}\sin(2\pi f_m t)\right) \tag{4.50}$$

where f_m is the frequency of the phase modulation. For a fiber length of 48.5 km and a dispersion coefficient of 16 ps/(km·nm), the simulated PM-to-AM conversion is shown in Figure 4.11 where Δi is the peak deviation from the average current $\langle i\rangle$ after square-law detection. This result agrees with the theoretical and experimental results in [104]. The theory in [104] is not valid for longer fiber lengths or higher frequencies; however, the extent of PM-to-AM conversion can always be simulated for any conditions. Intuitively, the PM-to-AM conversion would not increase without bound as the frequency in Figure 4.11 is increased. To illustrate this, consider a fiber length of 100 km with a dispersion of 17 ps/(km·nm). Also, to be consistent with the definition of RIN, the PM-to-AM conversion will be expressed as $\langle \delta i^2\rangle/\langle i\rangle^2$ where $\delta i = i-\langle i\rangle$. Figure 4.12a shows the PM-to-AM conversion for frequencies up to 20 GHz for the input signal in (4.50)

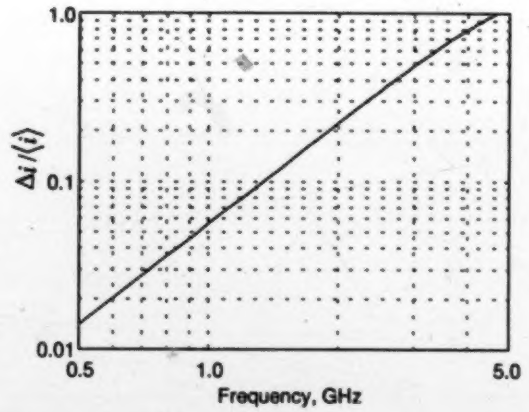

Figure 4.11 PM-to-AM conversion of an optical carrier that is phase modulated by a sinusoid.

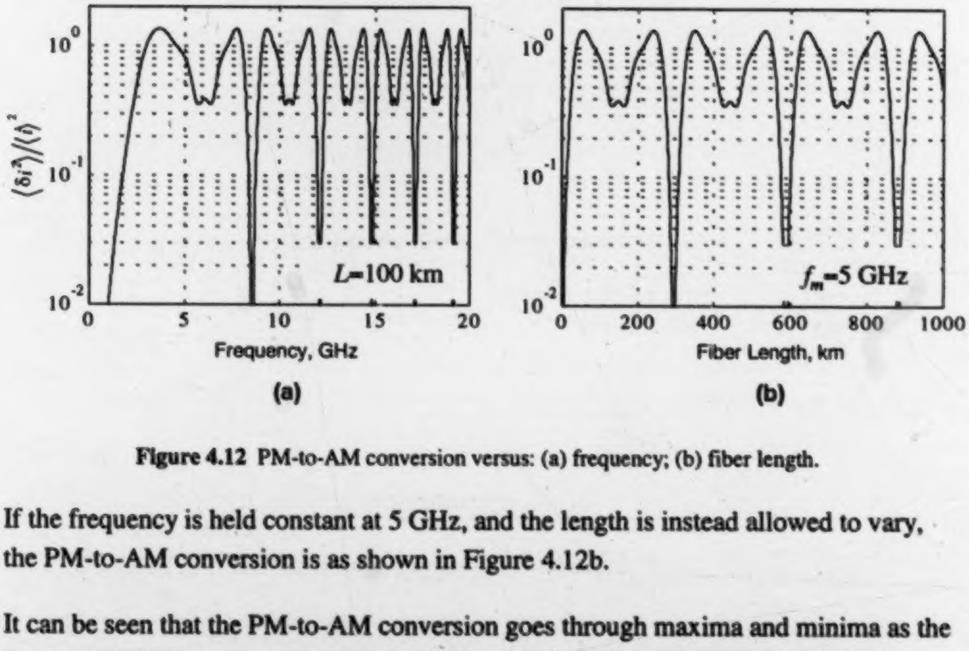

(a)

(b)

Figure 4.12 PM-to-AM conversion versus: (a) frequency; (b) fiber length.

If the frequency is held constant at 5 GHz, and the length is instead allowed to vary, the PM-to-AM conversion is as shown in Figure 4.12b.

It can be seen that the PM-to-AM conversion goes through maxima and minima as the frequency increases, or as the length increases. For an increasing length at a fixed frequency, the extreme values are equally spaced in length. For an increasing frequency at a fixed length, the frequency interval between extreme values decreases with increasing frequency. Figure 4.13 shows the corresponding detected photocurrent for various frequencies in Figure 4.12a. Consistent with Figure 4.12a, it can be seen that the current fluctuation is very strong at f_m=3.7 GHz and quite strong at f_m=10.5 GHz.

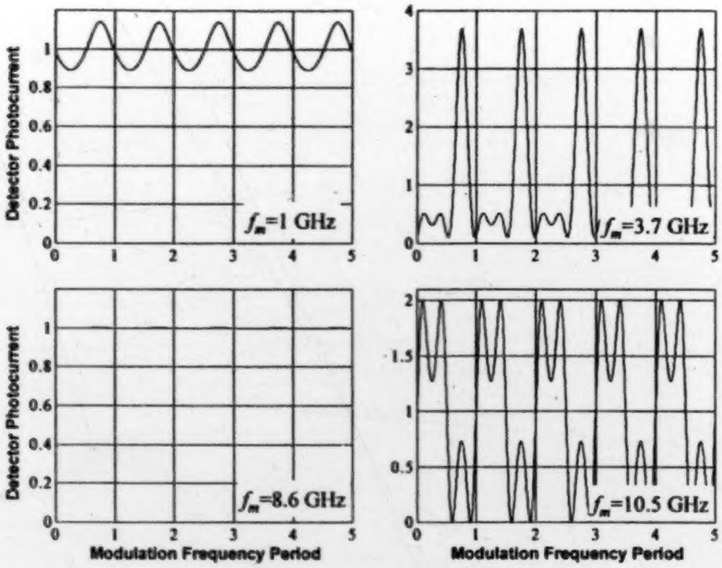

Figure 4.13 Detector photocurrent for various frequencies of the phase modulation corresponding to Figure 4.12a.

At f_m=8.6 GHz there is essentially no current fluctuation, corresponding to the null in Figure 4.12a. Also, the frequency content appears to be different for different modulation frequencies. For example, at f_m=1 GHz the current fluctuation appears to be almost sinusoidal with a frequency equal to the modulation frequency. At f_m=3.7 GHz and f_m=10.5 GHz there is clearly additional frequency content.

Figure 4.14 shows the PSD of the transmitted optical field referenced to the carrier, along with the baseband PSD of the detected photocurrent at various frequencies corresponding to Figure 4.12a. Note that the magnitude spectrum of the received optical field is the same as that transmitted; however, the phase relationship of spectral components in the received field's spectrum depends on the modulation frequency and fiber length. For a modulation depth of about $\pi/2$, it can be seen that the power in the fundamental is roughly equal to that in the carrier. For lower modulation frequencies, the majority of the power in the detected photocurrent is at the modulation frequency. As the modulation frequency is increased, however, the relative power in harmonics becomes strong, but then decreases as the modulation frequency is increased further. Hence, the PSD of the detected photocurrent appears to have a cyclic behavior that is synchronous with the extreme values in Figure 4.12.

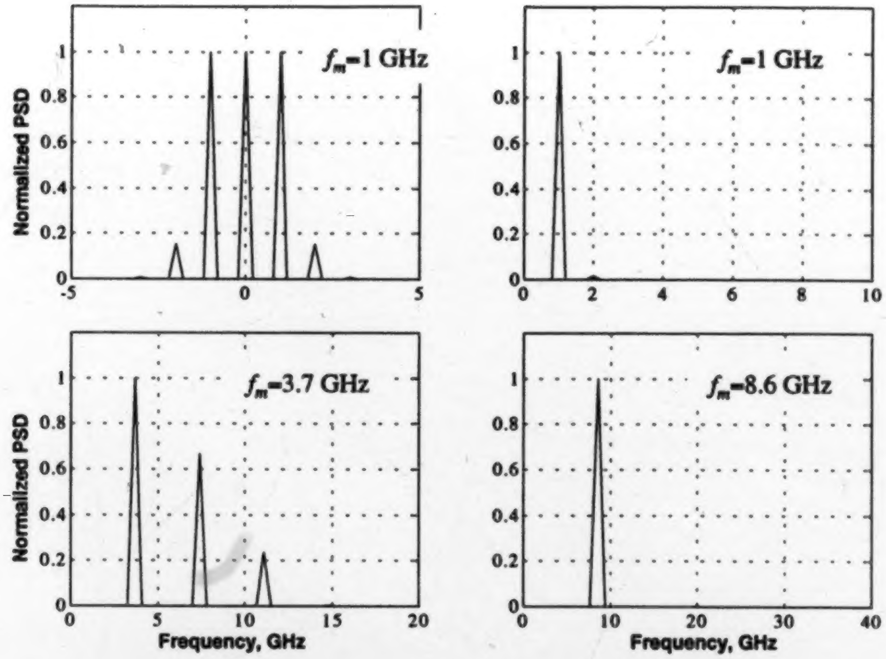

Figure 4.14 PSD of transmitted optical field referenced to the optical carrier (top left), and of the detected photocurrent at various frequencies corresponding to Figure 4.12a.

4.4.2 Spectral Density of PM-to-AM RIN

In the previous section, PM-to-AM conversion of a field that is phase modulated by a single sinusoid was considered. In this section, PM-to-AM conversion of a field with a random phase is considered. Under these conditions, the detected intensity, too, must be treated as a random variable. For example, [105] used a small-signal analysis to obtain the PM-to-AM conversion of a random phase, and the results were used in [106] to show the impact of PM-to-AM conversion on a DST system. However, that analysis requires the modulation depth of the intensity to be small compared to the average intensity. In another analysis, Petermann derived [101] the following expression for the RIN spectral density at the fiber output due to PM-to-AM conversion.

$$N(f) = 8(2\pi)^3 F_D^2 f^2 \Delta\upsilon \tag{4.51}$$

where the dispersion parameter F_D is given by (4.13) and $\Delta\upsilon$ is the source linewidth. Equation (4.51) was arrived at by expressing the output intensity in terms of $d^2\phi/dt^2$, where $\phi(t)$ is the random phase of the input optical field. Then, a white spectrum was assumed for the frequency noise $d\phi/dt$, yielding a Lorentzian lineshape, with a two-sided PSD given by $W_\phi(f)=2\pi\Delta\upsilon$. In deriving (4.51), Petermann neglected higher-order terms, which make (4.51) valid only for lengths up to about 30 km, over which a square dependence on fiber length is observed. A more general analysis was done by Yamamoto et al. where the random phase was expressed as a Fourier series with random coefficients. Assuming the same statistics for the phase noise as Petermann, the random Fourier coefficients were related to the phase noise PSD, and the following RIN spectral density was derived in [100]

$$N(f)=\frac{1}{2}\left[\sum_{n=0}^{\infty}4J_n\left(\frac{1}{f}\sqrt{\frac{2\Delta\upsilon}{\pi}}\right)J_{n+1}\left(\frac{1}{f}\sqrt{\frac{2\Delta\upsilon}{\pi}}\right)\sin\left(F_D(2n+1)(2\pi f)^2\right)\right]^2 \tag{4.52}$$

where J_n are Bessel functions of the first kind. For frequencies above a few hundred kHz and linewidths up to a few hundred MHz, the Bessel function arguments will be much less than 1. Therefore, the following approximations

$$J_0(x)\approx 1 \tag{4.53}$$

$$J_1(x)\approx\frac{x}{2}$$

$$J_n(x)\approx 0 \qquad (n>1)$$

can be used to simplify (4.52), to get

$$N(f)=\frac{4\Delta\upsilon}{\pi f^2}\sin^2\left(4\pi^2F_Df^2\right) \tag{4.54}$$

Note that when $\sin(x)\approx x$, i.e., x is small, (4.54) reduces to (4.51). Hence, the theory of Yamamoto et al. is consistent with Petermann's for short fiber lengths and/or over a low frequency range. However, (4.54) is more general because it is valid for any fiber length and/or frequency range. Using the identity $\sin^2(x)=\frac{1}{2}(1-\cos(2x))$, (4.54) can be put into the form of (4.12).

Assuming a linewidth of 10 MHz and a fiber dispersion of 17 ps/(km·nm) in (4.54), Figure 4.15 shows $N(f)$ for a fiber length of 100 km and 300 km.

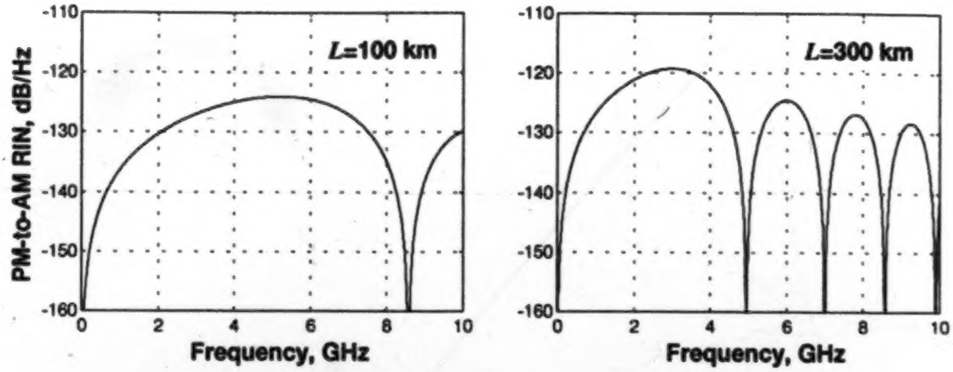

Figure 4.15 PM-to-AM RIN spectral density at 100 km (left) and 300 km (right).

It is interesting to note that, just as for the sinusoidal phase modulation of Figure 4.12a, the RIN spectral density has nulls spaced at decreasing frequency intervals as the frequency is increased. Note, too, that the lobes of $N(f)$ follow the envelope $2\Delta\upsilon/\pi f^2$.

4.4.3 RIN-Induced BER Floor

Knowing the PM-to-AM RIN spectral density, it is now possible to determine its impact on BER. To do this, the total RIN within the receiver's bandwidth must first be determined from

$$RIN = \int_0^\infty N(f)|H_{RX}(f)|^2 df \tag{4.55}$$

where $H_{RX}(f)$ is the receiver's transfer function. The total RIN can always be computed numerically for an arbitrary $H_{RX}(f)$; however, for the case where $H_{RX}(f)$ is an ideal lowpass filter with unit magnitude response, the integration of (4.55) can be evaluated to get equation (4.14). Now, for a particular receiver bandwidth B_e, the total RIN can be determined from (4.14) for any fiber length. Figure 4.16 shows the RIN-induced SNR=1/RIN versus fiber length for various receiver bandwidths, a fiber dispersion of 17 ps/(km·nm), and a source linewidth of 1 MHz. From (4.14) it can be seen that the total RIN scales linearly with the source linewidth; hence, the curves in Figure 4.16 would shift vertically by 3 dB for every factor of two change in linewidth. Using the same linewidth and fiber dispersion as Figure 4.16, Figure 4.17 shows the PM-to-AM RIN-induced SNR versus receiver bandwidth for various fiber lengths.

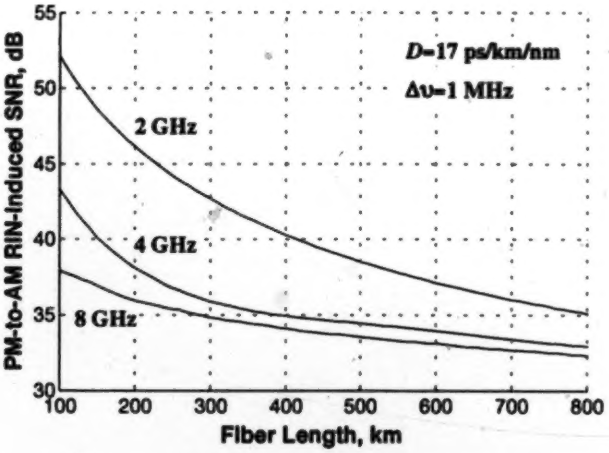

Figure 4.16 PM-to-AM RIN-induced SNR versus fiber length for different receiver bandwidths.

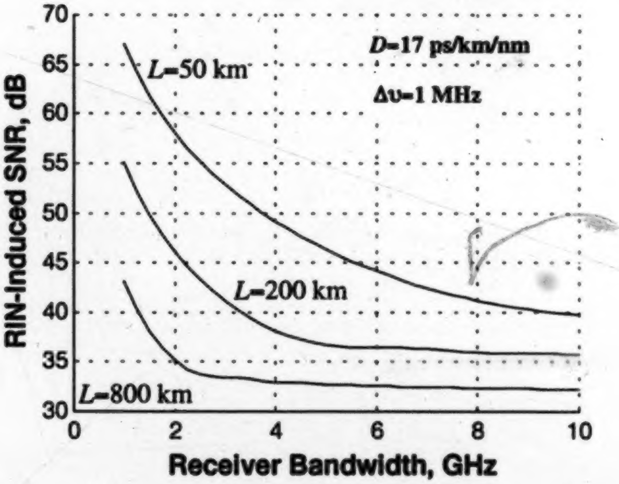

Figure 4.17 PM-to-AM RIN-induced SNR versus receiver bandwidth for different fiber lengths.

It was shown in the previous section that, when an M-ary signal is dominated by RIN, the ratio of adjacent levels should be the same for all levels when they are optimally spaced. If levels are not optimally spaced, then the BER will be essentially determined by the smallest ratio of adjacent levels. For example, for an M-ary ASK signal with *M* equally-spaced levels, the BER will be mostly influenced by errors in the decision circuit that discriminates between the top two levels. Letting $Q_x = (I_x - I_{x-1})/(\sigma_x + \sigma_{x-1})$ where I_x and I_{x-1} are the adjacent levels ($I_x > I_{x-1}$) that produce the smallest ratio $I_x/(I_{x-1})$, a good approximation to the BER can be written as

$$BER = \frac{2(M-1)}{M} Q(Q_x) \tag{4.56}$$

Note that (4.56) is an upper bound on the BER because it assumes that all decision circuits contribute equally to the error probability, a case that is strictly true only for optimally-spaced levels. A lower bound is obtained by assuming that only one decision circuit , i.e., that which has a threshold between I_x and I_{x-1}, makes errors. In that case, the multiplying factor in (4.56) becomes 2/*M*. Hence, the BER given by (4.56) is pessimistic by, at most, a factor *M*-1. Now, letting $k = I_x / I_{x-1}$, and knowing that $1/RIN = I_x^2/\sigma_x^2 = I_{x-1}^2/\sigma_{x-1}^2$, the following result can be obtained that relates the total RIN to a specified BER floor

$$RIN = \frac{1}{Q_x^2}\left[\frac{k-1}{k+1}\right]^2 \tag{4.57}$$

For example, consider a binary signal with an infinite extinction ratio for which $k \to \infty$. Using (4.56), $Q_x=6$ will give a BER=10^{-9}. Then, from (4.57) the RIN that will produce this BER floor is RIN=1/36, i.e., SNR=15.6 dB. Consider next a 4-ary ASK signal with equally-spaced levels, for which $k=3/2$. From (4.56) $Q_x=6.06$ and (4.57) gives RIN=1/918, i.e., SNR=29.6 dB. The required RIN-limited SNR improvement for an M-ary signal over a binary signal should not be confused with the required SNR improvement for an M-ary signal in the presence of stationary noise.

It is now possible to relate the source linewidth with an associated BER floor from PM-to-AM noise conversion. To do this, the required Q_x is first determined from (4.56). Then, the ratio of levels *k* is specified for a particular signaling scheme and (4.57) is used to determine the RIN value that will produce the specified BER. Next, the total RIN is calculated at a given fiber length and source linewidth, say 1 MHz, using (4.14). Finally, the total RIN is scaled linearly with the linewidth to obtain the required RIN value. For example, Figure 4.18 shows the linewidth that will produce a RIN-induced BER floor of 10^{-14} in: a binary signal having an infinite extinction ratio; a 4-ary ASK signal with equally-spaced levels and an infinite extinction ratio; a 4-ary ASK signal with an extinction ratio of 20 dB and optimally-spaced levels. In Figure 4.18, a fiber dispersion of 17 ps/(km-nm) was assumed. Also, the receiver bandwidth was set to 0.75 times the symbol rate for a 10 Gb/s signaling rate, i.e., 7.5 GHz for the binary signal and 3.75 GHz for the 4-ary ASK signal.

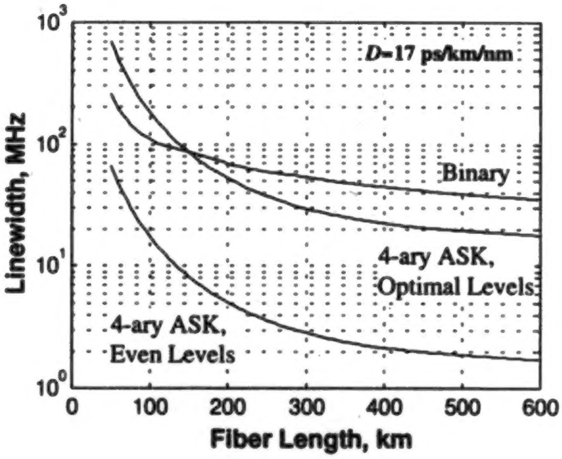

Figure 4.18 Linewidth that will produce a 10^{-14} BER floor for 10 Gb/s transmission.

At shorter fiber lengths, the 4-ary ASK signal with optimal level spacing is actually more immune to the effects of PM-to-AM RIN than the binary signal. The reason is evident from Figure 4.17 where the PM-to-AM RIN shows a strong dependence on receiver bandwidth between 3.75 and 7.5 GHz at shorter fiber lengths. As the fiber length is increased, however, the dependence on bandwidth is reduced significantly.

4.4.4 RIN in a Dynamic Noise model

It is apparent from (4.10) that the noise current from RIN depends on the square of the received optical power and, therefore, is a highly signal-dependent noise term. To make it compatible with the dynamic noise model, the filtering and time-delay effect of the receiver's impulse response must be taken into account, just as with signal shot noise or signal-spontaneous beat noise. To do this, the RIN will be treated as a filtered shot noise process, but with a time-varying intensity function that is proportional to the square of the instantaneous signal power. The following time-domain description of RIN results

$$\left\langle i_{RIN}^2(\tau)\right\rangle = \frac{RIN\Re^2}{2B_e}\int_{-\infty}^{\infty} P^2(t)h_r^2(\tau-t)dt \tag{4.58}$$

where *RIN* is the total RIN. Hence, *RIN*/B_e can be interpreted as an average RIN spectral density over the bandwidth of the receiver.

4.5 Summary

This chapter described various aspects of noise and how it can be modeled in an optical communication system. First, a description of the various noise sources was given. Then, a static noise model was described that allows for rapid calculations of BER and receiver sensitivity. The static model assumes an ideal received signal (zero ISI) where, in addition to basic system parameters, only a knowledge of the optical power in each level is required. Next, the issue of level spacing and power penalty in an M-ary ASK signal was treated. To account for an arbitrary received optical power and receiver response, a dynamic noise model based on [96] was described that fully accounts for ISI from all system impairments. Finally, noise associated with PM-to-AM conversion was discussed. It was shown that this noise, which scales linearly with the laser source linewidth, can produce a BER floor in long-haul links. A time-domain description of RIN, based on a filtered Poisson shot noise process, was also proposed.

5 Component Modeling and Related Topics

In this chapter, a description is given of the models used for important system components including electrical devices, external modulators, and erbium-doped fiber amplifiers. Frequency chirping in a Mach-Zehnder modulator is discussed extensively. Also, the origin of the fiber transfer function for singlemode fiber is explained.

5.1 Electrical Devices

All electrical components such as RF amplifiers, filters, power dividers/combiners, bias tees, DC blocks and cables were modeled as linear devices. Therefore, each device had an associated transfer function (or impulse response) and the cumulative response was modeled by simply cascading the component transfer functions. For ideal simulations, realizable filter structures such as Butterworth, Bessel, and customized pole-zero filters were used to model the frequency response of electrical components. An ideal NRZ pseudorandom bit sequence (PRBS) was computer generated and then passed through a lowpass filter to simulate the baseband information signal applied at the transmitter. The lowpass filter was chosen to produce rise and fall times and an overshoot typical of Gb/s NRZ signals. For more realistic simulations, discrete time records were acquired of the actual signal output from the BERT or GaAs logic devices, and then used in simulations. Also, 800-point frequency response records (magnitude and phase) from 50 MHz to 20 GHz were acquired using a network analyzer for all electrical, electro-optic and optoelectronic devices. These frequency response records were then used in simulations.

5.2 Mach-Zehnder External Modulators and Frequency Chirping

All simulations and experiments used an external modulator. Two types of external modulators were employed including $LiNb0_3$ (lithium niobate) and InP/InGaAsP devices. Although both are Mach-Zehnder (MZ) devices, they are modeled differently. All material presented here applies directly to a $LiNbO_3$ MZ device. Details of an InP/InGaAsP MZ device are covered in Section 5.2.7.

The emphasis of this section is on frequency chirping. Frequency chirping is a term used to describe the time variation in instantaneous frequency of a carrier. Although frequency chirping results in angle modulation of the carrier, this modulation is not intended to solely represent the baseband information signal. Instead, the resulting angle modulation is in addition to that produced by the intended modulation scheme, which is often amplitude modulation. In an optical communication system, frequency chirping can significantly degrade performance, but it can also enhance performance if it is introduced in a controlled manner. For example, if a directly modulated laser is used in a high-speed system, frequency chirping of the laser can significantly broaden the frequency content of the transmitted signal beyond the information bandwidth of the modulating signal. This can result in a dispersion limited distance of only a few kilometers in systems operating at high Gb/s rates. This limitation occurs because the extent of dispersion increases with transmission bandwidth in media such as standard fiber operating at 1550 nm. For this reason, the use of an external modulator in high-speed systems is very attractive because it is possible to operate the device chirp-free. It has been shown, though, that controlled frequency chirping (pre-chirping) of an externally modulated signal can improve system reach [107], [108]. It is somewhat paradoxical that the phenomenon, intended to be eliminated by the use of external modulation, is now desirable in external modulators. The reason for this has to do with the extent of frequency chirping and how it is introduced into the transmitted signal. In a MZ external modulator the amount of frequency chirping, and the polarity of the instantaneous frequency shift, can be controlled, producing a transmitted optical signal with better dispersion characteristics than an unchirped signal. In this section, frequency chirping in a MZ optical modulator is described in detail. Important considerations such as bias voltage, RF drive voltage and chirp parameter are described and related to the physical process that results in better dispersion performance.

5.2.1 Structure of a Mach-Zehnder Optical Modulator

A MZ optical modulator is an electro-optic device based on the principle of Mach-Zehnder interferometry. Figure 5.1 shows the basic structure of a MZ device.

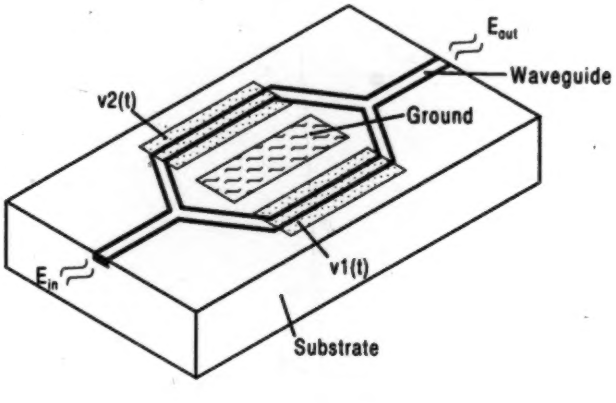

Figure 5.1 Basic structure of a Mach-Zehnder optical modulator.

It consists of a substrate with an embedded optical waveguide region in which light entering one end of the waveguide, E_{in}, is split equally into two separate arms and then recombined to give the output signal, E_{out}. The resulting output signal depends on the relative phase of the combining fields, which is determined by the optical path length of each arm. For example, if the combined fields are exactly 180 degrees out of phase, destructive interference will occur giving no signal at the output. If the combined fields are exactly in phase, the amplitude of the output signal will be a maximum because of constructive interference. In order to vary the optical path length of either arm, an electrode is placed over or beside it where a voltage can be applied. This results in an electric field through the waveguiding region of the arm that changes the effective index of refraction. In $LiNbO_3$ devices, the electro-optic (Pockels) effect causes the index of refraction to vary linearly with the strength of the electric field, and hence the applied voltage. If the direction of the electric field is reversed (i.e., voltage polarity is reversed), the index of refraction will change in the opposite sense. Therefore, by controlling the applied voltage at each electrode it is possible to achieve any phase difference between the combining signals. This allows the amplitude of the output light to be varied between zero (ideally) and some maximum value, determined by the power of the light input to the device.

For high-speed applications, the structure in Figure 5.1 would generally be a traveling-wave device. In that case, the driving voltage for each arm is applied at one end of the electrode with the other end terminated in a load equal to the characteristic impedance of the electrode (treated as a transmission line). The objective is to make the velocity of the electrode signal as close as possible to the velocity of light through the optical waveguide in order to maximize the frequency response of the device [109]. Traveling-wave devices also provide a larger interaction region between the electrical and optical signals and, therefore, require a lower voltage for a given phase shift.

5.2.2 Transfer Characteristic

If $v_1(t)=v_2(t)=0$, and assuming the length of each arm is the same, the complex envelope of the optical electric field at the output of the device is given by

$$E_{out}(t) = \frac{E_{in}(t)}{2}\exp(j\phi_o) + \frac{E_{in}(t)}{2}\exp(j\phi_o) = E_{in}(t)\exp(j\phi_o) \tag{5.1}$$

where ϕ_o is a constant phase shift and $E_{in}(t)$ is the complex envelope of the optical electric field input to the modulator. In other words, the output signal is a phase-shifted version of the input signal. If a time-varying voltage is applied to each arm the resulting phase shift in each arm will be time dependent. In this case, the output signal is

$$E_{out}(t) = \frac{E_{in}(t)}{2}\exp\left(j\phi_1(t)\right) + \frac{E_{in}(t)}{2}\exp\left(j\phi_2(t)\right) \tag{5.2}$$

where $\phi_1(t)$ and $\phi_2(t)$ are, respectively, the time-dependent phase shifts in arms 1 and 2 of the modulator. In order to proceed, it is necessary to find the phase terms, $\phi_1(t)$ and $\phi_2(t)$, in terms of the applied voltages, $v_1(t)$ and $v_2(t)$.

As mentioned earlier, the refractive index of the optical waveguide in each arm is linearly dependent on the strength of the electric field, which is itself linearly dependent on the applied voltage. The electro-optic effect can thus be summarized by the following equation for each arm in the modulator

$$\eta(t) = \eta_o - kv(t) \tag{5.3}$$

where $\eta(t)$ is the effective index of refraction in a given arm, $v(t)$ is the voltage applied to the electrode, η_o is the index of refraction with no applied voltage, and k is a constant. A positive value for k assumes that an applied positive voltage results in a lower index of refraction, i.e., decreases the optical path length. Now, the phase through a given arm is given by

$$\phi(t) = -\beta L = \frac{-2\pi\eta(t)}{\lambda} L_{MZ} \tag{5.4}$$

where λ is the free-space wavelength and L_{MZ} is the length of the MZ arm. Hence, using (5.3) in (5.4), the phase is

$$\phi(t) = \frac{-2\pi\eta_o L_{MZ}}{\lambda} + \frac{2\pi k L_{MZ} v(t)}{\lambda} \tag{5.5}$$

The first term in (5.5) is simply the constant phase shift in (5.1) and can be ignored. The second term shows that the phase shift varies linearly with the applied voltage. Assuming k is positive, the time-varying phase can be written as

$$\phi_1(t) = \frac{\pi v_1(t)}{V_\pi} \quad , \quad \phi_2(t) = \frac{\pi v_2(t)}{V_\pi} \tag{5.6}$$

where V_π is the switching voltage for the modulator, i.e., the voltage required for a phase shift of π radians. If the device is structured such that k is negative, the sign of the phase terms in (5.6) would be reversed. Note that the "polarity" assumption for k

does not detract from what follows, but does result in a sign reversal in some of the derived terms. These affected terms will be identified later on.

The complex envelope of the electric field at the output of the device can now be written from (5.2) and (5.6) as

$$E_{out}(t) = \frac{E_{in}(t)}{2}\exp\left(j\frac{\pi v_1(t)}{V_\pi}\right) + \frac{E_{in}(t)}{2}\exp\left(j\frac{\pi v_2(t)}{V_\pi}\right) \tag{5.7}$$

which, using the identity $2\cos(x) = \exp(jx) + \exp(-jx)$, can be put into the following form

$$E_{out}(t) = E_{in}(t)\cos\left[\frac{\pi}{2V_\pi}\left(v_2(t) - v_1(t)\right)\right]\exp\left[j\frac{\pi}{2V_\pi}\left(v_2(t) + v_1(t)\right)\right] \tag{5.8}$$

Dividing (5.8) by $E_{in}(t)$ gives the transfer characteristic $\psi_e(t)$ in the electric-field domain for the MZ modulator, as

$$\psi_e(t) = \cos\left[\frac{\pi}{2V_\pi}\left(v_2(t) - v_1(t)\right)\right]\exp\left[j\frac{\pi}{2V_\pi}\left(v_2(t) + v_1(t)\right)\right] \tag{5.9}$$

The transfer characteristic in the power domain is obtained by taking the square of the magnitude in (5.9) to get

$$\psi_p(t) = \cos^2\left[\frac{\pi}{2V_\pi}\left(v_2(t) - v_1(t)\right)\right] \tag{5.10}$$

which is a periodic function of the differential voltage, $v_2(t) - v_1(t)$, with period $2V_\pi$.

In summary, when a bandpass signal with complex envelope $E_{in}(t)$ is input to a MZ modulator, the output complex envelope is given by the product of the input complex envelope and the transfer characteristic in (5.9).

5.2.3 Frequency Chirping

The bandpass signal $e_{out}(t)$ at the output of the MZ modulator is

$$\begin{aligned} e_{out}(t) &= \mathrm{Re}\left\{E_{in}(t)\psi_e(t)\exp\left(j2\pi f_c t\right)\right\} \\ &= \mathrm{Re}\left\{A_{in}(t)\exp\left(j\phi_{in}(t)\right)A_\psi(t)\exp\left(j\phi_\psi(t)\right)\exp\left(j2\pi f_c t\right)\right\} \\ &= A_{in}(t)A_\psi(t)\cos\left(2\pi f_c t + \phi_\psi(t) + \phi_{in}(t)\right) \end{aligned} \tag{5.11}$$

where $A_\psi(t)$ is the magnitude of (5.9), $A_{in}(t)$ is the magnitude of the input signal's complex envelope, f_c is the optical carrier frequency, $\phi_\psi(t)$ is the phase of (5.9) and $\phi_{in}(t)$ is the phase of the input signal's complex envelope. The instantaneous angular frequency $\omega_i(t)$ of (5.11) is obtained by taking the time derivative of the cosine argument to get

$$\omega_i(t) = 2\pi f_c + \frac{d\phi_\psi}{dt} + \frac{d\phi_{in}}{dt} \tag{5.12}$$

Equations (5.11) and (5.12) are general in that the input signal itself may posses frequency chirping through the term $\phi_{in}(t)$. However, here we are interested in frequency chirping introduced by the MZ modulator, only. Therefore, the instantaneous frequency shift (chirp) introduced by the MZ modulator is given by $d\phi_\psi/dt$, or from (5.9) is

$$\frac{d\phi_\psi}{dt} = \frac{\pi}{2V_\pi}\left(\frac{dv_2(t)}{dt} + \frac{dv_1(t)}{dt}\right) \tag{5.13}$$

Note that the extent of frequency chirping is determined by the sum of the time-derivatives for the two drive voltages. In addition, the amount of chirp is inversely proportional to V_π for the MZ. As an example, consider a MZ modulator with $v_1(t) = \frac{1}{2}V_\pi + \frac{1}{2}V_\pi \cos(2\pi f_s t)$ and $v_2(t) = 0$, and with a continuous-wave optical input. Under these conditions a pulse train at frequency f_s will be produced at the output of the modulator. Figure 5.2 shows the resulting power pulse, carrier phase and frequency shift over one period for f_s=5 GHz. On the leading edge of the pulse the instantaneous frequency is decreased, reaching a minimum at 50 ps. On the falling edge of the pulse the instantaneous frequency is increased, reaching a maximum at 150 ps. The maximum deviation from the optical carrier frequency is ~4 GHz.

From (5.13) it might be tempting to say that external modulators with a larger V_π exhibit less frequency chirping; however, if the modulator is driven to the same extinction, then the peak-to-peak value of $v_1(t)$ and $v_2(t)$—and hence their time derivatives—must be scaled by the same factor as V_π, resulting in no change in the amount of frequency chirping. The next section explains how the frequency chirping in Figure 5.2 can lead to optical pulse compression.

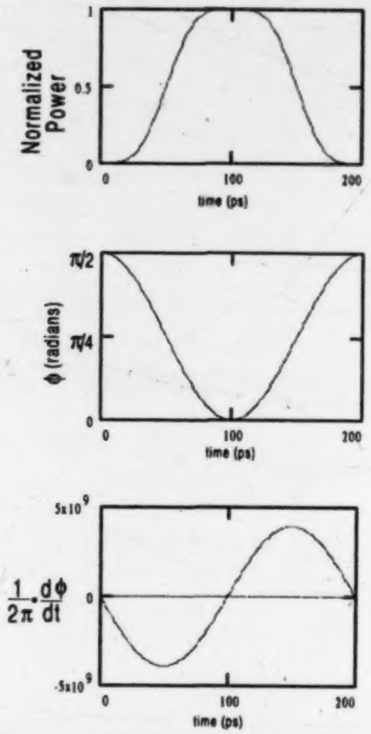

Figure 5.2 Chirping performance of a LiNbO$_3$ Mach-Zehnder modulator driven with a 5 GHz sinusoidal electrical drive: Optical power pulse (top); phase of output optical electric field (middle); instantaneous shift in optical carrier frequency in Hz (bottom).

5.2.4 Optical Pulse Compression

The group delay per unit distance in standard fiber is wavelength dependent, as shown in Figure 5.3.

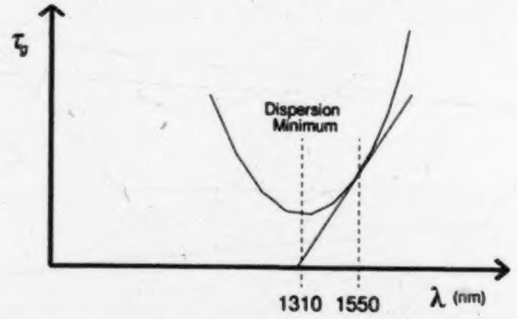

Figure 5.3 Group delay per unit distance versus wavelength for standard fiber.

At the dispersion minimum of ~1310 nm, the group delay remains essentially constant for small deviations from this minimum, i.e., the phase response of the fiber is approximately linear. However, at 1550 nm the group delay changes rapidly for small deviations from the operating wavelength. Over a range of practical interest, the group delay can be approximated by the positive-sloped tangential line shown in Figure 5.4. Note that a linear group delay (with non-zero slope) implies a quadratic phase response that will distort (disperse) the signal. Frequency chirping in a MZ modulator can take advantage of the group delay characteristic in Figure 5.3. Figure 5.4 shows how this is possible.

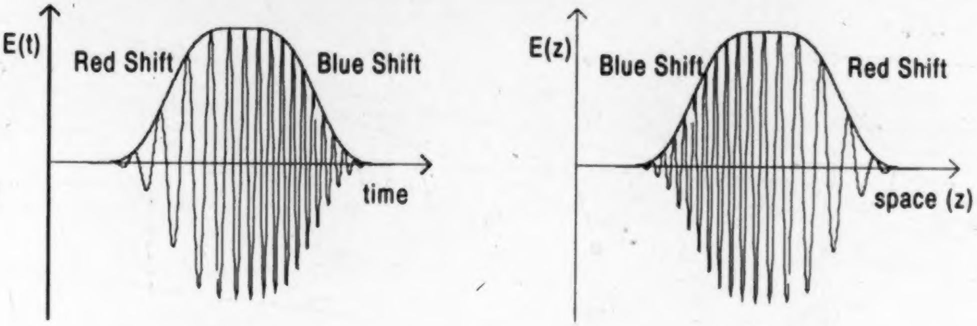

(a)

(b)

Figure 5.4 a) Optical electric field versus time for a chirped pulse; b) Optical electric field versus space for a chirped pulse.

In Figure 5.4a the instantaneous frequency is lower (red shifted) on the rising edge of the pulse and higher (blue shifted) on the falling edge of the pulse. The corresponding spatial chirped pulse at the input to the fiber would be as in Figure 5.4b (pulse traveling to the right). According to Figure 5.3, the rising edge will travel slower than the falling edge because of the difference in group velocity $v_g=1/\tau_g$. Therefore, as the pulse propagates along the fiber it will become compressed, giving it an anti-dispersive property. It should be pointed out that this intuitive argument is not fully justified because there is frequency content in the envelope itself that is affected by the quadratic phase response of the fiber. Regardless, simulated results along with other published results [108], [109], [110] verify that pulse compression does occur.

5.2.5 Chirp Parameter

As is often done with directly-modulated lasers, it is convenient to express the amount of frequency chirping in a MZ external modulator in terms of a parameter, α, called the chirp parameter. For a MZ optical modulator the instantaneous frequency shift can be related to the chirp parameter [111] in the same way as for the dynamic chirping in a laser, by

$$\frac{d\phi_v}{dt}=\frac{\alpha}{2S}\frac{dS}{dt} \tag{5.14}$$

where $S(t)$ is the instantaneous optical intensity. Now, $S(t)$ and dS/dt are related to the optical electric field $E(t)=A(t)\exp(j\phi(t))$ by

$$S(t)\propto A^2(t)\Rightarrow\frac{dS}{dt}\propto 2A(t)\frac{dA}{dt} \tag{5.15}$$

Solving (5.14) and (5.15) for α gives the following expression for the chirp parameter

$$\alpha(t)=\frac{\frac{d\phi_v}{dt}A(t)}{\frac{dA}{dt}} \tag{5.16}$$

Now, from (5.9) we have

$$A(t)=E_o\cos\left[\frac{\pi}{2V_\pi}\left(v_2(t)-v_1(t)\right)\right] \tag{5.17}$$

so that

$$\frac{dA}{dt}=\frac{-E_o\pi}{2V_\pi}\left(\frac{dv_2}{dt}-\frac{dv_1}{dt}\right)\sin\left[\frac{\pi}{2V_\pi}\left(v_2(t)-v_1(t)\right)\right] \tag{5.18}$$

where $E_0=$constant assumes that the input signal is continuous-wave light, i.e., we are only interested in frequency chirping introduced by the modulator itself. Using (5.13), (5.17) and (5.18) in (5.16) gives the chirp parameter explicitly in terms of the applied voltages $v_1(t)$ and $v_2(t)$, as

$$\alpha(t)=\frac{-\left(\frac{dv_2}{dt}+\frac{dv_1}{dt}\right)}{\left(\frac{dv_2}{dt}-\frac{dv_1}{dt}\right)\tan\left[\frac{\pi}{2V_\pi}\left(v_2(t)-v_1(t)\right)\right]} \tag{5.19}$$

Some useful expressions can be obtained when the voltages $v_1(t)$ and $v_2(t)$ have mathematically similar waveforms [107]. For example, consider the case where $v_1(t)$ and $v_2(t)$ are given by

$$\begin{aligned} v_1(t) &= V_{dc} + V_1 g(t) \\ v_2(t) &= V_2 g(t) \end{aligned} \tag{5.20}$$

where V_{dc} is a dc bias voltage and $g(t)$ is an arbitrary ac waveform normalized such that its peak-to-peak value is unity. V_1 and V_2 are constants equal to the peak-to-peak values of $v_1(t)$ and $v_2(t)$, respectively. Note that V_1 and/or V_2 can be negative resulting in an inverted ac waveform. If V_{dc}=$V_\pi/2$ and V_1<<V_π and V_2<<V_π (small-signal electrical drive conditions), then tan( ) in (5.19) is roughly equal to -1. Taking the time derivative of (5.20), and substituting the result into (5.19), gives

$$\alpha \approx \frac{V_2 + V_1}{V_2 - V_1} \tag{5.21}$$

Therefore, for small-signal drive conditions using mathematically similar waveforms and an appropriate DC bias, the chirp parameter is roughly constant and determined by the peak-to-peak values of the ac drive signals applied to each arm. Note that chirp-free operation (α=0) is achieved by setting V_1=-V_2, i.e., when one electrical drive (ac component) is an inverted replica of the other. This ensures that the time derivative of $v_1(t)$ is equal and opposite to the time derivative of $v_2(t)$, thus preventing any phase modulation (frequency shift), as given by (5.13). By choosing appropriate values for V_1 and V_2 it is possible to obtain any chirp parameter value in the range $(-\infty\ \infty)$.

As was done in [108], it is also useful to obtain expressions for the peak-to-peak amplitudes V_1 and V_2 in terms of the small-signal chirp parameter α. To account for the depth of intensity modulation, we will introduce a modulation index, β, given by

$$|V_2 - V_1| = \beta V_\pi \tag{5.22}$$

For example, setting V_2=$0.5V_\pi$ and V_1=$-0.5V_\pi$, or V_2=$1.5V_\pi$ and V_1=$0.5V_\pi$, will give β=1 and the modulator will be driven between maximum and minimum extinction. Solving (5.21) and (5.22) for V_1 and V_2 gives

$$V_1 = \frac{\beta V_\pi}{2}(\alpha - 1), \qquad V_2 = \frac{\beta V_\pi}{2}(\alpha + 1) \tag{5.23}$$

Hence, for a desired amount of chirp, α, and modulation depth, β, the required drive amplitudes are given by (5.23). Note that these results are also valid when the sign is inverted for both V_1 and V_2 in (5.23). Note, also, that in arriving at (5.23) the small-signal chirp parameter given by (5.21) was used. However, as β approaches unity the small-signal assumption is no longer valid. Therefore, it must be remembered that, although β can be close to unity in (5.23) for large-signal conditions, the chirp parameter in these expressions is for small-signal conditions. For large-signal conditions the chirp parameter in (5.19) is not constant. In fact, when $\beta=1$ the magnitude of the chirp parameter will vary between 0 and ∞. Figure 5.5 shows the time dependence of the chirp parameter for the chirped pulse in Figure 5.2 where $\beta=1$, as well as for $\beta=0.1$ and $\beta=0.5$. The solid line is the limiting case where β approaches zero, for which α takes on a constant value of -1. Note that the small-signal chirp parameter and the instantaneous large-signal chirp parameter are equal at the zero crossings of the applied ac signals, i.e., at the half power points of a transmitted optical pulse.

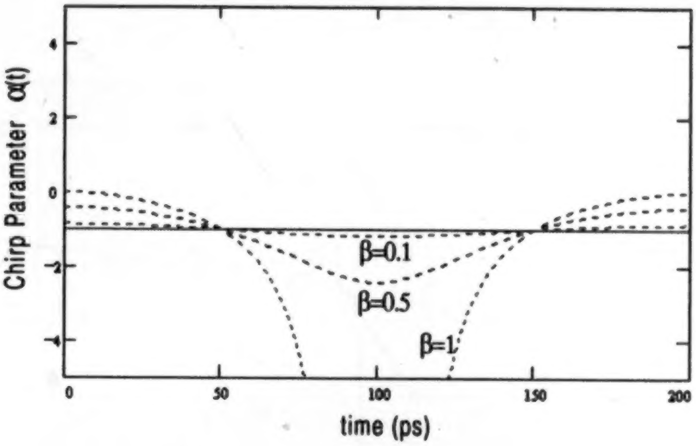

Figure 5.5 Time dependence of the chirp parameter for different modulation indices.

Throughout this discussion it was assumed that a positive voltage applied to a MZ arm resulted in a decrease in optical path length. If this assumption is reversed, i.e., k is assumed negative in (5.5), then the sign will be reversed in equations (5.13) and (5.19). In addition, the sign of the phase terms will be reversed in (5.6) through (5.9). Lastly, the role of V_1 and V_2 in (5.21) and (5.23) would be switched. The role of V_1 and V_2 is also switched if the dc bias point is changed from a positive slope on the transfer characteristic to a negative slope, or vice versa. For example, consider

Figure 5.6, which shows the power-domain transfer characteristic as a function of the differential voltage, $v_2 - v_1$.

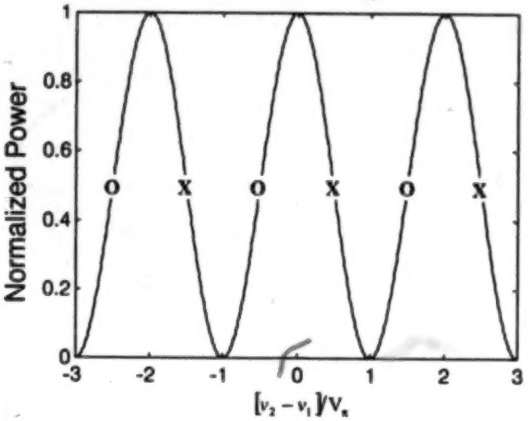

Figure 5.6 Power transfer characteristic versus normalized differential voltage for a LiNbO$_3$ Mach-Zehnder modulator: "O" and "X" denote bias points.

Assuming k is positive in (5.5), then V_1 and V_2 play the proper roles in (5.21) and (5.23) when the DC bias on arm 1 is set to $V_{dc} = 2nV_\pi + \frac{1}{2}V_\pi$ where n is any integer. This corresponds to the bias point marked by an "O" in Figure 5.6. If, however, the bias point is set to $V_{dc} = 2nV_\pi - \frac{1}{2}V_\pi$, corresponding to the points marked by an "X," then the roles of V_1 and V_2 are switched. Of course, based on symmetry, applying the DC bias to arm 2 (instead of arm 1) also switches the roles of V_1 and V_2.

5.2.6 Optical Extinction Ratio and Residual Chirp

Modeling the extinction ratio of a LiNbO$_3$ MZ in the power domain can be done as in [75] in which the power-domain transfer characteristic is expressed as

$$\psi_p(t) = \chi + (1 - 2\chi)\cos^2\left[\frac{\pi}{2V_\pi}(v_2(t) - v_1(t))\right] \tag{5.24}$$

where the maximum transmittance is 1-χ and the minimum transmittance is χ, corresponding to $\cos^2(\,)$=1 or 0, respectively. If the extinction ratio is defined as the ratio of maximum power to minimum power at the output of the device, then the extinction ratio in dB is

$$\delta_{dB} = 10\log\left[\frac{P_{max}}{P_{min}}\right] = 10\log\left[\frac{1-\chi}{\chi}\right] \tag{5.25}$$

As an example, if the extinction ratio is known to be 20 dB, then (5.25) could be solved for χ, i.e.,

$$\chi = \frac{1}{1+10^{\frac{\delta_{dB}}{10}}} \tag{5.26}$$

and this value used in (5.24) when modeling the device. Therefore, when only the output power is desired as a function of the voltages $v_1(t)$ and $v_2(t)$, (5.24) is a sufficient model that accounts for the optical extinction ratio. However, it is often necessary to model how the MZ device alters the phase of the optical electric field. For example, frequency chirping introduced by a MZ modulator requires an electric-field domain description of the transfer characteristic, precluding the use of (5.24). Hence, (5.9) must be modified to include the extinction ratio of the device. To do this, consider again Figure 5.1. An ideal MZ modulator would have Y-branch splitting/combining ratios that are exactly 50/50, as well as an equal amount of loss through each arm of the device. Under these conditions the combining fields at the output of the device would have identical amplitudes, which would provide an infinite extinction ratio. However, if the splitting/combining ratios are not exactly 50/50, or the loss through one arm is different than the other, then the amplitudes of the combining fields would be different, with a corresponding finite extinction ratio. Assuming an input E-field complex envelope of unity (continuous-wave light), the output optical field from the MZ can be expressed by

$$E_{out}(t) = \frac{1}{2}\exp\left(\frac{j\pi v_1(t)}{V_\pi}\right) + \frac{\gamma}{2}\exp\left(\frac{j\pi v_2(t)}{V_\pi}\right) \tag{5.27}$$

where γ is a scaling factor between 0 and 1 that accounts for a non-ideal device. Alternatively, the scaling factor could be applied to the first term in (5.27). The parameter γ is related to the optical extinction ratio δ, defined as the ratio of maximum to minimum optical power, by $\gamma = (\sqrt{\delta}-1)/(\sqrt{\delta}+1)$. For an ideal device, $\gamma=1$ for which the instantaneous frequency shift of the carrier (chirp) is given by (5.13). However, when $\gamma<1$, the zero-chirp drive condition will exhibit residual chirp as shown in Figure 5.7 where the E-field transfer characteristic of (5.27) is depicted as the sum of two phasors.

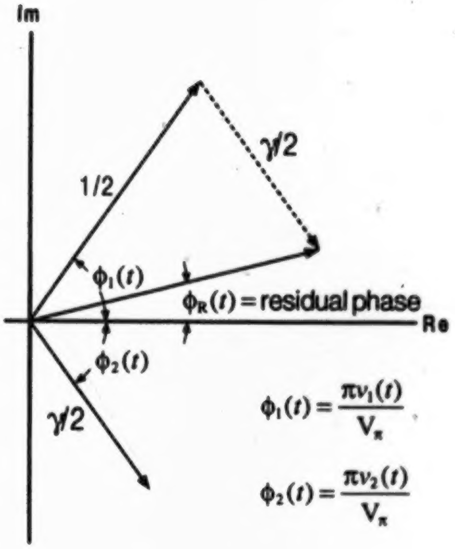
Im
γ/2
1/2
$\phi_1(t)$
$\phi_R(t)$ = residual phase
Re
$\phi_2(t)$
γ/2
$\phi_1(t) = \frac{\pi v_1(t)}{V_\pi}$
$\phi_2(t) = \frac{\pi v_2(t)}{V_\pi}$

Figure 5.7 Phasor diagram showing residual phase in the output field of a Mach-Zehnder modulator.

When $\gamma=1$, the resultant is always along the real axis; however, when $\gamma<1$ the resultant exhibits a time-varying residual phase, which necessarily manifests itself as residual chirp. Obviously, the amount of residual chirp depends on the value of γ and, therefore, the extinction ratio of the MZ device. It is also possible to put (5.27) into the form

$$\psi_e(t) = \cos\left[\frac{\pi}{2V_\pi}\left(v_2(t) - v_1(t)\right)\right]\exp\left[j\frac{\pi}{2V_\pi}\left(v_2(t) + v_1(t)\right)\right] - \frac{1}{2}(1-\gamma)\exp\left[\frac{j\pi v_2(t)}{V_\pi}\right] \tag{5.28}$$

which contains the transfer characteristic for an ideal device (first term) and a correction term (second term) that accounts for a finite extinction ratio. In arriving at (5.28) it was assumed in (5.27) that the optical field associated with $v_2(t)$ has a smaller amplitude than that associated with $v_1(t)$. If the converse is true, then $v_2(t)$ in the second term of (5.28) would be replaced by $v_1(t)$. Also, it was assumed that an increasing positive voltage across a given arm decreases the optical path length, i.e., k is positive in (5.5). If the device is structured such that the converse is true, then the sign of the phase terms in (5.28) will be reversed.

5.2.7 Multiple Quantum Well InP/InGaAsP Mach-Zehnder Modulator

Unlike $LiNb0_3$, this device uses a PIN structure made from III-V materials. The phase shift through a given arm is controlled by varying the reverse-bias voltage applied to the arm. A cross section of the device structure is shown in Figure 5.8.

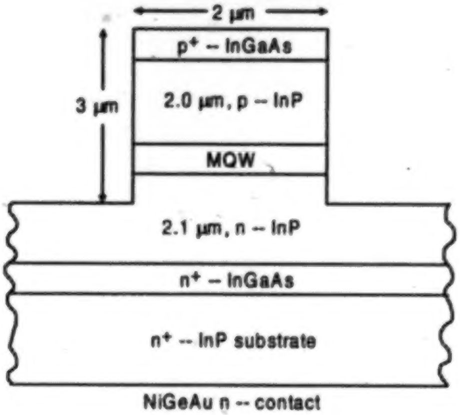

Figure 5. 8 Cross section of rib waveguide structure in a MQW InP/InGaAsP MZ Modulator (after [112]).

The MQW (multiple quantum well) intrinsic region consists of multiple InGaAs wells separated by InP barriers [112]. To eliminate higher-order modes from the InP cladding regions, InGaAs absorption layers are used [113]. The modeling of this device is fundamentally different than $LiNbO_3$ devices because the phase shift is not a linear function of the applied voltage. In addition, there is absorption that is a nonlinear function of the applied voltage. The generalized output field can be written as

$$E_{III\text{-}V}(t) = A_1(v_1(t))\exp(j\phi_1(v_1(t))) + A_2(v_2(t))\exp(j\phi_2(v_2(t))) \tag{5.29}$$

where $A_1(v)$ and $A_2(v)$ are the field amplitudes out of arms one and two of the MZ, respectively, and $\phi_1(v)$ and $\phi_2(v)$ are the phase shifts in arms one and two of the MZ, respectively. In [114], best fits to measured phase and absorption data were carried out where it was found that the phase had a square dependence on voltage, and that the field amplitudes were given by $A_{1,2}(v) \propto \exp(-k|v|^7)$ where k is a constant and v is the applied voltage. For the particular III-V device used in the present research, it was found that third-order polynomials could be fitted very well to the measured phase and amplitude data over the voltage range of interest. The method used to measure the field amplitude and phase in each arm is described in Chapter 6. Figure 5.9 shows a typical power transfer characteristic for a III-V device.

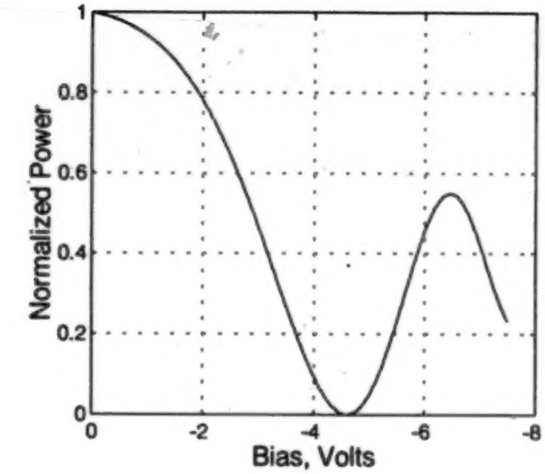

Figure 5.9 Transfer characteristic for a III-V MZ Modulator.

Note that, because of the voltage-dependant absorption, the output optical power is not a periodic function of the applied bias voltage, as with a $LiNbO_3$ device. Furthermore, the optical extinction ratio and chirping behavior of this device are dictated by the form of (5.29).

5.3 Fiber Transfer Function for Singlemode Fiber

It was mentioned in Chapter 3 that, when a modulated laser source is transmitted over singlemode fiber, the fiber channel cannot be modeled as a linear system acting on the optical power, but instead must be modeled as a linear system acting on the optical electric-field[3]. Consider the length of fiber L shown in Figure 5.10 where the input signal is $s_{in}(t)=a_{in}(t)\cos(2\pi f_o t+\phi_{in}(t))$ and the output signal is $s_{out}(t)=a_{out}(t)\cos(2\pi f_o t+\phi_{out}(t))$. Because the fiber can be modeled as a linear, time-invariant system in the electric-field domain, it has some transfer function $H(f)$ that characterizes its behavior.

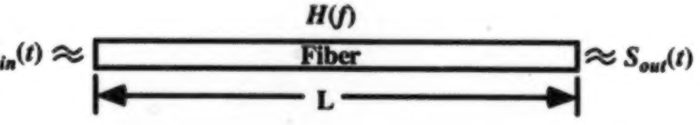

Figure 5.10 Fiber with length L and transfer function $H(f)$.

---

[3] This assumes that the optical intensity is sufficiently low that fiber nonlinear effects, such as self-phase modulation, are not significant.

The input and output signals represent the time-dependent electric field at the fiber input and output, respectively, and are assumed to be bandpass signals, i.e., the spectral width is small in comparison to the optical carrier frequency f_o, a condition that is always met in any practical system. We could just as well represent the input and output signals with their lowpass equivalent (complex envelope) through $u_{in}(t)=a_{in}(t)\exp(j\phi_{in}(t))$ and $u_{out}(t)=a_{out}(t)\exp(j\phi_{out}(t))$, which are the useful forms for simulation[4]. Let $s_{in}(t)\Leftrightarrow S_{in}(f)$ and $s_{out}(t)\Leftrightarrow S_{out}(f)$ be Fourier transform pairs for the input and output signals, respectively. Similarly, let $u_{in}(t)\Leftrightarrow U_{in}(f)$ and $u_{out}(t)\Leftrightarrow U_{out}(f)$ be transform pairs. Because the fiber span is modeled as a linear, time-invariant system in the electric-field domain, it must be true that

$$s_{out}(t)=s_{in}(t)*h_{BP}(t) \tag{5.30}$$

$$S_{out}(f)=S_{in}(f)H_{BP}(f)$$

or similarly,

$$u_{out}(t)=u_{in}(t)*h_{LP}(t) \tag{5.31}$$

$$U_{out}(f)=U_{in}(f)H_{LP}(f)$$

where "*" denotes convolution, and $h_{BP}(t)$ and $h_{LP}(t)$ are the bandpass and lowpass-equivalent impulse responses of the fiber, respectively, with corresponding transfer functions $H_{BP}(f)$ and $H_{LP}(f)$. Now, the objective is to find the appropriate form for $H_{LP}(f)$. This can be done by first finding $H_{BP}(f)$ and then converting it to $H_{LP}(f)$. Note that if the transfer function for a bandpass system is known, the lowpass-equivalent transfer function can be obtained by simply shifting the positive frequency response of the bandpass system down by an amount equal to the carrier frequency, as shown in Figure 5.11 (the reader may refer to [76], [78] for additional information on modeling bandpass communication systems).

---

[4] Bandpass systems are usually modeled by their lowpass equivalent so that the minimum sampling frequency is determined by the frequency content of the lowpass equivalent signal and not the carrier frequency f_o, which is usually much higher.

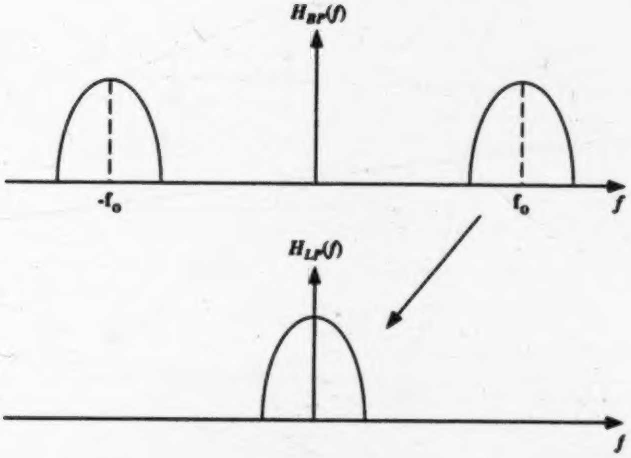

Figure 5.11 Transforming a bandpass transfer function to a lowpass equivalent.

Any transfer function is characterized by its magnitude and phase response and can, therefore, be expressed in the form $H(f) = A(f)\exp(j\phi(f))$. For optical fiber operating over a frequency range of only a few tens of GHz the magnitude response is essentially constant, except for a scaling factor due to fiber attenuation. Because a constant scaling factor does not result in signal distortion, we shall take $A(f)=1$ so that the fiber transfer function has the form $\exp(j\phi(f))$. Hence, it is the form of the phase term in the fiber transfer function that results in signal distortion. In deriving the fiber transfer function, certain terms will show up that can be omitted without changing the effect the transfer function has on signal distortion. For clarification, transfer functions comprised only of these terms will first be considered to show the resulting effect on the transmitted signal.

First, consider the ideal case where the fiber simply imposes a time delay T_o on the signal so that $u_{out}(t)=u_{in}(t-T_o)$. This is equivalent to saying that all frequency components that make up the signal are delayed by the same amount, namely T_o. The transfer function for such an ideal delay line is $H(f) = \exp(-j2\pi f T_o)$. In other words, a transfer function that has a unity magnitude response, and a phase response that is linearly proportional to frequency, only acts to delay the signal. Therefore, any phase term discarded that is linearly proportional to frequency simply removes the corresponding delay on the output signal. Next, consider a transfer function given by $\exp(jk)$ where k is a constant. For this case:

$$u_{out}(t)=\Im^{-1}\{U_{in}(f)\exp(jk)\}=\exp(jk)\,\Im^{-1}\{U_{in}(f)\}=\exp(jk)u_{in}(t)=a_{in}(t)\exp(j(\phi_{in}(t)+k))$$

where $\Im^{-1}\{\ \}$ denotes the inverse-Fourier transform. The corresponding bandpass signal is then $s_{out}(t)=a_{in}(t)\cos(2\pi f_o t+\phi_{in}(t)+k)$, which simply has a constant phase shift added to the optical carrier. In a direct detection system it is the square of the optical electric field that is detected, or equivalently the envelope of the instantaneous power, given by $P_{out}(t)\propto|u_{out}(t)|^2=a_{out}^2(t)$. Clearly, this has no dependence on the value of k. It is important not to confuse the effect a constant phase shift has on a baseband signal with that which it has on the lowpass equivalent considered here. In summary, constant phase terms, and those that are linearly proportional to frequency, can be omitted without changing the effect the transfer function has on signal distortion.

With this necessary background now in place, two methods for deriving the transfer function will be described.

Method One

This approach is based on material presented in [115]. First, the wavelength-dependent group delay $\tau(\lambda)$ is related to a linear dispersion parameter D, through

$$D=\frac{1}{L}\frac{d\tau}{d\lambda} \tag{5.32}$$

where L is the fiber length. Note that D is the first-order dispersion described in section 3.1.2 and that it is much larger than higher-order dispersion when standard singlemode fiber is operated at a wavelength around 1550 nm. Now, the group delay is related to the fiber's phase response by

$$\tau(f)=\frac{-1}{2\pi}\frac{d\phi}{df} \tag{5.33}$$

so that

$$\phi(f)=-2\pi\int_0^f \tau(f)df+\phi(0) \tag{5.34}$$

where, for any finite fiber length, it must be true that $\phi(0)=0$. Now, $\tau(f)$ can be reasonably approximated about the carrier frequency, f_o, by

$$\tau(f)\approx\tau_o+\left.\frac{d\tau}{df}\right|_{f_o}(f-f_o) \tag{5.35}$$

and, using $\lambda=c/f$, we can write

$$\frac{d\tau}{df} = \frac{d\tau}{d\lambda}\frac{d\lambda}{df} = DL\frac{d}{df}\left(\frac{c}{f}\right) = \frac{-DLc}{f^2} \tag{5.36}$$

Evaluating (5.36) at $f_o=c/\lambda_o$ and putting the result into (5.35), (5.34) can be evaluated to obtain

$$\phi(f) = -2\pi(\tau_o + DL\lambda_o)f + \frac{\pi DL\lambda_o^2 f^2}{c} \tag{5.37}$$

which gives the phase response of the bandpass system. Now, the lowpass equivalent transfer function can be obtained from $H_{LP} = \exp(j\phi(f+f_o))$, to get

$$H_{LP}(f) = \exp\left(j\frac{\pi DL\lambda_o^2 f^2}{c}\right) \tag{5.38}$$

where constant phase terms, and phase terms linearly proportional to frequency, have been discarded.

The form of (5.37) may seem inconsistent for the following reason. Although the impulse response of a lowpass-equivalent system is, generally, complex-valued, the impulse response of the corresponding bandpass system must be real-valued. This implies that the Fourier transform of the bandpass impulse response, which gives the bandpass transfer function, must be conjugate symmetric about $f=0$. In other words, $H_{BP}(f) = H_{BP}^*(-f)$. This is equivalent to saying that the magnitude response is symmetric about $f=0$ and that the phase response is anti-symmetric about $f=0$. Clearly, (5.37) is not anti-symmetric about $f=0$. This is because the expansion in (5.36) was done about $f_o>0$ so that the result in (5.37) is for positive frequencies only. If the expansion is done about $-f_o$, then the sign in (5.36) would be reversed with the sign of the phase in (5.37) also reversed, giving the required anti-symmetry for $\phi(f)$.

Method Two

An alternative approach to obtaining the fiber transfer function uses an expansion of the fiber's propagation constant [116]. The generalized fiber transfer function is given by

$$H_{BP}(f) = \exp(-j\beta(f)L) \tag{5.39}$$

where β is the fiber's propagation constant. Expanding β in a Taylor series about f_o gives

$$\beta(f) \approx \beta_o + \frac{d\beta}{df}(f - f_o) + \frac{1}{2}\frac{d^2\beta}{df^2}(f - f_o)^2 + \ldots \tag{5.40}$$

and since $\phi(f)=-\beta L$, then

$$\beta = \frac{-\phi(f)}{L}, \quad \frac{d\beta}{df} = \frac{-1}{L}\frac{d\phi}{df}, \quad \frac{d^2\beta}{df^2} = \frac{-1}{L}\frac{d^2\phi}{df^2} \tag{5.41}$$

and from (5.33)

$$\frac{d\phi}{df} = -2\pi\tau, \quad \frac{d^2\phi}{df^2} = -2\pi\frac{d\tau}{df} \tag{5.42}$$

Now, using (5.36) along with (5.41) and (5.42), we can write

$$\left.\frac{d\beta}{df}\right|_{f_o} = \frac{2\pi\tau_o}{L}, \quad \left.\frac{d^2\beta}{df^2}\right|_{f_o} = \frac{-2\pi\lambda_o^2 D}{c} \tag{5.43}$$

Then, putting this result into (5.40), the phase can be obtained as

$$\phi(f) = -\beta L = -\beta_o L - 2\pi\tau_o(f - f_o) + \frac{\pi\lambda_o^2 DL}{c}(f - f_o)^2 \tag{5.44}$$

Finally, evaluating (5.44) at $\exp(j\phi(f+f_o))$ and discarding constant and linear phase terms, the lowpass-equivalent transfer function of (5.38) is obtained.

In summary, chromatic dispersion results because the fiber has a nonlinear phase response to the optical electric field. Specifically, the phase response of the fiber is a quadratic function of frequency.

5.3.1 Modeling Chromatic Dispersion in the Power Domain

In intensity-modulated, direct-detection communication systems, care must be taken in applying the fiber transfer function when modeling chromatic dispersion. For these systems the optical power $P_{in}(t)$ at the input must first be expressed as a lowpass-equivalent electric field $E_{in}(t) \propto \sqrt{P_{in}(t)}\exp(j\phi_{in}(t))$. It is apparent that knowledge of $P_{in}(t)$ alone is not sufficient to predict the effect of chromatic dispersion because $\phi_{in}(t)$ must also be known. A theoretical treatment of this subject may simply assume that $\phi_{in}(t)=0$ so that $E_{in}(t) = \sqrt{P_{in}(t)}$. For example, $P_{in}(t)$ could be taken as a Gaussian pulse shape with $\phi_{in}(t)=0$, and the analysis carried through to show how fiber dispersion broadens Gaussian pulses as they propagate down the fiber. For directly-modulated lasers, the laser can be modeled by a set of coupled, first-order differential equations [96]. These equations can be expressed in terms of parameters that characterize the laser and can be solved numerically to arrive at $P_{in}(t)$ and $\phi_{in}(t)$. Other systems may use an external modulator where $\phi_{in}(t)$ is, generally, time-varying, although it is possible to operate some devices such that $\phi_{in}(t)$ is constant. Once $E_{in}(t)$ is known, $E_{out}(t)$ can be computed from $E_{out}(t) = \Im^{-1}\{\Im\{E_{in}(t)\}H_{LP}(f)\}$. The direct-detected signal is then obtained from $P_{out}(t) \propto |E_{out}(t)|^2$. Therefore, modeling chromatic dispersion in the power domain is possible using the electric-field domain fiber transfer function, provided a nonlinear time-domain transformation is used at the fiber input and output. An important point here is that, although the fiber can be treated as a linear system in the electric-field domain, it is not a linear system in the power domain. To illustrate this, consider the intensity modulation of a simple sinusoid where $P_{in}(t)=\sin(2\pi f_c t)+1$. For $f_c=5$ GHz and $\phi_{in}(t)=0$, a simulation of the resulting direct-detected signal after a distance of only 30 km is shown in Figure 5.12 for a fiber with $D=17$ ps/(km·nm). The original sinusoid is superposed for comparison.

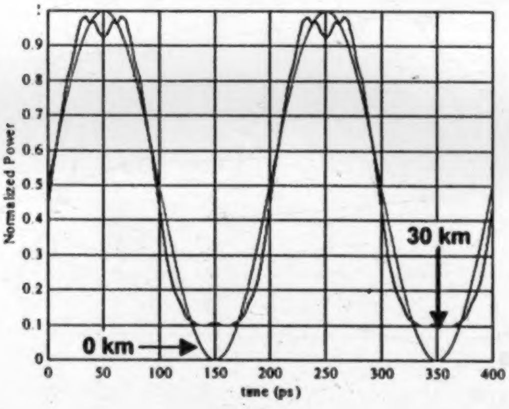

Figure 5.12 Signal distortion of a 5 GHz intensity-modulated tone after 30 km.

If this system were linear in the power domain, then the direct-detected signal, $P_{out}(t)$, would also be sinusoidal, of the same frequency as the input, and would have only the amplitude and/or phase affected by the fiber channel. Clearly, the response shown in Figure 5.12 contains additional frequency content after transmission over 30 km and, therefore, is nonlinear. The non-sinusoidal shape of the intensity envelope at the fiber's output, of course, depends on the transmission distance—Figure 5.12 is simply an example of the nonlinear distortion observed after transmission over 30 km.

5.4 Erbium-Doped Fiber Amplifiers

Erbium-doped fiber amplifiers (EDFAs) can be used as optical preamplifiers, inline amplifiers (nonregenerative repeaters), or post amplifiers. In a long-haul system, EDFAs are generally used in all three roles. An EDFA is essentially a laser without optical feedback. Conceptually, it is a simple device with few parts as shown in Figure 5.13.

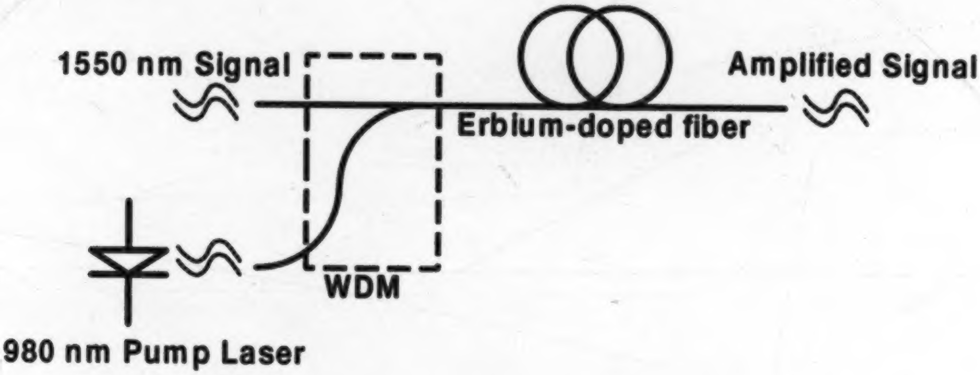

Figure 5.13 Parts of an erbium-doped fiber amplifier.

A pump laser, WDM (wavelength-division multiplexer) and a length of fiber (typically 10 to 30 m [117]) doped with the element erbium make up the amplifier. The doped fiber is a three-level system with populations in the ground state, metastable state and the pump state. A 980 nm laser (typically a few tens of mW) excites the erbium atoms from the ground state to the pump state, after which they quickly decay to the metastable state. The lifetime of a metastable state is quite long (≈12 ms) so that there is a significant accumulation of erbium atoms in that state, which produces a population greater than the ground state (called population inversion). Signal photons entering the erbium-doped fiber, then, cause stimulated emissions to the ground state, which can then cause further stimulated emissions, thereby amplifying the optical signal. In addition, spontaneous transitions occur, which can then be amplified to produce ASE. A WDM is required to combine the signal and pump power input to the doped fiber. It is also possible to use a 1480 nm pump laser, in which case the erbium atoms are pumped directly into the metastable state—here, the erbium-doped fiber behaves as a two-level system. EDFAs can effectively amplify signals over a range of about 1530 to 1560 nm, a bandwidth of about 4 THz.

Although it is possible to model EDFAs using physical parameters, such as doping concentration and profile, core geometry, absorption and emission cross sections, etc., it is more desirable—at least from a system design perspective—to model the device with a few characteristic parameters, especially those that are commonly cited by vendors. Three parameters often used to characterize an EDFA are small-signal gain G_o, output saturation power P_{sat}, and spontaneous emission factor n_{sp}. The output saturation power is the power output from the amplifier when the gain is compressed by $1/e$ ($\approx$4.3 dB). This parameter is analogous to the 1 dB gain compression power often specified for electrical amplifiers. The spontaneous emission factor characterizes the noise performance of the amplifier and is often specified as a noise figure through NF_{dB}=10log($2n_{sp}$). The following simplified model can be used to calculate the gain of an EDFA [98]

$$G = G_o \exp\left[(1-G)\frac{P_{in}}{P_{sat}}\right] \tag{5.45}$$

Hence, given the small-signal gain, input power and output saturation power, (5.45) can be solved numerically for the operating gain. Figure 5.14 shows the gain curve for an EDFA with G_o=30 dB and P_{sat}=+15 dBm.

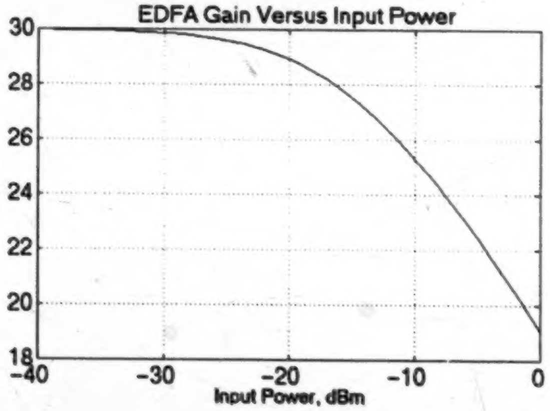

Figure 5.14 Gain curve for an EDFA with G_o=30 dB and P_{sat}=+15 dBm.

Note that in high-speed systems the gain saturating property of an EDFA is determined by the average input optical power, not the instantaneous power of a specific symbol. Hence, the EDFA does not distort the high-speed optical signal by, say, clipping symbols that contain a larger power. The optical signal is simply scaled, undistorted, by the operating gain of the EDFA.

5.5 Summary

A description was given of important components used in an optical communication system and how they can be modeled. The electric-field domain transfer characteristic for a $LiNbO_3$ MZ external modulated was derived that accounts for the optical extinction ratio of the device. Frequency chirping, pulse compression and chirp parameter were also discussed, as well as the fiber transfer function and the structure and modeling of an EDFA.

In a $LiNbO_3$ MZ modulator with dual-drive electrodes, the amount of frequency chirping is determined by the sum of the time derivatives of the applied voltages. Under proper bias conditions, and with appropriate driving voltages, optical pulse compression is possible in standard fiber operating away from the dispersion minimum. When the two arms of a MZ optical modulator are driven with mathematically similar waveforms, and an appropriate dc bias voltage is applied, the small-signal chirp parameter can be obtained from the peak-to-peak voltages at each arm. Similarly, for a specified chirp parameter and modulation index, the required peak-to-peak voltages can be determined. The chirp parameter is constant only under small-signal conditions. When the modulation index approaches unity, the variation in the chirp parameter becomes large. Therefore, when specifying the amount of chirp in terms of the chirp parameter, it must be remembered that this parameter is for small-signal conditions only, even though the modulator may be operating in the large-signal regime. The structure and modeling of a InP/InGaAsP MZ device is different than for a $LiNbO_3$ device. In particular, the phase shift and absorption in each arm of a III-V modulator is a nonlinear function of the applied voltage.

A modulated laser source operating over singlemode fiber can be modeled as a linear system in the electric-field domain. Time-domain operations can be used at the transmitter and receiver to account for the nonlinear nature of the system. The fiber transfer function imparts pure phase distortion, which is a quadratic function of frequency, on the optical field's spectrum. Two methods were presented for deriving the fiber's transfer function.

Lastly, the structure and modeling of an EDFA was presented. An EDFA can be characterized by three simple parameters: small-signal gain, output saturation power, and spontaneous emission factor.

6 Component Characterization

This chapter focuses on the methods used for characterizing important system components.

6.1 Laser Measurements

A CW laser source can be characterized by four important parameters: output power, wavelength, linewidth and RIN value. The output power can be measured directly with an optical power meter. Typical output powers for semiconductor lasers residing at TRLabs are from 0 to +4 dBm. The other parameters can be determined as described below.

6.1.1 Wavelength

The emission wavelength can be determined using a monochrometer. A monochrometer is the optical equivalent of a spectrum analyzer, i.e., it measures the power within a given resolution bandwidth that is scanned over a specified frequency range. Hence, the laser's emission wavelength can be obtained from the peak response of a monochrometer scan

6.1.2 Linewidth

Knowledge of the laser's linewidth is very important because it relates directly to the amount of PM-to-AM noise conversion, as discussed in Chapter 4. The delayed self-homodyne (DSH) method was used [118], which is illustrated in Figure 6.1.

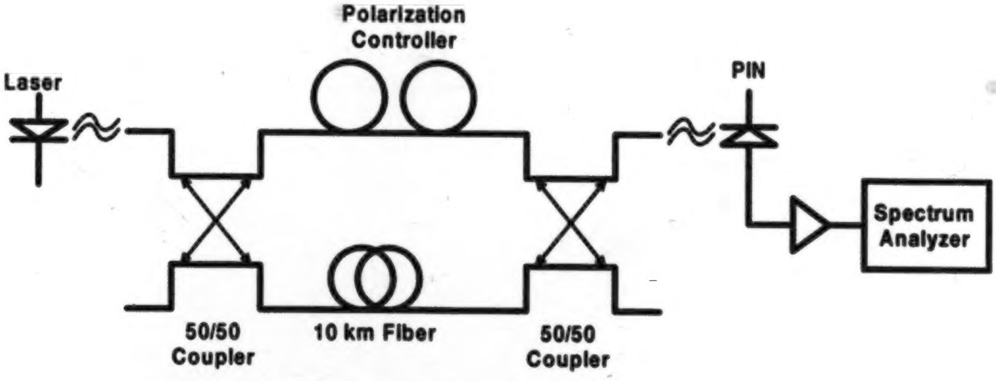

Figure 6.1 Setup for delayed self-homodyne linewidth measurement (after [118]).

A 50/50 coupler splits the laser light into two arms, one containing a polarization controller and the other a long length of fiber. The signals out of each arm are then combined with another 50/50 coupler to give an interference signal that is directly-detected using a PIN photodiode. A polarization controller is placed in one arm to align the polarization states of the combining fields and, therefore, maximize the interference signal incident on the photodiode. Hence, the setup in Figure 6.1 behaves as an unbalanced interferometer. The resulting electrical signal is then amplified and input to an RF spectrum analyzer. For this method to work, the differential delay through the interferometer must be greater than the coherence time of the laser source. Under these conditions the combined optical signals are uncorrelated, which, assuming a Lorentzian lineshape, produces a directly-detected baseband spectrum with a Lorentzian profile in which the one-sided 3-dB point is equal to the linewidth of the laser [118]. Given that the coherence time of a laser is roughly related to its linewidth by $\tau_c = 1/\Delta\upsilon$, a differential delay of 10 km gives a resolution of about 20 kHz. Figure 6.2 shows the DSH spectrum obtained for two different lasers.

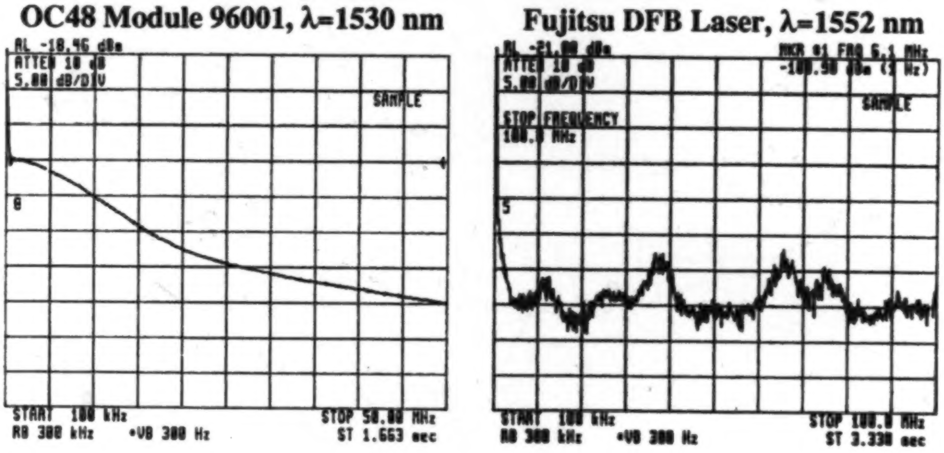
OC48 Module 96001, λ=1530 nm

Fujitsu DFB Laser, λ=1552 nm

Figure 6.2 DSH linewidth measurements for two lasers.

Note that the Fujitsu laser's spectrum contains significant side lobes. During measurements, the amplitude of the side lobes changed significantly over time periods less than one second and are believed to result from insufficient sidemode suppression in the laser. Most lasers, however, produced a very stable spectrum with a well defined linewidth like the one shown for the III-V module in Figure 6.2. Appendix C contains linewidth spectrum measurements for a variety of lasers.

6.1.3 RIN

The CW output of a laser will contain fluctuations in the intensity because of spontaneous emission and back reflections into the active medium. We shall call this *intrinsic* RIN to differentiate it from the RIN caused by PM-to-AM conversion, which was discussed in Chapter 4. The spectral density of RIN is, generally, not white, and the total RIN would require integrating the intrinsic RIN spectral density over the bandwidth of the receiver. Alternatively, for a given receiver response, the total RIN can be measured directly using the histogram feature of a digital oscilloscope. Then, an equivalent average RIN value (dB/Hz) can be specified that gives the total RIN measured when integrated over the receiver's bandwidth. Because it is the total RIN that is of interest in a Gb/s communication system, the histogram method was employed. The setup for doing the average RIN measurement is shown in Figure 6.3

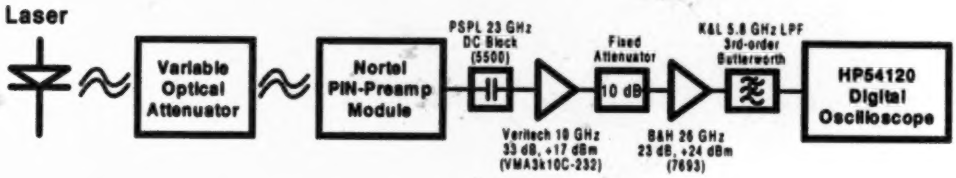
Laser
Variable Optical Attenuator
Nortel PIN-Preamp Module
PSPL 23 GHz DC Block (5500)
Veritech 10 GHz 33 dB, +17 dBm (VMA3k10C-232)
Fixed Attenuator
10 dB
B&H 26 GHz 23 dB, +24 dBm (7693)
K&L 5.8 GHz LPF 3rd-order Butterworth
HP54120 Digital Oscilloscope

Figure 6.3 Setup for measuring average laser RIN.

The oscilloscope's histogram feature samples a signal multiple times within a specified time window that is positioned relative to the trigger. Then, a distribution of the sampled values can be displayed along with statistical parameters such as the mean and variance. Because the noise considered here is stationary, any time window width, and delay offset from the trigger, is acceptable. To extract the RIN from measured histogram data, the contribution of other noises must be known. Furthermore, the photodiode's responsivity, and the net gain and NEB of all amplifiers and filters that follow, must be known. The photodiode's responsivity and the NEB and net gain of receiver components can be determined using the methods described later in this chapter. Now, to obtain the total RIN, the receiver noise alone is first measured using the histogram feature, i.e., the incident optical power is set to zero. Then, the optical power is set to a known CW value and the variance is measured again. Because the noises are statistically independent, the variances can be added:

$$\left\langle i^2 \right\rangle_{tot} = \left\langle i^2 \right\rangle_{RIN} + \left\langle i^2 \right\rangle_{shot} + \left\langle i^2 \right\rangle_{th} \tag{6.1}$$

Note that the mean square noise currents, referenced to the input of the oscilloscope, can be obtained by dividing the mean-square noise voltages, measured directly by the oscilloscope, by the square of the input impedance, i.e., 50^2. Now, $\left\langle i^2 \right\rangle_{th}$ and $\left\langle i^2 \right\rangle_{tot}$

are obtained directly from the histogram data, and the remaining noise terms are calculated from

$$\langle i^2 \rangle_{shot} = 2qP_L\Re B_e G_p$$
$$\langle i^2 \rangle_{RIN} = RIN(P_L\Re)^2 B_e G_p \tag{6.2}$$

where P_L is the optical power incident on the photodetector, and B_e and G_p are the NEB and power gain, respectively, for the receiver. Using the measured histogram data with (6.1) and (6.2), the only unknown is RIN, which is the desired average RIN per unit bandwidth for the laser.

Note that RIN increases with the square of received optical power and that shot noise is linearly proportional to optical power. Therefore, to ensure the RIN is not masked by shot noise, or thermal noise, the optical power should be set as high as possible. Measured RIN values using this method, which are typically -140 to -160 dB/Hz, are shown in Appendix C.

6.1.4 Laser Chirp

A large-signal model for the frequency chirp $d\phi/dt$ in a directly-modulated laser can be written as [119]

$$\frac{d\phi}{dt} = \frac{\alpha}{2}\left(\frac{d}{dt}\ln(P(t)) + \kappa P(t)\right) \tag{6.3}$$

where $P(t)$ is optical power, κ is a device-dependent parameter, and α is the linewidth enhancement factor for the laser. Typical values for α are from 5 to 8 [120]. The first term in (6.3) represents the dynamic chirp of a laser that is present when it is directly modulated. The second term is the adiabatic chirp, which, for a given device, is only a function of the steady-state output power. Dynamic chirping of a laser will not be considered further because all systems investigated in this research used the laser in a CW mode. The adiabatic chirp can be estimated by varying the injection current (optical power) and measuring the shift in the emission peak using a monochrometer. Adiabatic chirp can be expressed in units MHz/mA. A typical value for some of the lasers characterized at TRLabs is 2000 MHz/mA. Knowledge of the adiabatic chirp is not important when operating the laser in a CW mode. However, it can be used to estimate fiber dispersion by observing the temporal shift in a detected, modulated waveform as the laser current is adjusted. For example, if the wavelength shift is known to be about $\Delta\lambda$=0.15 nm when the current is adjusted by, say, 10 mA, then for a fiber length L and observed temporal shift Δt for the received signal, the fiber dispersion coefficient can be estimated from $D = \Delta t/(L\Delta\lambda)$. Fiber segments at TRLabs produced results around 17 to 18 ps/(km·nm) using this method.

6.2 Frequency Response of Electrical Components

One of the most important requirements in designing a multilevel Gb/s communication system is to accurately characterize the frequency response of components. This is necessary because it allows the impact of each device to be accurately predicted. By doing this, problematic devices, or combinations of devices, can be quickly identified and removed from a system design. Knowing the 3-dB bandwidth of a component is not sufficient because ultra-wideband devices typically exhibit large magnitude and phase fluctuations in the passband. For example, a passband ripple of ±1.5 dB is typical in wideband amplifiers. Other components such as filters, bias tees, DC blocking capacitors and power combiners can also impact system performance greatly. A flexible cable that is kinked, or a piece of semi-rigid cable that is bent improperly, can cause a system to fail completely. The importance of this aspect of system design cannot be overstated.

All electrical components were characterized by their small-signal S_{21} parameters (frequency response). Ideally, the response of electrical components that are cascaded would be given by the product of the individual transfer functions. However, no device is perfectly matched at its input and output, so that there would be some reflection at any connection point. Hence, each piece of coaxial cable behaves as a resonator, which can alter the overall frequency response. It was found that these resonances, generally, did not have a significant impact on the overall response. Regardless, if it is known how components will be cascaded, the overall S_{21} response can always be measured. All measured frequency response records contained 800 points, linearly spaced between 50 MHz and 20 GHz. They were acquired using an HP8510 network analyzer that was controlled by LabVIEW over a General Purpose Interface Bus (GPIB) where, to obtain the highest precision, the HP8510 was operated in frequency-step mode (not sweep mode) with each measured point averaged 64 times.

Figure 6.4 shows the frequency response of two wideband amplifiers – referred to as amps **A** and **B** – built by the same manufacturer. These amplifiers have the same model number and, therefore, have the same specifications, including a 3 dB bandwidth of 4.2 GHz.

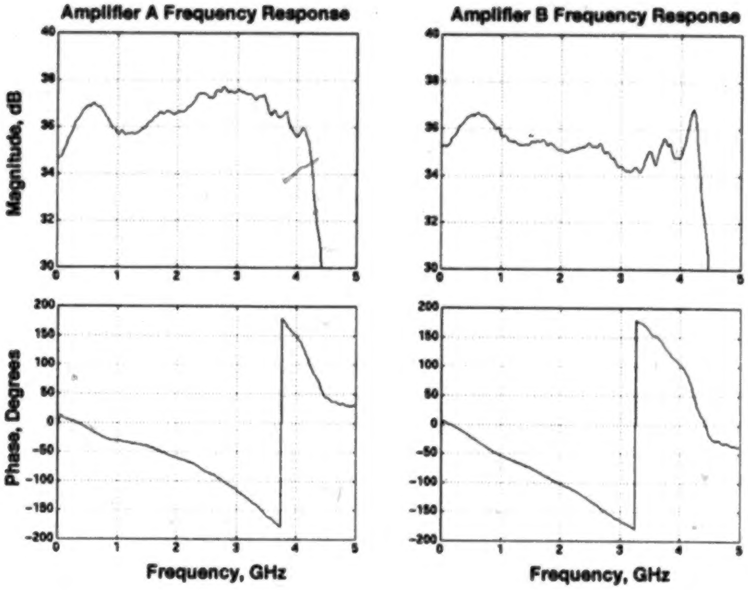

Figure 6.4 Frequency response of two wideband amplifiers having the same model number.

As can be seen from Figure 6.4, these amplifiers exhibit considerable ripple in the passband. To further illustrate the impact of this non-ideal response, Figure 6.5 shows eye diagrams at the output of amplifiers **A** and **B** for a 10 Gb/s (5 Gbaud) multilevel signal.

The output of amplifier **A** shows clear visible eyes, whereas the output of amplifier **B** shows complete eye closure. Also shown in Figure 6.5 is an eye diagram for one of the 5 Gb/s tributaries input to the multilevel symbol generator, as well as the multilevel signal at its output, i.e., input to the amplifier.

Note that a conventional binary system is quite robust because it can usually tolerate the non-ideal behavior of devices, provided an associated penalty from eye closure is acceptable. A multilevel signal, however, is much more sensitive to fluctuations in the frequency response. Appendix D contains measured frequency response data for a variety of components.

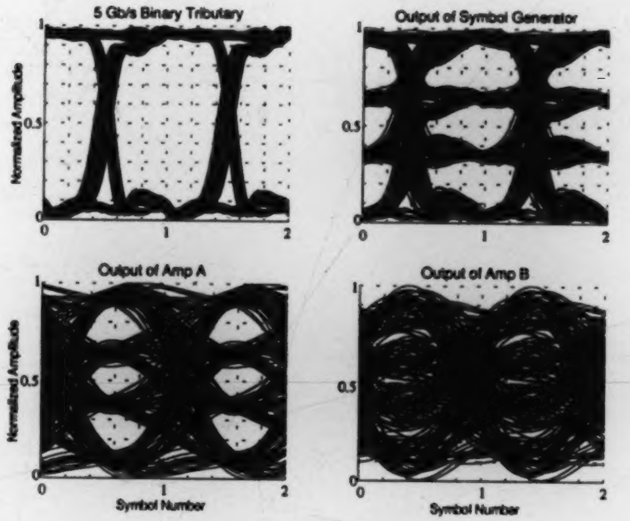

Figure 6.5 Eye diagrams: (top left) 5 Gb/s binary tributary input to multilevel symbol generator; (top right) 5 Gbaud signal output from symbol generator; (bottom left) output from amplifier **A**; (bottom right) output from amplifier **B** .

6.3 Frequency Response of Modulators and Photodetectors

Electro-optic devices, too, have to be characterized for their frequency response. For external modulators the transfer characteristic is nonlinear, as was described in Chapter 5. Therefore, to measure its frequency response the device must be operated in a linear region of its transfer characteristic. Unfortunately, the HP8510 network analyzer only operates on electrical signals; hence, any measurement of an external modulator must be coupled with the response of a photodetector, as shown in Figure 6.6.

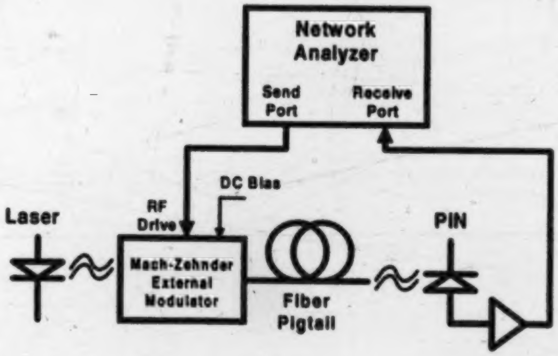
Network Analyzer
Send Port
Receive Port
DC Bias
Laser
RF Drive
Mach-Zehnder External Modulator
Fiber Pigtail
PIN

Figure 6.6 Setup for measuring the frequency response of an external modulator and photodetector.

There are methods to isolate the response of either the external modulator or photodetector [121], but they require excessively large signals applied to the modulator, or a spectrum analyzer that has a fundamentally-mixed front end over the bandwidth of the measurement. These approaches were not practical for the system considered here. For a back-to-back link operating in the linear range of the external modulator, a network analyzer frequency response characterization is completely valid and quite accurate. For large signal operation over many kilometers of fiber, however, the frequency response of the modulator and photodetector should, at least in principle, be separated. However, it was found that placing the cascaded small-signal response entirely at the transmitter predicted very similar results to placing it entirely at the receiver. Hence, it did not seem crucial, or even necessary, to separate the response of the external modulator and the photodetector. However, it was imperative to account for the frequency response. Indeed, many of the external modulators and/or photodetectors residing at TRLabs would not work at all with a 10 Gb/s 4-ary ASK communication system, even though they had sufficient bandwidth. This was due entirely to their poor passband frequency response. These devices would work in a 10 Gb/s binary system, but not without a significant ISI penalty. Only the Nortel InP/InGaAsP MZ module and the AT&T $LiNbO_3$ MZ had a response good enough to be used in a 10 Gb/s 4-ary ASK system. Also, only the Nortel PIN/Preamp module was of sufficient quality for a 4-ary ASK system. Appendix D shows the measured response data for external modulators and photodetectors.

6.4 Modulator RF Switching Voltage

Determining the switching voltage, V_π, at dc for a MZ modulator is relatively simple. Here, the dc bias voltage would be adjusted while measuring the optical output power. Then, the difference in bias levels, corresponding to the maximum and minimum optical powers, would give the dc V_π of the modulator. For example, Figure 6.7 shows the measured transfer characteristic for a Lucent $LiNbO_3$ MZ, which was obtained by sweeping the dc bias and measuring the output optical power. For this MZ the dc V_π is about 3.5 V. When using a MZ device as an external modulator, however, the RF V_π (i.e., ac V_π) must be known so that the amplitude of the RF signal applied to the modulator can be set to give full switching of the device. In many MZs, there are separate dc and RF ports connected to separate electrodes in the device. It is not uncommon, for example, for the dc V_π to be, say, 4 V and the RF V_π to be 9 V. Even when the dc bias and RF signal share the same electrode (these devices use a bias tee) the dc and RF switching voltages can be quite different, particularly when there is any mismatch as seen by the RF source.

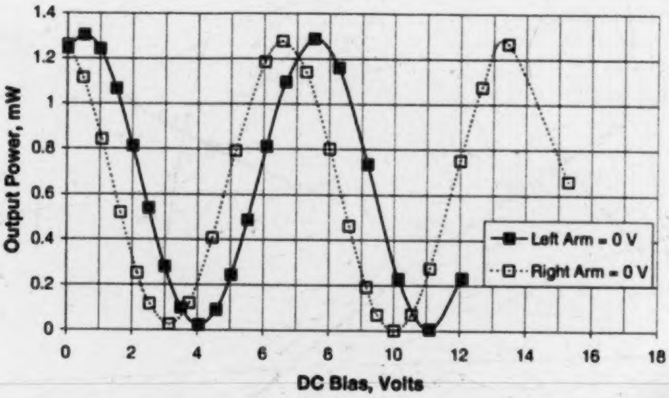

Figure 6.7 DC transfer characteristic for Lucent $LiNbO_3$ MZ.

A network analyzer can be used to measure the RF V_π using the setup of Figure 6.6. To do this, recall that the power output from a $LiNbO_3$ MZ is

$$P(v) = P_m \cos^2\left(\frac{\pi v}{2V_\pi}\right) \tag{6.4}$$

where P_m is the maximum output power and v is the applied voltage. Now, from (6.4) it follows that

$$\frac{dP}{dv} = \frac{-\pi P_m}{2V_\pi}\sin\left(\frac{\pi v}{V_\pi}\right) \tag{6.5}$$

Assuming the modulator is biased at its most linear region (i.e., the half-power point on its transfer characteristic) where the operating point is $v=V_\pi/2$, and assuming a small ac signal applied to the modulator, we can write

$$P_{pp} = \frac{\pi P_m}{2V_\pi} v_{pp,Tx} \tag{6.6}$$

where P_{pp} is the peak-to-peak optical power variation corresponding to an applied sinusoidal voltage having a peak-to-peak amplitude $v_{pp,Tx}$. Now, the peak-to-peak voltage at the receive port of the network analyzer can be obtained from

$$v_{pp,Rx} = \frac{\pi P_m v_{pp,Tx} \Re R_L G_v}{2V_\pi} \tag{6.7}$$

where R_L is the total resistance seen by the photocurrent and G_v is the voltage gain of the receiver's electrical amplifier. The S_{21} parameter magnitude displayed by the network analyzer is

$$\left|S_{21}(f)\right|_{dB} = 20\log\left[\frac{v_{pp,Rx}}{v_{pp,Tx}}\right] = 20\log\left[\frac{\pi P_m \Re(f) R_L G_v(f)}{2\mathrm{V}_\pi(f)}\right] \tag{6.8}$$

where frequency-dependent terms have been identified. The amplifier gain can usually be calibrated out. Hence, if $\Re(f)$ is known, $\mathrm{V}_\pi(f)$ can be solved for. For low frequencies, it is often reasonable to assume that $\Re(f)\approx\Re(f\approx0)$, i.e., that the responsivity is constant. This approximation is useful because the dc responsivity is very easy to determine, as shown in section 6.8. For high-quality photodetectors, it is often safe to assume that the responsivity is constant over many GHz. Using this method, the RF V_π of the Lucent MZ used in Figure 6.7 is about 4.1 V, which agrees with that specified by Lucent.

6.5 Transfer Characteristic of Multiple Quantum Well InP/InGaAsP Mach-Zehnder Modulator

In this research, an InP/InGaAsP Mach-Zehnder (III-V MZ) modulator was used for many experiments. As described in Chapter 5, the transfer characteristic of this device is quite different than that of a $LiNbO_3$ device. In addition, the III-V MZ was packaged in a module that contained a laser source, isolators, lenses, the III-V MZ, and a fiber pigtail output. Hence, only the output power from the module could be measured. Therefore, determining the phase shift and absorption in each arm of the MZ could only be done indirectly through measurements of the net output optical power. The generalized transfer characteristic is of the form

$$\psi_e(t) = k\left[A_1\left(v_1(t)\right)e^{j\phi_1(v_1(t))} + A_2\left(v_2(t)\right)e^{j\phi_2(v_2(t))}\right] \tag{6.9}$$

where k is a constant, v_1 and v_2 are the voltages applied to arms one and two of the MZ, A_1 and A_2 are the field amplitudes output from arms one and two, and ϕ_1 and ϕ_2 are the phase shifts in arms one and two, respectively. For convenience k will be set to unity. Let $V_n=\{V_1, V_2, V_3,\ldots\}$ be a set of discrete voltages at which to evaluate $v_1(t)$ and $v_2(t)$. The procedure, then, is to determine the amplitude and phase of each arm at each discrete voltage V_n to give $A_{1,n}$, $\phi_{1,n}$, $A_{2,n}$ and $\phi_{2,n}$. Then, curves can be fitted to this data to obtain a mathematical model for the III-V MZ. To obtain the field amplitude in arm one, the voltage applied to arm two is first set quite large, say, -10 V. This essentially shuts off arm two because the absorption at that voltage is very high. Then, the amplitude in arm one is obtained directly from

$$A_{1,n} = \sqrt{P_n} \tag{6.10}$$

where P_n is the measured output power corresponding to voltage V_n. Similarly, by setting the voltage across arm one to a large value, the field amplitudes $A_{2,n}$ can be determined. With the field amplitudes now known at each voltage V_n, the phase shift in a given arm can be determined by considering the phasor diagram in Figure 6.8.

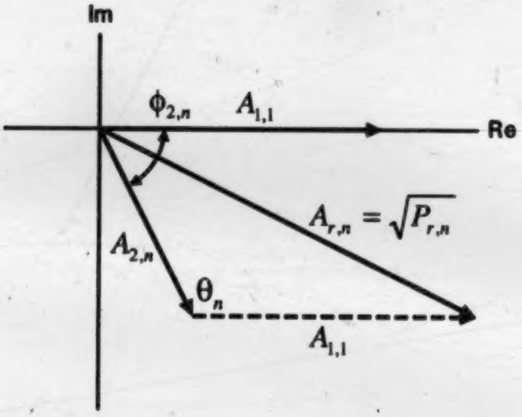

Figure 6.8 Phasor diagram showing calculation of phase.

For example, to determine the phase element $\phi_{2,n}$, the voltage across arm one is set to zero. Also, the phase element $\phi_{1,1}$, which serves as a reference, is assigned a phase of zero radians. Next, the voltage across arm two is set to a particular V_n and the output optical power $P_{r,n}$ is measured to obtain the resultant field amplitude, $A_{r,n}$. Note that θ_n can be obtained from the law of cosines, from which the desired phase element then follows, i.e.,

$$\theta_n = \cos^{-1}\left[\frac{A_{2,n}^2 + A_{1,1}^2 - A_{r,n}^2}{2A_{2,n}A_{1,1}}\right] \tag{6.11}$$

$$\phi_{2,n} = \pi - \theta_n$$

This procedure is repeated using all values of V_n for each arm. Figure 6.9 shows the measured field amplitude and phase through each arm of the MZ using the method described here. In addition, third-order polynomial fits to the measured data are shown.

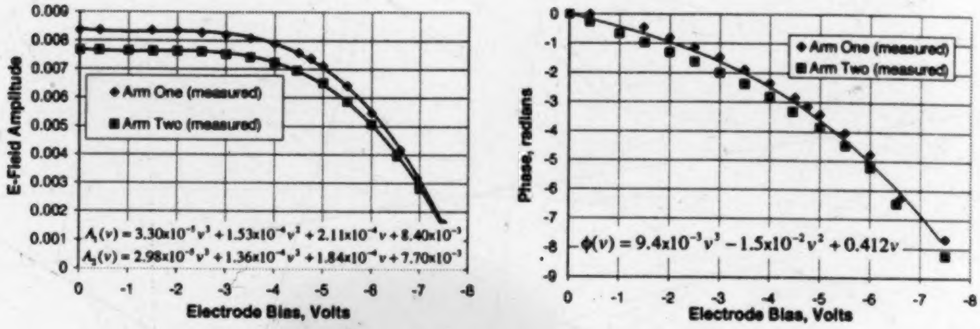

Figure 6.9 Meausred amplitude (left) and phase (right) for a III-V MZ.

From Figure 6.9 it can be seen that the field amplitudes output from each arm are slightly different, suggesting that the absorption in one arm is slightly higher than the other, or that the input and/or output Y-branches are not ideal. It is also evident that there is a slight imbalance between the phase of each arm. To account for this, the phase y-intercept was set to –0.1 radians for arm two, and 0 radians for arm one. Figure 6.10 shows the transfer characteristic curves for various bias conditions using the third-order polynomial fits of Figure 6.9. Also shown are the measured transfer characteristic curves for the same bias conditions.

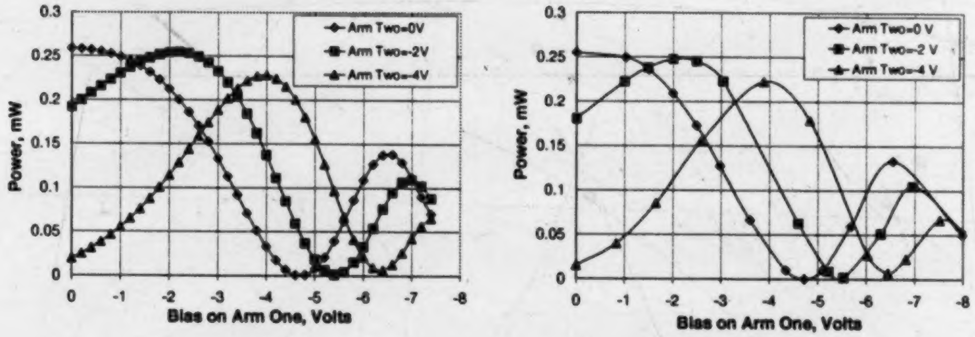

Figure 6.10 III-V MZ transfer characteristic: (left) modeled using curve fits for amplitude and phase; (right) measured.

It can be seen that the modeled amplitude and phase produces transfer characteristic curves that are in good agreement with the measured curves.

6.6 EDFAs

It was mentioned in Chapter 5 that an EDFA can be modeled by three basic parameters, including the spontaneous emission factor (or noise figure), small-signal gain, and output saturation power. Because of WDM and/or splice losses, the gain of the erbium-doped fiber will be larger than the connector-to-connector gain of the EDFA module. However, if the EDFA's noise figure and gain are measured from fiber connector input to connector output, it is not necessary to know the internal coupling losses of the device. In other words, the calculated signal and noise power using the external parameters will be the same as that obtained using the internal parameters with internal coupling losses. Therefore, all EDFAs were characterized by external parameters. It is straightforward to show that if G_i, $n_{sp,i}$ and $P_{sat,i}$ are the internal gain, spontaneous emission factor and output saturation power, respectively, then they are related to the external parameters by

$$G = c_1 G_i c_2 \tag{6.12}$$

$$n_{sp} = n_{sp,i} \frac{c_2(G_i - 1)}{(G - 1)}$$

$$P_{sat} = c_2 P_{sat,i}$$

where c_1 and c_2 are, respectively, the internal input and output coupling efficiencies.

To measure the external EDFA parameters, the setup in Figure 6.11 was used.

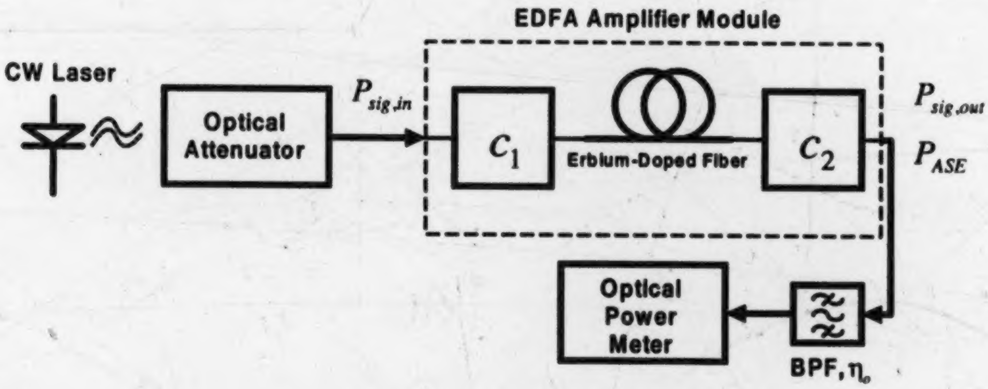

Figure 6.11 Setup for measuring external EDFA parameters.

In Figure 6.11, $P_{sig,in}$ is the input signal power, $P_{sig,out}$ is the output signal power, P_{ASE} is the ASE power output from the EDFA, and η_o is the insertion loss of the optical bandpass filter. Three equations can now be written for determining the EDFA's parameters:

$$P_{ASE} = 2n_{sp}h\upsilon(G_o - 1)B_o \tag{6.13}$$

$$P_{tot} = P_{sig,in}G_o\eta_o + P_{ASE}\eta_o \tag{6.14}$$

$$P_{tot} = P_{sig,in}G\eta_o + 2n_{sp}h\upsilon(G - 1)B_o\eta_o \tag{6.15}$$

where B_o is the bandwidth of the optical bandpass filter, G_o is the EDFA small-signal gain, G is the operating gain (may be compressed) and P_{tot} is the total power (signal + ASE) incident on the power meter. Small-signal operating conditions are assumed in (6.13) and (6.14), i.e., $G \approx G_o$. First, the optical power meter reading is recorded for $P_{sig,in}=0$. Correcting for η_o, the ASE power in (6.13) can then be determined. Next, $P_{sig,in}$ is set to a small value such that the total power incident on the power meter is, say, 3 dB higher than for $P_{sig,in}=0$. At this point, it is assumed that the input optical power is sufficiently small that $G \approx G_o$. Therefore, P_{ASE} determined from (6.13) can be subtracted from (6.14), which can then be solved for the small-signal gain. Then, G_o can be used with the initial reading for P_{ASE} in (6.13) to obtain the spontaneous emission factor, n_{sp}. With n_{sp} now known, the saturated gain of (6.15) can be solved for any input signal power. Of course, this assumes that n_{sp} does not change when the amplifier gain saturates. This assumption is reasonable for gain saturation up to about 3-5 dB [122]. For extremely saturated conditions, n_{sp} will be larger; however, because the total output power will be dominated by amplified signal, the error in the actual gain calculation using (6.15) will be small. Figure 6.12 shows gain curves obtained using the measurement method described here for a particular EDFA at two different wavelengths. Appendix C contains gain curves and calculated parameters at a variety of wavelengths for all EDFAs residing at TRLabs. P_{sat} is easily determined from a plot of the EDFA's gain.

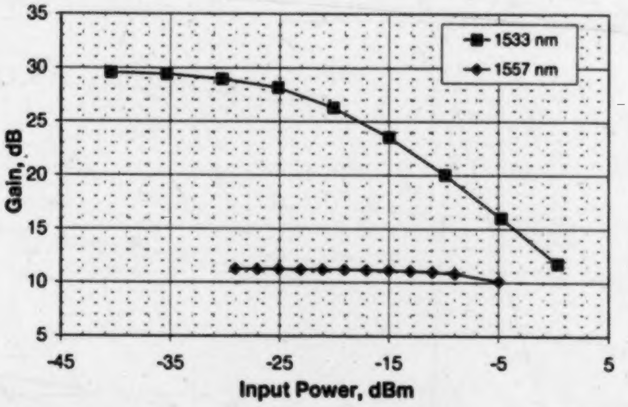

Figure 6.12 Measured gain curve for an EDFA operating at 1533 nm and 1557 nm.

From Figure 6.12 it can be seen that the gain for this EDFA is strongly dependent on the wavelength. As a general rule, the wavelength dependence of gain roughly follows the ASE emission spectrum for a particular EDFA. Figure 6.13 shows a monochrometer scan of the ASE spectrum from the EDFA of Figure 6.12. Presently, there is much effort being directed toward the design of EDFAs with a flat gain over a very wide bandwidth because of the significant interest in WDM lightwave systems where, ideally, each channel would experience the same gain through an EDFA.

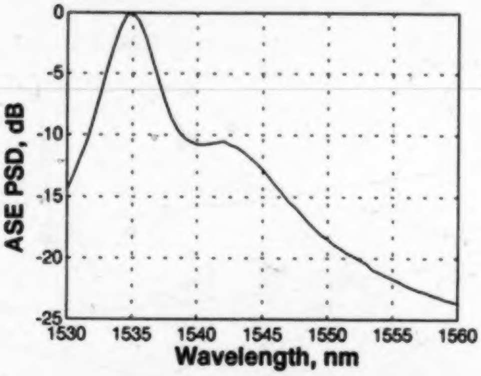

Figure 6.13 Monochrometer scan of ASE spectral density.

The method employed here for determining EDFA parameters is quite useful because of its simplicity. If it is desired to know n_{sp} for hard-saturated conditions, then a polarization splitter and controller can be used at the output of the EDFA, which would allow the ASE and amplified signal power to be calculated from power measurements.

6.7 Optical Bandpass Filters

Tunable Fabry-Perot optical bandpass filters were used in all experiments to limit the amount of ASE output from an EDFA. This is particularly important at the receiver because the amount of spontaneous-spontaneous beat noise depends on the bandwidth of the optical filter. In addition, in some cases it is necessary to filter the ASE output from an EDFA postamp and/or in-line amplifiers to prevent saturating the gain of following EDFAs in a cascade. Also, to obtain higher gain, two EDFAs can be directly cascaded and used as a single EDFA. Here, too, a BPF must be placed between EDFAs to prevent the first EDFA from saturating the second. When calculating noise, the noise-equivalent bandwidth of the filter following an optical preamplifier must be known. To measure this noise-equivalent bandwidth the setup in Figure 6.14 was used.

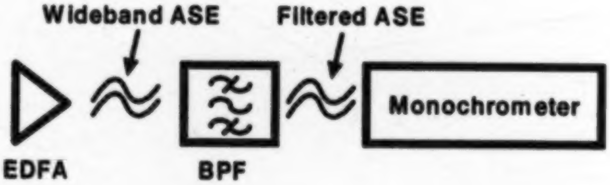

Figure 6.14 Setup for measuring optical filter bandwidth.

Here, the ASE output from an EDFA is used as a wideband source, which is then filtered by the bandpass filter prior to a monochrometer scan. If the ASE spectral density were truly white, then the profile of the monochrometer scan would give the transmission response of the filter. However, as is evident in Figure 6.13, the ASE spectral density is wavelength dependent. To correct for this, a monochrometer scan of the ASE alone, i.e., with no BPF, can be taken and then calibrated out of the filter response scan. Finally, the 3-dB optical bandwidth can be determined be simply reading off the wavelengths corresponding to the half-power points in a filter scan. For noise characterization, however, the noise-equivalent bandwidth is a more appropriate parameter, which can be determined by integrating the calibrated filter scan. To facilitate optical filter bandwidth calculations, LabVIEW was used to acquire data records of filtered and unfiltered ASE. These were then read into MATLAB and processed to obtain the bandwidths. Appendix C contains transmission response plots for a variety of BPFs, along with their calculated bandwidths. As an example, Figure 6.15 shows the transmission response of a typical Fabry-Perot optical filter with a 3-dB bandwidth of 1.34 nm and a noise-equivalent bandwidth of 1.56 nm.

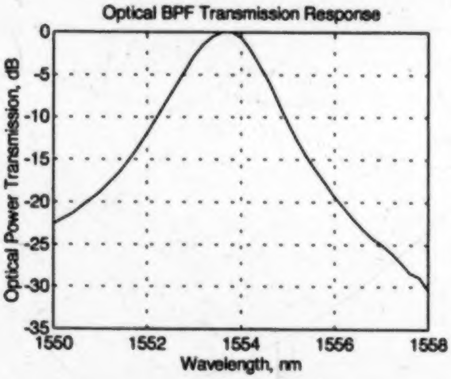

Figure 6.15 Transmission response for a Fabry-Perot optical bandpass filter.

6.8 Photodetector Responsivity

The responsivity of photodetectors can be determined by applying CW light to the photodetector, and then measuring the resulting photocurrent. Hence, the responsivity is given by

$$\Re = \frac{I_{ph}}{P_{opt}} \tag{6.16}$$

where I_{ph} is the measured photocurrent and P_{opt} is the incident optical power. Note that this is the dc responsivity. Appendix C contains responsivity measurements for two photodetectors.

6.9 Transimpedance Gain of Nortel PIN-Preamp Module

Much of the experimental work used a PIN-preamp module that was provided by Nortel Technologies. The module consists of a high-speed PIN photodiode and a transimpedance preamplifier. Therefore, to predict signal levels at the output of the module, the preamplifier transimpedance gain had to be known. To measure the transimpedance gain, the setup in Figure 6.16 can was used.

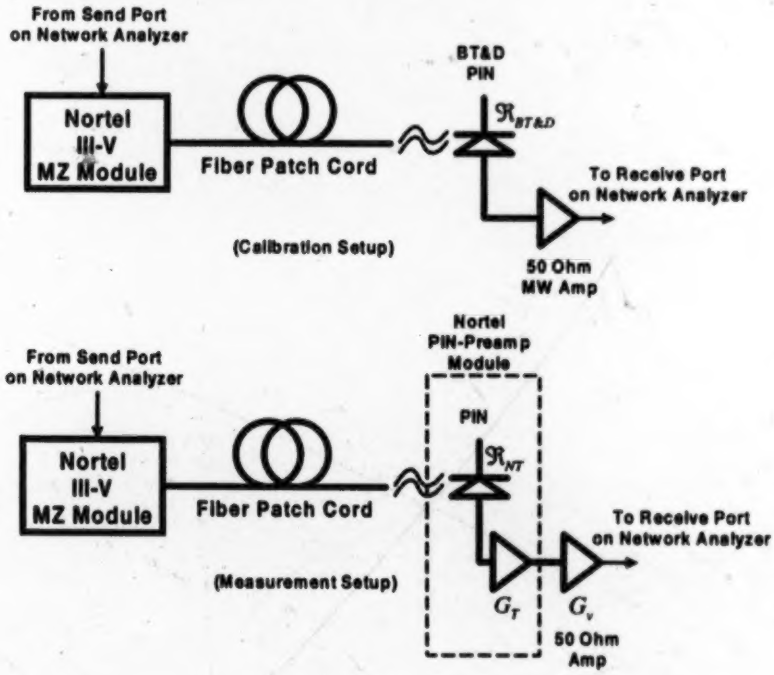
From Send Port on Network Analyzer
Nortel III-V MZ Module
Fiber Patch Cord
BT&D PIN
$\Re_{BT\&D}$
To Receive Port on Network Analyzer
(Calibration Setup)
50 Ohm MW Amp
From Send Port on Network Analyzer
Nortel III-V MZ Module
Fiber Patch Cord
Nortel PIN-Preamp Module
PIN
$\Re_{NT}$
To Receive Port on Network Analyzer
(Measurement Setup)
G_T
G_v
50 Ohm Amp

Figure 6.16 Setup used for measuring transimpedance gain of Nortel PIN-preamp module.

In Figure 6.16, the calibration setup is used to measure the magnitude response $S_{21,BT\&D}$ using the BT&D photodetector. Then, the measurement is repeated, but with the BT&D photodetector replaced by the Nortel PIN-preamp module to obtain $S_{21,NT}$. The difference in the response measurements is then

$$S_{21,diff} = S_{21,NT} - S_{21,BT\&D} = 20\log\left[\frac{\Delta P\Re_{NT}G_T G_v}{\Delta P\Re_{BT\&D}R_L G_v}\right] \tag{6.17}$$

$$= 20\log\left[\frac{\Re_{NT}G_T}{\Re_{BT\&D}R_L}\right]$$

Where ΔP is the amplitude variation of the received optical power, G_T is the transimpedance gain of the PIN-preamp module, R_L=50 Ω is the input impedance of the electrical amplifier, $\Re_{BT\&D}$ is the responsivity of the BT&D photodetector, and $\Re_{NT}$ is the responsivity of the photodetector in the Nortel module. Hence, the transimpedance gain is obtained from

$$G_T = \frac{\Re_{BT\&D}}{\Re_{NT}} R_L 10^{S_{21,diff}/20} \tag{6.18}$$

Using the measured values of $\Re_{BT\&D}$=0.58 and $\Re_{NT}$=0.69, the transimpedance gain was determined to be G_T=500 Ohms.

6.10 RF Amplifier Noise Figure

In some of the earlier experiments, a 50-Ohm gain block was used as an electrical preamplifier in the receiver. Therefore, to predict the receiver noise the amplifier's noise figure had to be known. As a general rule, the noise figure is frequency dependent. When an amplifier is used over a wide frequency range, however, an average noise figure can be specified that gives the same noise as integrating the noise spectral density over the bandwidth of the receiver. The histogram feature for measuring noise power described in section 6.1.3 can be used to determine the noise figure for an electrical amplifier. To do this, the input of the amplifier is first terminated in a matched load, usually 50 Ω. Then, the histogram feature on a digital oscilloscope can be used to measure the total noise power, which in this case is entirely receiver noise. The noise factor F can then be obtained from

$$\langle v^2 \rangle_{th} = kTFB_e R_L G_p \tag{6.19}$$

where $R_L=50\ \Omega$ is the input termination resistance, B_e is the bandwidth of all cascaded electrical components, and G_p is the net power gain of all electrical components. Note that, if the gain of the electrical amplifier is not large, additional amplifiers may need to be added to obtain sufficient gain for a noise power reading. Recall from section 4.1.1, though, that the net noise figure will still be approximately equal to that of the preamplifier. Note, too, that the factor of 4 is not included in (6.19) because of the voltage divider at the input to the amplifier under test, as described in section 4.1.1. Using this technique, the noise figures for a number of amplifiers were measured. In all cases, noise figures between 3 and 8 dB were obtained, consistent with the specifications from the manufacturers.

6.11 GaAs Logic Devices

A variety of GaAs logic devices were used in experiments including D-type flip flops (D-FFs), an AND gate, OR gate, XOR gate, 2:1 selector, 4:1 MUX, 1:4 DEMUX and a clock distributor. All devices can operate at up to 10 Gb/s—the 2:1 selector can operate as fast as 18 Gb/s. They were purchased from NEL (NTT Electronics Technology Corporation) as flat-pack integrated circuits. The ICs were mounted on printed circuit boards, and then put into sliver-plated aluminum enclosures. Greg May, a previous graduate student, did the design work for packaging the ICs, although the aluminum enclosures were slightly modified for most of the ICs used here. Figure 6.17 shows a packaged D-FF.

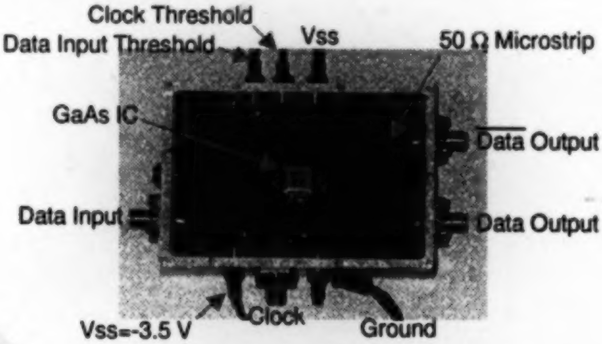

Figure 6.17 GaAS D-FF logic module.

Measured rise and fall times for these devices were typically 30 to 40 ps. Logic levels are nominally 0 V (logical ONE) and –1V (logical ZERO); however, outputs from these devices typically produce a logical ZERO voltage of –1.2 to –1.5 V. Figure 6.18 shows a typical output waveform from a GaAs logic device operating at 5 Gb/s.

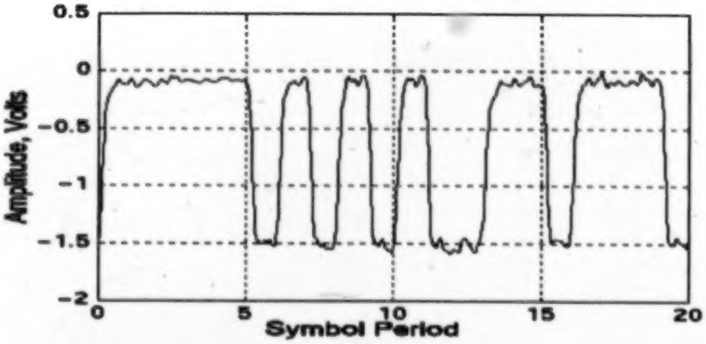

Figure 6.18 Output waveform of a GaAs logic device operating at 5 Gb/s.

To assess the sensitivity of the D-FFs, which were used as decision circuits, an OC-48 (2.5 Gb/s) signal was input to the device and the output was connected to the error detector on the BERT. Then, while simultaneously adjusting the data input threshold level, the amplitude of the input signal was decreased until error-free operation was no longer possible (BER>10^{-9}). It was found that the amplitude of the input signal could be as small as 25 mV$_{pp}$ for error-free operation, indicating excellent sensitivity for the device. The sensitivity of the BERT's error detector input was measured to be about 80 mV$_{pp}$.

Figure 6.19 shows the S_{11} parameter for a typical D-FF input.

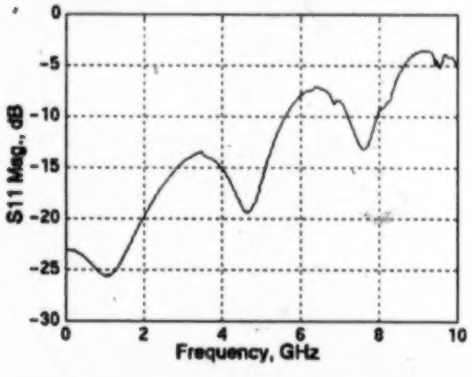

Figure 6.19 S_{11} magnitude response of D-FF input.

The input mismatch becomes quite poor for frequencies above 5 GHz. Note that the resonant lobes are spaced roughly 3 GHz apart, corresponding to a resonant cavity length of about 3 cm. This is the length of the microstrip line between the flangemount connector and the input pin on the IC package, i.e., the two points where an impedance mismatch is expected.

6.12 Summary

This chapter explained the methods used for characterizing important components used in a lightwave communication system. Knowledge of these components is required to predict the viability and performance of a particular system architecture. Furthermore, realistic simulations are possible when device parameters are well known. This allows for a more direct comparison of simulations and experimental results and, therefore, allows for a better evaluation of a system model.

7 System Simulation and Discussion

Simulation results are presented in this chapter, much of which are based on the static and dynamic noise models presented in Chapter 4. First, ideal simulations based on the static noise model are presented that give a first approximation of performance. Then, simulations based on the dynamic noise model are presented, where issues such as chromatic dispersion, frequency chirping and linear filtering are addressed. Finally, a discussion about realistic simulations using characterization data for real components is given. Realistic simulations were an essential precursor to the 4-ary ASK laboratory experiments.

At an earlier stage, BOSS (Block Oriented Systems Simulator) and SPW (Signal Processing WorkSystem) were used to simulate the response of various systems. Unfortunately, these simulators are quite slow and became increasingly cumbersome to use as more analyses were performed. Therefore, simulations were migrated over to MATLAB where, eventually, all simulations were performed. MATLAB provides a rich, high-level programming language for technical applications and is very efficient at processing and manipulating large arrays of data. Moreover, MATLAB contains an extensive set of function libraries (called toolboxes) for performing tasks in areas such as control systems and digital signal processing.

Unless stated otherwise, all references to receiver sensitivity in this chapter imply a target BER of 10^{-9}, and all simulations are for systems operating at an aggregate bit rate of 10 Gb/s.

7.1 Fiber Optic Communication System Simulator (FOCSS)

A significant component of this research was the development of a software simulation environment using MATLAB for the simulation of optical communication systems employing singlemode fiber and external modulators. This simulator was called Fiber Optic Communication System Simulator (FOCSS) and supports a fully-developed graphical user interface (GUI). Figure 7.1 shows the main menu structure of FOCSS and the variety of analyses that can be accessed from it. A User's Guide and Programmer's Note are being written for FOCSS and will be filed as TRLabs internal reports. The Programmer's Note contains a description of the logical structure of FOCSS and a complete code listing. FOCSS was used for all simulations, except those based on the static noise model for which the MATLAB program in Appendix B was used.

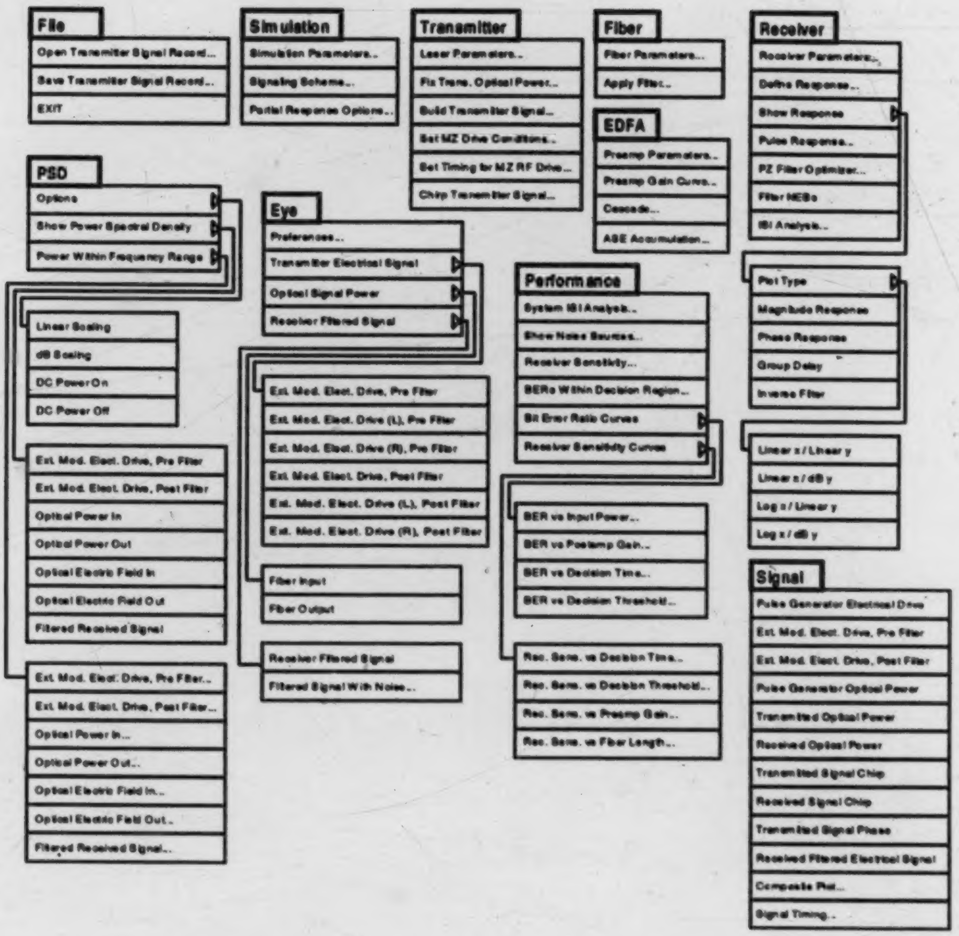
File
Open Transmitter Signal Record...
Save Transmitter Signal Record...
EXIT
Simulation
Simulation Parameters...
Signaling Scheme...
Partial Response Options...
Transmitter
Laser Parameters...
Fix Trans. Optical Power...
Build Transmitter Signal...
Set MZ Drive Conditions...
Set Timing for MZ RF Drive...
Chirp Transmitter Signal...
Fiber
Fiber Parameters...
Apply Filter...
EDFA
Preamp Parameters...
Preamp Gain Curve...
Cascade...
ASE Accumulation...
Receiver
Receiver Parameters...
Define Response...
Show Response
Pulse Response...
PZ Filter Optimizer...
Filter NEBs
ISI Analysis...
PSD
Options
Show Power Spectral Density
Power Within Frequency Range
Linear Scaling
dB Scaling
DC Power On
DC Power Off
Ext. Mod. Elect. Drive, Pre Filter
Ext. Mod. Elect. Drive, Post Filter
Optical Power In
Optical Power Out
Optical Electric Field In
Optical Electric Field Out
Filtered Received Signal
Ext. Mod. Elect. Drive, Pre Filter...
Ext. Mod. Elect. Drive, Post Filter...
Optical Power In...
Optical Power Out...
Optical Electric Field In...
Optical Electric Field Out...
Filtered Received Signal...
Eye
Preferences...
Transmitter Electrical Signal
Optical Signal Power
Receiver Filtered Signal
Ext. Mod. Elect. Drive, Pre Filter
Ext. Mod. Elect. Drive (L), Pre Filter
Ext. Mod. Elect. Drive (R), Pre Filter
Ext. Mod. Elect. Drive, Post Filter
Ext. Mod. Elect. Drive (L), Post Filter
Ext. Mod. Elect. Drive (R), Post Filter
Fiber Input
Fiber Output
Receiver Filtered Signal
Filtered Signal With Noise...
Performance
System ISI Analysis...
Show Noise Sources...
Receiver Sensitivity...
BERs Within Decision Region...
Bit Error Ratio Curves
Receiver Sensitivity Curves
BER vs Input Power...
BER vs Postamp Gain...
BER vs Decision Time...
BER vs Decision Threshold...
Rec. Sens. vs Decision Time...
Rec. Sens. vs Decision Threshold...
Rec. Sens. vs Preamp Gain...
Rec. Sens. vs Fiber Length...
Plot Type
Magnitude Response
Phase Response
Group Delay
Inverse Filter
Linear x / Linear y
Linear x / dB y
Log x / Linear y
Log x / dB y
Signal
Pulse Generator Electrical Drive
Ext. Mod. Elect. Drive, Pre Filter
Ext. Mod. Elect. Drive, Post Filter
Pulse Generator Optical Power
Transmitted Optical Power
Received Optical Power
Transmitted Signal Chirp
Received Signal Chirp
Transmitted Signal Phase
Received Filtered Electrical Signal
Composite Plot...
Signal Timing...

Figure 7.1 Menu structure of FOCSS.

7.2 Ideal Simulations Based on a Static Noise Model

Simulations presented in this section are based on the static noise model described in Chapter 4, where an ideal NRZ signal with zero ISI is assumed. Only binary and 4-ary ASK signals are considered here and, unless stated otherwise, the system parameters shown in Figure 7.2 were used. Note that the electrical receiver bandwidth was taken as 0.7 times the symbol rate.

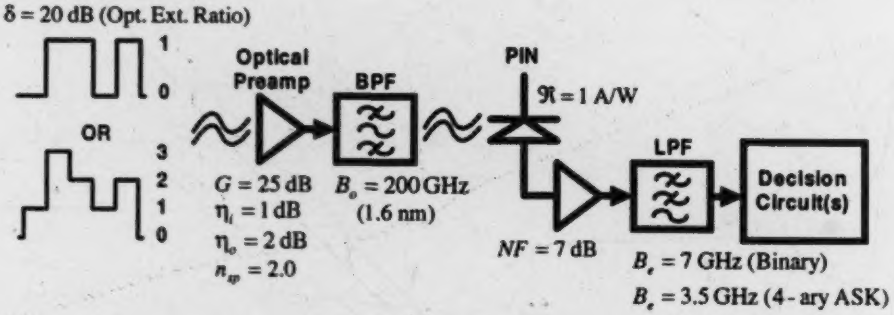

δ = 20 dB (Opt. Ext. Ratio)
1
0
OR
3
2
1
0
Optical Preamp
$G = 25$ dB
$\eta_i = 1$ dB
$\eta_o = 2$ dB
$n_{sp} = 2.0$
BPF
$B_o = 200$ GHz
(1.6 nm)
PIN
$\Re = 1$ A/W
$NF = 7$ dB
LPF
$B_e = 7$ GHz (Binary)
$B_e = 3.5$ GHz (4-ary ASK)
Decision Circuit(s)

Figure 7.2 Block diagram and system parameters used for simulations based on a static noise model.

7.2.1 *Effect of Optical Filter Bandwidth and Spontaneous Emission Factor*

Figure 7.3 shows the effect of optical filter bandwidth and spontaneous emission factor on the receiver's sensitivity. To facilitate the following discussion, let I_{th1}, I_{th2} and I_{th3} be the decision thresholds between levels **0** and **1**, **1** and **2**, and **2** and **3**, respectively, in a 4-ary ASK signal.

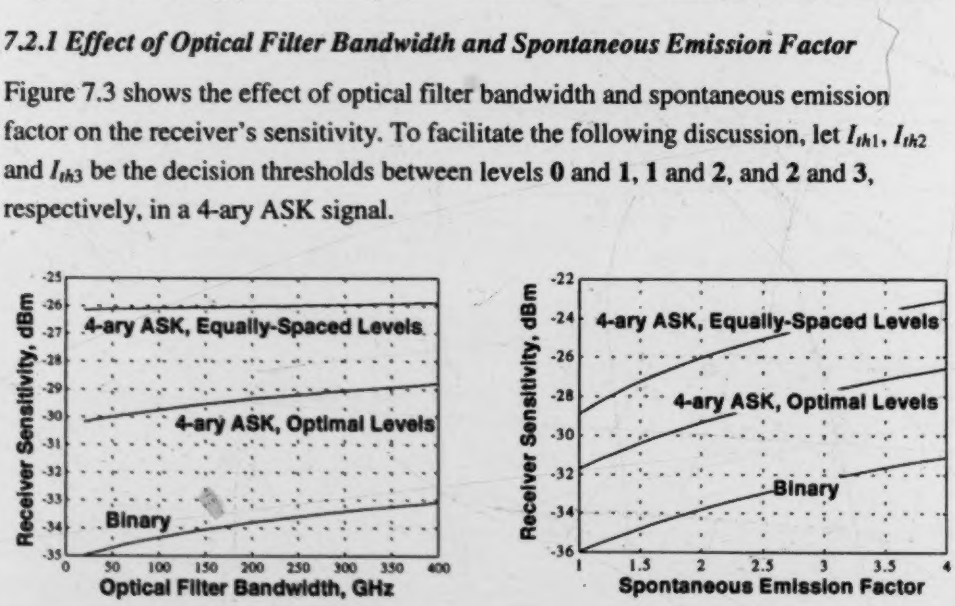

Figure 7.3 Receiver sensitivity versus optical filter bandwidth (left), and spontaneous emission factor (right) for binary and 4-ary ASK signals.

Note that the 4-ary ASK signal with equally-spaced levels shows a much weaker dependence on optical filter bandwidth than a binary signal or a 4-ary ASK signal with optimal levels. This is expected because, when the levels are equally-spaced, the BER is essentially determined by errors made with respect to I_{th3} because of the dominance of signal-spontaneous beat noise. Recall from (4.3) and (4.5) that signal-spontaneous beat noise does not depend on the optical filter bandwidth. When the levels are optimally spaced, however, errors made by all decision circuits contribute significantly to the BER. For this case, the noise in a **0**, where the optical power is very small, is dominated by spontaneous-spontaneous beat noise, which does depend on the optical filter bandwidth, and/or by thermal noise. Therefore, if the spontaneous-spontaneous beat noise is reduced, I_{th1} is lowered. This then allows the power in a **1** to be reduced, which then allows I_{th2} to be lowered, and so on. The same argument applies to the binary signal. Hence, a 4-ary ASK signal with optimal levels, or the binary signal, shows a stronger dependence on optical filter bandwidth, although the dependence is still moderate. For example, reducing the bandwidth from a typical value of 200 GHz (1.6 nm) to 20 GHz (information bandwidth), only offers an improvement of about 1 dB in a binary signal. In the absence of thermal noise, the improvement is increased to about 2 dB. The dependence of the receiver's sensitivity on the optical preamplifier's spontaneous emission factor in Figure 7.3 is significant for all signals because both signal-spontaneous beat noise and spontaneous-spontaneous beat noise depend on the spontaneous emission factor. Typical noise figures ($NF = 10\log(2n_{sp})$) for commercial EDFAs are 4 to 6 dB. Hence, the penalty for using an optical preamplifier with a non-ideal noise figure is, at most, about 2 dB. In the absence of thermal noise the penalty is, at most, about 3 dB.

7.2.2 Power Penalty for M-ary ASK

It was shown in Chapter 4 that the *optical* power penalty for using M-ary signaling over binary signaling is given by $(M-1)/\sqrt{\log_2(M)}$ when there is stationary noise only, suggesting a 3.3 dB power penalty for a 4-ary ASK signal. Unfortunately, the noise in an optically-preamplified communication system is signal dependent, which will increase the power penalty. From Figure 7.3 the power penalty is between 7 and 9 dB when the levels are equally spaced, and between 4 and 5 dB when the levels are optimally spaced. Hence, a 3 to 4 dB improvement in receiver sensitivity for a 4-ary ASK signal is offered by using optimally-spaced levels over equally-spaced levels. Although not shown in Figure 7.3, an 8-ary ASK signal with equally-spaced levels has a power penalty of about 13 to 15 dB, i.e., about 6 dB larger than the 4-ary ASK signal.

7.2.3 Effect of Optical Preamplifier Gain on Receiver Sensitivity

An optical preamplifier provides gain for the optical signal prior to photodetection, thus reducing the required received optical power for a given photocurrent. Figure 7.4 shows receiver sensitivity versus optical preamplifier gain.

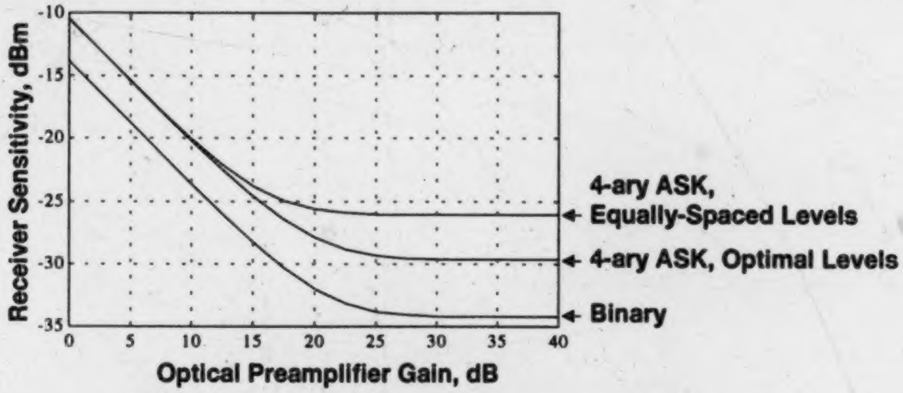

Figure 7.4 Receiver sensitivity versus optical preamplifier gain.

At low gains, receiver noise (stationary noise) dominates and the improvement in sensitivity is equal to the gain of the preamplifier. As the gain becomes large, signal-spontaneous beat noise dominates and the receiver sensitivity reaches a plateau because the signal power and noise power, then, both increase as G^2, i.e., the signal-to-noise ratio becomes fixed for a given received optical power. It is evident from Figure 7.4 that there is no advantage to using an optical preamplifier with a gain larger than about 25-30 dB for a binary signal or a 4-ary ASK signal with optimally-spaced levels. For a 4-ary ASK signal with equally-spaced levels, there is no significant improvement offered for gains larger than about 20-25 dB. Note, too, that photodiodes have a maximum rating for the incident optical power, typically 0 to +5 dBm; hence, using a preamplifier with a very high gain may not be practical. Also evident from Figure 7.4 is that, when the gain is large, the receiver's sensitivity will be rather insensitive to the insertion loss at the output of the optical preamplifier. For example, if the preamplifier gain is 30 dB, a 5 dB output insertion loss would have essentially the same effect as decreasing the gain to 25 dB, which would not significantly impact the receiver's sensitivity. The input insertion loss, however, should be kept to a minimum because it scales one-to-one with the receiver's sensitivity. Finally, note that the results in Figure 7.4 used a 7 dB noise figure for the electrical receiver. If this noise figure were larger, then the plateaus in Figure 7.4 would be reached at a larger optical preamplifier gain because of a larger receiver noise. For practical systems, however, a 7 dB noise figure is somewhat pessimistic, and would likely only occur in a system using a 50 Ω gain block as an electrical preamplifier. For systems employing a transimpedance preamplifier, the receiver noise would be lower, and the plateaus in Figure 7.4 would be reached at a lower optical preamplifier gain. Hence, the optical preamplifier gain requirements cited above are both practical and reasonable.

7.2.4 Power Penalty from a Non-Zero Laser Linewidth

It was shown in Chapter 4 that a finite source linewidth results in RIN from PM-to-AM conversion in a dispersive fiber, and results were presented that related a BER floor to the source linewidth. If the BER floor is not much lower than the target BER, a significant power penalty will result. For example, Figure 7.5 shows BER versus received power for a binary system in which RIN-induced BER floors are present.

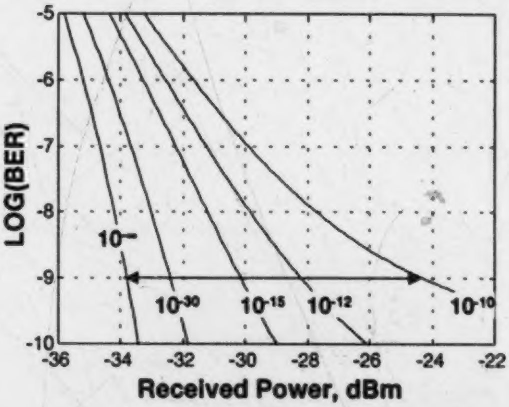

Figure 7.5 BER versus received power for a binary system in which various BER floors are present.

Assuming a target BER of 10^{-9}, the power penalty is about 1.5 dB if there is a RIN-induced BER floor at 10^{-30}, and increases to almost 10 dB, as shown by the double-headed arrow in Figure 7.5, if the BER floor is at 10^{-10}. Recall from section 4.4.3 that the PM-to-AM RIN-induced BER floor depends on the source linewidth and, therefore, the power penalty will depend on the linewidth. Figure 7.6 shows power penalty versus linewidth for a binary signal, a 4-ary ASK signal with optimal levels, and a 4-ary ASK signal with equally-spaced levels. Note that each curve approaches a vertical asymptote at a linewidth that produces a BER floor at 10^{-9}.

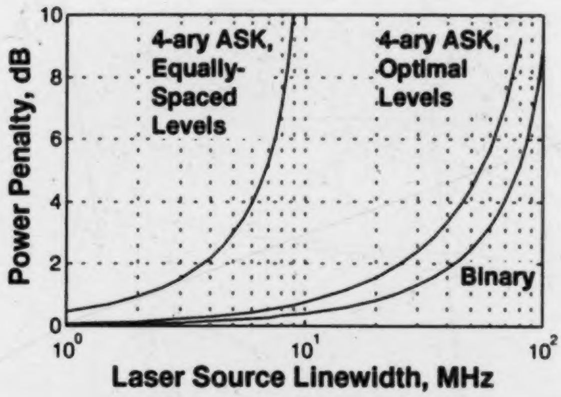

Figure 7.6 Power penalty versus source linewidth for binary and 4-ary ASK signals.

The PM-to-AM RIN used in Figure 7.6 assumes a fiber length of 200 km and a dispersion coefficient of 17 ps/(km·nm). Note that Figure 7.6 represents a best-case scenario because the signal is assumed to be ideal, with no ISI. For an ideal 4-ary ASK signal, it can be seen that the impact of laser linewidth is significantly reduced if the level spacing is optimized. However, even a small amount of distortion would preclude the use of the optimal level weights used in Figure 7.6, as explained in section 7.3.5.

7.2.5 Quantum-Limited Receiver Sensitivity

To evaluate the performance of a communication system it is useful to compare the receiver's sensitivity to that achieved under ideal conditions. For example, consider the direct detection of a binary intensity-modulated signal. If there are no external noise sources present, there is still a minimum received power required because of the quantum nature of light. Assuming a coherent light source, the number of photons that arrive in a given time interval is a Poisson-distributed random variable [123]. Therefore, if the expected number of photons during a logical **1** is $\tilde{n}$, the probability of receiving n photons is

$$p(n) = \frac{\tilde{n}^n e^{-\tilde{n}}}{n!} \tag{7.1}$$

Assuming that no photons are sent during a **0**, and that the receiver can detect a single photon, then an error will occur only when no photons are received during a **1**. Hence, the required average number of photons in a **1** to obtain a target BER is obtained from

$$BER = \frac{1}{2}p(n=0) = \frac{1}{2}e^{-\bar{n}} \tag{7.2}$$

For example, for $BER = 10^{-9}$ the average number of photons in a 1 must be 20. Therefore, the average number of photons per bit is 10. This is the well known quantum limit for a binary signal and corresponds to a received average power of

$$P_{rec} = \frac{10hcB}{\lambda} \tag{7.3}$$

where h is Planck's constant, c is the free-space speed of light, λ is the free-space optical wavelength, and B is the bit rate. For example, a 10 Gb/s binary signal operating at 1550 nm has a quantum-limited sensitivity of –48.9 dBm.

It is also possible to obtain the quantum-limited sensitivity for an optically-preamplified system using an ideal amplifier for which $n_{sp} = 1$. Henry has shown [124] that the quantum limit is 38 photons per bit when the optical filter bandwidth is equal to the bit rate. If the statistics are assumed Gaussian, then the predicted quantum limit becomes 42 photons per bit [125]. Hence, the quantum-limited sensitivity is about 6 dB worse than with no optical preamplifier. The quantum limit can also be estimated using the program in Appendix B by making all parameters ideal: infinite optical extinction ratio; optical bandwidth equal to the bit rate; receiver bandwidth equal to ½ the bit rate; no RIN or receiver noise; spontaneous emission factor equal to unity; one polarization mode; arbitrarily large optical preamplifier gain. Doing this for a binary signal gives 42 photons per bit, which agrees with the results in [125]. Similarly, this can be done for an M-ary ASK signal by setting the optical bandwidth to the symbol rate (not the bit rate) and the receiver bandwidth to one-half the symbol rate. Assuming equally-spaced levels, the calculated quantum-limited sensitivity is 1030 photons per symbol, or 515 photons per bit, for a 4-ary ASK signal. If the levels spacing is optimized, the quantum limit becomes 282 photons per symbol, or 141 photons per bit. The calculation can also be done for an 8-ary ASK signal with equally-paced levels, which gives a quantum limit of 6063 photons per symbol, or 2021 photons per bit.

7.3 Ideal Simulations Based on a Dynamic Noise Model

Simulations presented in this section are based on the dynamic noise model described in Chapter 4. The system response was determined using the model in Figure 3.3, except that here a more elaborate transmitter is used. A functional block diagram of the system simulated in FOCSS is shown in Figure 7.7.

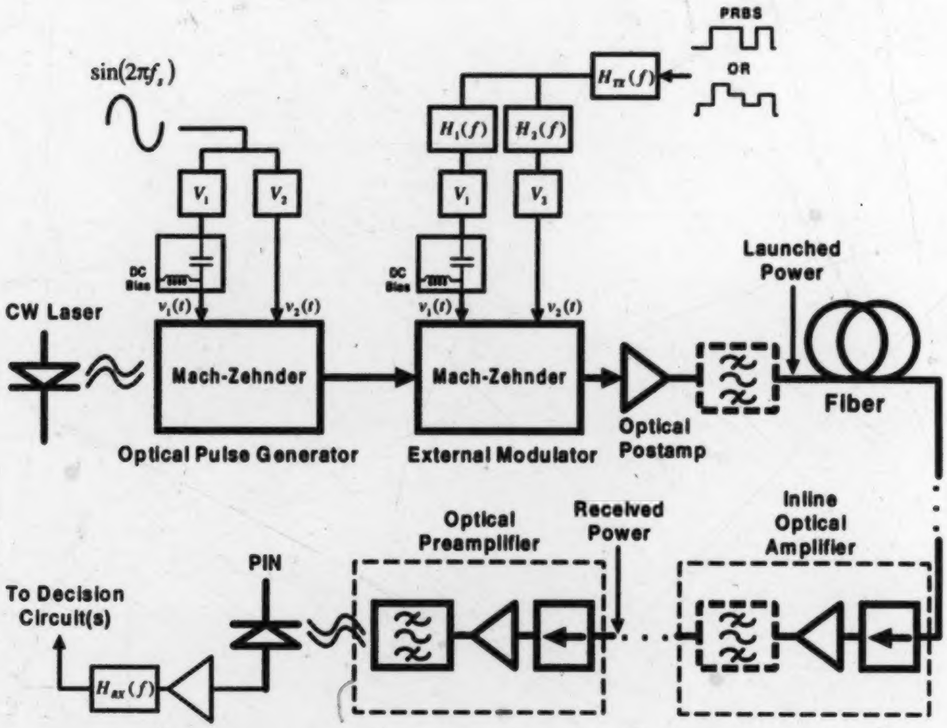
PRBS
OR
$\sin(2\pi f_s)$
$H_{TX}(f)$
$H_1(f)$
$H_2(f)$
V_1
V_2
V_1
V_2
DC Bias
DC Bias
$v_1(t)$
$v_2(t)$
$v_1(t)$
$v_2(t)$
CW Laser
Mach-Zehnder
Mach-Zehnder
Launched Power
Fiber
Optical Postamp
Optical Pulse Generator
External Modulator
Inline Optical Amplifier
Received Power
Optical Preamplifier
PIN
To Decision Circuit(s)
$H_{RX}(f)$

Figure 7.7 Block diagram of optical communication system simulated in FOCSS.

The generalized transmitter consists of two MZs in cascade. The first MZ acts as an optical pulse generator that can produce realizable RZ pulse shapes by applying a sinusoidal voltage to each arm of the modulator. The sinusoidal voltage is split into two arms, and then multiplied by the weights V_1 and V_2 to produce the correct amplitude and polarity for a specified amount of chirp, as discussed in Chapter 5. Also, an appropriate DC bias is added to one arm of the MZ. The signal output from the pulse generator is then input to the second MZ, which functions as the external modulator. A binary or M-ary NRZ signal is filtered by $H_{TX}(f)$, which could represent the response of amplifiers or a lowpass filter. $H_{TX}(f)$ could also represent the response of a partial response filter, such as a delay-and-add circuit, to generate a polybinary or polyquaternary signal. The filtered signal is then split into two arms where each signal can be filtered further—for example, the filter in one arm might represent the response of a pulse inverter, or an inverting amplifier. Then, each signal is multiplied by an appropriate constant to achieve a specified amount of chirp. Finally, an appropriate DC bias is added to one arm of the modulator. The detailed model for the MZs, which accounts for the optical extinction ratio and frequency chirping, was explained in Chapter 5. Note that, unless stated otherwise, $LiNbO_3$ MZ devices are assumed.

An optical preamplifier is assumed present in all simulations. An optical postamp is also assumed, but only insomuch as it would normally be present to boost the signal power launched into the fiber to provide a higher system gain[5]. For any practical configuration, however, it should be noted that the ASE from the postamp—as observed at the photodetector—would usually be insignificant compared to that generated by the optical preamplifier. Hence, only the noise performance of the optical preamplifier need be considered in the absence of inline amplifiers. If inline optical amplifiers are present, however, the accumulation of ASE can become significant, as explained in section 7.4.4. Bandpass filters are assumed at the output of each optical amplifier to limit the amount of ASE, which might otherwise result in unwanted gain compression of amplifiers. Isolators are assumed at the input of each optical amplifier to reduce the accumulation of backscattered noise (from signal or ASE), and may also be placed at the output of EDFAs to provide further isolation. In the following simulations, optical bandpass filters and isolators are simply modeled by an appropriate insertion loss, and are assumed to not affect the shape of the signal.

The simulations presented here assume ideal, but realizable, lowpass filters to bandlimit the signal at the transmitter and receiver. Recall from Chapter 3 that there are methods for designing a realizable overall response that minimizes ISI in linear systems. For the system considered here, however, the nonlinear nature of the MZ transfer characteristic and fiber dispersion make it difficult to offer precise statements about optimal filters. Regardless, there are some guidelines that can be followed. For example, if the bandwidth of the receiver filter is too small, the signal will be distorted with an increase in ISI from the excessive bandlimiting. If the bandwidth is too high, more noise will be passed, which will increase the probability of error. Moreover, the nonlinear distortion residing at higher frequencies will not be filtered out, as discussed in section 7.3.4. In [103], the influence of various receiver filter structures on the system type considered here was investigated extensively. The conclusion reached in that work is consistent with what practitioners have known for some time: Good results are obtained using a lower-order filter having a cutoff at about sixty to seventy percent of the symbol rate.

---

[5] System gain is the difference between the launched optical power and the required power at the receiver; hence, a larger system gain allows for a higher link loss and, therefore, a longer distance to be spanned without repeaters (regenerative or nonregenerative).

In conducting simulations, and assuming an appropriate receiver filter, it was found that bandlimiting the signal applied to the modulator offered little improvement. Two exceptions are the AM-PSK and three-level intensity duobinary signals, as discussed in section 7.3.4, in which bandlimiting at the transmitter becomes important. From a practical standpoint, bandlimiting the electrical signal at the transmitter is unavoidable in a Gb/s system because of device limitations. Higher bandwidth components are much more expensive and, therefore, would not likely be used unless absolutely necessary. To reflect practical constraints, simulations presented here assume the electrical signal at the transmitter is bandlimited to between 65 % and 100 % of the symbol rate. For example, a fifth-order Butterworth response with a cutoff equal to the symbol rate was used in most results, whereas some results used a third-order Butterworth with a cutoff at 65 % of the symbol rate. All simulations are for an aggregate bit rate of 10 Gb/s and, unless stated otherwise, assumed the following parameters: optical preamplifier with internal 25 dB gain and $n_{sp}=2$, and a 1.5 dB input and output insertion loss; electrical preamplifier noise figure equal to 3 dB; PIN photodiode with a responsivity equal to 0.75 A/W; third-order Butterworth response at the receiver with a cutoff at 0.65 the symbol rate; optical filter bandwidth equal to 180 GHz (1.5 nm); laser RIN=-155 dB/Hz; 1550 nm carrier with zero (ideal) linewidth; fiber dispersion coefficient of $D=17$ ps/(km·nm).

7.3.1 Dispersion Immunity of Signaling Schemes

In this section the dispersion immunity is evaluated for the various signaling schemes. These simulations assume zero chirp and an infinite intrinsic[6] extinction ratio for the external modulator. The effect of frequency chirp and a finite intrinsic extinction ratio is treated in sections 7.3.2 and 7.3.3.

7.3.1.1 Binary

These binary simulations are intended to serve as a reference in which to compare all other results. Figure 7.8 shows receiver sensitivity versus distance for RZ and NRZ signaling formats.

---

[6] By intrinsic, it is meant the extinction ratio that is intrinsic to the device, which results from asymmetry in Y-branches or an unequal loss through the MZ arms, not that which results from the shape or amplitude of the applied electrical signal.

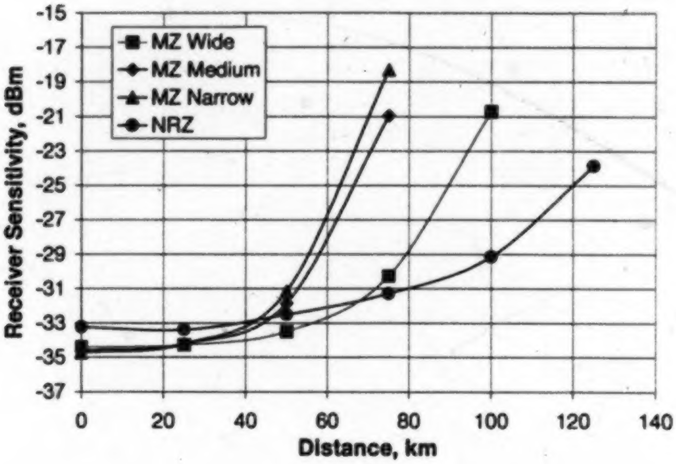

Figure 7.8 Receiver sensitivity versus distance for RZ and NRZ binary signals.

There are three RZ pulse shapes considered: MZ Wide, MZ Medium and MZ Narrow. These represent realizable RZ pulse shapes that are obtained by applying a sinusoidal electrical signal to a $LiNbO_3$ MZ. A MZ Medium pulse shape is obtained by biasing the MZ at the half power point of its transfer characteristic and applying a sinusoid having an amplitude equal to $V_\pi/2$ and a frequency equal to the symbol rate. The MZ Narrow and MZ Wide pulse shapes are obtained by applying a sinusoid having an amplitude equal to V_π and a frequency equal to one-half the symbol rate, biased at minimum and maximum extinction, respectively. Figure 7.9 shows the various RZ pulse shapes input to the fiber, as well as a sample trace of a filtered NRZ signal.

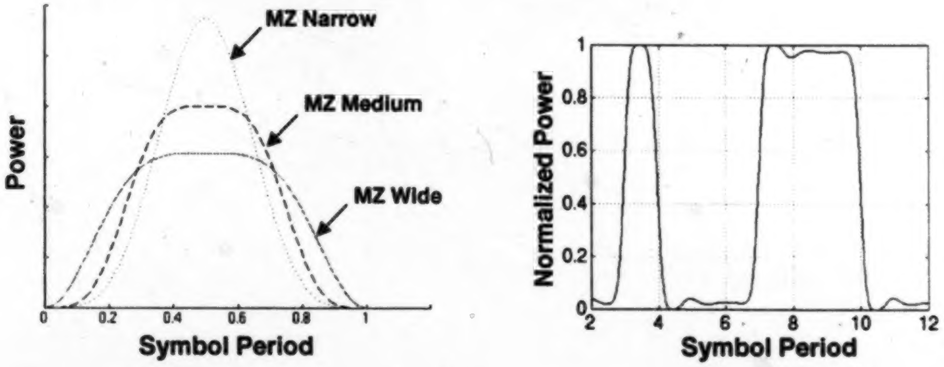

Figure 7.9 Optical signals input to fiber: (left) RZ pulse shapes; (right) Filtered NRZ optical signal.

Note that, for the RZ pulse shapes, there is no filtering of the RF signal applied to the external modulator, i.e., it is an ideal NRZ PRBS that simply acts to gate the pulses.

For the transmitted NRZ signal, the voltage applied to the pulse generator is constant so that CW light is input to the external modulator. Then, an ideal NRZ PRBS is filtered by a 10 GHz, fifth-order Butterworth response prior to being applied to the external modulator.

From Figure 7.8 it can be seen that the baseline sensitivity (that at zero distance) is better for the RZ signals than for the NRZ signal. As the distance increases, however, the power penalty[7] increases more rapidly for the RZ pulses for which a 1 dB power penalty is observed at about 35, 40 and 50 km for the MZ Narrow, Medium and Wide pulses, respectively. For the NRZ signal, a 1 dB penalty occurs at about 60 km, and the increase in penalty is much more gradual for distances beyond this. The improvement in dispersion immunity of NRZ pulses over RZ pulses was also observed for M-ary ASK signals. There is an increase in higher frequency content as the pulse width is reduced for the RZ pulses; therefore, it is reasonable to expect the narrower pulses to be more dispersive—the RZ simulations simply confirm this idea. Because of the improved dispersion immunity, and a simpler implementation, only NRZ signals will be considered from this point forward. Figure 7.9 shows eye diagrams of the NRZ filtered received signal at various distances.

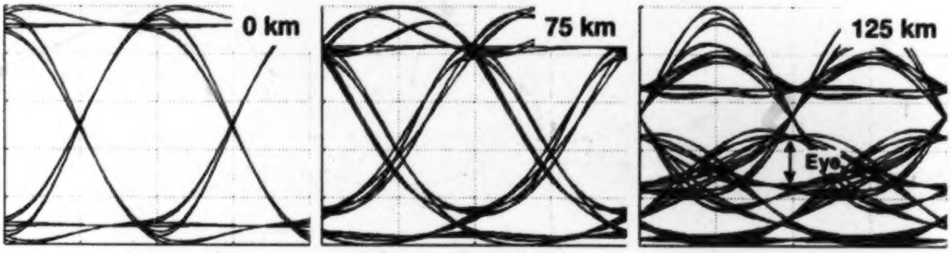

Figure 7.10 Eye diagrams of received filtered NRZ binary signal at 0, 75 and 125 km.

7.3.1.2 Duobinary

Duobinary is a special case of the more generalized polybinary signals described in Chapter 2. A duobinary signal is obtained by passing a binary signal through the polybinary filter in Figure 2.3, but with only one delay element in the filter. Hence, duobinary signals contain correlation between two adjacent bits. Recall that it is possible to decode the binary information from independent decisions on the three-level duobinary signal, provided the binary signal is first precoded, as described in Chapter 2. Figure 7.11 shows two methods for implementing a duobinary filter.

---

[7] In the context used here, power penalty is the difference in receiver sensitivity between that at a given distance and that at zero distance.

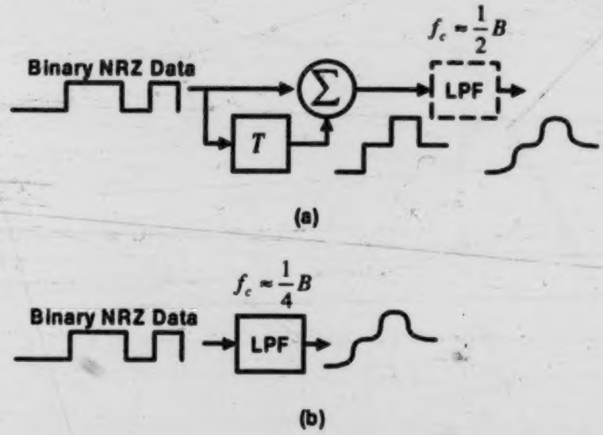

Figure 7.11 Two methods for implementing a duobinary filter: (a) delay-and-add filter followed by an optional band-limiting filter; (b) lowpass filter will a cutoff at about ¼ the bit rate.

The input signal is assumed to be an ideal (zero rise and fall times) NRZ binary signal. A delay-and-add circuit will produce the ideal duobinary signal shown in Figure 7.11(a). At this point, it is permissible to bandlimit the ideal duobinary signal to about ½ the bit rate, although not mandatory. Alternatively, the ideal NRZ signal can be passed through a LPF with a cutoff at around ¼ the bit rate, as shown in Figure 7.11(b). The LPF approximates a duobinary filter by providing the rolloff of the delay-and-add circuit at lower frequencies, while concurrently bandlimiting the signal at higher frequencies. Both of the filter structures in Figure 7.11 are considered.

Determining the best location for a duobinary filter in a system that is linear from electrical input to electrical output is more obvious than the system considered here. For example, recall from Chapter 3 that multimode fiber acts as a LPF on the optical power, with a cutoff frequency inversely proportional to fiber length. The filtering effect imposed by the fiber could be used as part of the duobinary filter, providing a longer transmission distance. If the fiber channel is not a band-limiting component, it still may be desirable to use a duobinary filter placed at the receiver. This could be the case, for example, when the receiver noise PSD increases with frequency. In this case, the tradeoff between the number of levels at the decision circuit and the reduction in noise from a narrower receiver bandwidth can improve the error probability [126]. In terms of system response only, the location of the duobinary filter is not important in a linear system due to the commutative law for cascaded transfer functions. For the system considered here, however, the commutative law does not hold, thus raising the question: Is there an advantage to placing the duobinary filter at the transmitter rather than the receiver, or vice versa? Figure 7.12 shows receiver sensitivity versus distance for systems in which a duobinary filter is placed at either the transmitter or receiver. When placed at the transmitter, three optical intensity levels are transmitted. When placed at the receiver, two intensity levels are transmitted, but then converted to a three-level electrical signal at the receiver by the duobinary filter.

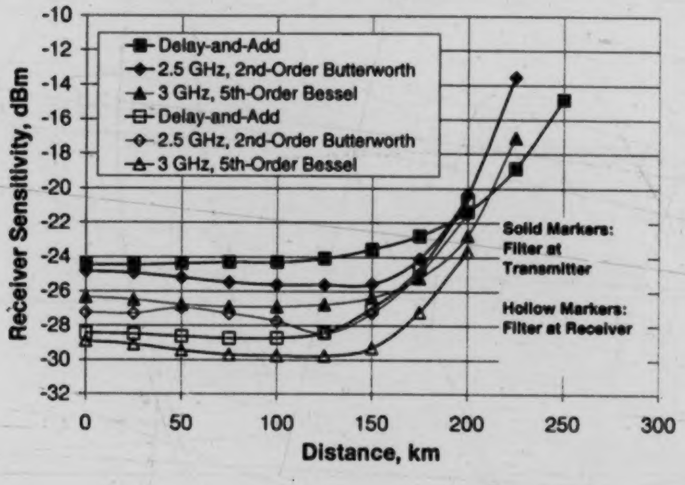

Figure 7.12 Receiver sensitivity versus distance for systems employing a duobinary filter at the transmitter or receiver.

In Figure 7.12 the delay-and-add filter is assumed ideal and is followed by a 5 GHz, twelfth-order Butterworth response to bandlimit the duobinary signal. As mentioned, this bandlimiting is not mandatory insofar as generating a duobinary signal; however, as shown later in this section, and discussed further in section 7.3.4, a band-limiting filter is required to obtain any benefit from duobinary signaling when transmitting over dispersive fiber. Results using a LPF approximation to a duobinary filter are also shown in Figure 7.12 where a 2.5 GHz, second-order Butterworth response and a 3 GHz, fifth-order Bessel response are used. The Bessel filter produces a duobinary signal with less ISI than the Butterworth filter, with a corresponding baseline sensitivity improvement of about 2 dB. It can be seen that a 1 dB dispersion penalty is reached at about 150 km when using a band-limited delay-and-add filter at either the transmitter or receiver. For duobinary filters consisting of a single LPF, this distance is extended to about 170 km. In terms of dispersion immunity, there is no significant difference with respect to the location of the duobinary filter, i.e., transmitter or receiver. Placing the duobinary filter at the receiver, however, does provide a better baseline receiver sensitivity because of a reduced receiver NEB, resulting from the continuous rolloff of the filter. Figure 7.13 shows eye diagrams of the received duobinary signal at various distances for a system using a 3 GHz, fifth-order Bessel filter at the receiver.

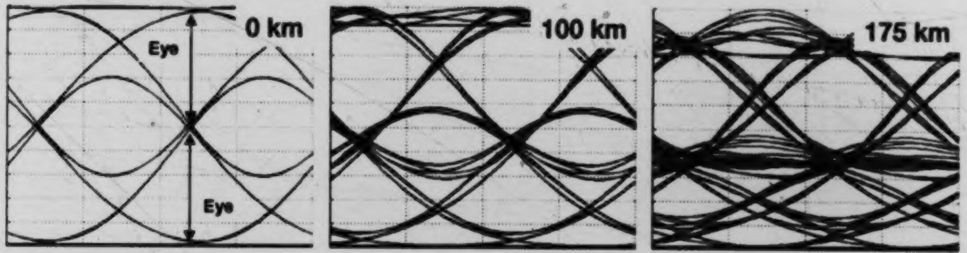

Figure 7.13 Eye diagrams of received filtered duobinary signal at 0, 100 and 175 km.

It should be noted that closure of the bottom eye has less impact than closure of the top eye because of the signal dependence of noise. Of course, if the bottom eye is degraded significantly in comparison to the top eye, a point is eventually reached where errors within it will begin to dominate.

Further insight into the nature of duobinary signaling can be gained by observing the evolution of a binary eye diagram as the bandwidth of the receiver filter is changed, or as the fiber length is increased. Consider Figure 7.14, which shows an eye diagram for the received optical power in a back-to-back system, and corresponding eye diagrams of the filtered electrical signal at the receiver for various receiver bandwidths. The optical power is the result of an ideal NRZ signal, filtered by a 10 GHz, fifth-order Butterworth response, being applied to the external modulator. A fifth-order Bessel filter is used at the receiver with the indicated 3 dB cutoff frequency. It can be seen that the 10 GHz filter passes the optical binary signal without significantly altering its shape, as expected. As the receiver bandwidth is reduced, the shape of the filtered signal is changed to a greater extent. Note that the optical eye has three clear openings: the usual binary eye, and apparent duobinary eyes. Assuming, the binary signal was appropriately precoded, the information can be obtained from the apparent duobinary eyes by applying the duobinary decoding rule discussed in Chapter 2. Next, observe how the binary eye closes as the receiver bandwidth is reduced, and how the duobinary eyes widen. The receiver bandwidth of 3 GHz corresponds to a LPF approximation of a duobinary filter. Further bandlimiting results in closure of the duobinary eyes, as shown by the 2 GHz receiver filter in Figure 7.14. It is interesting to note that the duobinary signal is actually inherent in a binary signal, before any receiver filtering.

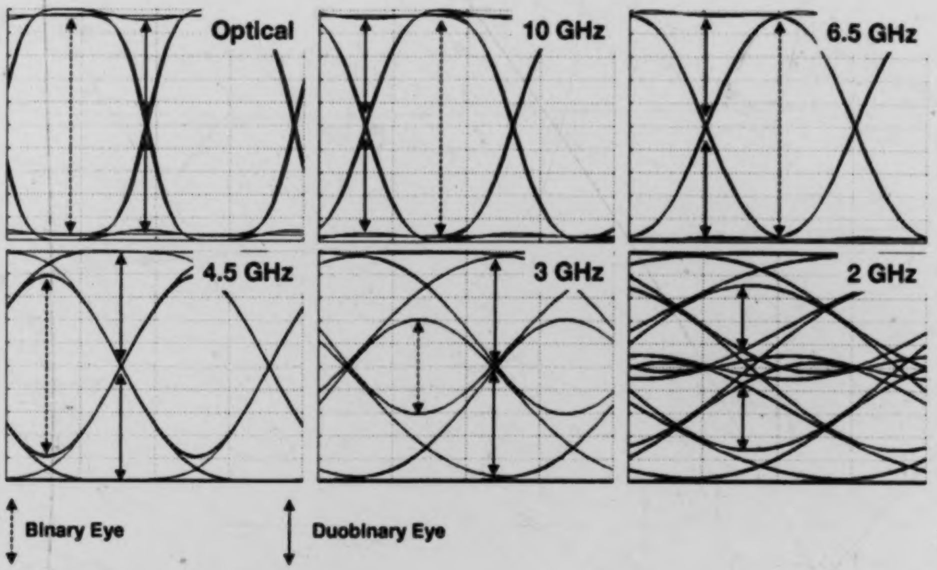

Figure 7.14 Eye diagrams for an optical back-to-back system: (top left) optical power incident on photodetector; all other eye diagrams are for the received electrical signal filtered by a fifth-order Bessel filter with the indicated 3 dB cutoff.

Rather than viewing a duobinary filter as a delay-and-add operation that *creates* a three-level signal from a two-level signal, it can also be viewed as a filter that passes the duobinary signal inherent in a binary signal with non-zero rise and fall times.

It was mentioned that the lower bandwidth requirement of a duobinary signal can be used to increase the span of a multimode system by allowing the fiber to be a part of the duobinary filter. It turns out that this is also partially true for the singlemode system considered here, as illustrated in Figure 7.15. The received optical eye is shown in the top of Figure 7.15 in which the binary and duobinary eyes are identified. Directly below each optical eye is the corresponding eye diagram of the electrical signal at the receiver, filtered by a 3 GHz, fifth-order Bessel filter (duobinary filter). As the distance is increased to 50, and then 100 km, it appears that the fiber has a pseudo-lowpass filter effect on the optical intensity, at least in terms of closing the binary eye and widening the duobinary eyes. Also clearly present, however, is higher-frequency nonlinear distortion, which is so severe at 175 km that the optical eyes are completely closed. After passing the signal through a band-limiting filter (duobinary filter), however, the duobinary signal is recovered, i.e., the eyes are once again clearly visible. Hence, the duobinary filter acts to remove the higher-frequency nonlinear distortion and expose the duobinary signal.

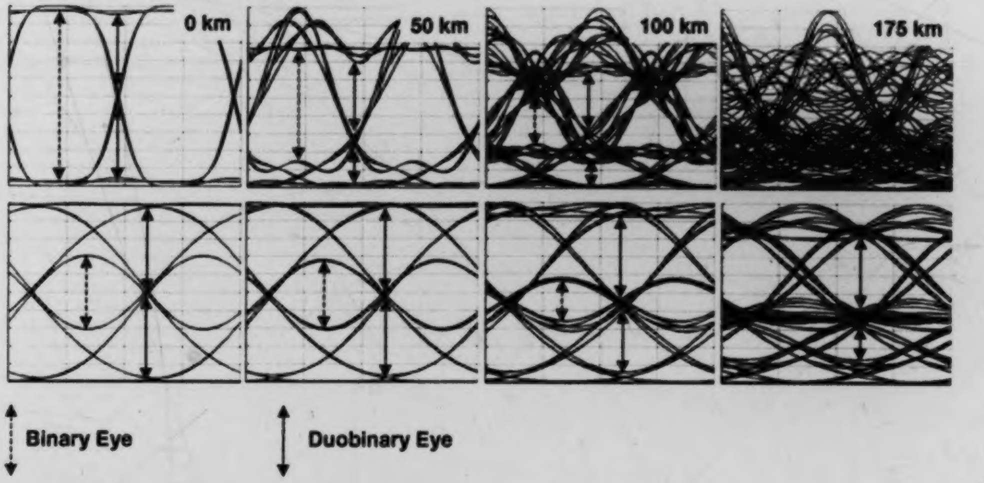

Figure 7.15 Eye diagrams versus distance: (top) received optical power; (bottom) filtered electrical signal after being passed through a duobinary filter.

In the above discussion, an explanation was provided for why a duobinary filter placed at the receiver provides an improvement in the dispersion-limited transmission distance. However, this does not clearly explain why a duobinary filter placed at the transmitter provides an improvement. That discussion will be left until section 7.3.4.

7.3.1.3 Polybinary

Polybinary signals with more than three levels were also considered. Recall that these are generated by adding additional delay elements to the polybinary filter in Figure 2.3. As with duobinary signals, it was found that the dispersion immunity was about the same when the polybinary filter was placed at either the transmitter or receiver. Because the baseline sensitivity is better with the polybinary filter placed at the receiver, i.e., the reciever will have a lower NEB, results will only be presented for that case. Figure 7.16 shows receiver sensitivity for 5-level and 7-level polybinary signals corresponding to a polybinary filter with 3 and 5 delay elements, respectively. The polybinary filter used to generate the results in Figure 7.16 consists of an ideal delay-and-add circuit followed by a twelfth-order, 5 GHz Butterworth filter to bandlimit the signal. It can be seen that a 1 dB penalty is observed at about 80 and 90 km, respectively, for the 7-level and 5-level polybinary signals. Moreover, there is a baseline penalty of about 4.5 dB and 6.5 dB, respectively, for the 5-level and 7-level polybinary signals in comparison to a duobinary receiver that uses a fifth-order, 3 GHz Bessel filter. Clearly, there is no advantage to using polybinary signals with more than three levels.

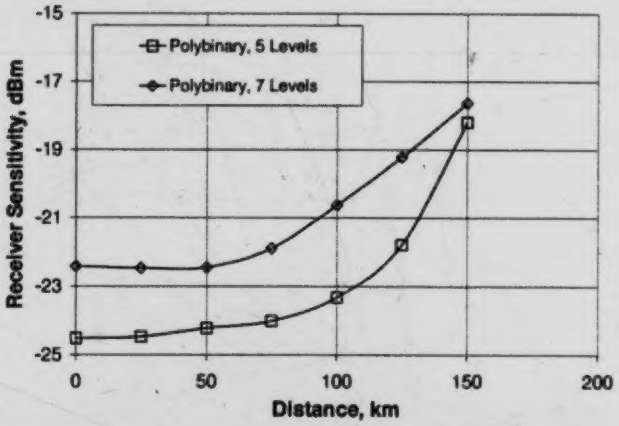

Figure 7.16 Receiver sensitivity versus distance for 5-level and 7-level polybinary signals.

Figure 7.17 shows eye diagrams of the filtered 5-level and 7-level polybinary signals at various distances.

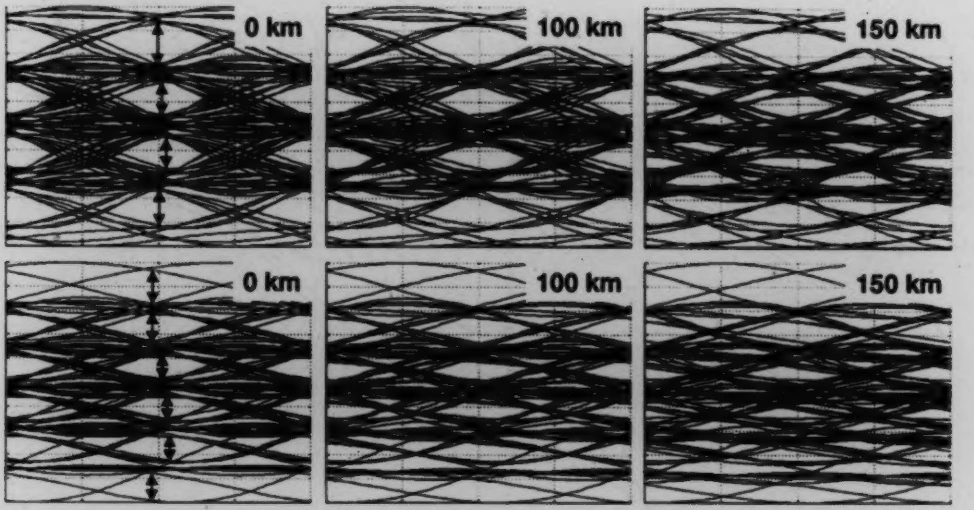

Figure 7.17 Eye diagrams of 5-level (top) and 7-level (bottom) polybinary signals.

It was stated in Chapter 2 that the reason for considering higher-order polybinary signals is that they concentrate more power at lower frequencies and, therefore, may be more dispersion tolerant. Unfortunately, polybinary signals still require the same transmission bandwidth as a binary signal. This is best understood by observing that the symbol width remains equal to the bit period, regardless of the number of levels in a polybinary signal. Changing the amplitude of a pulse does not change the response requirement of a channel to produce zero or little ISI. Hence, polybinary signals, too, must satisfy Nyquist's Criterion[8] for zero ISI. This statement holds true for all polybinary signals, including duobinary. This may seem to contradict a statement often made in the literature: A duobinary signal requires one-half the transmission bandwidth of a binary signal. It should be noted, though, that this statement is of practical origin, not theoretical origin, as it is often interpreted. To demonstrate this, consider Figure 7.18, which shows a binary information sequence, consisting of impulses, input to one of two possible channels.

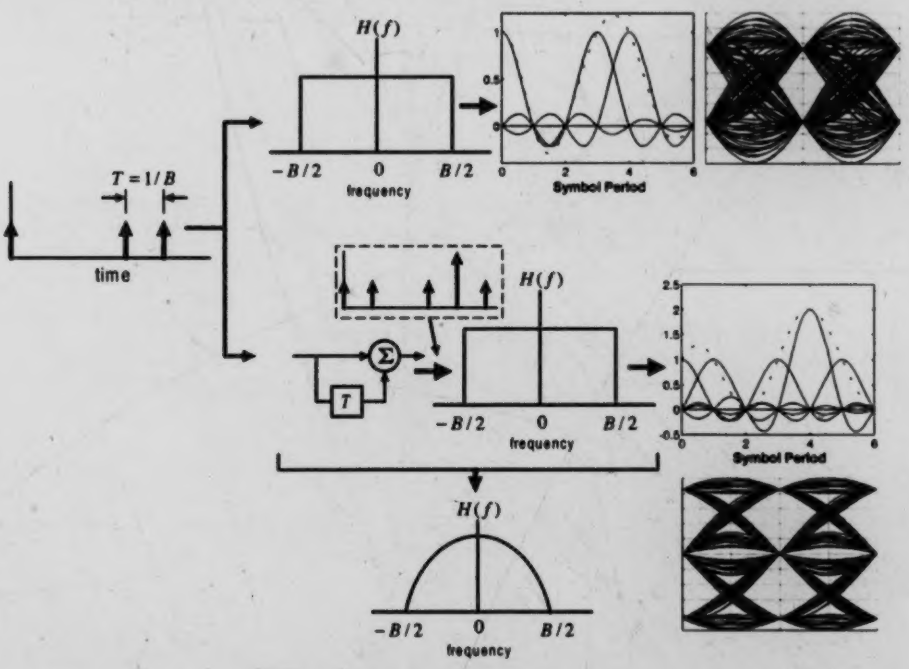

Figure 7.18 Minimum bandwidth channels for a binary signal (top) and a duobinary signal(bottom).

The channel shown at the top of Figure 7.18 has the minimum bandwidth required to produce a band-limited binary signal at the output with zero ISI. For this case, the ideal brick-wall filter has a one-sided bandwidth equal to $B/2$, and has a corresponding impulse response given by a sinc function with zero crossing spaced $T=1/B$ apart (excluding those that bound the main lobe). Each impulse generates a sinc-function impulse response that does not interfere with the peak responses at other points in time, as shown to the right of the brick wall filter in Figure 7.18 where individual impulse responses are shown with a solid line, and the superposition of all pulses is shown with a dashed line. The resulting binary eye diagram with zero ISI is also shown. Consider next the case where the binary information sequence of impulses is passed through an ideal delay-and-add circuit, as shown in Figure 7.18. This produces an information sequence consisting of impulses at the output of the delay-and-add circuit, except now an impulse takes on one of three possible weights, not just two. The spacing between the duobinary impulses, however, is still equal to T; hence, the response requirement of the following filter is no different than for the binary case, i.e., the position of zero crossings in the impulse response of the following filter does not depend on the weight of the impulse at the input. Note that for higher-level polybinary signals the same argument holds. Figure 7.18 shows the resulting impulse responses, and their superposition, at the output of the brick-wall filter for the duobinary signal, as well as the resulting zero-ISI eye diagram. As mentioned in Chapter 2, an ideal delay-and-add filter has a periodic transmission response that is monotonic decreasing between $f=0$ and $f=B/2$. Therefore, the overall transmission response of the delay-and-add circuit followed by an ideal brick-wall filter is as shown at the bottom of Figure 7.18. Note that both the binary channel and the duobinary channel must be capable of passing energy at frequencies up to $B/2$. In other words, the minimum theoretical bandwidth is the same for binary and duobinary signals. For a binary signal, however, the magnitude response of the channel must be perfectly flat over this bandwidth, which is not practical in a real system. For the duobinary signal, the response rolls off over this bandwidth, which is a more practical characteristic of many channels. If the binary channel contains a rolloff in its response, then the bandwidth over which the channel must be able to pass energy must be increased, as discussed in Chapter 3.

---

[8] A corollary of Nyquist's Criterion is that the overall system bandwidth must be at least one-half the bit rate in order to transmit a signal with zero ISI.

The polybinary signals shown in Figure 7.17 were generated using an ideal polybinary filter, bandlimited to $B/2$ by a twelfth-order Butterworth response. The Butterworth filter was used as a realizable approximation to an ideal lowpass filter and introduces some ISI because of its non-ideal magnitude response and a rather large group delay variation near the cutoff frequency. If an ideal lowpass filter were used, however, there would still be a significant amount of ISI present in the eye diagram because the input signal does not consist of impulses—instead, it is a somewhat bandlimited binary NRZ signal. Of course, a cleaner polybinary eye diagram is possible by increasing the bandwidth of the band-limiting filter that follows the delay-and-add circuit at the receiver. But as mentioned in section 7.3.1.2, increasing the bandwidth of the receiver passes more nonlinear distortion, which degrades the signal when transmitting over dispersive fiber. To illustrate this, if the 5 GHz, twelfth-order Butterworth response is replaced by a 10 GHz fifth-order Bessel response, then the resulting 5-level polybinary signal will be as shown in Figure 7.19.

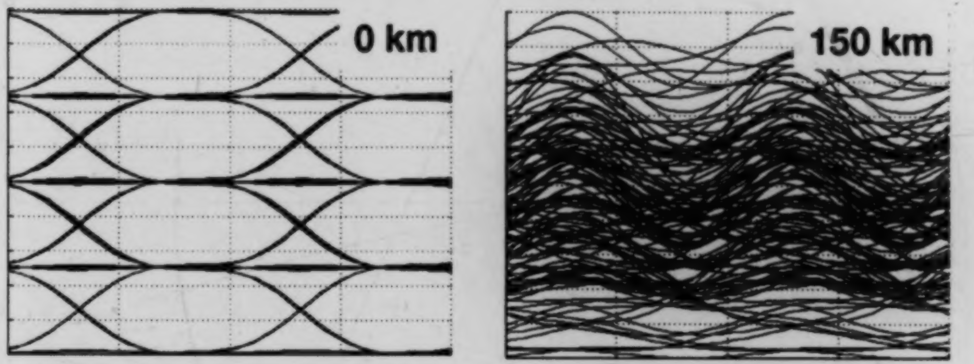

Figure 7.19 Eye diagram after 0 km and 150 km for a 5-level polybinary signal that has been bandlimited to 10 GHz.

Although the signal shows very symmetrical eye openings with little ISI at 0 km, the eyes become completely closed at 150 km because of the additional nonlinear distortion passed by the receiver. Figure 7.19 should be contrasted with Figure 7.17.

7.3.1.4 M-ary ASK

Figure 7.20 shows receiver sensitivity versus distance for 4-ary ASK and 8-ary ASK signals. Also shown is a curve for a polyquaternary (7 levels) signal generated by using a 1.5 GHz, fifth-order Bessel filter at the receiver. Note that, unlike for polybinary signals, the symbol period of an M-ary signal operating at a given aggregate bit rate decreases with an increase in the number of levels. Specifically, the aggregate bit rate B and the symbol period T are related by $T = (1/B)\log_2(M)$. From Figure 7.20 it can be seen that 4-ary ASK and 8-ary ASK signals experience a 1 dB penalty at about 200 and 475 km, respectively. This corresponds to a distance improvement of about 3.3 and 7.9 times, respectively, over the NRZ binary signal in Figure 7.8. The polyquaternary signal has a 1 dB penalty at about 300 km. Figure 7.21 shows eye diagrams of the filtered received signal for 4-ary and 8-ary ASK signals at various distances.

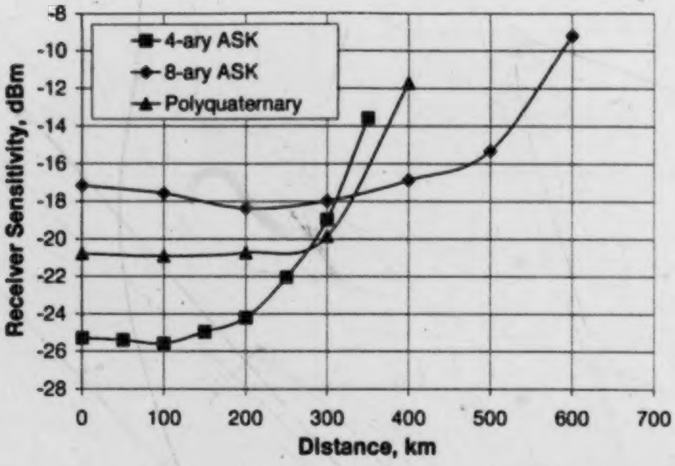

Figure 7.20 Receiver sensitivity versus distance for 4-ary ASK, 8-ary ASK and polyquaternary (7 levels) signals.

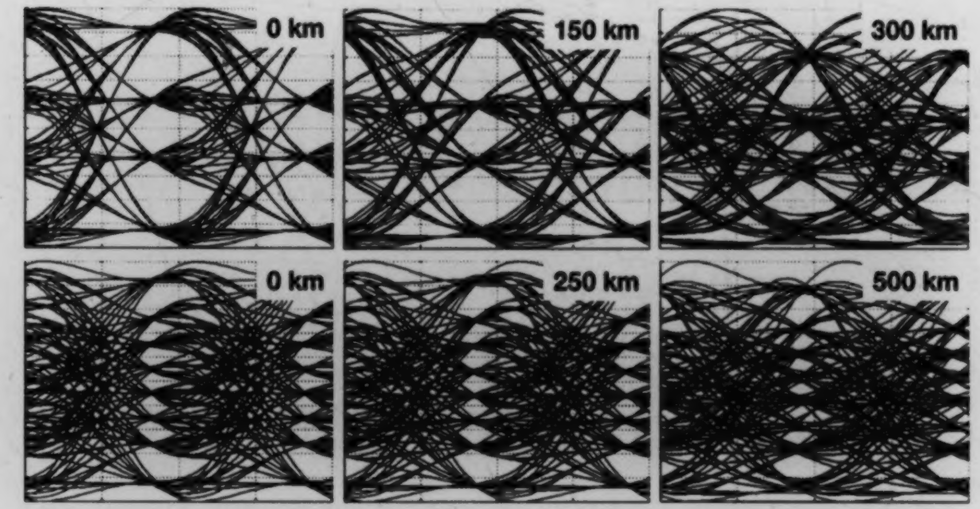

Figure 7.21 Eye diagrams at various distances for 4-ary ASK (top) and 8-ary ASK (bottom).

There are practical issues to consider for polyquaternary and 8-ary ASK signals, as discussed later on. In addition, it is possible to improve the performance of a 4-ary ASK signal by considering the effects of residual chirp that would always be present in any real system, and by adjusting the weights of the electrical signal applied to the modulator. These issues will be discussed later in this chapter.

7.3.1.5 Optical AM-PSK Duobinary

Recall from Figure 2.6 that an optical AM-PSK duobinary signal is generated by applying a duobinary electrical signal to a MZ external modulator biased at maximum extinction. This produces a binary intensity-modulated signal; however, the PSD of the optical field is duobinary. Receiver sensitivity versus distance is shown in Figure 7.22 for AM-PSK systems that uses 1) a delay-and-add filter followed by a band-limiting 5 GHz, twelfth-order Butterworth response, 2) a 2.5 GHz second-order Butterworth filter, and 3) a 3 GHz fifth-order Bessel filter to generate the duobinary electrical signal applied to the modulator. It is also possible to apply a 5-level polybinary signal to the modulator to generate a 3-level intensity-modulated optical signal. A result for a 5-level AM-PSK signal is also shown in Figure 7.22. Note that for the 5-level AM-PSK signal it is possible to decode the binary information at the receiver from independent decisions on each 3-level intensity-modulated symbol, provided the signal is properly precoded, as discussed in Chapter 2.

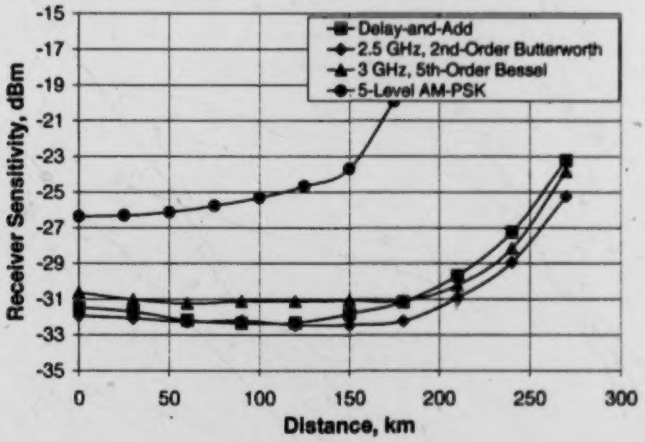

Figure 7.22 Receiver sensitivity versus distance for AM-PSK polybinary signals using various duobinary filters at the transmitter.

It can be seen that an optical AM-PSK duobinary signal allows transmission out to about 200 km with a dispersion penalty less than 1 dB. There is clearly no advantage to using a higher-level AM-PSK polybinary signal. An important advantage of an AM-PSK duobinary signal is that it requires no modification to a conventional binary receiver. It should be noted that the receiver electrical bandwidth requirement for an AM-PSK duobinary signal is the same as for a conventional binary signal, i.e., in both cases a binary, intensity-modulated signal is detected; yet, there is a significant improvement in dispersion immunity for the AM-PSK signal. The reason for this improvement is discussed in section 7.3.4. A clue, however, is evident in Figure 7.23, which shows eye diagrams of the received optical intensity at various distances for a system that uses a 3 GHz, fifth-order Bessel filter to generate the duobinary signal applied to the external modulator. Eye diagrams of the corresponding received electrical signal at each distance are shown directly below each optical eye in Figure 7.23.

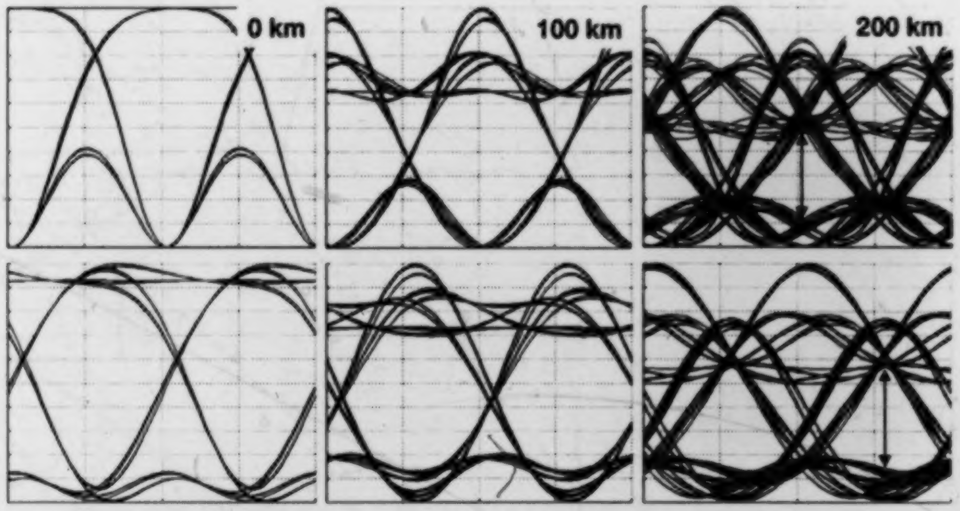

Figure 7.23 Eye diagrams of the received optical intensity (top) and the filtered electrical signal (directly below) for an AM-PSK signal.

Observe that the amount of nonlinear distortion present in the optical intensity at even 200 km appears to be much less than that at 175 km in Figure 7.15.

7.3.2 Residual Chirp from a Finite Optical Extinction Ratio

In the previous section, only systems using an external modulator with an infinite (ideal) intrinsic extinction ratio were considered. This corresponds to a MZ that has input and output Y-branches that are perfectly symmetric (i.e., 50/50 splitting/combining ratios) and an identical loss through each arm. No MZ is perfect, however, and will always possess a finite intrinsic extinction ratio. Recall from section 5.2.6 that a finite DC optical extinction ratio is accompanied by residual chirp. It is possible to specify the asymmetry in Y-branches as a design requirement and, thereby, introduce a desired amount of negative chirp [127] where the frequency chirping is, strictly speaking, not residual because it is controlled by carefully adjusting the splitting/combining ratio of Y-branches. What is easy to determine about a MZ device, however, is its intrinsic (DC) optical extinction ratio. The results presented here illustrate the impact of residual chirp, expressed in terms of a finite intrinsic optical extinction ratio, on binary, M-ary ASK and duobinary transmissions.

Let the voltages $v_1(t)$ and $v_2(t)$ be applied to arm 1 and arm 2, respectively, of a MZ modulator. Consider a device biased about the midpoint of its transfer characteristic, and driven in a push-pull (balanced) manner with $v_1(t)=V_\pi/2-a(t)$ and $v_2(t)=a(t)$ where $a(t)$ is an ac-coupled, 10 Gb/s binary signal, band-limited to about 6.5 GHz. To drive the modulator between maximum and minimum extinction, the peak-to-peak value of $a(t)$ would be set to $V_\pi/2$. Also, consider a MZ modulator with a 10 dB extinction ratio resulting from a lower amplitude for the field from arm 2 in equation (5.27). It is important to note that the extinction ratio considered here is that intrinsic to the MZ device (measured under DC conditions), and not that caused by varying the amplitude of the RF signal(s) driving the modulator. Under these conditions there is a red shift on the rising edge of pulses and a blue shift on the falling edge, in which case the polarity of the residual chirp is termed *negative* and can result in an improvement in dispersion immunity, as discussed in section 5.2.4. If the lower amplitude field is instead from arm 1 in (5.27), then there would be positive residual chirp for which there is a blue shift on the rising edge of pulses and a red shift on the falling edge; for this case, the dispersion immunity of the signal can be greatly reduced. Note that for M-ary ASK signals, too, the residual chirp will be either negative or positive, i.e., there will be a red shift when the optical intensity is increasing and a blue shift when it is decreasing, or conversely.

Next consider a system using AM-PSK duobinary signaling for which the modulator is biased at maximum extinction and the peak-to-peak amplitude of $a(t)$ is set to V_π. Recall from Chapter 2 that $a(t)$ is a duobinary (three-level) signal with a space represented by the middle level and a mark by the lowest and highest levels, or vice versa. A property of the duobinary signal is that marks alternate between the lowest and highest levels whenever they are separated by an odd number of spaces. However, the polarity of the residual chirp on a transmitted pulse also alternates, as shown in Figure 7.24. This implies that, unlike for other signaling formats, the residual chirp accompanying a MZ with a finite DC extinction ratio will always degrade the performance of an AM-PSK duobinary signal.

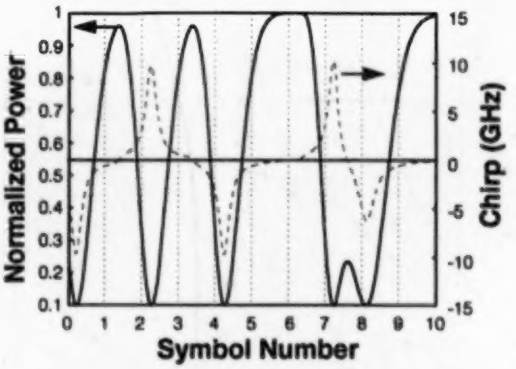

Figure 7.24 Polarity of residual chirp alternates in an AM-PSK duobianry signal.

Figure 7.25 shows receiver sensitivity versus distance for various signaling schemes in which positive or negative residual chirp is present due to a finite DC optical extinction ratio.

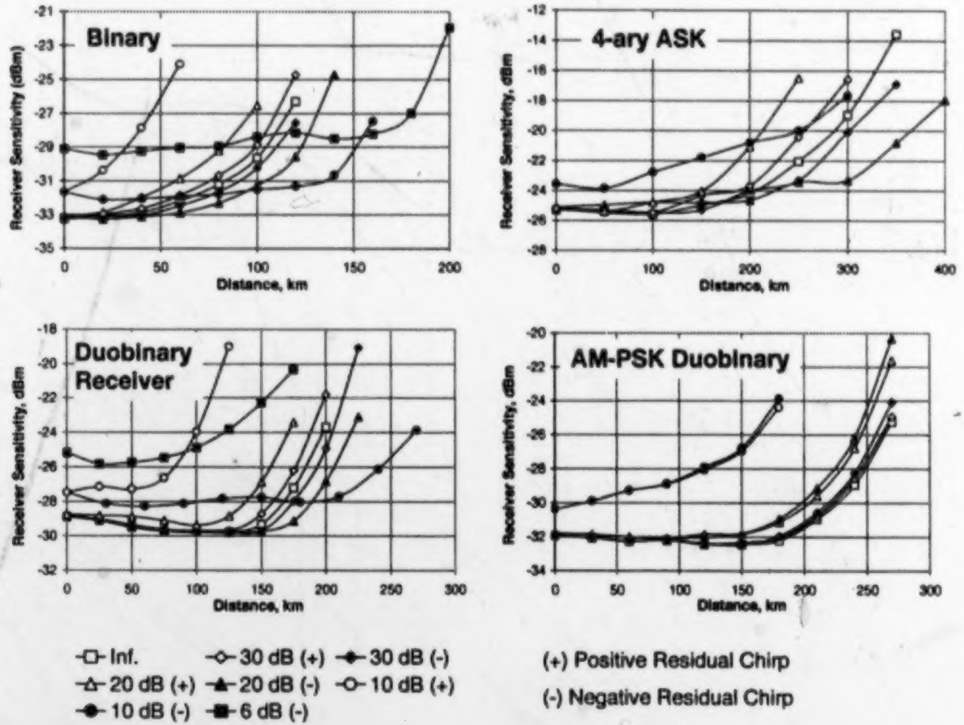

Figure 7.25 Effect of residual chirp from a finite DC optical extinction ratio on various signaling schemes.

Because a 3 GHz, fifth-order Bessel filter gave the best result in Figure 7.12, it was also used for the duobinary receiver in Figure 7.25. Similarly, because a 2.5 GHz, second-order Butterworth filter gave the best result at longer distances in Figure 7.22, it was used for the AM-PSK duobinary signal in Figure 7.25.

From Figure 7.25 it can be seen that all signaling formats, except AM-PSK duobinary, benefit from some amount of negative residual chirp. Conversely, positive residual chirp severely degrades performance. For example, Figure 7.25 shows that the dispersion-limited distance of a binary signal can be extended out to about 140 km if a MZ having a 10 dB DC extinction ratio is used. Of course, this assumes that the residual chirp is negative; if the residual chirp were positive, then the signal could be transmitted, at most, a few tens of km, while incurring a significant power penalty (about 5.5 dB at 50 km). It should be noted that reversing the polarity of residual chirp on any $LiNbO_3$ MZ can be accomplished by simply changing the bias voltage by V_π, i.e., by moving the bias point from a positive slope on the power transfer characteristic to a negative slope, or vice versa. Note that the AM-PSK duobinary signal does not benefit from a finite DC extinction ratio because the polarity of chirp is not the same for all symbols, as previously discussed. Hence, it is not meaningful to call the residual chirp positive or negative for an AM-PSK signal. Clearly, a MZ with a DC extinction ratio better than 20 dB is necessary to obtain the expected benefit from an AM-PSK signal. This is in stark contrast to the other signaling schemes where an extinction ratio of about 10 to 20 dB is beneficial for binary and duobinary signals, and an extinction ratio of about 20 dB is beneficial for a 4-ary ASK signal.

7.3.3 Transmission with Controlled Frequency Chirping

It is well known that controlled frequency chirping of MZ modulators can be used to extend the system reach of binary digital lightwave systems operating at 1550 nm over standard singlemode fiber [1, 2]. This is accomplished by operating a dual-drive modulator in a push-pull manner in which the signal applied to one arm is an inverted and weighted replica of that applied to the other arm. The idea is to adjust the weighting of the applied signals to obtain a desired amount of frequency chirping in which a transmitted optical pulse is red shifted on the rising edge and blue shifted on the falling edge, as discussed in Chapter 5. In this section, the effect of controlled frequency chirping on 4-ary ASK and AM-PSK signals is discussed. In addition, results are presented showing the interrelationship between controlled frequency chirping and the residual chirp accompanying a finite DC optical extinction ratio.

Figure 7.26 shows receiver sensitivity versus the chirp parameter described in Chapter 5 for a binary system using an external modulator with various DC extinction ratios and residual chirp polarity.

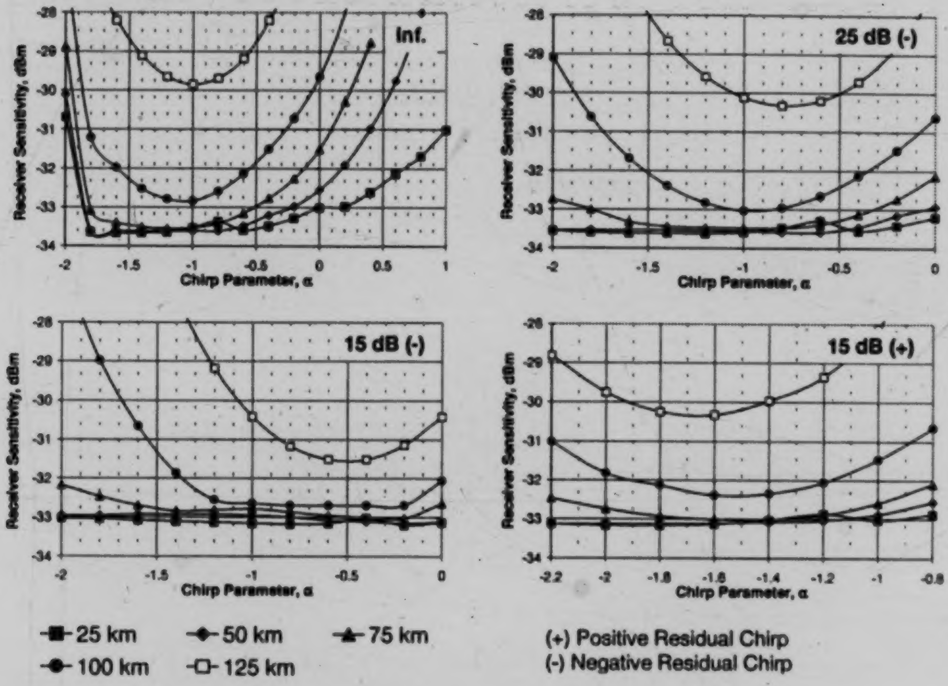

Figure 7.26 Receiver sensitivity versus chirp parameter for a binary system using an external modulator with various DC extinction ratios and residual chirp polarity.

As the distance is increased the signal becomes more sensitive to variation in the chirp parameter. For a MZ with an ideal extinction ratio, a negative chirp of –1 is optimal for all distances. As the extinction ratio of the MZ is lowered, and assuming negative residual chirp, the optimum chirp parameter is closer to zero. Conversely, if the residual chirp is positive, the optimal negative chirp becomes more negative. These results seem reasonable because, as the negative residual chirp is increased through a lower DC extinction ratio, less controlled negative chirp is needed to obtain the best performance. If the residual chirp is positive, however, then more controlled negative chirp is needed to compensate for the deleterious positive residual chirp. Regardless, it can be seen that the improvement offered by controlled negative chirp is less significant when there is already negative residual chirp resulting from a finite DC optical extinction ratio.

Controlled frequency chirping can also be imparted on a 4-ary ASK signal, as shown in Figure 7.27.

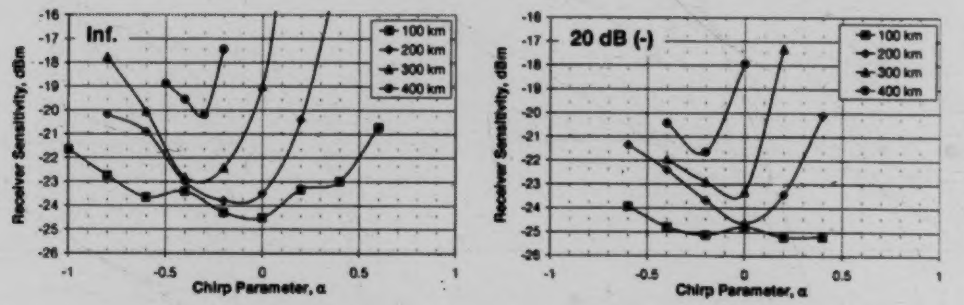

Figure 7.27 Receiver sensitivity versus chirp parameter for a 4-ary ASK system using an external modulator with an ideal and 20 dB DC exticntion ratio.

As for the binary signal, the 4-ary-ASK signal becomes more sensitive to the chirp parameter as the fiber length increases. For the case when the extinction ratio is 20 dB, however, and assuming negative residual chirp, there is no improvement offered by adding additional controlled chirp for distances up to about 300 km.

Figure 7.28 shows receiver sensitivity versus chirp parameter for an AM-PSK duobinary signal having an ideal DC extinction ratio.

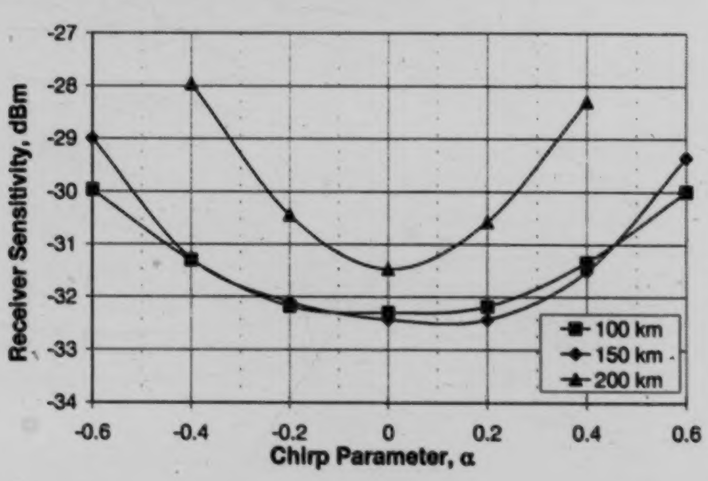

Figure 7.28 receiver sensitivity versus chirp parameter for an optical AM-PSK duobinary signal.

Note that, because the MZ is biased at maximum extinction for an AM-PSK signal, it is not really meaningful to call the chirp negative or positive. What should be deduced from Figure 7.28 is that driving the modulator with unbalanced signals will not improve performance because the chirp polarity of the transmitted intensity-modulated pulses is reversed each time a **1** is separated by an odd number of **0**s, as shown previously in Figure 7.24.

7.3.4 Relationship between Filter Response and Chromatic Dispersion in Duobinary Optical Communication Systems

In this section it is shown that limiting the spectral occupancy of a duobinary optical signal, which can be achieved by an appropriate choice of electrical transmitter filter response, is necessary to receive a benefit from duobinary transmission in singlemode optical communication systems. It is explained why such bandlimiting gives an improvement in dispersion immunity, and why ideal duobinary signaling is ineffective. The results are in good agreement with published experimental work.

In this present thesis (through simulation) and in other work in the literature, duobinary signaling has been demonstrated to improve the dispersion immunity of 10 Gb/s 1550 nm lightwave systems operating over standard fiber. Various approaches have been experimentally verified, including the use of a duobinary receiver in conjunction with a binary transmitter [58], [59], duobinary intensity modulation at the transmitter [60], [61], and optical AM-PSK duobinary signaling [62], [63], [64], [65]. Simulation and experimental results in [128] demonstrated that no improvement in dispersion immunity over a conventional binary system is observed when "ideal" AM-PSK duobinary signaling is used. In that work, the authors state that "the spectral bandwidth of the sequence is not the relevant parameter for assessing the dispersion tolerance." By "ideal" AM-PSK duobinary, it is meant that the signal which drives the modulator is an NRZ duobinary (three-level) electrical signal with zero rise and fall times. Recent work [129] proposes an explanation, based on an interference phenomenon between marks and spaces, for the improvement observed in optical AM-PSK duobinary systems that possess a finite optical extinction ratio. In this present thesis, however, a different explanation is given that is based on communications theoretic principles [130]. It is explained here that, in order to receive any benefit, the spectrum of the AM-PSK optical electric field must be bandlimited to $f_o \pm B/2$ where f_o is the optical carrier frequency and B is the bit rate.

Figure 7.29 shows simulations of receiver sensitivity versus distance for lightwave systems using an optical preamplifier and different transmission filter structures for both conventional NRZ binary and AM-PSK duobinary signaling. In Figure 7.29 the ideal duobinary signals are generated by the delay-and-add filter shown in Figure 7.11, and then bandlimited by various Butterworth filters with the indicated 3 dB cutoff frequency and filter order, prior to driving the modulator. Additionally, a case is shown where the duobinary signal is generated by passing an ideal NRZ binary signal through a 2.5 GHz, second-order Butterworth filter prior to driving the modulator. Also shown in Figure 7.29 are results for duobinary transmission with three optical intensity levels where, again, a significant improvement in dispersion immunity is achieved when the ideal duobinary signal is bandlimited prior to driving the modulator. However, a significant baseline penalty is incurred because of the increased number of levels at the decision circuit along with the signal dependence of signal-spontaneous beat noise. Note that all results in Figure 7.29 use the same receiver filter, i.e., a 6.5 GHz, third-order Butterworth response.

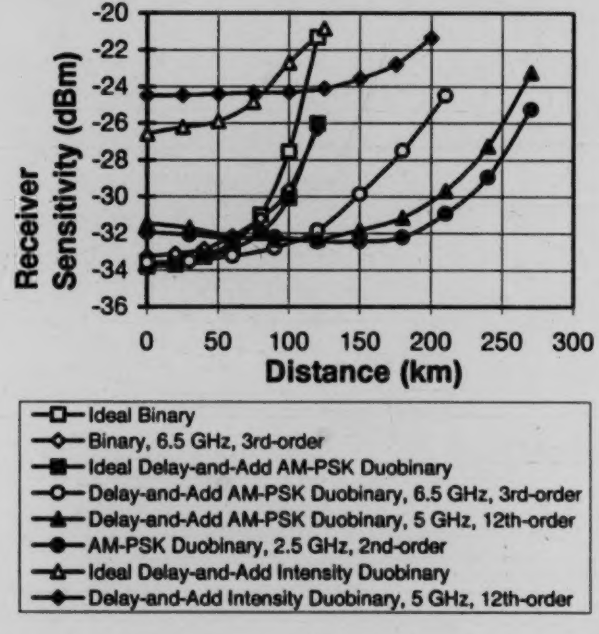

Figure 7.29 The effect of various electrical transmitter filter structures on receiver sensitivity versus distance for 10 Gb/s binary, duobinary and AM-PSK duobinary systems.

The requirement to restrict the spectral occupancy of the electrical duobinary signal, prior to driving the modulator, can be explained as follows. The spectrum of the optical field for an ideal duobinary signal has the first nulls at $f_o \pm B/2$. It is well known that this signal can be bandlimited to $f_o \pm B/2$ while preserving sufficient information to recover the binary data. Standard singlemode fiber operating at 1550 nm imparts pure phase distortion on the optical field's spectrum for which the dispersive part of the fiber transfer function is of the form $\exp(jkf^2)$ where k is a constant and f is measured relative to f_o, as discussed in section 5.3. Because of the square dependence on frequency, this phase distortion will impart a larger phase shift on frequency components farther away from the carrier. Although only a small portion of the optical power is at frequencies beyond $f_o \pm B/2$, the phase distortion of these spectral components, if they are not suppressed, will be manifested as an increase in nonlinear distortion of the intensity envelope that is directly detected at the receiver. Because a square-law detector outputs a signal proportional to the intensity envelope, it is ultimately the nonlinear, intensity-envelope distortion falling within the bandwidth of the electrical receiver that determines the dispersion-limited distance. Recall that the electrical receiver bandwidth requirement for conventional binary and the AM-PSK duobinary signal is the same; however, the amount of nonlinear distortion that falls within this bandwidth can be reduced for the AM-PSK signal by limiting the spectral occupancy of its optical field to $f_o \pm B/2$, resulting in an improvement in dispersion immunity. Note that it is not just permissible, but essential that the spectral occupancy of the optical duobinary signal be bandlimited. This could be accomplished with an optical bandpass filter having a passband equal to B centered about the optical carrier. Alternatively, this can be accomplished by limiting the bandwidth of the baseband duobinary electrical signal to $B/2$ (single-sided), prior to driving the modulator. The modulator then imparts this signal onto the optical carrier with the desired suppression of spectral components beyond $f_o \pm B/2$. Note that this is true even though the external modulator does not, strictly speaking, behave as a linear modulator, as shown later in Figure 7.30. For duobinary intensity modulation, the spectrum of the optical field is not pure duobinary, but closely resembles that of a duobinary signal with a resulting benefit from bandlimiting the signal, but again only if the driving signal is bandlimited to $B/2$. Intuitively, a given amount of nonlinear distortion in the optical intensity envelope will have a greater impact as the number of intensity levels is increased. Hence, a three-level intensity duobinary signal should not be expected to span as long a distance as a two-level intensity optical AM-PSK duobinary signal, consistent with the results in Figure 7.29, as well as [60], [61]. Note that if the transmitter electrical bandlimiting is weak, i.e., the 3 dB cutoff is somewhat greater than $B/2$, or the filter rolloff is gradual, then only a partial benefit will be achieved. This is the case in Figure 7.29 for the AM-PSK duobinary signal that uses a 6.5 GHz, third-order lowpass filter to bandlimit the ideal duobinary signal prior to driving the modulator. This may explain why some of the experimental results in the references did not span as long a distance as others. Note that it is also possible to reduce the amount of nonlinear, intensity-envelope distortion that falls within the bandwidth of the receiver by using a signaling scheme that allows for a reduced receiver bandwidth, such as a duobinary receiver, as discussed in Section 7.3.1.2. However, as with a duobinary transmitter, it is imperative that a duobinary receiver also be hard bandlimited to *B*/2.

To further illustrate the importance of bandlimiting the optical field of a duobinary signal, and how this can be accomplished using a LPF at the transmitter, Figure 7.30 shows the optical field's PSD for an AM-PSK signal, and the resulting eye diagram of the filtered receiver electrical signal after transmission over 200 km for the case when the optical field is not bandlimited (ideal duobinary), and bandlimited by an ideal optical BPF with band edges at $f_o \pm B/2$. Also shown in Figure 7.30 is the field's PSD and resulting receiver eye diagram when the duobinary signal applied to the external modulator is bandlimited to *B*/2 by an ideal LPF. Hence, it can be seen that electrical bandlimiting of the duobinary signal applied to the modulator accomplishes the task of suppressing the side lobes of the optical field's spectrum beyond $f_o \pm B/2$.

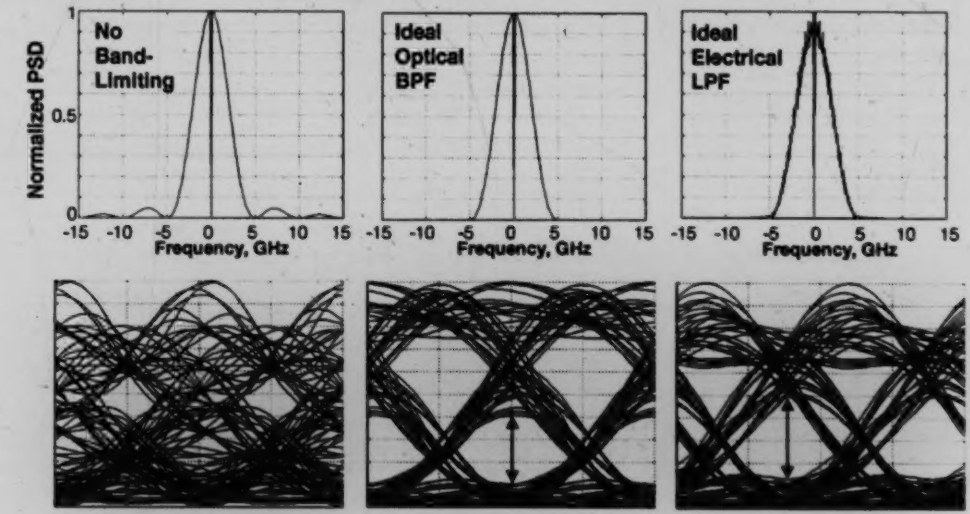

Figure 7.30 PSD of the optical electric field (top) and corresponding filtered receiver eye diagrams (bottom) after transmission over 200 km.

Results presented in Figure 7.29 used Butterworth responses to bandlimit the electrical duobinary signal at the transmitter. However, a variety of response types are amenable to the filter requirements. For example, when the delay-and-add circuit is followed by a band-limiting filter, the important requirement is to hard bandlimit the electrical signal to *B*/2, without introducing a significant amount of ISI in the duobinary signal applied to the modulator. Also, the rolloff order does not necessarily need to be as high as that used in Figure 7.29 where a twelfth-order Butterworth response was used to approximate an ideal lowpass filter. For example, if this is instead an eight or fourth-order filter, with the same cutoff, the simulated sensitivity at 210 km degrades by 0.16 and 1.31 dB, respectively, because of the resulting increase in spectral content above *B*/2. Also, the duobinary filter can be implemented as a single lowpass filter with a cutoff at about 0.25 times the bit rate. Such a filter approximates the rolloff of a delay-and-add circuit while concurrently providing the required bandlimiting. Again, many different filter types will work, including structures such as Butterworth or Bessel. Note, too, that the AM-PSK duobinary signaling scheme is quite tolerant to modest amounts of ISI in the duobinary electrical signal applied to the modulator because of the limiting nature of the Mach-Zehnder's transfer characteristic. This alleviates the need for strict filter specifications. Indeed, the 2.5 GHz Butterworth response used in Figure 7.29 produces an electrical duobinary signal with a modest amount of ISI, yet it gives good results in the filtered receiver response after transmission over 200 km.

In this section it was explained that limiting the spectral occupancy of a duobinary optical field reduces the amount of nonlinear distortion falling within the bandwidth of the receiver. In section 7.3.1.2 it was explained that the amount of nonlinear distortion falling within the bandwidth of the receiver can be reduced by using a signaling scheme that allows for a reduced receiver bandwidth, such as a duobinary receiver. A general observation is that, in terms of the overall system response, limiting the bandwidth of the transmitter or receiver is necessary to minimize the impact of fiber dispersion. It is not necessary, however, to limit both. For example, if the receiver bandwidth is reduced to the minimum allowable for a conventional binary system, say, 60-70 % the bit rate, then limiting the transmitter bandwidth to the bit rate will give similar results as a transmitter having a bandwidth equal to 5 or 10 times the bit rate. If the receiver bandwidth is not minimized, however, then reducing the bandwidth of the transmitter to less than that of the receiver will substantially improve the dispersion immunity of the signal. In other words, it is the minimum of the transmitter and receiver bandwidth that dictates the dispersion immunity of the system. For a conventional binary signal, it is not possible to reduce the transmitter bandwidth to lower than about 60-70 % of the bit rate without introducing a significant amount of ISI due to an insufficient bandwidth to pass the signal. The receiver bandwidth, however, can also be made as low as about 60-70 % of the bit rate. Therefore, from a practical standpoint, it is the receiver bandwidth that should be minimized because it will also minimize the noise and, therefore, provide the best receiver sensitivity. In the case of a system that uses a duobinary transmitter, it is possible to hard bandlimit the transmitter signal to about *B*/2, which is lower than the minimum required receiver bandwidth. Hence, in the case of a duobinary transmitter, the minimum bandwidth is set at the transmitter.

7.3.5 Optimal Level Spacing and ISI

It was shown in Section 4.2.2 that the optimal level spacing of an M-ary ASK signal depends on which noise sources are dominant. For example, for the practical case when signal-spontaneous beat noise dominates, it was shown that the optimal normalized level weights of the optical intensity for a 4-ary ASK signal are 0, 1/9, 4/9 and 1, respectively, for the lowest to highest levels. Unfortunately, the constraints imposed by linear filtering and fiber dispersion, as well as the practical implementation of such level weights, prevents the optimal weights from being used. Consider, for example, an ideal 4-ary ASK NRZ signal with optimal weights input to the fiber. Figure 7.31 shows the eye diagram at 0 km and 250 km for the filtered receiver signal.

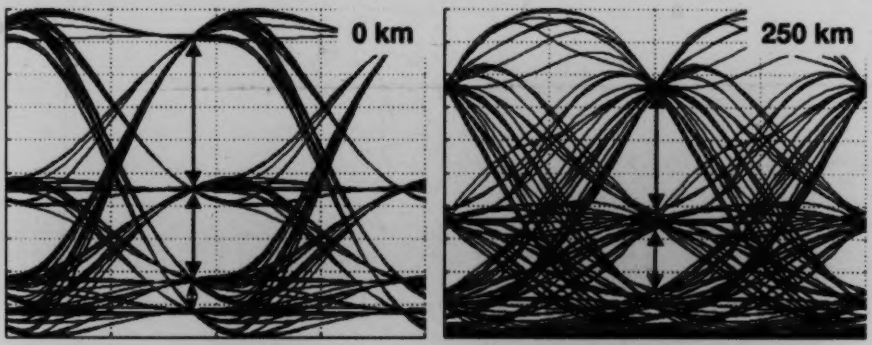

Figure 7.31 Eye diagrams of a 4-ary ASK signal using optimal level weights.

Even at 0 km the optimal level weights would be impractical because of the significant temporal closure of the bottom eye. At 250 km the bottom eye is essentially closed because of dispersion. For the multilevel symbol generator used in experiments in this work, there is a constraint on the level spacing that can be achieved. Recall that the 4-ary electrical signal applied to the external modulator is obtained by summing two binary signals of different weights using a power combiner. This necessarily imposes the constraint that the normalized level weights of the electrical multilevel signal, ε_1 and ε_2, sum to unity. An additional degree of freedom is offered by varying the peak-to-peak amplitude of the 4-ary signal and/or the bias point of the external modulator. In so doing, the nonlinear nature the MZ's transfer characteristic can be used to obtain various level spacings in the optical intensity. Figure 7.32 shows receiver sensitivity versus distance for a 4-ary ASK signal using various weights for the binary tributaries that are summed to give the multilevel signal applied to the modulator. A 20 dB optical extinction ratio is assumed with negative residual chirp.

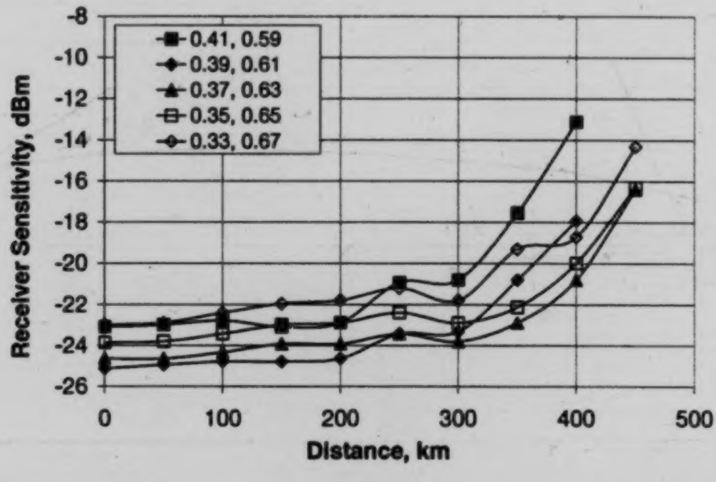

Figure 7.32 receiver sensitivity versus distance for various level weights of the electrical signal applied at the modulator.

In Figure 7.32 the normalized weights ε_1=0.37 and ε_2= 0.63 offer the best performance for distances beyond about 250 km. It should be remembered, though, that these levels weights may not be optimal for other system parameters. For example, the non-ideal frequency response of an external modulator, or electrical components at the transmitter and/or receiver, may affect the choice of level weights.

7.3.6 Overview of Expected Reach for Signaling Schemes

In previous sections, the dispersion immunity of various signaling schemes was compared. It was shown that the residual chirp, which accompanies a MZ with a finite DC extinction ratio, can enhance performance in some systems and degrade performance in others. It was also demonstrated that the benefit from controlled frequency chirping can be diminished when residual chirp is present. Also, for M-ary ASK signals, it was explained that varying the level weights of the multilevel signal affects the dispersion performance. Therefore, a comparison of the various signaling schemes may favor one signaling format over another, depending on the system parameters used in evaluating performance. Some useful conclusions, however, can be made. For example, polybinary signals with more than three levels are of no practical use. Also, duobinary transmission of three optical intensity levels is not as appealing as placing the duobinary filter at the receiver because, although both cases give about the same dispersion tolerance, a duobinary receiver offers a lower noise bandwidth at the receiver, with an associated improvement in receiver sensitivity. To be fair, a practical set of parameters should be assumed when making a comparison. For example, a DC optical extinction ratio of 20 dB is reasonable for a MZ device. Negative residual chirp is also a reasonable assumption because it can always be obtained by appropriately setting the DC bias point. Also, using the normalized level weights ε_1=0.37 and ε_2=0.63 for a 4-ary signal applied to the modulator is practical because they are easily implemented. Under these conditions, Figure 7.33 shows receiver sensitivity versus distance for the most promising signaling schemes.

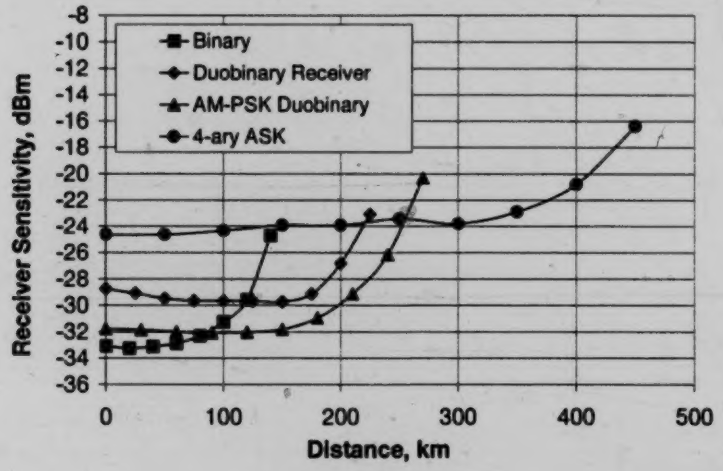

Figure 7.33 Receiver sensitivity versus distance for various signaling schemes.

For distances up to about 100 km, conventional binary signaling is adequate. For distances from 100 km to 200 km, the AM-PSK duobinary signal is probably the best suited because it requires no modification to the structure of the receiver, a minor modification to a conventional binary transmitter, and offers a receiver sensitivity comparable to a conventional binary signal. It is unlikely that a duobinary receiver would ever be used over an AM-PSK signal because of its higher baseline receiver sensitivity and requirement for a modified receiver structure. The 4-ary ASK signal can span distances up to about 350 km and, therefore, may be suitable for links between 200 km and 350 km. A 4-ary ASK signal has the disadvantage of a much higher baseline sensitivity and a modified receiver structure, but has the advantage of requiring all logic components at the transmitter and receiver to operate at only one-half the bit rate of all other signaling schemes—because electrical bandwidth is a major limitation in high-speed systems, this attribute may make 4-ary signaling appealing at shorter distances, too. Higher-level signals, such as 8-ary ASK and the polyquaternary signals, are probably not practical at present because of the excessively large power required at the receiver, an increasingly complex receiver structure, and a greater vulnerability to the non-ideal frequency response of system components, as discussed in section 7.4.1. Fiber nonlinearities would also likely have a significant impact on long-distance transmissions for these signals.

7.3.7 Power Penalty from a Non-Zero Laser Linewidth

In section 7.2.4 it was shown that a significant power penalty due to PM-to-AM noise conversion can occur when a laser with a non-zero linewidth is used. In that section, however, ideal signals with zero ISI were assumed. If ISI is introduced from system impairments such as non-ideal linear filtering at the transmitter and/or receiver, or chromatic dispersion, then it is expected that the PM-to-AM RIN-induced power penalty will become significant at narrower linewidths. Figure 7.34 shows receiver sensitivity versus linewidth at various distances for binary, duobinary and M-ary ASK signals that accounts for electrical filtering and chromatic dispersion.

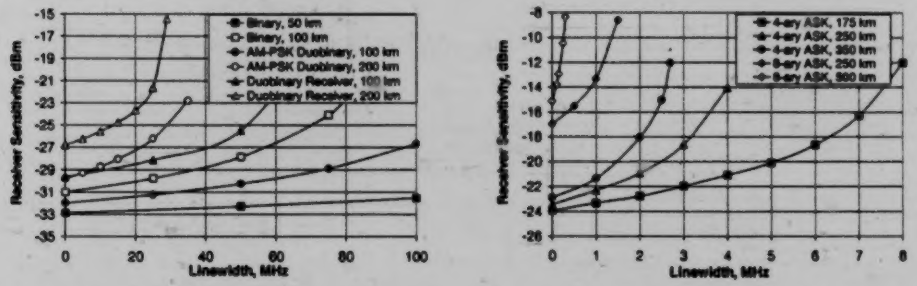

Figure 7.34 Receiver sensitivity versus source linewidth: (left) binary and duobinary systems; (right) M-ary ASK systems.

Assuming a maximum allowable PM-to-AM RIN-induced power penalty of 2 dB, a binary signal can tolerate a source linewidth as high as about 100 MHz when transmitting over 50 km, and a linewidth of about 40 MHz when transmitting over 100 km. For the AM-PSK duobinary signal, the linewidth must be no larger than roughly 50 MHz and 20 MHz, respectively, when transmitting over 100 km and 200 km. For a system using a duobinary filter at the receiver, the linewidth requirements are reduced to around 30 MHz and 15 MHz when transmitting over

100 km and 200 km, respectively. Therefore, another reason for using an AM-PSK duobinary signal over a duobinary receiver to span the 100 to 200 km range is that it has a less stringent linewidth requirement. A linewidth no greater than about 3 MHz, 1.5 MHz and 1 MHz is required for the 4-ary ASK signal when transmitting over 175 km, 250 km and 350 km, respectively. Hence, a 4-ary ASK signal requires a very narrow linewidth source. An 8-ary ASK signal requires an extremely narrow linewidth—about 700 kHz for transmission over 250 km, and 150 kHz for transmission over 500 km. This is yet another reason higher-level M-ary signals may not be practical for long-distance transmission.

7.3.8 Optical Inline Amplifiers and ASE Accumulation

To achieve the longest unrepeatered span, an optical postamp and preamp can be used to obtain the largest system gain possible. A practical launched optical power (output from an optical postamp) might be, say, +10 dBm. Practical receiver sensitivities for binary, 4-ary ASK and 8-ary ASK signals are around -33 dBm, -25 dBm and -17 dBm, respectively. Therefore, assuming a fiber attenuation of 0.2 to 0.25 dB/km, unrepeatered transmission is possible for distances up to 170-215 km for binary, 140-175 km for 4-ary ASK, and 110-135 km for 8-ary ASK. For distances beyond these, optical inline amplifiers can be used as nonregenerative repeaters to overcome fiber attenuation. Unfortunately, ASE accumulates when optical amplifiers are added to the system, which results in more signal power required at the receiver to obtain the same target BER.

Once system parameters have been set, the ratio of optical signal power to ASE power incident on the photodetector can be related to the BER or receiver sensitivity. For example, for a system using only an optical preamplifier and the same system parameters used in section 7.3, this ratio is 6.1 dB, 14.1 dB and 22.2 dB, respectively, for binary, 4-ary ASK and 8-ary ASK signals. If the ASE is increased by adding additional amplifiers to the system, then ASE-dependent noise terms will increase and, therefore, the received optical signal power must be increased to maintain the target BER. If the ASE power is increased by a factor k due to additional optical amplifiers, then increasing the signal power by the same factor k will produce the same ratio of signal power to ASE power as without optical inline amplifiers. Note that maintaining the signal-to-ASE power ratio at the photodetector by increasing the signal power will, at worst, result in a BER equal to that with no inline amplifiers. To see this, note that the electrical SNR is related to optical power by

$$SNR = \frac{k_1 P_{sig}^2}{k_2 P_{sig}^2 + k_3 P_{sig} + k_3 P_{ASE} + k_4 P_{ASE}^2 + k_5 P_{sig} P_{ASE} + k_6} \tag{7.4}$$

where k_1-k_6 are constants, and P_{sig} and P_{ASE} are, respectively, the signal and ASE power incident on the photodiode. In (7.4) the terms in the denominator represent the various noise sources, which include (reading from left to right) RIN, signal shot noise, ASE shot noise, spontaneous-spontaneous beat noise, signal-spontaneous beat noise, and receiver thermal noise. Assuming the gain of the optical preamplifier is fixed, P_{sig} will increase by the same amount as the received power, i.e., that input to the optical preamp. If P_{ASE} and P_{sig} are increased by the same factor k, i.e., the ratio P_{sig}/P_{ASE} is kept constant, then from (7.4) the electrical signal power will increase by a factor k^2, whereas noise terms will either increase by a factor k^2 (RIN, signal-spontaneous beat noise and spontaneous-spontaneous beat noise), increase by a factor k (signal and ASE shot noise), or not increase at all (receiver thermal noise). Therefore, when the optical signal-to-ASE power ratio is maintained, the electrical SNR will be, at worst, equal to that in the absence of inline amplifiers. In practical cases, beat noises will dominate, which are proportional to k^2, and the SNR will be essentially held constant.

To determine whether or not transmission over a given distance is feasible, the signal-to-ASE power ratio can be plotted at the output of each amplifier stage in a cascade . For example, consider an optical postamp with a 10 dB gain and an average input power of 0 dBm, which gives a launched optical power of +10 dBm. To ensure that the power output from any inline amplifier does not exceed +10 dBm (i.e., may want to avoid fiber nonlinearities), it will be assumed that the interlink loss is equal to the gain of each amplifier stage. Assuming n_{sp}=2 for all amplifiers, Figure 7.35 shows the ratio of signal to ASE power at each amplifier stage for 40 km and 80 km amplifier spacings. The total interlink loss from splices, fiber, filters, isolators, etc., is assumed to be 16 dB and 28 dB, respectively, for the 40 and 80 km links. Note that Figure 7.35 shows the signal-to-ASE power ratio at the output of each amplifier stage, not that incident on the photodiode. After a few stages, however, the accumulation of ASE from inline amplifiers will be much larger than that added by the optical preamp, for which the signal-to-ASE power ratio will be essentially the same as that incident on the photodetector. Note that for 40 km spacings and 150 stages (6000 km), P_{sig}/P_{ASE} is greater than the required 6.1 dB cited earlier for a binary signal. Therefore, it is possible to transmit a binary signal over many thousands of km when amplifiers are spaced 40 km apart.

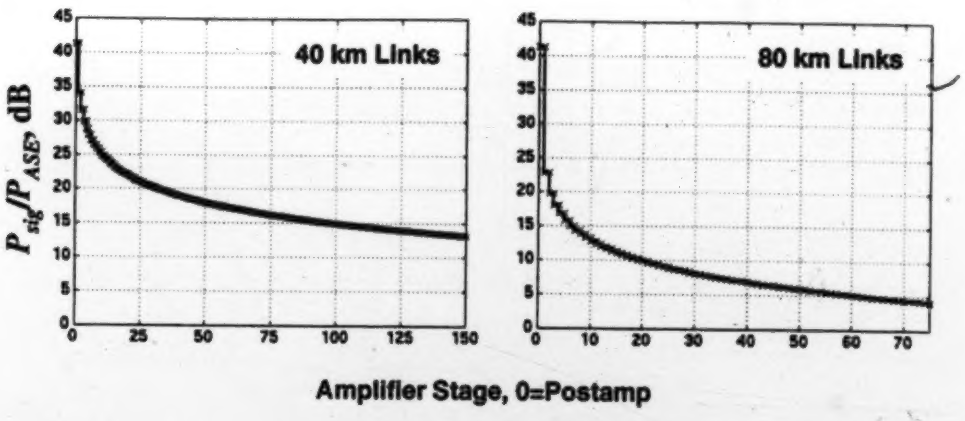

Figure 7.35 Ratio of optical signal power to ASE power at each amplifier stage for 40 km and 80 km amplifier spacings.

For 80 km spacings, the binary signal would be limited to about 45 stages, or 3600 km. For a 4-ary ASK signal, it can be seen that the ~14 dB signal-to-ASE power ratio is reached at about 125 stages (5000 km) for 40 km spacings, and about 8 stages (640 km) for 80 km spacings. For an 8-ary ASK signal the ~22 dB signal-to-ASE power ratio is reached at about 15 stages (600 km) for 40 km spacings, whereas 80 km spacing is not practically realizable.

The above analysis does not consider the effects of fiber dispersion. Also, the required signal-to-ASE power ratio depends on system parameters such as optical and electrical bandwidth. Regardless, the above results give an indication of the limitations of inline amplifiers for various signaling schemes. For the dispersive system considered here, dispersion limits binary transmission to, at most, about 200 km (i.e., binary intensity modulation using AM-PSK duobinary modulation of the optical field). Because this distance is comparable to the maximum unrepeatered span of 170-215 km cited earlier, system designs are possible without the use of inline amplifiers. For distances longer than 200 km, M-ary ASK signaling can be used, but will require inline amplifiers because the distance is well beyond the maximum unrepeatered length of 140-175 km for a 4-ary ASK signal. Accounting for dispersion, Figure 7.36 shows BER versus launched optical power (power output from the postamp) for a 4-ary signal using 40 and 80 km amplifier spacings and a total transmission distance of 160 and 320 km. For comparison, results are also shown for an 8-ary ASK signal at distances of 320 and 640 km.

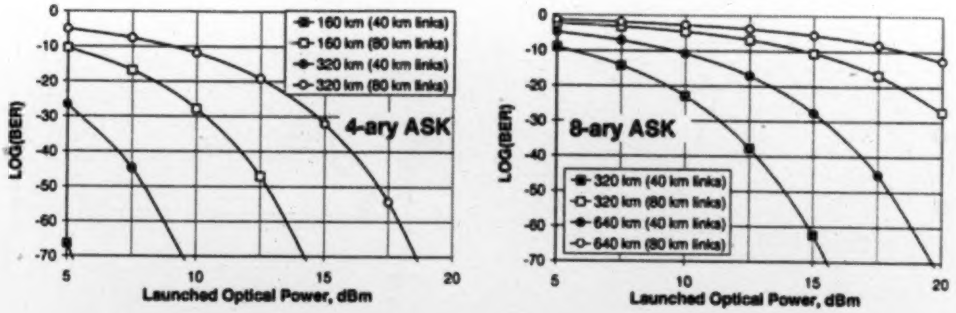

Figure 7.36 BER versus launched optical power for 4ary ASK and 8-ary ASK signals.

It can be seen that the required power launched into the fiber becomes very large, in excess of +15 dBm, for an 8-ary ASK signal using 80 km amplifier spacings. For powers this high and total distances of 320 to 640 km, self phase modulation (SPM) will likely impact performance greatly [103]. For distances up to 320 km, a launched power of about +12 dBm is sufficiently high for a 4-ary ASK signal; however, SPM may be significant for this case, too.

7.4 Realistic System Simulation

All simulations to this point assumed an ideal PRBS, ideal frequency responses for all system components, and an ideal transfer characteristic for a $LiNbO_3$ MZ external modulator. In section 6.2, however, it was explained that the non-ideal frequency response of system components can have a significant impact on performance. To determine whether or not a real design is feasible, it was necessary to account for the frequency response of all system components, such as amplifiers, power dividers, bias tees, filters, external modulators, photodetectors, among others. A LabVIEW Virtual Instrument (VI) was written to acquire real frequency response data from measurements using an HP8510 network analyzer. The frequency response data was then used in simulations. Similarly, a LabVIEW VI was written and used with an HP54120 digital oscilloscope to extract time records of the actual electrical signals (binary or 4-ary) applied at the transmitter. Because the BERT residing at TRLabs cannot operate faster than 3 Gb/s, additional GaAs logic was used to time-multiplex an OC-48 signal (2.48832 Gb/s) output from the BERT up to an OC-96 rate (4.97664 Gb/s) using a 2:1 selector, or up to an OC-192 rate (9.95328 Gb/s) using a 4:1 multiplexer. Details about the multiplexing operations are provided in Chapter 8. An OC-48 PRBS length of 2^7-1 (127 bits) was used in all experiments and simulations. This results in an OC-96 sequence length of 254 bits, and an OC-192 sequence length of 508 bits after time-division multiplexing. Each time record was recorded using at least 25 samples per symbol, and each sample was averaged at least

64 times to reduce the effects of noise. Figures 7.37 shows a 10 Gb/s binary trace and its eye diagram acquired from the output of a GaAs 4:1 multiplexer. Similarly, Figure 7.38 shows a 10 Gb/s 4-ary trace and its eye diagram for a signal obtained by summing two 5 Gb/s binary signals, of unequal weights, output from a GaAs 2:1 selector.

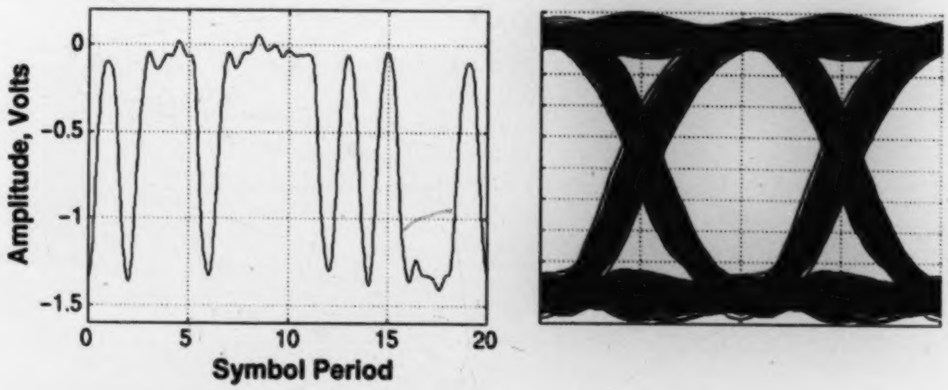

Figure 7.37 Trace and eye diagram for a signal output from a GaAs 4:1 Multiplexer operating at 10 Gb/s.

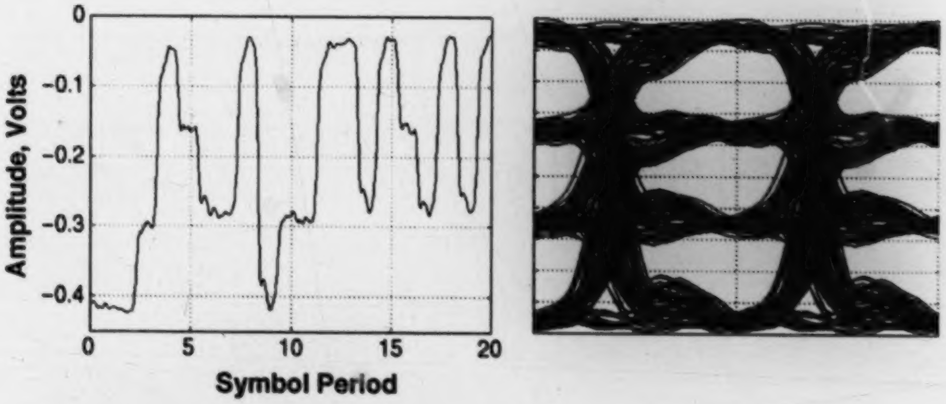

Figure 7.38 Trace and eye diagram of a 10 Gb/s 4-ary ASK electrical signal used at the transmitter.

Figure 7.37 and 7.38 show that the real NRZ signals applied at the transmitter are already somewhat bandlimited and contain a modest amount of ISI

7.4.1 Effect of Component Frequency Response

At an earlier stage in this work, $LiNbO_3$ MZ devices obtained from ETEK and UTP, and photodetectors obtained from BT&D and NEW FOCUS, were used in experimental setups. Although it was possible to demonstrate binary transmissions at up to 10 Gb/s using these components, every attempt to demonstrate a 10 Gb/s 4-ary ASK system, even in an optical back-to-back configuration, had failed. It was later determined that the non-ideal frequency responses of the external modulator and photodetector were the main limiting factors. Fortunately, Nortel Technologies provided a III-V MZ and PIN photodetector that were of much higher quality than other devices. A $LiNbO_3$ MZ was also obtained from Lucent Technologies that provided much better performance than devices from either ETEK or UTP. To illustrate the impact of these devices, consider two system configurations: one using a UTP MZ with a BT&D photodetector, and one using a Nortel MZ with a Nortel photodetector. Amplifiers are also needed at the transmitter and receiver to achieve the necessary signal amplitude to drive the modulator or decision circuit at the receiver. Using the real frequency response of two 26 GHz amplifiers from B&H, a 15 GHz amplifier from SHF, and a 10 GHz amplifier from Veritech, Figure 7.39 shows the frequency response for these amplifiers cascaded with the measured small-signal response of the two different combinations of modulator and photodetector.

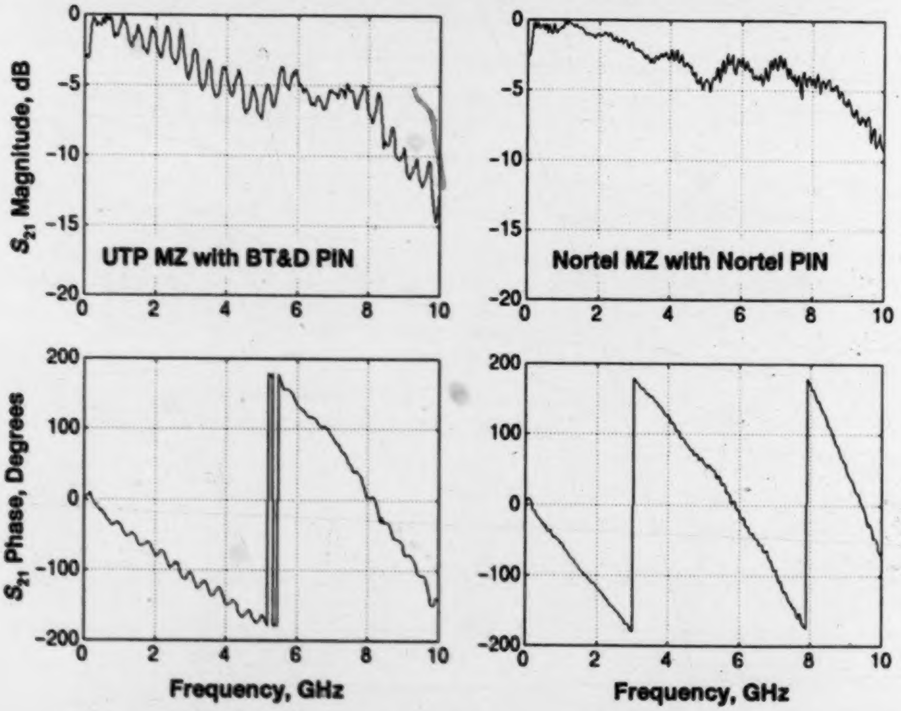

Figure 7.39 Small-signal magnitude and phase response of overall system: (left) using UTP modulator and BT&D photodetector; (right) using Nortel MZ with Nortel PIN photodetector.

The *ringing* in the magnitude response using the BT&D photodetector is believed to be caused by a poor mismatch between the photodiode, which did not have a load resistor, and the 50 Ohm transmission line it connects to. Using the acquired traces in Figures 7.37 and 7.38 to drive the MZ, and the frequency responses from Figure 7.39, eye diagrams of the received binary and 4-ary electrical signals are shown in Figures 7.40 and 7.41, respectively, for an optical back-to-back link.

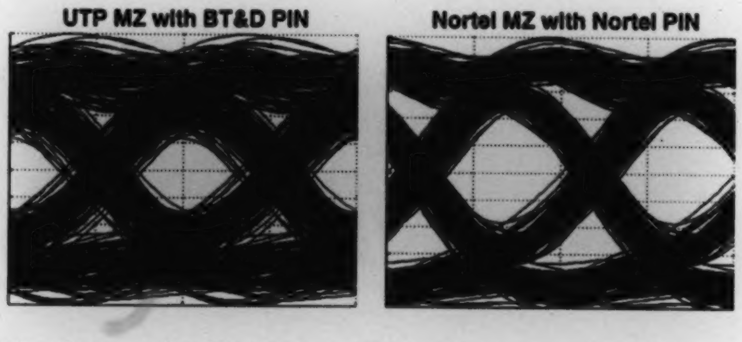

Figure 7.40 Eye diagrams of 10 Gb/s binary received signal for a system using the frequency responses from Figure 7.39.

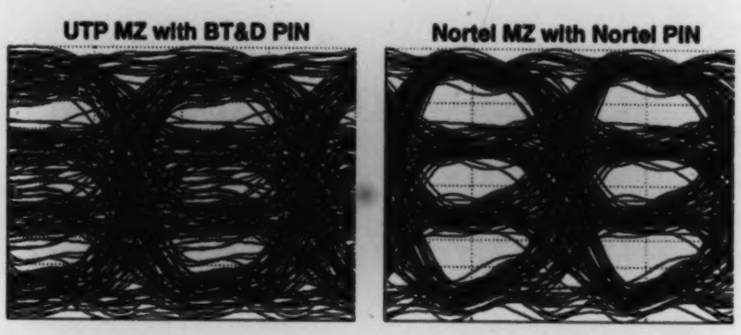

Figure 7.41 Eye diagrams of 4-ary ASK 10 Gb/s received signal for a system using the frequency responses from Figure 7.39.

Although the binary signal can operate at 10 Gb/s for both responses, the eye is noticeably smaller when using the UTP and BT&D devices. The middle eye is completely closed in the 4-ary ASK signal when using the UTP and BT&D devices. Using the Nortel devices, however, provides a substantial improvement.

There are additional components that would be used in a laboratory implementation, such as bias-tees, dc blocking capacitors, power dividers/combiners and a lowpass filter in the receiver to limit noise. These components, too, affect the overall response. Figures 7.40 and 7.41 are intended to illustrate that the system's response is very sensitive to the particular components chosen, and that achieving the system reaches and receiver sensitivities obtained using ideal simulations is not likely because of the significant amount of ISI introduced by the non-ideal frequency response of components. Moreover, the increase in ISI from non-ideal responses will result in a narrower linewidth requirement for the laser to avoid a BER floor, or to minimize the power penalty, due to PM-to-AM noise conversion. As an example, Figure 7.42 shows receiver sensitivity versus linewidth for a 4-ary ASK system using acquired data for system components.

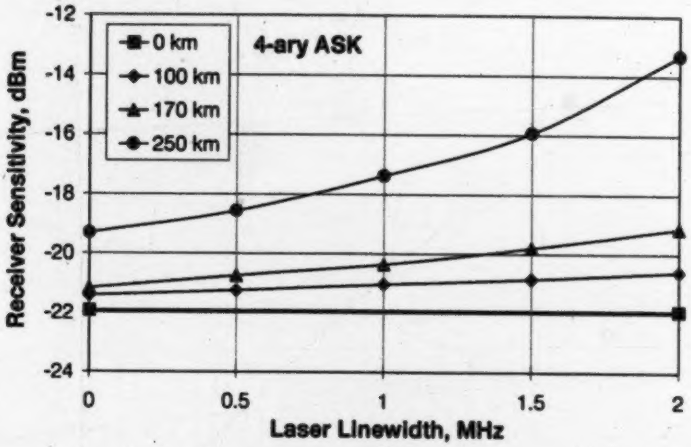

Figure 7.42 Receiver sensitivity versus laser linewidth for a 4-ary ASK system using acquired data for modeling components.

Using ideal components and assuming transmission over 250 km, a 2 dB PM-to-AM RIN induced power penalty will be produced using a laser with a linewidth of about 2 MHz, according to Figure 7.34. When the real component data is used, however, the linewidth requirement is reduced to about 1 MHz, as shown in Figure 7.42.

7.4.2 Bias and Drive Conditions for an InP/InGaAsP Mach-Zehnder Modulator

It was explained in section 5.2.7 and section 6.5 that the amplitude and phase of the field output from each arm of a III-V MZ can be modeled by curve fits to measured data. For long distance transmissions, frequency chirping has a significant impact on performance and greatly influences the maximum distance that can be spanned. It was demonstrated in sections 7.3.2 and 7.3.3 that negative chirp can significantly increase the dispersion-limited transmission distance. The chirp introduced by a III-V MZ depends on the bias applied to each arm, as well as the amplitude and shape of the applied RF signals. To help determine the optimal drive conditions for this device, simulations were carried out using real component and response data and various drive conditions for the III-V MZ. It was found that both binary and 4-ary ASK signals possessed good dispersion immunity when the left and right arm DC biases were set to –2.0 V and –4.5 V, respectively, and when the amplitude applied to the left arm was about 2.0 V_{pp} and the amplitude applied to the right arm was 0.75 to 1 V_{pp}. Figure 7.43 shows the optical intensity envelope and frequency chirp at the fiber input for a binary and 4-ary ASK signal using these optimized drive conditions.

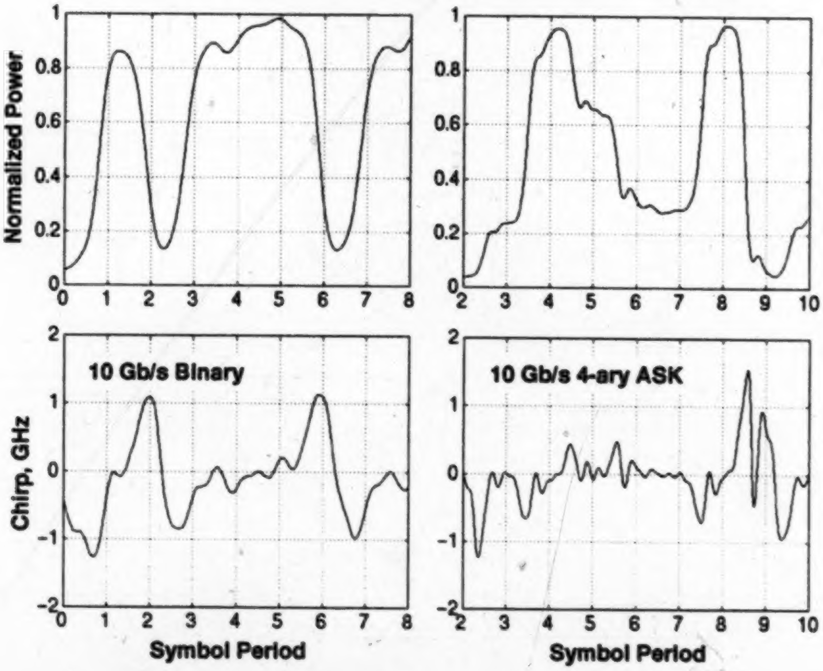

Figure 7.43 Intensity envelope and frequency chirp for a binary signal (left) and a 4-ary ASK signal (right) using optimized drive conditions for a III-V MZ.

For both signals there is a red shift on the rising edge of pulses and a blue shift on the falling edge, giving a negative chirp on the transmitted signal, with a maximum frequency deviation of about 1 to 1.5 GHz. Note that the maximum frequency deviation in the 4-ary ASK signal occurs when the optical power swings between the highest and lowest values, corresponding to the maximum rate of change of the applied RF signals, as discussed in section 5.2.3.

Realistic system simulations of receiver sensitivity, BER, and expected reaches will be presented in Chapter 8 where they can be compared to experimental results.

7.5 Summary

Simulation results were presented in this chapter that are based on the static and dynamic noise models described in Chapter 4. The effect of varying system parameters such as the optical filter bandwidth, preamplifier gain or noise figure was investigated for binary and M-ary ASK signals. The power penalty for using M-ary signaling over binary signaling was discussed, as well as the quantum limit for binary, 4-ary and 8-ary ASK signals. Results were presented showing the dispersion immunity of all signaling schemes investigated, and the impact of residual chirp and controlled frequency chirping on the various signals was discussed, as well as practical issues regarding optimal level spacing. An explanation was provided for why ideal AM-PSK duobinary signaling is ineffective and why bandlimiting the signal at the transmitter or receiver is important to minimize nonlinear distortion in the signal passed to the decision circuit. ASE accumulation in systems using optical inline amplifiers, and its impact on binary and M-ary ASK signals, was investigated. Finally, some comments were made explaining the need to account for non-ideal device behavior in system simulations.

8 Experimental Results

A significant part of this research was the complete design, construction and testing of a 4-ary ASK optical communication system operating at 10 Gb/s. In addition, to serve as a benchmark for comparison, experiments were conducted for 10 Gb/s binary systems. Details about the experimental setups are given in this chapter, and the results are compared to predictions from realistic simulations. The first experiments presented are on noise measurements, and were intended to verify the adopted noise model.

8.1 Noise Measurements

To verify the adopted noise model, experiments were conducted to measure the noise in an optically-preamplified system. The setup used for the noise measurements is shown in Figure 8.1 where some of the measurements made use of an optical postamp and fiber.

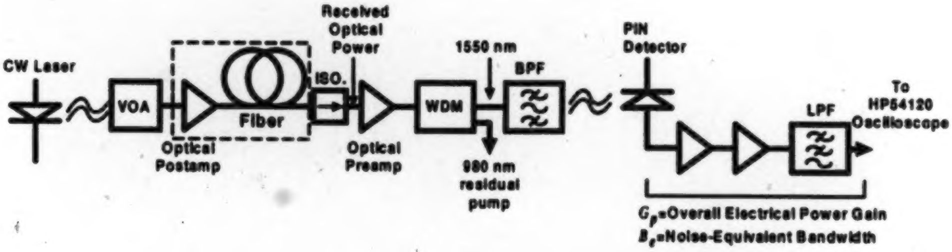
CW Laser
VOA
Optical Postamp
Fiber
ISO.
Received Optical Power
Optical Preamp
WDM
1550 nm
BPF
980 nm residual pump
PIN Detector
LPF
To HP54120 Oscilloscope
G_p=Overall Electrical Power Gain
B_e=Noise-Equivalent Bandwidth

Figure 8.1 Setup for measuring noise in an optically-preamplified system.

A variable optical attenuator (VOA) was used to control the amount of optical power input to the EDFA postamp or preamp, and the output from the EDFA preamp was filtered by a 1.4 nm BPF and square-law detected by a PIN photodetector. The resulting noise current was then amplified and measured using the histogram feature on an HP54120 digital oscilloscope. All components were characterized for their relevant parameters, as discussed in Chapter 6, and the noise calculated from the expressions in section 4.1 was compared to the noise measured . To do this comparison, all noises were referenced to the current through the photodiode, and expressed as a power given by $\langle i^2 \rangle R$ where $\langle i^2 \rangle$ is the mean-square noise current and R is a 50 Ω load resistance. Therefore, the noise voltage measured using the histogram feature of the oscilloscope had to be scaled to give the corresponding noise current through the photodiode. This required a knowledge of the overall NEB and power gain of the electrical receiver, which was determined using network analyzer measurements, as described in Chapter 6.

A substantial amount of residual pump power at 980 nm was observed at the output of the EDFA preamp. It was necessary to remove this power using a WDM because of the additional noise that was otherwise present. This observation was made during initial noise measurements in which the WDM was omitted, as shown by the measured and calculated noise levels in Figure 8.2.

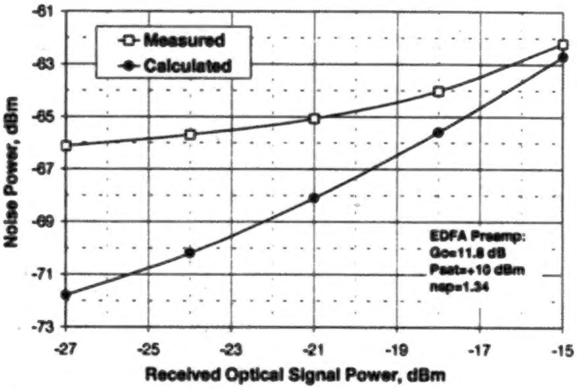

Figure 8.2 Measured and calculated noise for an optically-preamplified receiver with residual pump power.

At lower received powers, the measured noise was substantially larger than that calculated. This additional noise was removed when a WDM was placed at the output of the EDFA preamp module, suggesting that the source must have been 980 nm residual pump power present at the output. It should be noted that a WDM was already built into the EDFA module for the purpose of removing residual pump power. However, a small amount of residual pump power (-13 dBm) was passed by the 1550 nm port on the internal WDM (i.e., the WDM did not separate the 980/1550 nm signals with infinite isolation). At this power, the extra noise in Figure 8.2 would result if the RIN value for the pump laser were about –120 dB/Hz, a reasonable value. Therefore, it is believed that RIN from the residual pump power was responsible for the increased noise. All other noise measurements and experiments used a WDM at the output of the optical preamp to remove the residual pump power.

To clearly see the signal dependence of signal-spontaneous beat noise, a higher gain optical preamp was used. Results for the measured and calculated noises are shown in

Figure 8.3. The calculated dependence of noise on received optical power agrees well with the noise measured, indicating that the noise model for an optically-preamplified receiver is valid. Note that the 1:1 slope at higher received powers corresponds to the region where signal-spontaneous beat noise dominates, i.e., noise is linearly proportional to received optical power.

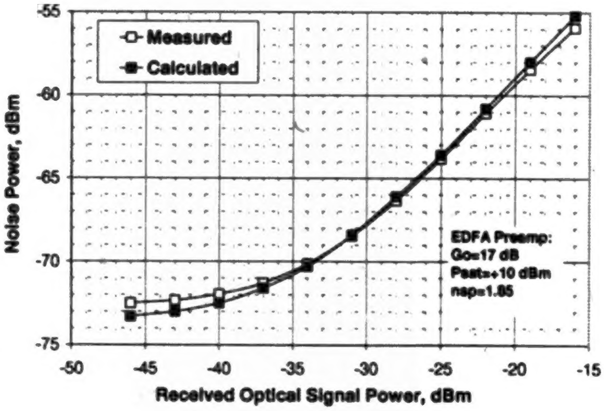

Figure 8.3 Measured and calculated noise for a receiver using an EDFA preamplifier.

A third noise measurement was performed using an optical postamp, 100 km of fiber, and an optically-preamplified receiver. For this case, the noise power was calculated and measured as a function of the optical power input to the postamp, as shown in Figure 8.4.

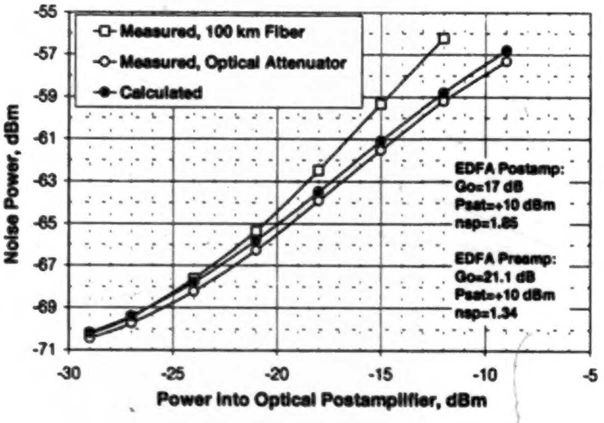

Figure 8.4 Measured and calculated noise for a system using an optical postamplifer, 100 km of fiber (or optical attenuator), and an optically-preamplified receiver.

For higher powers into the optical postamp, the measured noise increased much more rapidly than that calculated. To investigate the source of the additional noise, the fiber was replaced with an optical attenuator having the same loss as that measured through the 100 km fiber span. The noise measurement was then repeated with the result shown in Figure 8.4. For this case the measured and calculated noises agree very well, suggesting that the increased noise present with fiber must be due to the fiber itself. This was the first evidence of the PM-to-AM RIN discussed in Chapter 4. Figure 8.5 shows results from another noise experiment using an optical postamp, 100 km of fiber, and an optical preamp. Two calculated results are shown: one that does not include PM-to-AM noise conversion, and one that does. The measured linewidth for the laser, which was used in the PM-to-AM noise calculations, was 35 MHz.

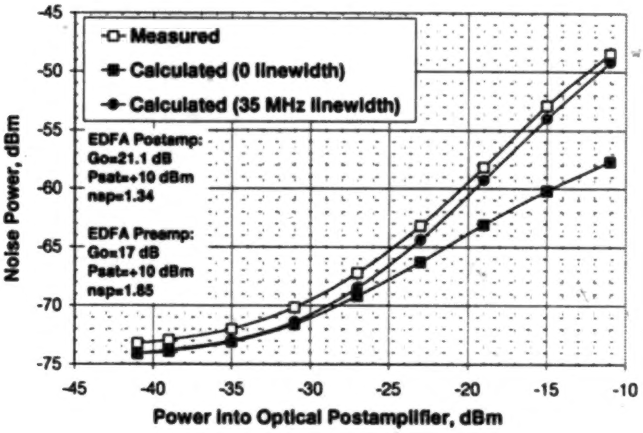

Figure 8.5 Measured and calculated noise for a system using an optical postamplifer, 100 km of fiber, and an optically-preamplified receiver.

Good agreement between theory and experiment is obtained when RIN from PM-to-AM noise conversion is included in calculations. The results in Figures 8.4 and 8.5 provide strong experimental evidence that PM-to-AM noise conversion does, in fact, occur.

A few comments should be made about the EDFAs used in experiments. Recall from Chapter 6 that the gain of an EDFA essentially follows the ASE emission spectrum, which is strongly wavelength dependent for the EDFAs used in these experiments, as shown in Figure 6.13. There were four EDFAs available for experiments, and for the source wavelength of 1557 nm used for experiments in this section, the gains of the EDFAs were quite low, between 8.4 and 11.8 dB for each amplifier. Therefore, to obtain larger gains, many experiments used two EDFAs in cascade, which were characterized and modeled as a single EDFA. Parameters for the EDFAs used in these experiments are indicated in the respective figures.

To determine the noise current through the photodiode using histogram measurements on an oscilloscope, the power gain G_p and noise-equivalent bandwidth B_e had to be accurately known for the receiver, which were determined using network analyzer measurements. In practice, B_e depends on the reference point used for a system's gain or loss. For example, the gain of a typical wideband electrical amplifier will have 2 to 3 dB ripple in its passband, and it is possible to define B_e using the maximum or minimum gain, or something in-between, through

$$B_e = \frac{1}{G_p}\int_0^\infty |H(f)|^2 \, df \tag{8.1}$$

where $H(f)$ is the frequency response of the device. For example, Figure 8.6 shows two calculated values of B_e for a wideband amplifier, based on either the maximum or minimum gain within the passband.

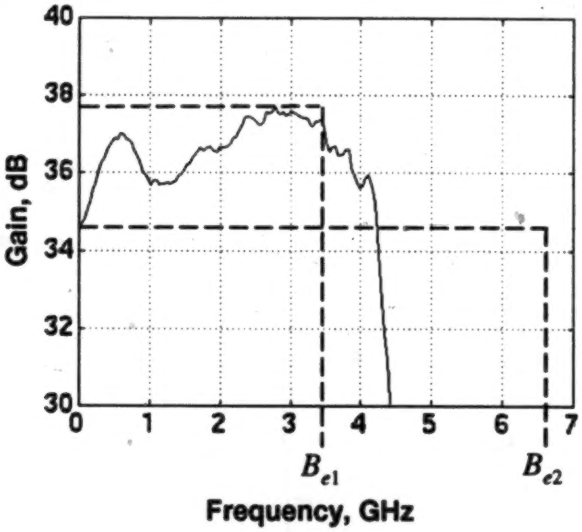

Figure 8.6 Defining noise-equivalent bandwidth for a component with a practical frequency response.

Using the minimum gain near DC gives B_e=6.7 GHz, whereas using the maximum gain at about 3 GHz gives B_e=3.4 GHz.

Note that either definition for B_e will give the correct noise at the output of the system because the noise PSD is multiplied by G_pB_e where G_p is the power gain used in calculating B_e.

8.2 10 Gb/s Binary Transmission Experiments

8.2.1 Experimental Setup

Figure 8.7 shows the optical setup used in conducting 10 Gb/s binary transmission experiments.

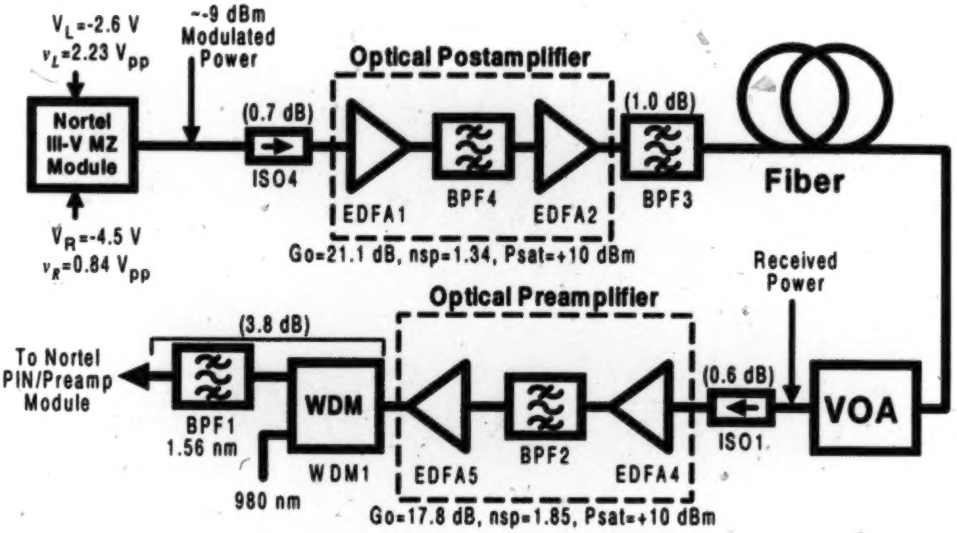
VL=-2.6 V
vL=2.23 Vpp
~-9 dBm
Modulated
Power
Optical Postamplifier
Nortel
III-V MZ
Module
(0.7 dB)
ISO4
EDFA1
BPF4
EDFA2
(1.0 dB)
BPF3
Fiber
VR=-4.5 V
vR=0.84 Vpp
Go=21.1 dB, nsp=1.34, Psat=+10 dBm
Received
Power
Optical Preamplifier
(3.8 dB)
To Nortel
PIN/Preamp
Module
BPF1
1.56 nm
WDM
WDM1
980 nm
EDFA5
BPF2
EDFA4
(0.6 dB)
ISO1
VOA
Go=17.8 dB, nsp=1.85, Psat=+10 dBm

Figure 8.7 Optical setup used in 10 Gb/s transmission experiments.

These experiments used the Nortel III-V MZ module. The module's laser was biased at 55 mA, and the DC biases and amplitudes of the modulating signals applied to the III-V device were as shown in Figure 8.7. To obtain sufficient gain, two EDFAs were used in cascade as an optical postamp and as an optical preamp. An isolator preceded the postamp to prevent ASE from entering the III-V MZ, and a BPF was placed at the output of the postamp to ensure the gain peak in the ASE spectrum did not saturate the gain of the optical preamp. An isolator also preceded the optical preamp to prevent backscattered ASE. As mentioned in the previous section, the WDM at the output of the preamp was needed to remove the residual pump that otherwise produced additional noise. To obtain BER measurements, a VOA was used to vary the received power. The average power launched into the fiber was +7.7 dBm.

For the EDFAs in Figure 8.7, the postamp had a higher gain and lower n_{sp} value than the preamp, suggesting that the roles of these two amplifiers should, maybe, be reversed. Although exchanging the roles of these amplifiers would improve the receiver's sensitivity, the overall performance of the system would actually be worse. In other words, for the *available* source power, the maximum ratio possible for the signal to ASE power incident on the photodetector would be degraded. In all experiments, the best performance for the overall system was used as the criteria for placing EDFAs, not just the performance of an isolated receiver.

To obtain a 10 Gb/s signal to drive the modulator, it was necessary to time-division multiplex the 2.5 Gb/s data output from an HP71600 BERT, as shown in the electrical transmitter setup in Figure 8.8.

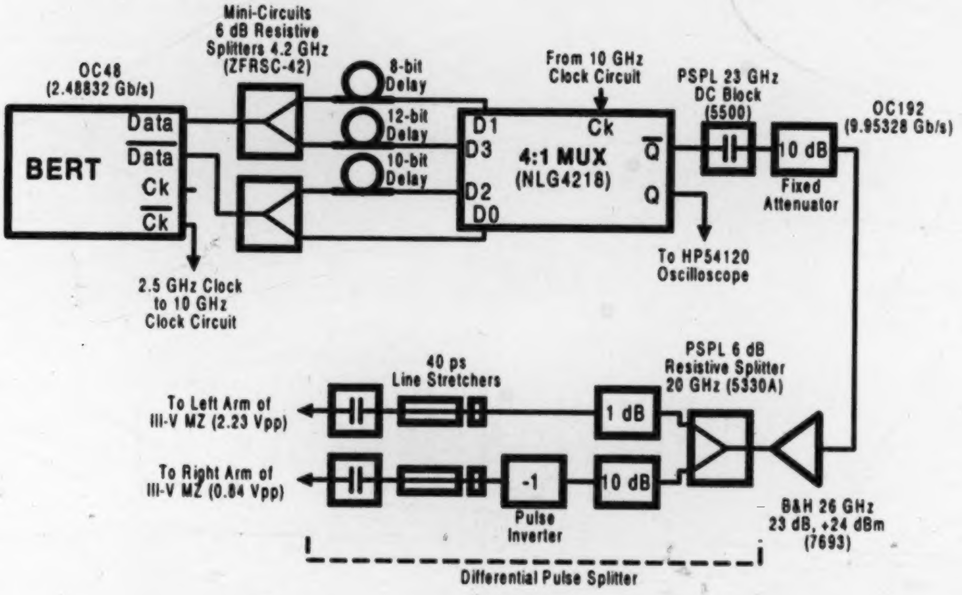
Mini-Circuits
6 dB Resistive
Splitters 4.2 GHz
(ZFRSC-42)
OC48
(2.48832 Gb/s)
BERT
Data
$\overline{\text{Data}}$
Ck
$\overline{\text{Ck}}$
8-bit Delay
12-bit Delay
10-bit Delay
From 10 GHz Clock Circuit
D1
D3
D2
D0
Ck
4:1 MUX
(NLG4218)
$\overline{Q}$
Q
PSPL 23 GHz
DC Block
(5500)
10 dB
Fixed Attenuator
OC192
(9.95328 Gb/s)
To HP54120 Oscilloscope
2.5 GHz Clock
to 10 GHz
Clock Circuit
40 ps
Line Stretchers
PSPL 6 dB
Resistive Splitter
20 GHz (5330A)
To Left Arm of
III-V MZ (2.23 Vpp)
To Right Arm of
III-V MZ (0.84 Vpp)
1 dB
10 dB
-1
Pulse Inverter
B&H 26 GHz
23 dB, +24 dBm
(7693)
Differential Pulse Splitter

Figure 8.8 Eletrical transmitter setup for 10 Gb/s binary experiments.

Four 2.5 Gb/s tributaries were provided to the 4:1 MUX by splitting the output data and its complement from the BERT, and then delaying each tributary by an integer number of bit periods with respect to one another. The 10 Gb/s signal output from the 4:1 MUX was amplified, and then passed through a differential pulse splitter to obtain the correct amplitude and polarity for the signals applied to the III-V MZ electrodes. The 10 GHz clock applied to the 4:1 MUX was derived from the 2.5 GHz clock output from the BERT using the circuit shown in Figure 8.9. The clock generating circuit operated as follows. First, the 2.5 GHz clock from the BERT was amplified, and then split and input to the intermediate frequency (IF) and local oscillator (LO) ports of a double-balanced mixer. This provided a 5 GHz tone at the output of the mixer, synchronized to the 2.5 GHz tone at the input; hence, the mixer was used as a frequency doubler.

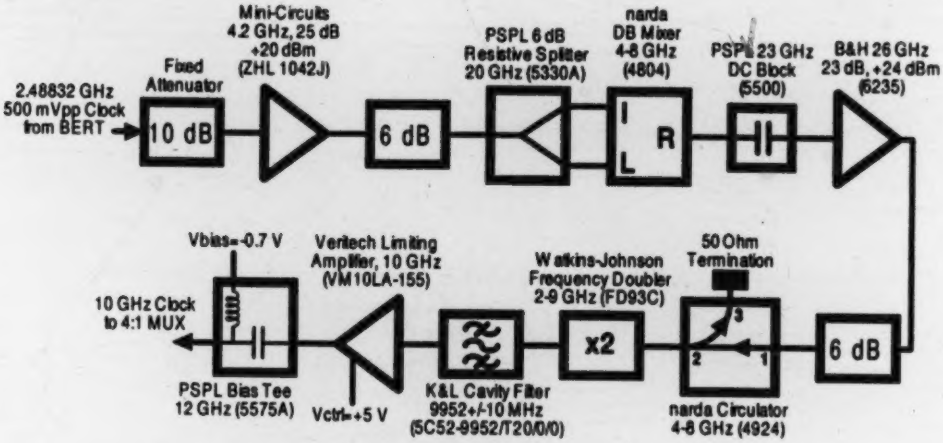
Mini-Circuits
4.2 GHz, 25 dB
+20 dBm
(ZHL 1042J)
Fixed
Attenuator
2.48832 GHz
500 mVpp Clock
from BERT
10 dB
6 dB
PSPL 6 dB
Resistive Splitter
20 GHz (5330A)
narda
DB Mixer
4-8 GHz
(4804)
I
L
R
PSPL 23 GHz
DC Block
(5500)
B&H 26 GHz
23 dB, +24 dBm
(5235)
Vbias=-0.7 V
Veritech Limiting
Amplifier, 10 GHz
(VM10LA-155)
Watkins-Johnson
Frequency Doubler
2-9 GHz (FD93C)
50 Ohm
Termination
10 GHz Clock
to 4:1 MUX
x2
3
2
1
6 dB
PSPL Bias Tee
12 GHz (5575A)
Vctrl=+5 V
K&L Cavity Filter
9952+/-10 MHz
(5C52-9952/T20/0/0)
narda Circulator
4-8 GHz (4924)

Figure 8.9 10 GHz clock generating circuit.

Then, the 5 GHz tone was amplified and input to another frequency doubler to obtain a synchronous 10 GHz tone. The circulator preceding the frequency doubler isolated the reflected energy from the output of the B&H amplifier. To remove spurious frequency components and provide a clean and stable tone, a cavity filter centered at 9.952 GHz was used at the output of the frequency doubler. A limiting amplifier was used to maintain a constant amplitude—the control voltage applied to the limiting amplifier allowed the output swing to be set at about 1 V_{pp}. Finally, a bias tee was used to DC bias the clock applied to the 4:1 MUX.

The experimental setup for the electrical receiver is shown in Figure 8.10, and the magnitude and phase response is shown in Figure 8.11.

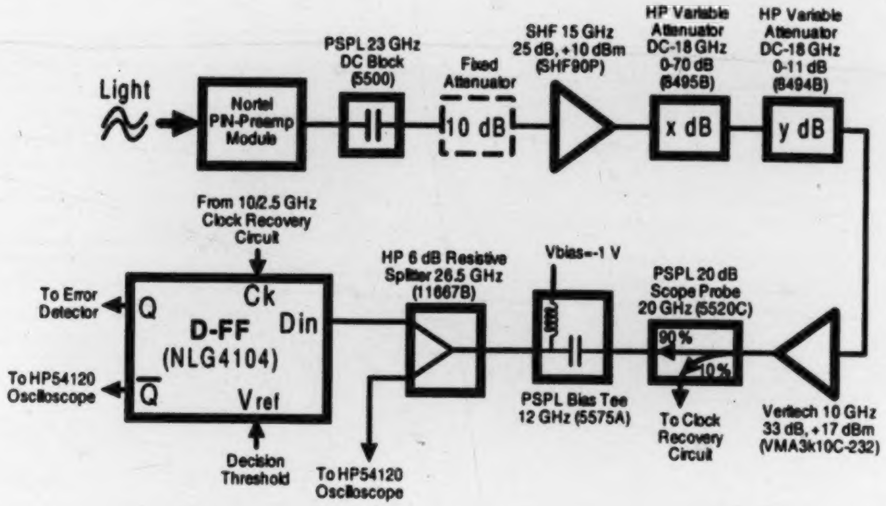
Light
Nortel PIN-Preamp Module
PSPL 23 GHz DC Block (5500)
Fixed Attenuator
10 dB
SHF 15 GHz 25 dB, +10 dBm (SHF90P)
HP Variable Attenuator DC-18 GHz 0-70 dB (8495B)
x dB
HP Variable Attenuator DC-18 GHz 0-11 dB (8494B)
y dB
From 10/2.5 GHz Clock Recovery Circuit
To Error Detector
To HP54120 Oscilloscope
Q
Ck
D-FF
Din
(NLG4104)
Q̄
Vref
Decision Threshold
To HP54120 Oscilloscope
HP 6 dB Resistive Splitter 26.5 GHz (11667B)
Vbias=-1 V
PSPL Bias Tee 12 GHz (5575A)
PSPL 20 dB Scope Probe 20 GHz (5520C)
90%
10%
To Clock Recovery Circuit
Veritech 10 GHz 33 dB, +17 dBm (VMA3k10C-232)

Figure 8.10 Eletrical receiver setup for 10 Gb/s binary experiments.

Note that the frequency response shown includes the small-signal response of the III-V MZ and PIN-Preamp module, as well as all other components at the receiver.

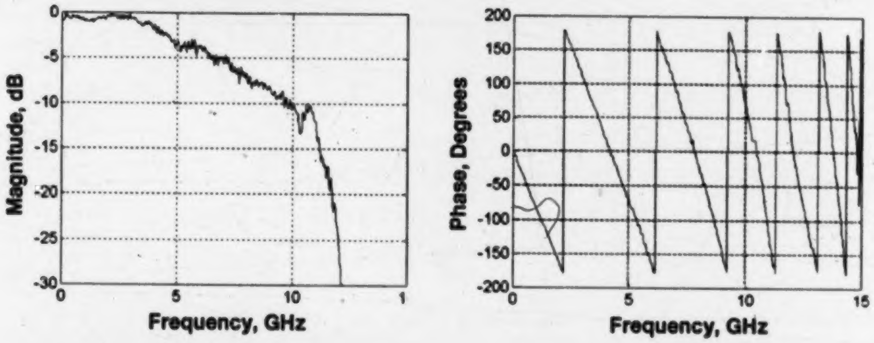

Figure 8.11 Magnitude (left) and phase (right) response of system for 10 Gb/s binary experiments.

Light output from the optical preamp was input to the Nortel PIN-preamp module. A DC blocking capacitor was used to remove the offset voltage present at the output of the PIN-preamp module. Depending on the amount of power incident on the photodetector, a 10 dB attenuator may have been placed at the output of the Nortel module to prevent saturating the following amplifier. An SHF 15 GHz amplifier and a Veritech 10 GHz amplifier were then used to further amplify the signal. Two HP variable attenuators preceded the last electrical amplifier to manually control the amplitude of the electrical signal input to the decision circuit (D-FF). One attenuator, which could be set in 10 dB increments, was used for coarse adjustments, and the other, which could be set in 1 dB increments, was used for fine adjustments. A bias tee was used to obtain the necessary negative offset for the signal applied to the GaAs D-FF, which served as a decision circuit. The HP splitter following the bias tee allowed the amplitude and quality of the received signal to be monitored. Because the BERT operated at 2.5 Gb/s, the signal input to the error detector had to be at this rate. Therefore, the D-FF was clocked at 2.5 GHz, thereby making decisions on every fourth bit of the 10 Gb/s signal at its input. The 2.5 GHz clock was obtained by extracting a small portion of the received signal with a 20 dB probe, as shown in Figure 8.10, and then providing this signal to the clock recovery circuit, which is shown in Figure 8.12. Recall from Chapter 2 that the PSD of an NRZ signal has a null at the bit rate; therefore, there is, ideally, no power at the signaling rate to be extracted and used as a clock. By introducing a nonlinearity, however, it is possible to transfer energy from lower frequencies to the signaling rate. To do this, energy centered about one-half the bit rate was extracted from the signal using an amplifier having a passband from 2 to 8 GHz. The signal was then input to a frequency doubler (nonlinearity) to introduce power at the signaling rate.

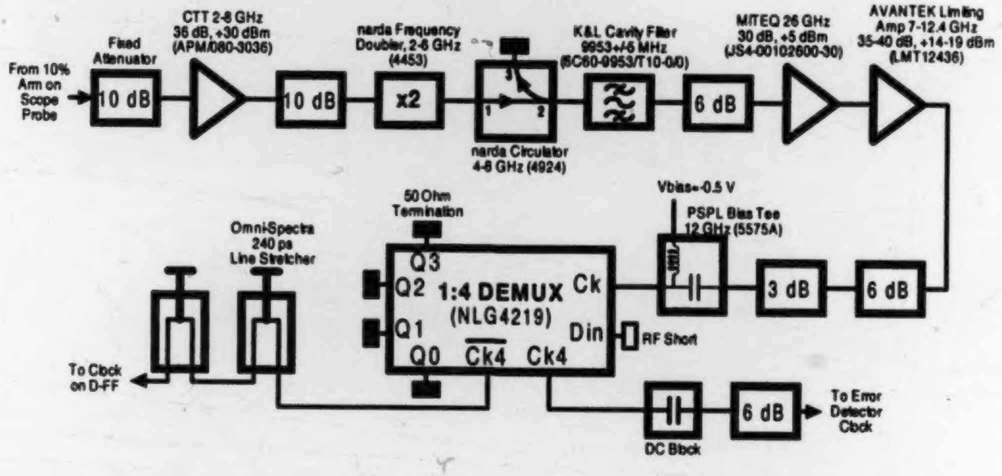
From 10% Arm on Scope Probe
Fixed Attenuator
10 dB
CTT 2-8 GHz 36 dB, +30 dBm (APM/080-3036)
10 dB
narda Frequency Doubler, 2-6 GHz (4453)
x2
narda Circulator 4-8 GHz (4924)
1
2
3
K&L Cavity Filter 9953+/-6 MHz (6C60-9953/T10-0/0)
6 dB
MITEQ 26 GHz 30 dB, +5 dBm (JS4-00102600-30)
AVANTEK Limiting Amp 7-12.4 GHz 35-40 dB, +14-19 dBm (LMT12436)
Vbias=-0.5 V
PSPL Bias Tee 12 GHz (5575A)
3 dB
6 dB
50 Ohm Termination
Q3
Q2
1:4 DEMUX
(NLG4219)
Q1
Q0
Ck4
Ck4
Ck
Din
RF Short
Omni-Spectra 240 ps Line Stretcher
To Clock on D-FF
DC Block
6 dB
To Error Detector Clock

Figure 8.12 Clock recovery circuit used in 10 Gb/s binary transmission experiments.

A cavity filter was then used to extract the desired tone at 9.95328 GHz (OC-192 rate), which was then amplified and input to a limiting amplifier to control the amplitude of the recovered clock. A 1:4 DEMUX was used as a divide-by-four circuit to obtain a 2.5 (2.48832) GHz clock signal that was synchronous with the recovered 10 GHz clock. The 2.5 GHz clock was then provided to the error detector and the decision circuit (D-FF). Finally, two 240 ps line stretchers were used in cascade so that the clock applied to the D-FF could be time shifted by ±240 ps. This allowed the

BER to be observed for all four tributary slot times within the 10 Gb/s multiplexed signal. In all cases, the worst BER observed was recorded as the 10 Gb/s BER in all results.

8.2.2 Experimental Results

Measured BER curves for transmission over 0, 75 and 125 km are shown in Figure 8.13. For comparison, simulated results using an acquired time record of the PRBS applied at the transmitter, and acquired frequency records of all system components, are also shown. At 0 km, a receiver sensitivity of about –17 dBm was obtained for a system without an optical preamp, and about –27 dBm for a system with an optical preamp. The simulated results are within 2 dB of experimental results at 0 km. For transmission over 125 km, the experimental BER curve appears to bend toward a BER floor, which is expected because of PM-to-AM RIN. However, the error floor appears to be lower than that predicted by the simulation result. Figure 8.14 shows simulated and experimental eye diagrams at 0 km and 125 km of the filtered received signal applied to the decision circuit.

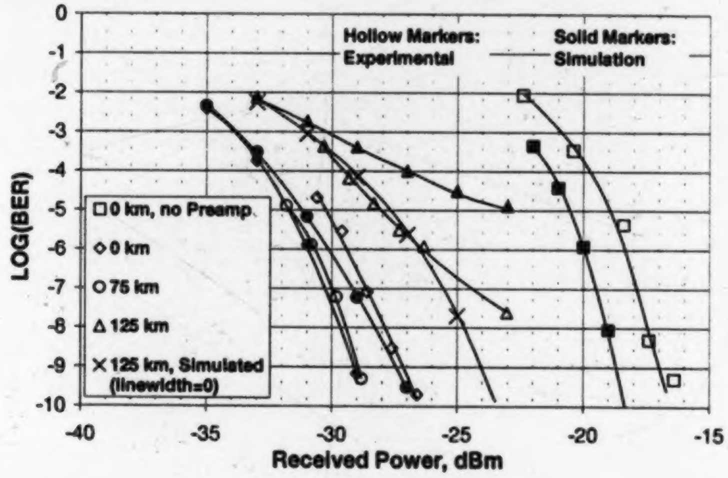

Figure 8.13 Experimental and simulated BER curves for 10 Gb/s binary transmission experiments.

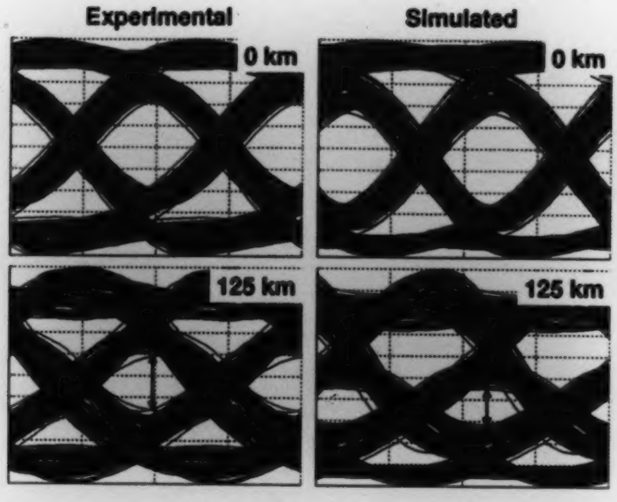

Figure 8.14 Simulated and experimental eye diagrams for 10 Gb/s binary transmissions.

The simulated eye is more closed at 125 km, possibly due to SPM and/or an inaccuracy in modeling the chirp imparted by the III-V MZ. Regardless, because of a more closed eye, it is expected that the simulated BER curve at 125 km would indicate a BER floor that is higher than for the experimental case.

In obtaining experimental eye diagrams, a technique was employed that allows more detail to be observed in the acquired eye than is usually possible. Normally, an eye diagram is viewed on a digital oscilloscope set to persistence mode. In this mode, the scope is triggered every few clock cycles in which a single sample of the signal is obtained and shown as a pixel on the display. The persistence setting determines how long the pixel sample remains on the display. After many samples are taken, an eye diagram results. An advantage of this method is that an eye diagram can be generated quickly, usually in 1 to 5 seconds. Unfortunately, each sample also contains the noise present in the signal and, if the signal-to-noise ratio is not sufficiently high, it can be difficult to tell whether a sampled pixel within an eye is due to noise, or to a deviant trace that passes through the eye. To reduce the amount of noise, the oscilloscope can be put into an averaging mode where each displayed pixel is the result of averaging many samples taken at some instant in time relative to the trigger. For a meaningful signal to result, however, the scope must be triggered at the same point in the PRBS. Therefore, the result shown on the oscilloscope's display is a trace showing a portion of the PRBS, not an eye diagram. To obtain an eye diagram, it is necessary to acquire the entire time-averaged PRBS and then superimpose multiple traces, each shifted by an integer number of bit periods. The advantage to generating an eye diagram in this way is that individual traces become clearly visible within the eye, even when the original signal is excessively noisy. This gives a clear picture of the system's response and any ISI that is present.

Because the maximum number of samples (time intervals) that can be acquired in a given acquisition event is 1024 for the HP54120 oscilloscope, it was necessary to acquire portions (sub-records) of the PRBS and then concatenate them to build up the entire time record to be used in constructing a time-averaged eye diagram. For example, assuming each symbol must be represented by at least 16 samples, a maximum of 64 symbols in the PRBS could be recorded in a given acquisition event. Therefore, for a PRBS with, say, 512 symbols, 8 acquisition events would be needed to construct the entire PRBS. At a given signaling rate, the time required to acquire each sub-record depends on the number of samples recorded and the number of times each sample is averaged. Therefore, the time elapsed between the acquisition of the first sub-record and the last could be several minutes. This elapsed time becomes a problem if the trigger source and the PRBS do not precisely maintain their timing relationship with respect to one another over the acquisition time of all sub-records. In an optical back-to-back configuration, it was found that the timing relationship between the trigger output from the pattern generator and the received PRBS was maintained over several minutes; hence, it was possible to acquire the entire PRBS with the effects of noise averaged out. For transmission over tens of km or more, however, the received PRBS exhibited a significant temporal drift because of changes in the transit time through the fiber, due to random fluctuations in ambient conditions. To circumvent this problem, an attempt was made to extract the lowest non-DC frequency component in the received signal, which is equal to the PRBS pattern rate, and use it to trigger the oscilloscope. Although there was no difficulty in obtaining the desired tone, it was not possible to obtain a trigger pulse with a rising edge that was clean enough to be useful. Note that the rising edge of the trigger pulse must be well defined within a window of a few ps, which is a very small fraction of the tone's period. An alternative method was, therefore, used in which the temporal drift was corrected in software. In this method, the PRBS is recorded over one PRBS period, plus a few extra bits. Then, a window, W_2, containing a few symbols from the end of the acquired PRBS is compared to an equal-length window, W_1, positioned exactly one PRBS period earlier in the acquired time record. If no temporal drift is present, then the records in the windows, W_1 and W_2, would be the same. If there is temporal drift in the acquired time record, however, then these windows will contain records that are different. The procedure, then, is to shift the record in W_1 in increments or decrements of one sample, and then compare it to W_2. The number of shifted samples that produces the best agreement between W_1 and W_2 is then used as an estimate to the amount of temporal drift present in the time record. A square-error calculation was used to determine how well correlated W_2 and W_1 were, as shown in Figure 8.15.

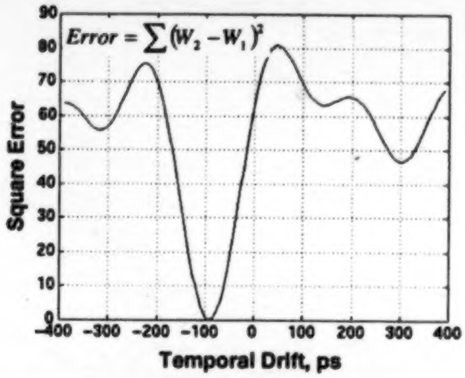

Figure 8.15 Plot of square error calculation versus temporal drift.

The result in Figure 8.15 is for a 10 Gb/s binary signal after transmission over 50 km, which shows a temporal drift of about 90 ps, or about one symbol period. Assuming that the drift occurs at a constant rate over the acquisition of all sub-records, it is possible to interpolate between samples in the original time record to construct a new time record with the temporal drift removed. Figure 8.16 shows the resulting eye diagrams corresponding to the drift in Figure 8.15.

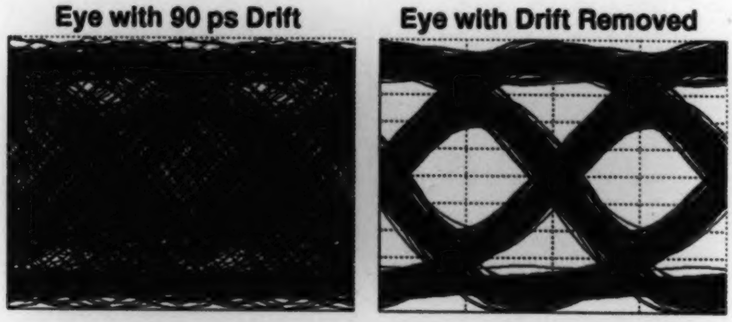

Figure 8.16 10 Gb/s binary eye diagrams before and after correction for temporal drift.

If the drift does not occur uniformly over the entire acquisition time, then the above method will not work. However, it was found that, even for the longest distances of 225 km considered here, the assumption that the drift is uniform was valid in all cases but one. This suggests that fluctuations in the temporal response of the fiber's optical path length are rather slow, occurring over many minutes. For even longer distances, however, or for longer acquisition times, the assumption of uniform drift may become invalid. One way to correct for a non-uniform drift might be to acquire each sub-record twice. Then, these could be compared to one another, as described above, to obtain a curve fit to the time-varying drift.

8.3 10 Gb/s 4-Level ASK Transmission Experiments

Two sets of experiments were carried out for a 4-ary ASK system operating at 10 Gb/s: one using a Nortel III-V MZ module, and another using a dual-arm $LiNbO_3$ MZ obtained from Lucent Technologies. The laser built into the III-V MZ module operated at 1557 nm, where the gain of the EDFAs was quite low, and had a measured linewidth of about 35 MHz. For experiments using the $LiNbO_3$ MZ, a laser operating at 1533 nm was used, where the gain of the EDFAs was much higher, and had a measured linewidth of about 4 MHz. Appendix C shows gain curves for the EDFAs operating at these two wavelengths, as well as the measured linewidths for these lasers.

8.3.1 Experimental Setup

Optical inline amplifiers were used for experiments over distances greater than 100 km. To determine viable spacings for inline amplifiers, the ratio of signal power to ASE power incident on the photodetector was calculated using measured parameters for the amplifiers at the operating wavelength. For example, for transmission over 225 km using the $LiNbO_3$ MZ with a 1533 nm source, amplifiers were spaced every 75 km, as shown in Figure 8.17.

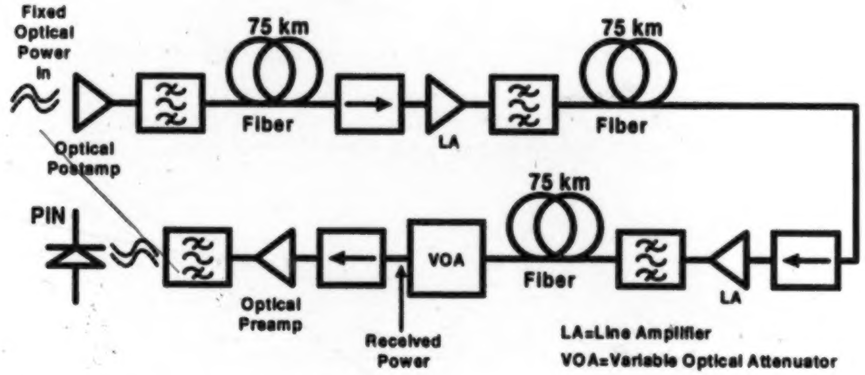

Figure 8.17 Optical link used for 10 Gb/s 4-ary transmission experiments over 225 km.

The average power input to the optical postamp was about -6 dBm for the setup in Figure 8.17, and Figure 8.18 shows the ratio of signal power to ASE power, the operating gain, and the signal power at the output of each amplifier stage.

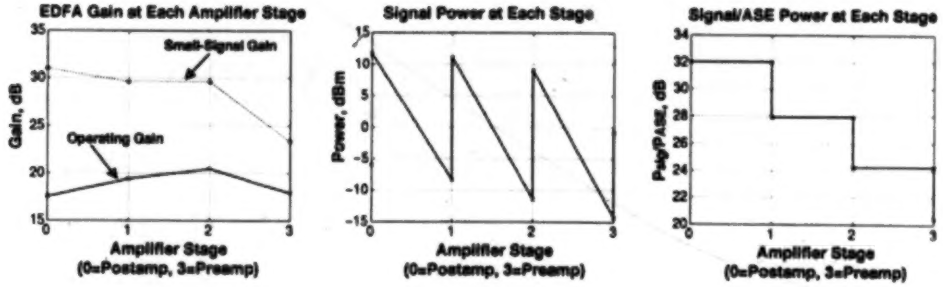

Figure 8.18 EDFA operating conditions for transmission over 225 km: (left) small-signal gain and operating gain of each amplifier; (middle) optical power output from each amplifier; (right) ratio of signal power to ASE power at the output of each amplifier.

Figure 8.19 shows the electrical transmitter used in 4-ary ASK experiments.

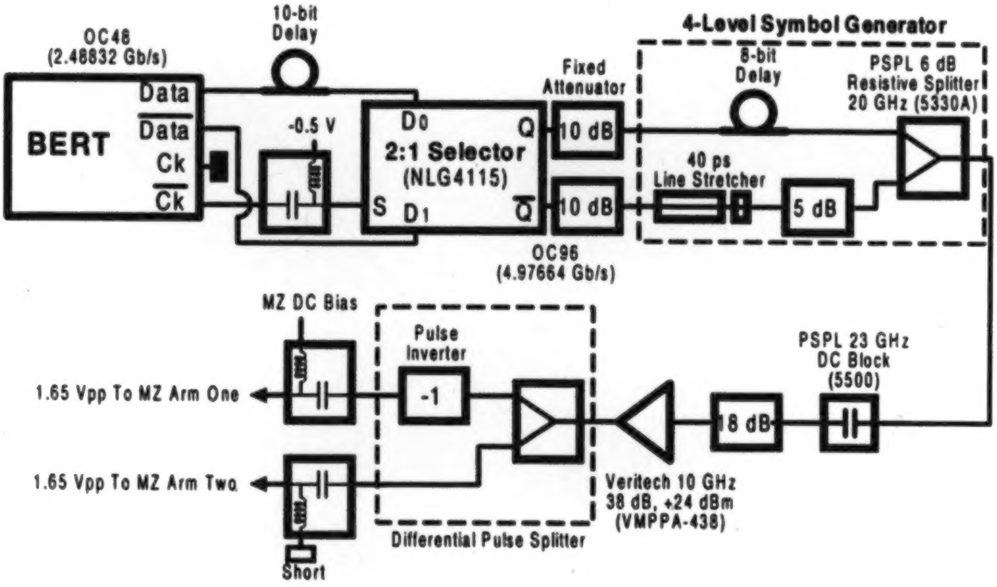
OC48
(2.48832 Gb/s)
BERT
Data
Data
Ck
Ck
10-bit
Delay
-0.5 V
D0
2:1 Selector
(NLG4115)
S
D1
Q
Q
Fixed
Attenuator
10 dB
10 dB
OC96
(4.97664 Gb/s)
4-Level Symbol Generator
8-bit
Delay
40 ps
Line Stretcher
5 dB
PSPL 6 dB
Resistive Splitter
20 GHz (5330A)
PSPL 23 GHz
DC Block
(5500)
8 dB
Veritech 10 GHz
38 dB, +24 dBm
(VMPPA-438)
Pulse
Inverter
-1
Differential Pulse Splitter
MZ DC Bias
1.65 Vpp To MZ Arm One
1.65 Vpp To MZ Arm Two
Short

Figure 8.19 Electrical transmitter for 10 Gb/s 4-ary ASK experiments.

To obtain a 5 Gb/s binary data source, a 2:1 selector was used to time-division multiplex the 2.5 Gb/s data and its complement output from the BERT. One of the tributaries output from the BERT was delayed by an integer number of bit periods to simulate two independent 2.5 Gb/s signals. The 2:1 selector was driven by the 2.5 GHz clock provided by the BERT: when the clock was high, input D_0 appeared at the output, and when the clock was low, input D_1 appeared at the output. Note that the 2:1 selector also provided the complement of the output time-division multiplexed signal at 5 Gb/s. The 4-ary ASK electrical signal was obtained by weighting the outputs from the 2:1 selector and summing the result, as shown by the 4-level symbol generator in Figure 8.19. One of the arms in the 4-ary symbol generator was delayed by an integer number of bit periods to simulate two independent 5 Gb/s binary tributaries, and a line stretcher was used to precisely align the binary signals input to the power combiner (resistive splitter). Because the power combiner provided an isolation of only 6 dB between its input ports, 10 dB pads (fixed attenuators) were placed at the outputs of the 2:1 selector to ensure that they were adequately isolated. The 4-ary electrical signal was then amplified and input to a differential pulse splitter to obtain the signals necessary to drive the MZ in a push-pull mode. Finally, a bias tee was used to set the bias point on the MZ's transfer characteristic.

The setup in Figure 8.19 was used with the $LiNbO_3$ MZ device. For experiments using the III-V MZ, a 26 GHz B&H amplifier was used in place of the Veritech amplifier, and fixed attenuators were placed in each arm of the differential pulse splitter to obtain the desired asymmetric drive for the III-V MZ. Also, a 6 dB pad, rather than a 5 dB pad, was used in the 4-ary symbol generator, and the bias tees were not used because the DC bias was applied to pins located on the III-V module. For experiments using the $LiNbO_3$ MZ, the signals applied to each arm of the MZ had equal amplitudes of 1.65 Vpp. For experiments using the III-V MZ, the signals applied to the left and right arm of the MZ had amplitudes of 2.0 Vpp and 0.75 Vpp, respectively, and DC biases of -2.6 V and -4.5 V, respectively.

Figure 8.20 shows the setup for the electrical receiver used in 4-ary ASK experiments. The operation of this receiver is the same as that used in binary experiments. Because of the reduced bandwidth requirement of the 4-ary ASK signal over the binary signal, a 5.8 GHz LPF was placed at the output of the receiver to limit the amount of noise and provide pulse shaping. The setup in Figure 8.20 was used in experiments that employed the $LiNbO_3$ MZ device. For experiments using the III-V device, a 10 GHz Veritech amplifier (VMPPA-438) was used in place of the B&H amplifier.
Figure 8.21 shows the magnitude and phase response for the setup that used the Nortel III-V module, and for the setup that used the $LiNbO_3$ MZ. Note that the frequency response shown includes the small-signal response of the external modulator and photodetector, as well as all other components at the receiver. Swapping the B&H and Veritech amplifiers between the transmitter and receiver for the two sets of 4-ary ASK experiments was done because it was determined after the first set of experiments that the Veritech amplifier tended to limit the signal when the signal was quite noisy, making measurements at higher BERs difficult.

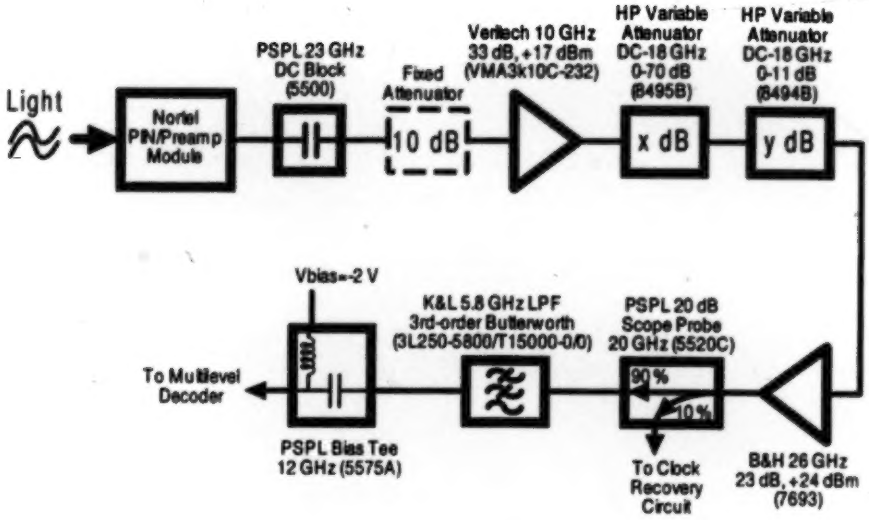
Light
Nortel PIN/Preamp Module
PSPL 23 GHz DC Block (5500)
Fixed Attenuator
10 dB
Vertech 10 GHz 33 dB, +17 dBm (VMA3k10C-232)
HP Variable Attenuator DC-18 GHz 0-70 dB (8495B)
x dB
HP Variable Attenuator DC-18 GHz 0-11 dB (8494B)
y dB
B&H 26 GHz 23 dB, +24 dBm (7693)
PSPL 20 dB Scope Probe 20 GHz (5520C)
90 %
10 %
To Clock Recovery Circuit
K&L 5.8 GHz LPF 3rd-order Butterworth (3L250-5800/T15000-0/0)
Vbias=-2 V
PSPL Bias Tee 12 GHz (5575A)
To Multilevel Decoder

Figure 8.20 Electrical receiver used in 10 Gb/s 4-ary ASK experiments.

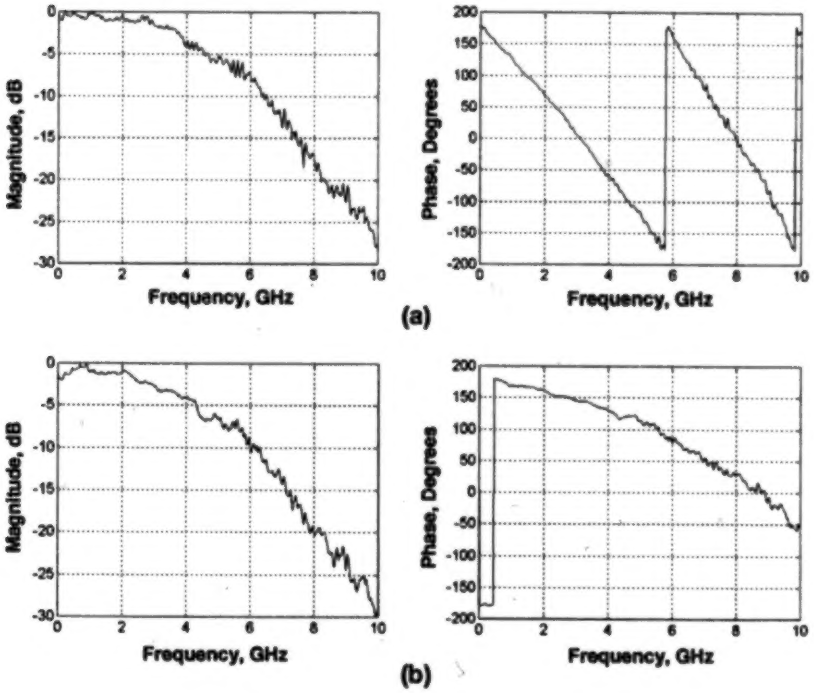

Figure 8.21 System frequency response for 10 Gb/s 4-ary ASK experiments: (a) frequency response using the Nortel III-V MZ module; (b) frequency response using the Lucent $LiNbO_3$ MZ.

A DC bias of –2 V was applied to the signal prior to the multilevel decoder. Also, the peak-to-peak amplitude of the signal applied to the decoder was nominally 4 V. After the 12 dB insertion loss of the 4-way splitter in the decoder, a 4-ary ASK signal with a -0.5 V DC offset and a peak-to-peak amplitude of 1 V was provided to the input of each decision circuit. Figure 8.22 shows the multilevel decoder used to recover the binary tributaries.

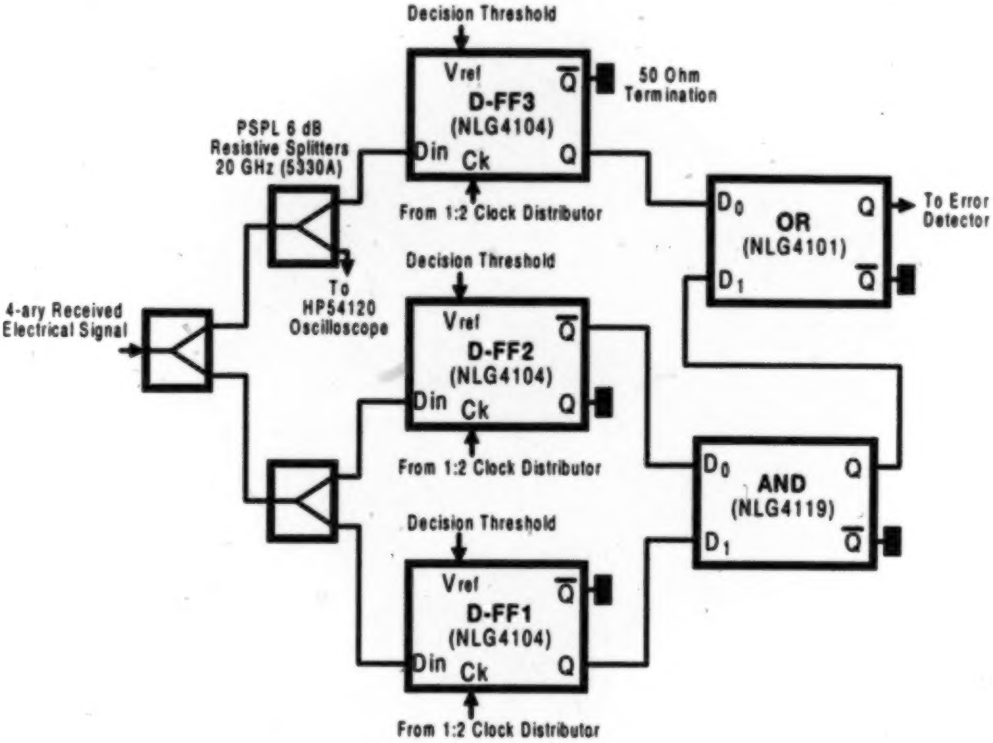
Decision Threshold
Vref
D-FF3
(NLG4104)
Din
Ck
Q
$\overline{Q}$
50 Ohm Termination
PSPL 6 dB Resistive Splitters 20 GHz (5330A)
From 1:2 Clock Distributor
To HP54120 Oscilloscope
4-ary Received Electrical Signal
Decision Threshold
Vref
D-FF2
(NLG4104)
Din
Ck
Q
$\overline{Q}$
From 1:2 Clock Distributor
Decision Threshold
Vref
D-FF1
(NLG4104)
Din
Ck
Q
$\overline{Q}$
From 1:2 Clock Distributor
D_0
OR
(NLG4101)
D_1
Q
$\overline{Q}$
To Error Detector
D_0
AND
(NLG4119)
D_1
Q
$\overline{Q}$

Figure 8.22 Multilevel decoder used in 10 Gb/s 4-ary ASK experiments.

In constructing the multilevel decoder, the propagation time through each logic device was carefully measured, and pieces of semirigid coaxial cable were cut to precise lengths to ensure proper timing of the signals. For example, the cable connecting output Q on D-FF3 to input D_0 on the OR gate had to introduce a precise delay to account for the propagation time through the AND gate. One of the outputs in the 1:4 splitter was used to monitor the amplitude of the signal applied to the decision circuits, as well as the quality of the eye.

A small portion of the received electrical signal was extracted using a 20 dB scope probe and input to the clock recovery circuit shown in Figure 8.23.

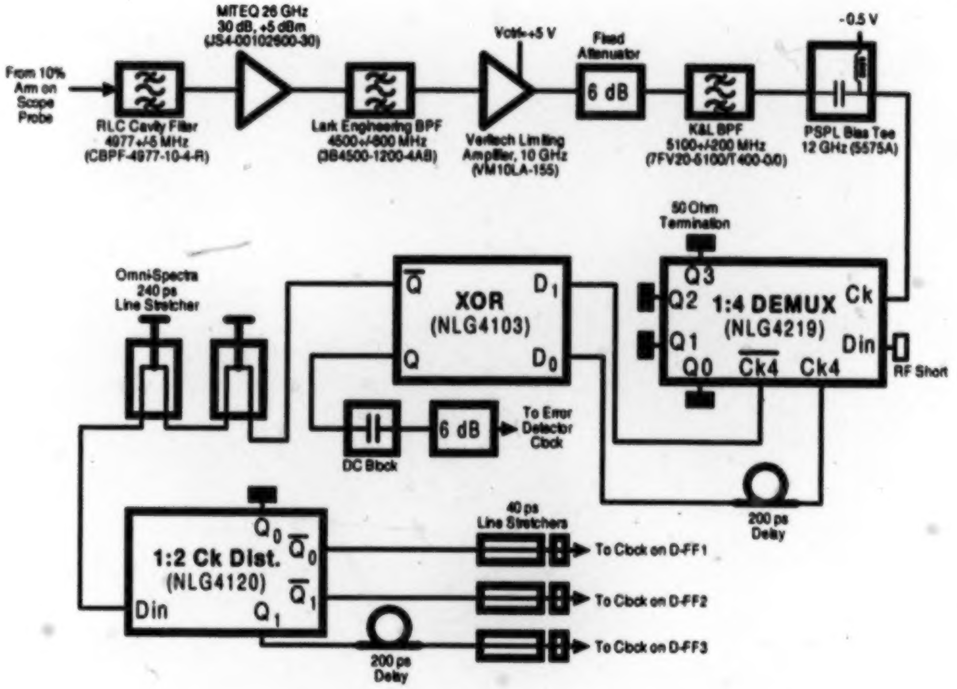

MITEQ 26 GHz
30 dB, +5 dBm
(JS4-00102600-30)
Vctl=+5 V
Fixed Attenuator
-0.5 V
From 10% Arm on Scope Probe
6 dB
RLC Cavity Filter
4977+/-5 MHz
(CBPF-4977-10-4-R)
Lark Engineering BPF
4500+/-600 MHz
(3B4500-1200-4AB)
Vertech Limiting Amplifier, 10 GHz
(VM10LA-155)
K&L BPF
5100+/-200 MHz
(7FV20-5100/T400-0/0)
PSPL Bias Tee
12 GHz (5575A)
50 Ohm Termination
Omni-Spectra 240 ps Line Stretcher
$\overline{Q}$
XOR
(NLG4103)
D_1
Q
D_0
Q3
Q2
1:4 DEMUX
(NLG4219)
Ck
Q1
Din
Q0
$\overline{Ck4}$
Ck4
RF Short
6 dB
To Error Detector Clock
DC Block
200 ps Delay
40 ps Line Stretchers
Q_0
$\overline{Q}_0$
1:2 Ck Dist.
(NLG4120)
$\overline{Q}_1$
Din
Q_1
To Clock on D-FF1
To Clock on D-FF2
To Clock on D-FF3
200 ps Delay

Figure 8.23 Clock recovery circuit used in 10 Gb/s 4-ary ASK experiments.

At first, the intention was to extract a tone at 2.5 GHz from the received electrical signal and use it to clock the D-FFs, thereby making decisions on every second M-ary symbol (Recall that the error detector operates at 2.5 GHz). It was found, however, that the amount of power at this frequency was very low, more than a factor of ten lower than the power at 5 GHz, and it was not possible to extract a usable tone. This may seem to contradict an earlier statement where it was said that the power at the symbol rate of an NRZ signal is ideally zero. It should be noted, however, that the signal is not an ideal NRZ signal because: 1) the binary signal output from the GaAs logic devices, used in constructing the 4-ary electrical signal at the transmitter, contains power at the bit rate, i.e., it is not, strictly speaking, equivalent to an ideal NRZ signal passed through a LPF, and 2) a nonlinearity is introduced by the MZ's transfer characteristic, and by the square-law detection process after transmission over a non-zero fiber length. Figure 8.24 shows the PSD of the filtered received signal at 0 km for a 4-ary ASK signal. Note that, because the signal is periodic, the PSD actually consists of line spectra.

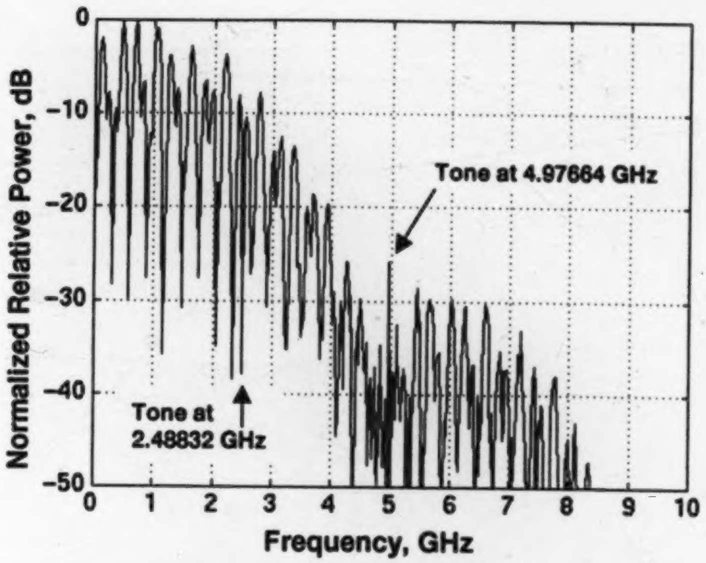

Figure 8.24 PSD of electrical 4-ary ASK signal at the receiver.

For non-zero distances the amount of power at 4.97664 GHz depends on the distance; however, for all distances considered it was always significantly larger than the power at 2.48832 GHz. In fact, over certain distances, there can be a substantial amount of power at the symbol rate because of the nonlinearity introduced by fiber dispersion followed by square-law detection. Therefore, for many link lengths, it is not necessary to introduce a nonlinearity, as was described for the binary experiments, in a clock recovery circuit.

The clock recovery circuit in Figure 8.23 operated as follows. First, the frequency component at 4.97664 GHz (i.e., the symbol rate) was extracted using a high-Q cavity filter. The tone was then amplified and input to a limiting amplifier to control the amplitude of the clock signal. A BPF was placed at the output of the first amplifier stage to remove out-of-band noise from the amplifier and, therefore, reduce the amount of jitter. It was found that placing a BPF at the output of the limiting amplifier provided further improvement in the quality of the recovered tone. A 1:4 DEMUX was then used as a divide-by four circuit to obtain a clock at 1.24416 GHz (OC-24 rate). Then, an exclusive OR (XOR) gate was used as a frequency doubler to obtain a clock signal at 2.48832 GHz. Note that the frequency doubling was accomplished by providing the 1.24416 GHz clock and its complement output from the 1:4 DEMUX to the input of the XOR gate, but with one signal delayed by 200 ps (i.e., one-quarter clock period). One of the XOR outputs was used to clock the error detector, and the other was used to drive a 1:2 clock distributor. Finally, the outputs of the clock distributor were used to clock the three D-FFs used as decision circuits in the multilevel decoder. Note that the decision time for each D-FF could be independently adjusted using the 40 ps linestretchers shown in Figure 8.23. A delay of 200 ps (one-half clock period) was inserted at one output of the clock distributor to phase match the signal with the complemented outputs. Because the received multilevel signal was at a 5 GHz symbol rate, decisions were made on every second symbol to obtain a 2.5 Gb/s signal at the output of the multilevel decoder, which was the required data rate for the error detector on the BERT. Two 240 ps linestretchers were used in cascade to provide up to ±240 ps of delay to the clock signal, which allowed decisions to be made on either multilevel sub-sequence. In all cases, the worst BER was recorded as the BER for the 10 Gb/s 4-ary ASK signal. Note, too, that one of the binary tributaries is recovered by decisions using D-FF2 only, whereas the other tributary requires decisions by all three decision circuits, as described in Chapter 1. Only the tributary requiring decisions by all three decision circuits was considered because it always gives the worst BER.

8.3.2 Experimental Results

BER versus received optical power is shown in Figure 8.25 for 4-ary ASK transmission experiments using the Nortel III-V MZ module.

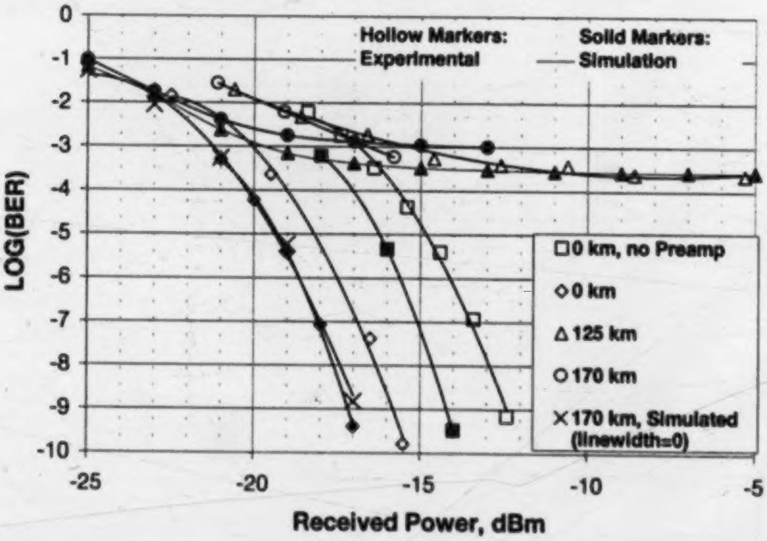

Figure 8.25 BER versus received optical power for 4-ary experiments using the Nortel III-V MZ module.

Measured receiver sensitivities at 0 km were -15.8 dBm and -12.5 dBm, respectively, for a system with and without optical preamplification. Simulated results predict a sensitivity to within about 1.5 dB of experimental results at 0 km. The improvement offered by optical preamplification in Figure 8.25 is only marginal because the gain of the EDFA preamp was only 8.4 dB, with a 0.6 dB input insertion loss and a 3.8 dB output insertion loss. Two EDFAs were used in cascade as an optical postamp, which provided a launched average power of +8.2 dBm, and an inline amplifier was placed at 100 km for experiments at 125 km and 170 km. To obtain higher gain for the inline amplifier at the 1557 nm operating wavelength, a circulator and reflecting loop mirror were used, as shown in Figure 8.26. This allowed the signal to experience two passes through the EDFA to obtain a larger gain. The BPF prevented reflected ASE from saturating the gain of the EDFA. Using the scheme in Figure 8.26 it was possible to increase the gain of the EDFA from 11.5 dB (single pass) to 17.6 dB (double pass).

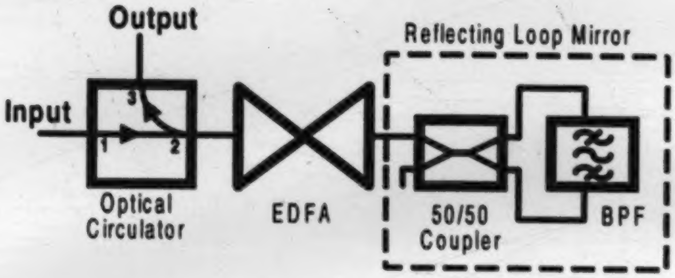

Figure 8.26 EDFA using a reflecting loop mirror to obtain a double-pass gain.

BER floors are clearly present in Figure 8.25 when transmitting over 125 km and 170 km. A simulated result is also shown at 170 km for a laser with a zero linewidth (ideal), which indicates that BER=10^{-9} should have been possible in the absence of PM-to-AM RIN.

Experiments were also conducted using the III-V module over distances of 0, 50, 75 and 100 km using two EDFAs in cascade as an optical preamp, which provided a small-signal gain of 17.8 dB and an output saturation power of +10 dBm. Figure 8.27 shows BER versus received optical power for these experiments.

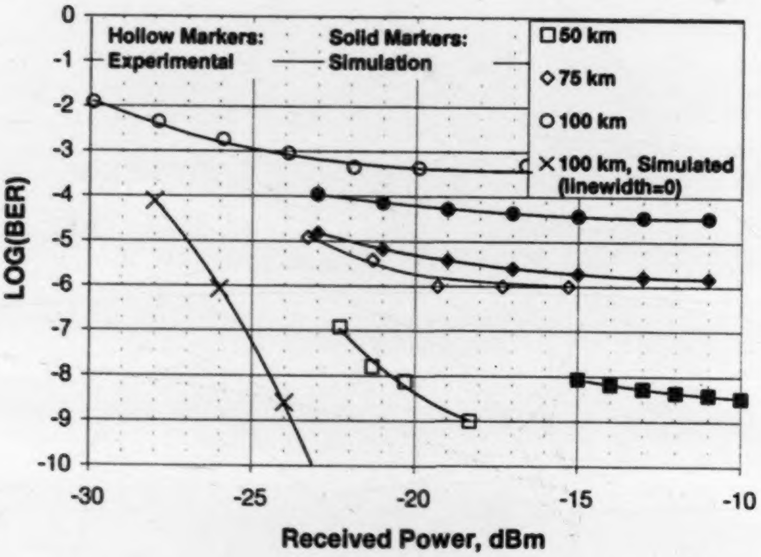

Figure 8.27 BER versus received optical power for 4-ary experiments using the Nortel III-V MZ module, and two EDFAs in cascade as an optical preamp.

At 50 km it was possible to obtain BER=10^{-9} for a received power of -18.3 dBm. Although there appears to be a bending of the experimental BER curve toward an error floor at 50 km, the error floor is lower than the ~10^{-9} BER floor predicted by simulation. At 75 km, both the simulated and experimental error floors are at about BER=10^{-6}. At 100 km the experimental BER curve exhibits an error floor between 10^{-3} and 10^{-4}, whereas the simulation result predicts an error floor between 10^{-4} and 10^{-5}. Also shown in Figure 8.27 is a simulated BER curve at 100 km is in the absence of PM-to-AM RIN, i.e., a source linewidth of zero was assumed.

It was mentioned that when the signal-to-noise ratio is not sufficiently high, it can be difficult to obtain detailed information about ISI from an eye diagram. For example, Figure 8.28 shows an experimental eye diagram at 170 km obtained directly from the display of the HP54120 oscilloscope. Also shown in Figure 8.28 is a simulated eye diagram in the presence of noise, which was generated using the detailed noise model in FOCSS. These eye diagrams appear to have about the same amount of noise, which is highly signal dependent and gives rise to a BER floor between 10^{-3} and 10^{-4}, as shown in Figure 8.25. From the eye diagrams in Figure 8.28, it is difficult to determine detailed information about the system's response and the amount of ISI present.

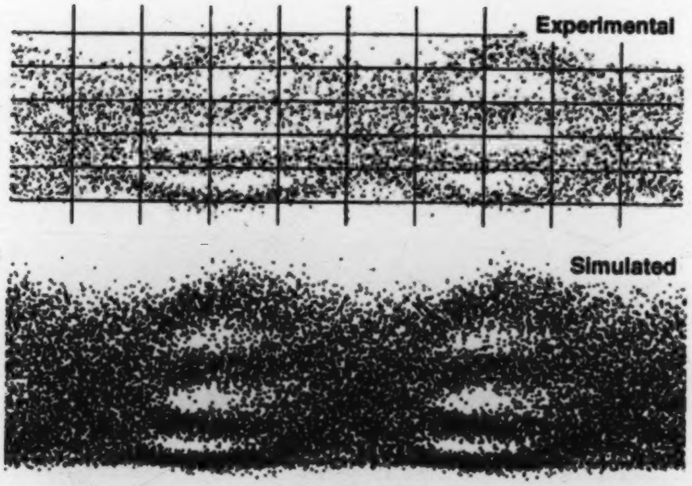

Figure 8.28 Experimental and simulated eye diagrams for a 4-ary ASK signal transmitted over 170 km.

However, using the time-averaged eye diagram approach discussed for binary signals, much more detail can be observed, as shown in Figure 8.29. The time-averaged experimental eye diagram at 170 km in Figure 8.29 should be contrasted with that in Figure 8.28.

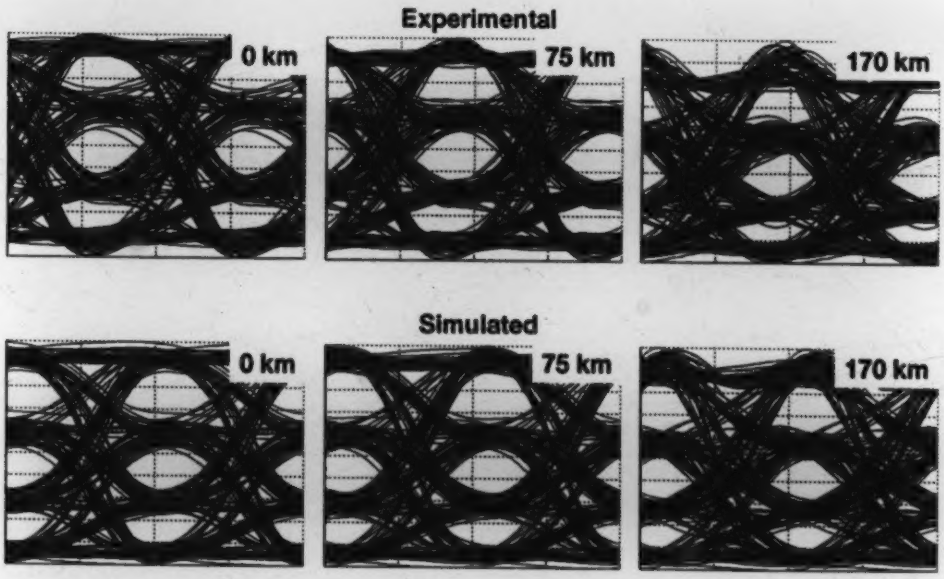

Figure 8.29 Experimental and simulted eye diagrams for 10 Gb/s 4-ary ASK experiments using the Nortel III-V MZ module.

Experiments were also performed for 4-ary ASK transmission at 10 Gb/s using a $LiNbO_3$ MZ external modulator and a 1533 nm laser source having a linewidth of ~4 MHz. Experimental and simulated results for BER versus received optical power are shown in Figure 8.30. The optical preamp used for the results in Figure 8.30 had a small-signal gain of 23.3 dB, a spontaneous emission factor of 2.1, and an output saturation power of +2.0 dBm.

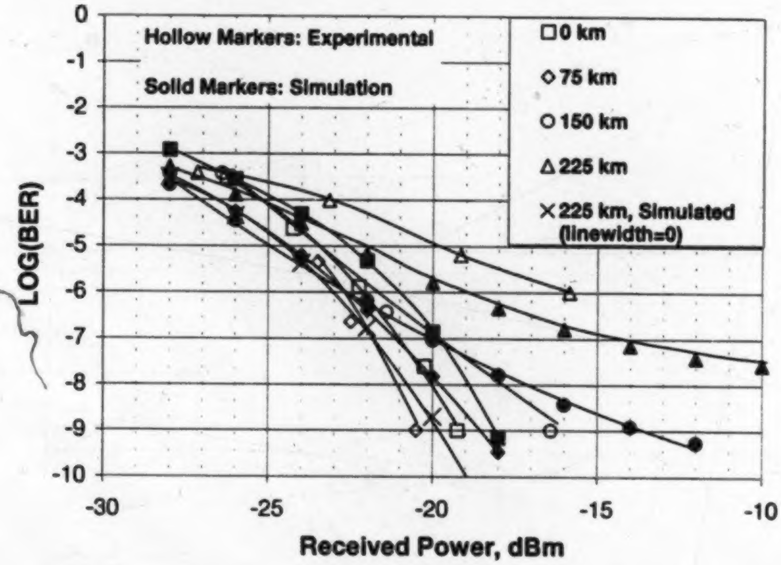

Figure 8.30 BER versus received optical power for experiments using a dual-drive $LiNbO_3$ MZ and a narrow-linewidth laser.

Here, BER=10^{-9} was possible for distances up to 150 km, although the BER curve shows signs of bending toward a BER floor. For transmission over 225 km it was not possible to obtain BER=10^{-9} with the available power, and the BER curve shows clear signs of bending toward a BER floor. Simulation results predict the BER floor to be at about BER=10^{-8} when transmitting over 225 km. A simulated result is also shown for transmission over 225 km using a zero-linewidth source. Note that the experiments at 0 and 75 km used an optical postamp and an optical preamp, but did not use inline amplifiers. The transmission experiment over 150 km used an inline amplifier at 75 km, and the experiment over 225 km used inline amplifiers at 75 km and 150 km where, as shown in Figure 8.18, the launched optical power was +11.7 dBm.

Figure 8.31 shows experimental and simulated eye diagrams for experiments using the $LiNbO_3$ MZ device.

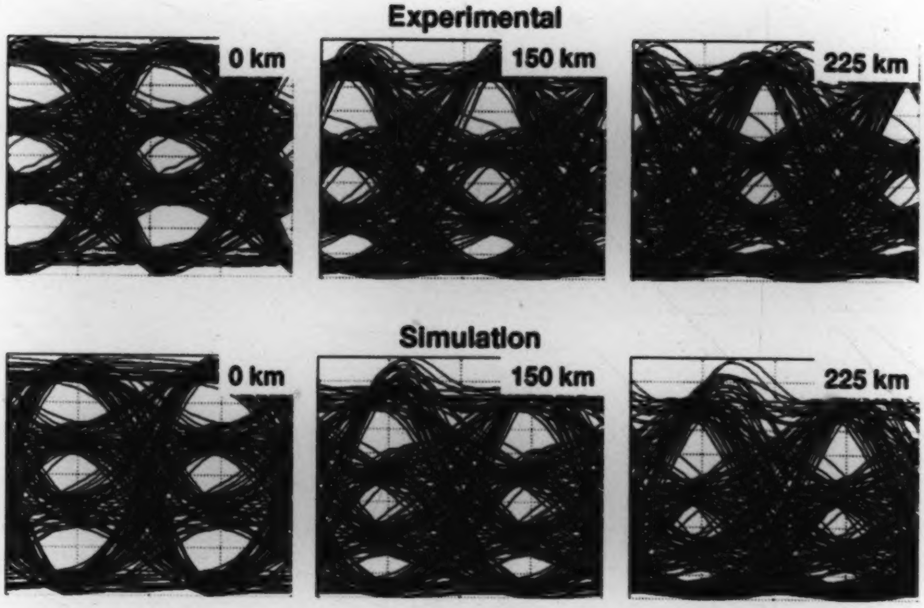

Figure 8.31 Experimental and simulted eye diagrams for 10 Gb/s 4-ary ASK experiments using the Lucent LiNbO$_3$ MZ modulator.

It should be mentioned that all eye diagrams presented are for the filtered received electrical signal passed to the multilevel decoder. Also, because an inverting amplifier was present in all receiver structures, all eye diagrams were inverted (signal multiplied by −1) for the purpose of illustration.

8.4 Summary

This chapter presented results for 10 Gb/s transmission experiments using binary and 4-ary ASK signaling. Experimental results for noise measurements were also presented, which clearly showed the presence of RIN from PM-to-AM noise conversion. These noise measurements also clearly demonstrated the validity of the adopted noise model. Details were provided on the setups used in all experiments, and a method was explained for obtaining eye diagrams in which noise is essentially removed, thereby providing much more information about the system's response. Simulation results using acquired data for all system components were also presented and compared to experimental results.

9 Summary and Conclusions

This research investigated the potential of M-ary ASK, polybinary, polyquaternary, and AM-PSK polybinary signaling schemes for increasing the capacity of digital, lightwave systems. The premise for exploring these signal types was that, because spectral components closer to the optical carrier experience a lower phase distortion than those components farther away, a dispersion improvement may be offered for signals in which the spectrum is more concentrated about the optical carrier. All signaling methods were investigated through theoretical considerations and computer simulation, and an extensive simulator called FOCSS was constructed to perform a multitude of analyses on all signaling schemes explored. The experimental component of this research focussed on M-ary ASK, where the complete design, construction and testing of a 4-ary ASK lightwave system operating at 10 Gb/s was carried out.

A brief overview of the evolution of fiber-optic communication systems was given in Chapter 1. It was explained that the advent of EDFAs and the low loss of standard singlemode fiber at ~1550 nm has generated much interest in transmission at this wavelength. Unfortunately, chromatic dispersion becomes a major limitation as the bit rate or distance is increased. Furthermore, for bit rates of many Gb/s the speed or frequency response of electrical components becomes a limitation. Therefore, much effort has been directed at methods for combating chromatic dispersion and/or overcoming the bottleneck imposed by electronics. Many methods for increasing the capacity of a lightwave system were described in Chapter 1 including Optical Time-Division Multiplexing (OTDM), Wavelength-Division Multiplexing (WDM), Optical Phase Conjugation (OPC), Dispersion-Supported Transmission (DST), Dispersion Compensating Fiber (DCF), fiber Bragg gratings, pre-chirping, soliton transmission, partial-response signaling and M-ary ASK signaling. These should not necessarily all be viewed as competing technologies. For example, any of these schemes are, at least in principle, compatible with WDM.

Details of the various signaling schemes explored were given in Chapter 2 including PSD calculations, and precoding and decoding of polybinary and polyquaternary signals. Chapter 3 explained how the modeling of a system using a laser diode and singlemode fiber is distinctly different than for a system using an LED with singlemode or multimode fiber. For the latter, the entire system can be modeled as a linear baseband system where the fiber acts as a lowpass filter on the optical intensity envelope. For a system using a laser diode and singlemode fiber, however, the fiber cannot be modeled as a linear system in the power domain, but can be modeled as a linear system acting on the optical electric field, which is a bandpass signal. Unlike LED and multimode fiber based systems, this system is nonlinear from electrical input to electrical output because of the nonlinear transfer characteristic of the external modulator and the square-law detection process. Performance measures for communications systems were also described in Chapter 3 including BER, receiver sensitivity and eye diagrams.

In Chapter 4, a description was given of the various noise sources present in an optically-preamplified system including: receiver thermal noise; shot noise from signal, ASE and dark current; signal-spontaneous and spontaneous-spontaneous beat noises; and laser RIN. A thorough analysis of RIN resulting from PM-to-AM noise conversion was also given. PM-to-AM RIN results whenever a source with a non-zero linewidth is used over dispersive fiber. It scales linearly with the source linewidth and increases monotonically with an increasing receiver bandwidth or fiber length. Because RIN is proportional to the square of received optical power, it gives rise to a BER floor, which must be kept sufficiently below the target BER to avoid an excessive power penalty. Chapter 4 also described the two noise models employed including a static noise model, which assumes an ideal NRZ signal with zero ISI, and a dynamic noise model, which accounts for ISI from all system impairments.

Optimal level spacing based on a static noise model was investigated in Chapter 4 for a 4-ary ASK signal. Level weights were normalized between the minimum and maximum optical power where a logical **0** corresponds to minimum power and a logical **3** corresponds to maximum power. Hence, optimal level weights were expressed as $\{0, \varepsilon_1, \varepsilon_2, 1\}$ where ε_1 and ε_2 are, respectively, the normalized weights for a logical **1** and a logical **2**. When only stationary noise is present, levels should be equally spaced, i.e., $\varepsilon_1=1/3$ and $\varepsilon_2=2/3$, as expected. When noise that is linearly proportional to signal power dominates, such as signal-spontaneous beat noise or signal shot noise, the optimal level weights are $\varepsilon_1=1/9$ and $\varepsilon_2=4/9$, assuming an infinite extinction ratio. As the extinction ratio is degraded, these level weights gradually approach those for stationary noise, i.e., equally-spaced levels. When noise that is proportional to the square of received optical power dominates, such as RIN, the optimal level weights depend on the optical extinction ratio, δ, through $\varepsilon_1 = (\delta^{1/3} - 1)/(\delta - 1)$ and $\varepsilon_2 = (\delta^{2/3} - 1)/(\delta - 1)$ where δ is the ratio of the optical power in a logical **3** to that in a logical **1**. It was also explained in Chapter 4 that when stationary noise dominates, the power penalty for using 4-ary ASK over binary in a direct-detection lightwave system is given by $(M-1)/\sqrt{\log_2(M)}$ where M is the number of levels.

The dynamic noise model employed is based on the theory in [96]. Although the work in [96] imposes a constraint between the optical filter bandwidth and the simulation sampling interval, it was suggested that this constraint may be removed if summations are interpreted as numerical evaluations of continuous-time integrals. By doing this, it may be possible to simulate systems with very narrow bandwidths and to account for the response of an arbitrary optical filter by simply filtering the optical field by the appropriate filter. It was also shown in Chapter 4 that when summations are interpreted as numerical evaluations of continuous integrals, it is possible to arrive at a time-domain expression for signal-spontaneous beat noise that is of the same functional form as signal-dependent shot noise. A time-domain description for RIN was also proposed in which it is modeled as a filtered shot noise process with an intensity function that is proportional to the square of the received instantaneous optical power.

Modeling of important system components was discussed in Chapter 5. Electric-field domain transfer characteristics for $LiNbO_3$ and multiple quantum well III-V MZ modulators were presented. In an ideal $LiNbO_3$ MZ the phase shift in each arm is a linear function of the applied voltage, and the loss through each arm is independent of the applied voltage, resulting in a transfer characteristic that is a periodic function of the applied voltage. For a III-V MZ, the phase shift and loss in each arm is a nonlinear function of the applied voltage, producing an aperiodic transfer characteristic. In MZ external modulators, frequency chirping can be introduced in a controlled manner such that a pulse is red shifted on the rising edge and blue shifted on the falling edge, leading to pulse compression over certain distances. For $LiNbO_3$ devices, the frequency chirp is proportional to the sum of the time derivatives of the voltages applied to the two electrodes. Residual frequency chirp can also arise when MZs with asymmetric Y-branches and/or unequal loss through each arm are used. The polarity of residual chirp can be reversed by changing the bias point on the MZ's transfer characteristic. A small-signal chirp parameter is often used to express the amount of chirp in a MZ; for large-signal conditions, the chirp parameter is time-varying. Chapter 5 also described the lowpass-equivalent transfer function for dispersive fiber, and two methods for deriving the transfer function were presented. Finally, it was explained that EDFAs can be modeled by three characterizing parameters: small-signal gain, output saturation power, and spontaneous emission factor.

Chapter 6 explained the methods used for characterizing various system components. For example, it was shown how the histogram feature on a digital oscilloscope can be used to determine the RIN value of a laser or the noise figure of an electrical amplifier, or how laser linewidths can be measured using a delayed self-homodyne technique. A network analyzer was an essential tool for characterizing many devices. It was used to measure the frequency response of components, to determine the RF switching voltage of a MZ, and to determine the gain of a transimpedance amplifier. Chapter 6 also presented a method for determining the electric-field domain transfer characteristic of a III-V MZ, in which only observations of the output optical power were required. Finally, a simple method was described for characterizing an EDFA.

Simulation results were presented in Chapter 7 based on the static and dynamic noise models. The static noise model was useful for rapid BER and receiver sensitivity calculations in the absence of ISI, and was used with ideal system parameters to estimate the quantum limit for binary, 4-ary ASK and 8-ary ASK signals in optically-preamplified systems. For binary signals, a quantum limit of 42 photons per bit was obtained, which is in agreement with [125]. For a 4-ary ASK signal with equally-spaced levels, a quantum limit of 515 photons per bit was obtained, which is about 11 dB higher than for a binary signal. If the level spacing is optimized, however, the quantum limit for a 4-ary ASK signal can be improved to 141 photons per bit, or about 5.3 dB higher than a binary signal. A quantum limit of 2021 photons per bit was obtained for an 8-ary ASK signal with equally-spaced levels, which is about 16.8 dB higher than for a binary signal. For a practical set of parameters (non-ideal) the power penalty for using M-ary ASK is slightly reduced. For example, a penalty of about 7 to 9 dB is expected for a 4-ary ASK signal with equally-spaced levels, and about 4 to 5 dB when optimal level spacing is used. It was explained, however, that implementing optimal level spacing may not be practical at Gb/s rates; hence, a realistic power penalty for 4-ary ASK over binary signaling is about 7 to 9 dB. This is substantially larger than the 3.3 dB predicted for the case when there is stationary noise, only. Consequently, the signal dependence of signal-spontaneous beat noise substantially increases the power required for a 4-ary ASK signal in an optically-preamplified system.

The dynamic noise model was used in assessing the dispersion tolerance of the various signaling formats where a $LiNbO_3$ MZ external modulator was assumed. For polybinary signals, only the duobinary signal offers an improvement in dispersion immunity because higher-level polybinary signals do not further reduce the required bandwidth. Duobinary intensity modulation and a duobinary receiver offer about the same improvement in dispersion immunity; however, the duobinary receiver offers a better baseline sensitivity because of its lower NEB. M-ary ASK can be used to increase the dispersion-limited distance, but at the expense of a much higher baseline sensitivity (7 to 9 dB). Optical AM-PSK duobinary signaling is very attractive because is does not posses an inherent penalty in baseline receiver sensitivity. Furthermore, it is a carrierless signal, which may reduce the impact of fiber nonlinearities such as SBS.

Residual chirp accompanying a MZ with a finite DC optical extinction ratio can either enhance or degrade performance in binary, duobinary and M-ary ASK signals. It was explained, however, that negative residual chirp can always be obtained for these signals by biasing the MZ at an appropriate point. Unfortunately, this is not the case for an AM-PSK duobinary signal where it was shown that residual chirp always degrades performance because of the alternating chirp polarity on MARKS separated by an odd number of SPACES. Therefore, when optical AM-PSK duobinary signaling is used, a MZ with the largest DC extinction ratio possible should be used. For practical systems, a DC extinction ratio of at least 20 dB will keep the residual, chirp-induced penalty to within about 1 dB.

Assuming a DC optical extinction ratio of 20 dB, the expected dispersion-limited transmission distance for binary, duobinary, AM-PSK duobinary and 4-ary ASK are, respectively, around 100 km, 200 km, 200 km and 350 km. Because the reach for an AM-PSK duobinary signal is as far as a binary signal combined with a duobinary receiver, there is no reason to use a duobinary receiver over an optical AM-PSK duobinary signal. Therefore, based on dispersion immunity alone, one might suggest that conventional binary signaling is suitable for transmission between 0 and 100 km, that AM-PSK duobinary signaling is suitable for transmission between 100 and 200 km, and that 4-ary ASK is suitable for transmission between 200 and 350 km. Unfortunately, other impairments make M-ary signaling unattractive for long-haul transport. For example, the source linewidth must be less than ~1 MHz to minimize the impact of PM-to-AM RIN when transmitting over distances of 200 to 350 km. This linewidth is about a factor of ten smaller than that required for an AM-PSK signal operating over 200 km. Also, because of the increased number of levels, an M-ary signal requires a larger SNR at the receiver, which means the ratio of optical signal-to-ASE power must be substantially higher than for a binary or AM-PSK duobinary signal. For example, for the parameters used in simulations, the signal-to-ASE power ratio required for a binary signal is ~6 dB, whereas a 4-ary ASK signal requires a ratio of ~14 dB. The implication here is that, for practical launched powers, inline amplifiers would be required at least every 60 to 80 km when transmitting a 4-ary ASK signal over distances in the 200 to 350 km range. An advantage of the 4-ary ASK signal over all other signals is that it reduces the bit rate of all logic components at the transmitter and receiver by a factor of two. Similarly, the required bandwidth of electrical components is reduced. However, because of the increased number of levels, a 4-ary ASK signal is considerably more sensitive to frequency response fluctuations present in real devices.

Experimental results were presented in Chapter 8 for binary and 4-ary ASK transmission at 10 Gb/s. Experimental noise measurements were also performed to verify the adopted noise model in which the amount of noise as a function of received optical power was measured using the histogram feature on a digital oscilloscope. The amount of noise measured and its dependence on received optical power showed good agreement with that predicted by the adopted noise model, suggesting that the noise model is valid. Moreover, noise measurements over 100 km of fiber clearly showed the presence of RIN from PM-to-AM noise conversion, and the PM-to-AM RIN predicted by theory agreed with that measured when the 35 MHz linewidth measured for the laser was used in theoretical calculations.

For binary experiments using the Nortel III-V MZ biased to obtain negative chirp, a receiver sensitivity of -17 dBm was obtained for a system without an optical preamplifier. For a system with an optical preamplifier, a sensitivity of -27.1 dBm was obtained at 0 km, -29 dBm at 75 km, and -28.0 dBm at 100 km. At 125 km a BER of 2.5×10^{-8} was measured for the maximum available received power of -23 dBm. The experimental BER curve at 125 km clearly showed signs of bending toward a BER floor. The receiver sensitivity predicted by FOCSS was better than that measured by up to 2 dB for an optical back-to-back link, with or without an optical preamplifier. For longer distances, FOCSS predicted a BER floor worse than that indicated in measurements. An observation of simulated and measured eye diagrams, however, showed that the measured eye diagram was slightly more open than that predicted by FOCSS when transmitting over 125 km of fiber. A method was presented for obtaining time-averaged experimental eye diagrams that clearly show the detail of individual traces.

For 4-ary ASK experiments using the Nortel III-V MZ module, a receiver sensitivity of -12.5 dBm was measured at 0 km for a system without optical preamplification, whereas a sensitivity of -15.8 dBm was obtained when using a low-gain optical preamp. The receiver sensitivity predicted by FOCSS was better than that measured by up to 1.8 dB at 0 km. For a set of experiments using a higher-gain optical preamplifier, a receiver sensitivity of -18.3 dBm was obtained at 50 km, although the BER curve showed clear signs of bending toward a BER floor. For transmission experiments at 75 km a 10^{-6} error floor was observed. For transmission over 100 km and 170 km a BER floor between 10^{-3} and 10^{-4} was observed. FOCSS predicted BER floors to within one order of magnitude of those measured for these experiments.

A narrower linewidth source (~4 MHz) was available for 4-ary ASK experiments that used the Lucent $LiNbO_3$ MZ. Receiver sensitivities of -19.2 dBm, -20.5 dBm and -16.4 dBm, respectively, were measured at 0 km, 75 km and 150 km for an optically-preamplified system. The receiver sensitivities predicted by FOCSS were worse than those measured by up to 2 dB for distances up to 150 km. It is believed that transmission over 150 km with $BER=10^{-9}$ was possible because of the much lower RIN from PM-to-AM noise conversion. For transmission over 225 km, a BER of 10^{-6} was measured for the maximum available optical power of -15.9 dBm, and the BER curve showed clear signs of bending toward a BER floor. FOCSS predicted a BER floor of 10^{-8} at this distance.

Principal Research Contributions of this Work

Through these experiments, the feasibility of a 4-ary ASK lightwave system operating at 10 Gb/s was demonstrated, the validity of the adopted noise model was confirmed, and the experimental verification of RIN from PM-to-AM noise conversion and an assessment of its impact on performance in binary and 4-ary ASK lightwave systems was achieved. Finally, the accuracy of FOCSS was confirmed by the good agreement between experimental and simulated BER curves, receiver sensitivities and eye diagrams.

Although it was found that 4-ary ASK signals are more dispersion tolerant than binary signals, it is believed that 4-ary ASK signaling does not offer a practical solution to chromatic dispersion because of the inherently large (7 to 9 dB) power penalty and the requirement of inline amplifiers spaced sufficiently close to maintain the required ratio of optical signal power to ASE power. For this reason, further investigation of higher-level M-ary signals (> 4 levels) for combating chromatic dispersion is highly questionable. Probably the most promising attribute of 4-ary ASK is that it doubles the bit rate for a given symbol rate. This *may* make 4-ary ASK a viable option for increasing the capacity of point-to-point, short-haul communication links in which optical amplifiers are not used, maybe even in a WDM environment: Recall that, when the noise is not signal dependent, the penalty for using 4-ary ASK over binary is

3.3 dB. This is only about a two-fold increase in optical power, which is roughly the same increase in power that would result when doubling the number of channels in a WDM system. Of course, this comment only applies to point-to-point WDM links in the absence of optical amplifiers. For future WDM networks where optical amplifiers are inevitable, it is unlikely that M-ary ASK signaling at Gb/s will be of practical use.

It was stated that the premise for exploring the various signal schemes was that, because spectral components closer to the carrier experience a lower phase distortion than those components farther away, a dispersion improvement may be offered for signals in which the spectrum is more concentrated about the optical carrier. It was found, however, that this rationale is not sufficiently explicit, and that a more incisive statement can be made: An improvement in dispersion immunity is offered over conventional binary signaling if the amount of nonlinear distortion falling within the bandwidth of the receiver is reduced, which can be accomplished by 1) using a signaling scheme that allows for a reduced receiver bandwidth, such as duobinary filtering at the receiver, or 2) using a signaling scheme that allows the optical spectrum to be limited to a narrower spectral range, such as AM-PSK duobinary signaling. It was explained that limiting the spectral occupancy of the optical field can be achieved by bandlimiting the electrical signal applied to the modulator, and that it is the minimum bandwidth of the transmitter and receiver that is the important parameter for assessing the dispersion immunity of the signals considered. For example, for a given receiver bandwidth, bandlimiting at the transmitter has a significant effect only if its bandwidth can be reduced further compared to the receiver. This, for example, is the case for an AM-PSK duobinary signal. It should be noted, however, that, although these conclusions are supported by the signaling schemes investigated here, the role of the absence or presence of carrier, and its phase relationship to the modulated signal, is not completely understood—Recall that, unlike all other signals explored, AM-PSK duobinary is a carrierless signaling scheme. Moreover, angle modulation from frequency chirping also affects the signal's spectrum. For example, positive and negative frequency chirping can both broaden the optical spectrum, yet positive chirp can degrade performance, whereas negative chirp can enhance performance. Obviously, an observation of the spectral occupancy alone is not sufficient to explain this phenomenon, and if a spectral-domain based explanation is to be provided, it must consider the phase relationships of spectral components, not just the amplitudes.

Future Work

There are many activities that could serve as a research thrust for future projects. Incorporating a nonlinear model for the fiber into FOCSS would be very useful, especially since much of the work being conducted at TRLabs is now focussing on 10 Gb/s transmission over distances of many hundreds of kilometers where fiber nonlinear effects such as SPM are expected to be significant. It was also suggested that it may be possible to remove the constraint between the sampling frequency and optical filter bandwidth imposed by the adopted dynamic noise model. Further theoretical work to test this idea, followed by experimental verification, would be useful. More research into the nature of PM-to-AM noise conversion is also warranted. For example, it is not understood how PM-to-AM conversion is affected, if at all, by the modulating signal, or by power-induced fiber nonlinearities. Optical AM-PSK duobinary signaling appears to be a very promising signaling scheme, and further work directed at better understanding it is justified. For example, it was explained that residual frequency chirp, or controlled chirp introduced by adjusting the amplitudes of the signals applied to the modulator, degrades the performance of an optical AM-PSK duobinary signal. This does not, however, preclude the use of an alternative pre-chirping method, such as a cascaded phase modulator or direct frequency modulation of a laser, to introduce the correct polarity of chirp on all transmitted symbols. Projects exploring these pre-chirping methods on an optical AM-PSK duobinary signal would be interesting. The benefit obtained from frequency chirping has been explained in the literature in terms of pulse compression that occurs over certain distances when there is, respectively, a red and blue shift on the rising and falling edge of pulses. Providing a spectral-domain description of the benefit obtained from frequency chirping may lead to a more fundamental understanding of this phenomenon. Other projects on optical AM-PSK duobinary could include studying how the absence of carrier affects the SBS threshold, or the nonlinear interaction of transmitted channels in a WDM system.

10 References

[1] Y. Yano et al., "2.6 Terabit/s WDM Transmission Experiment using Optical Duobinary Coding," *ECOC'96*, vol. 5 (post-deadline paper ThB.3.1), September 1996.

[2] T. Ito et al., "Feasibility study on over 1 bit/s/Hz high spectral efficiency WDM with optical duobinary coding and polarization interleave multiplexing," *OFC'97*, TuJ1, pp. 43-45, 1997.

[3] P. S. Henry, "Lightwave Primer," *IEEE Journal of Quantum Electronics*, vol. QE-21, no. 12, pp. 1862-1879, December 1985.

[4] J.M. Senior, *Optical Fiber Communications*, Prentice Hall, 1992.

[5] S. Geckeler, *Optical Fiber Transmission Systems*, Artech House, Inc., 1987.

[6] H. Izadpanah et. al., "Distortion-Free Amplification of High-Speed Test Patterns Up to 100 Gbit/s With Erbium-Doped Fibre Amplifiers," *Electronics Letters*, vol. 27, no. 3, pp. 196-197, January 31, 1991.

[7] E. Voges, A. Neyer, "Integrated-Optic Devices on $LiNbO_3$ for Optical Communication," *Journal of Lightwave Technology*, vol. LT-5, no. 9, pp. 1229-1238, September 1987.

[8] L. Thylen, "Integrated Optics in $LiNbO_3$: Recent Developments in Devices for Telecommunications," *Journal of Lightwave Technology*, vol. 6, no. 6, pp. 847-861, June 1988.

[9] I. P. Kaminow, "Polarization in Optical Fibers," *IEEE Journal of Quantum Electronics*, vol. QE-17, no. 1, pp. 15-22, January 1981.

[10] M. Tsubokawa, Y. Sasaki, "Limitation of Transmission Distance and Capacity Due to Polarization Dispersion in a Lightwave System," *Electronics Letters*, vol. 24, no. 6, pp. 350-352, March 17, 1988.

[11] C. D. Poole et al., "Fading in Lightwave Systems due to Polarization-Mode Dispersion," *Digest of Conference on Optical Fiber Communications*, Paper TuI3, 1990.

[12] R. S. Tucker, "16 Gbit/s Fibre Transmission Experiment Using Optical Time-Division Multiplexing," *Electronics Letters*, vol. 23, no. 24, pp. 1270-1271, November 19, 1987.

[13] G. Eisenstein et al., "Optical Time-Division Multiplexed Transmission System Experiment at 8 Gbit/s," *Electronics Letters*, vol. 23, no. 21, pp. 1115-1116, October 8, 1987.

[14] G. Eisenstein et al., "Optical Time-Division Multiplexed Transmission at 8 Gbits/s Using Single Laser and Semiconductor Optical Power Amplifier," *Electronics Letters*, vol. 25, no. 16, pp. 1034-1036, August 3, 1989.

[15] G. E. Wickens, "20 Gbit/s, 205 km Optical Time Division Multiplexed Transmission System," *Electronics Letters*, vol. 27, no. 11, pp. 973-974, May 23, 1991.

[16] Anders Djupsjöbacka, "Time Division Multiplexing Using Optical Switches," *IEEE Journal on Selected Areas in Communications*, vol. 6, no. 7, pp. 1227-1231, August 1988.

[17] S. Kawanishi et al., "400 Gb/s TDM Transmission of 0.98 ps Pulses over 40 km Employing Dispersion Slope Compensation," *OFC'96*, post-deadline paper PD24, February 1996.

[18] Y. K. Park et al., "A field Demonstration of 20 Gb/s Capacity Transmission over 360 km of Installed Standard (Non-DSF) Fiber," *IEEE Photonics Technology Letters*, vol. 7, no. 7, pp. 816-818, July 1995.

[19] R. W. Tkach et al., "Transmission of Eight 20 Gb/s Channels Over 232 km of Conventional Single-Mode Fiber ," *IEEE Photonics Technology Letters*, vol. 7, no. 11, pp. 1369-1371, November 1995.

[20] A. H. Gnauck et al., "One terabit/s transmission experiment," *OFC'96*, post-deadline paper PD20, February 1996.

[21] H. Onaka et al., "1.1 Tb/s WDM transmission over a 150 km 1.3 um zero-dispersion single-mode fiber," *OFC'96*, posp-deadline paper PD19, February 1996.

[22] P. F. Wysocki et al., "Erbium-Doped Fiber Amplifier Flattened Beyond 40 nm Using Long-Period Grating," *OFC'97*, posp-deadline paper PD2, February 1997.

[23] B. Clesca et al., "Gain Flatness Comparison Between Erbium-Doped Fluoride and Silica Fiber Amplifiers With Wavelength-Multiplexed Signals," *IEEE Photonics Technology Letters*, vol. 6, no. 4, pp. 509-512, April 1994.

[24] Jean-Luc Beylat et al., "Flat-gain fiber optical amplifiers for WDM networks," *ECOC'95*, paper Th.L.1.7, pp. 1095-1102, September 1995.

[25] M. Nishimura et al., "Gain-flattened erbium-doped fiber amplifiers for WDM transmission," *OFC'97 Technical Digest*, paper WF1, pp. 127, February 1997.

[26] A. MORI et al., "1.5 um Broadband Amplification by Tellurite-Based EDFAs," *OFC'97*, post-deadline paper PD1, February 1997.

[27] H. Kogelnik, "WDM NETWORKS: A U.S. PERSPECTIVE," *ECOC'96*, paper MoA.2.2, pp. 81-85, September 1996.

[28] R. S. Vodhanel et al., "National-Scale WDM Networking Demonstration by MONET Consortium," *OFC'97*, post-deadline paper PD27, February 1997.

[29] R. T. Hofmeister et al., "Project LEARN – Light Exchangable, Add/Drop Ring Network," *OFC'97*, post-deadline paper PD25, February 1997.

[30] D. J. Blumenthal et al., "Physical Limitations to Scalability of WDM All-Optical Networks," *Optics & Photonics News*, pp. 16-22, February 1997.

[31] Marko Erman "What Technology is Required for the Pan-European Network, what is Available and What is Not," *ECOC'96*, paper TuB.2.2, pp. 87-94, September 1996.

[32] K. E. Stubkjaer, "WAVELENGTH CONVERSION DEVICES AND TECHNIQUES," *ECOC'96*, paper ThB.2.1, pp. 33-40, September 1996.

[33] P. M. Hill et al., "Optical Polarization Division Multiplexing at 4 Gb/s," *IEEE Photonics Technology Letters*, vol. 4, no. 5, pp. 500-502, May 1992.

[34] P. M. Hill et al., "OPTICAL POLARIZATION DIVISION MULTIPLEXING AT 8 GB/S WITH NOVEL CLOCK AND CARRIER RECOVERY," ECOC'92, paper Tu A5.6, pp. 165-168, 1992.

[35] K. Fukuchi et al., "POLARIZATION SHIFT KEYING – DIRECT DETECTION (PolSK-DD) SCHEME FOR FIBER NONLINEAR EFFECT INSENSITIVE COMMUNICATION SYSTEM," ECOC'92, paper Tu A5.7, pp. 169-172, 1992.

[36] L. F. Mollenauer et al., "Long-Distance Propagation Using Lumped Amplifers and Dispersion shifted Fiber," *Journal of Lightwave Technology*, vol. 9, no. 2, pp. 194-197, February 1991.

[37] F. Pirio et al., "Future ultra-high capacity transoceanic submarine systems," *ECOC'96*, paper WeC.2.1, pp. 95-99, September 1996.

[38] E. Brun-Maunand et al., "RECENT PROGRESS ON SOLITON SYSTEMS," *ECOC'96*, paper WeC.3.1, pp. 93-100, September 1996.

[39] D. Le Guen et al., "200 Gb/s 100 km-span soliton WDM transmission over 1000 km of standard fiber with dispersion compensation and pre-chirping," *OFC'97*, post-deadline paper PD17, February 1997.

[40] M. Nakazawa et al., "100 Gb/s WDM (20 Gb/s x 5 channels) soliton transmission over 10,000 km using in-line synchronous modulation and optical filtering," *OFC'97*, post-deadline paper PD21, February 1997.

[41] Bob Jopson and Alan Gnauck, "Dispersion Compensation for Optical Fiber Systems," *IEEE Communications Magazine*, pp. 96-102, June 1995.

[42] A. Yariv et al., "Compensation for channel dispersion by nonliear optical phase conjugation," *Optics Letters*, vol. 4, no. 2, pp. 52-54, February 1979.

[43] S. Watanabe et al., "Compensation of Chromatic Dispersion in a Single-Mode Fiber by Optical Phase Conjugation," *IEEE photonics Technology Letters*, vol. 5, no. 1, pp. 92-95, January 1993.

[44] Xiupu Zhang, "Optical Spectral Inversion and its Applications in Long-Haul Fiber Transmission," Technical University of Denmark Ph.D. Thesis, October 1996.

[45] Xiupu Zhang et al., "Long-Distance Transmission Over Standard Fiber by Use of Mid-Way Phase Conjugation," *IEEE Photonics Technology Letters*, vol. 7, no. 7, pp. 819-821, July 1995.

[46] B. Wedding, "New method for optical transmission beyond dispersion limit," *Electronics Letters*, vol. 28, no. 14, pp. 1298-1300, 1992.

[47] B. Wedding and B. Franz, "Unregenerated optical transmission at 10 Gb/s via 204 km of standard singlemode fiber using a directly modulated laser diode," *Electronics Letters*, vol. 29, no. 4, pp.402-404, 1993.

[48] B. Wedding et al., "Dispersion-Supported Transmission of 20 Gbit/s over 53 km Standard Singlemode Fibre," *Electronics Letters*, vol. 31, no. 7, pp. 566-568, 1995.

[49] A. M. Vengsarkar, "Dispersion compensating fibers," *OFC'97 Technical Digest*, paper ThA2, pp. 233-234, February 1997.

[50] R. I. Laming et al., "Fiber gratings for dispersion compensation," *OFC'97 Technical Digest*, pp. 234-235, February 1997.

[51] F. Ouellette et al., "All-Fiber Devices for Chromatic Dispersion Compensation Based on Chirped Distributed Resonant Coupling," *Journal of Lightwave Technology*, vol. 12, no. 10, pp. 1728-1738, October 1994.

[52] D. Atkinson et al., "Numerical Study of 10-cm Chirped-Fiber Grating Pairs for Dispersion Compensation at 10 Gb/s over 600 km of Nondispersion Shifted Fiber," *IEEE Photonics Technology Letters*, vol. 8, no. 8, pp. 1085-1087, August 1996.

[53] M. J. Cole et al., "Continuously chirped, broadband dispersio-compensating fibre gratings in a 10 Gbit/s 110 km standard fibre link," *ECOC'96*, paper ThB.3.5, pp. 19-22, September 1996.

[54] R. Kashyap et al., "EIGHT WAVELENGTH x 10 Gb/s SIMULTANEOUS DISPERSION COMPENSATION OVER 100KM SINGLE-MODE FIBRE USING A SINGLE 10 NANOMETER BANDWIDTH, 1.3 METER LONG, SUPER-STEP-CHIRPED FIBRE BRAGG GRATING WITH A CONTINUOUS DELAY OF 13.5 NANOSECONDS," *ECOC'96*, paper ThB.3.2, pp. 7-10, September 1996.

[55] P. Kabal and S. Pasupathy, "Partial-Response Signaling," *IEEE Transactions on Communications*, vol. com-23, no. 9, pp. 921-934, September 1975.

[56] Adam Lender, "Correlative Digital Communication Techniques," *IEEE Trans. on Communications Technology*, vol. COM-12, pp. 128-135, 1964.

[57] Adam Lender, "Correlative level coding for binary-data transmission," *IEEE Spectrum*, pp. 104-115, 1966.

[58] G. May, "Distance and Bandwidth Enhancement of Fiber Optic Trnamission," University of Alberta Masters Thesis, September 1993.

[59] G. May et al., "Extended 10 Gb/s Fiber Transmission Distance at 1538 nm Using a Duobinary Receiver," *IEEE Photonics Technoogy Letters*, vol. 6, no. 5, pp. 648-650, 1994.

[60] X. Gu and L.C. Blank, "10 Gbit/s unrepeatered three-level optical transmission over 100 km of standard fibre," *Electronics Letters*, vol. 29, no. 25, pp. 2209-2211, 1993.

[61] X. Gu et al., "10 Gbit/s, 138 km uncompensated duobinary transmission over installed standard fibre," *Electronics Letters*, vol. 30, no. 23, pp. 1953-1954, 1994.

[62] K. Yonenaga et al., "Optical duobinary transmission system with no receiver sensitivity degradation," *Electronics Letters*, vol. 31, no. 4, pp. 302-304, 1995.

[63] S. Kuwano et al., "10 Gbit/s repeaterless transmission experiment of optical duobinary modulated signal," *Electronics Letters*, vol. 31, no. 16, pp. 1359-1361, 1995.

[64] A. J. Price and N. Le Mercier, "Reduced bandwidth optical digital intensity modulation with improved chromatic dispersion tolerance," *Electronics Letters*, vol. 31, no. 1, pp. 58-59, 1995.

[65] A. J. Price et al., "210 km Repeaterless 10 Gb/s Transmission Experiment Through Nondispersion-Shifted Fiber Using Partial Response Scheme," *IEEE Photonics Technology Letters*, vol.7, no. 10, pp. 1219-1221, 1995.

[66] K. Fukuchi et al., "10 Gbit/s-120 km standard fiber transmission employing a novel optical phase-encoded intensity modulation for signal spectrum compression," *OFC'97 Technical Digest*, paper ThH3, pp. 270-271, February 1997.

[67] T. Ono et al., "Demonstration of high-dispersion tolerance of 20 Gbit/s optical duobinary signal generated by a low-pass filtering method," *OFC'97 Technical Digest*, paper ThH1, pp. 268-269, February 1997.

[68] K. Ennser et al., "Phase-encoded duobinary transmission over non-dispersion shifted fibre links using chirped grating dispersion compensators," *Electronics Letters*, vol. 33, no. 1, pp. 72-74, January 1997.

[69] W. H. Loh et al., "Dispersion Compensated 10 Gbit/s Transmission over 700 km of Standard Single Mode Fiber with 10 cm Chirped Fiber Grating and Duobinary Transmitter," *OFC'96*, post-deadline paper PD30, February 1996.

[70] B. Wedding et al., "MULTI-LEVEL DISPERSION SUPPORTED TRANSMISSION AT 20 GBIT/S OVER 46 KM INSTALLED STANDARD SINGLEMODE FIBRE," *ECOC'96*, paper MoB.4.4, pp. 91-94, September 1996.

[71] L. Raddatz et al., "Fiber-optic m-ary modulation scheme using multiple light sources," *OFC'97 Technical Digest*, paper WL36, pp. 198-199, February 1997.

[72] M. Nakhla, "Error Probability for Multilevel Digital Systems in Presence of Intersymbol Interference and Additive Noise," *IEEE Transactions on Communications*, vol. 42, no. 7, pp. 2380-2383, July 1994.

[73] P. Crespo et al., "Transmission of Four Level Signals Using LED and Single Mode Fibers for Loop Applications," *International Conference on Communications*, pp. 593-598, 1988.

[74] J. H. Winters and R. D. Gitlin, "Electrical Signal Processing Techniques in Long-Haul Fiber-Optic Systems," *IEEE Transactions on Communications*, vol. 38, no. 9, pp. 1439-1452, September 1990.

[75] K. Benterud, "Fiber Optic Transmission Using Optical Time Division Multiplexing," University of Alberta Maters Thesis, Fall 1993.

[76] J. G. Proakis, *Digital Communications*, McGraw-Hill, 1989.

[77] K. Feher and A. Lender, *Digital Communications, Microwave Applications*, Prentice Hall, pp. 144-182, 1981.

[78] Michel C. Jeruchim, Philip Balaban, and K. Sam Shanmugan, *Simulation of Communication Systems*, Plenum Press, 1992.

[79] J. L. Gimlett and N. K. Cheung, "Dispersion Penalty Analysis for LED/Single-Mode Fiber Transmission Systems," *Journal of Lightwave Technology*, vol. 4, no. 9, pp. 1381-1391, September 1986.

[80] D. Y. Yu, et al., "Design of partial response data transmission filters with specified stopband attenuation," *IEE Proceedings-G*, vol. 138, no. 3, June 1991.

[81] L. F. Lind and S. E. Nader, "OPTIMAL ANALOGUE FILTERS FOR DATA TRANSMISSION," *IEEE International Symposium on Circuits and Systems*, pp. 344-347, April 1977.

[82] L. F. Lind and S. E. Nader, "Design Tables for a Class of Data Transmission Filters," Electronics Letters, vol. 13, no. 19, pp. 564-567, September 1977.

[83] L. F. Lind and S. E. Nader, "Realizable filters that minimize intersymbol interference," *The Radio and Electronics Engineer*, vol. 48, no. 12, pp. 612-618, December 1978.

[84] L. F. Lind and S. E. Nader, "REALIZABLE MATCHED FILTERS FOR MINIMAL INTERSYMBOL INTERFERENCE," *IEEE International Symposium on Circuits and Systems*, pp. 441-445, April 1978.

[85] S. E. Nader and L. F. Lind, "Optimal Data Transmission Filters," *IEEE Transactions on Circuits and Systems*, vol. 26, no. 1, pp. 36-45, January 1979.

[86] L. F. Lind and A. A. De Albuquerque, "DATA TRANSMISSION FILTERS FOR DUOBINARY SYSTEMS," Electronics Letters, vol. 16, no. 6, pp. 228-230, Mach 1980.

[87] L. F. Lind and A. A. De Albuquerque, "The design of optimal partial response data transmission filters," *The Radio and Electronic Engineer*, vol. 52, no. 3, pp. 122-126, Mach 1982.

[88] P. Diament and M. C. Teich, "Evolution of the Statistical Properties of Photons Passed Through a Traveling-Wave Laser Amplifier," *IEEE Journal of Quantum Electronics*, vol. 28, no. 5, pp. 1325-1333, May 1992.

[89] S. L. Danielsen et al., "Detailed Noise Statistics for an Optically Preamplified Direct Detection Receiver," *Journal of Lightwave Technology*, vol. 13, no. 5, pp. 977-981, May 1995.

[90] L. F. B. Ribeiro et al., "Performance Evaluation of EDFA Preamplifier Receivers Taking into Account Intersymbol Interference," *Journal of Lightwave Technology*," vol. 13, no. 2, pp. 225-231, February 1995.

[91] P. A. Humblet and M. Azizoglu, "On the Bit Error Rate of Lightwave Systems with Optical Amplifiers," *Journal of Lightwave Technology*, vol. 9, no. 11, pp. 1576-1582, November 1991.

[92] D. Marcuse, "Calculation of Bit-Error Probability for a Lightwave System with Optical Amplifiers and Post-Detection Gaussian Noise," *Journal of Lightwave Technology*, vol. 9, no. 4, pp. 505-513, April 1991.

[93] D. Ben-Eli et al., "Performance Bounds and Cutoff Rates of Quantum Limited OOK with Optical Amplification," *IEEE Journal on Selected Areas in Communications*, vol. 13, no. 3, pp. 510-530, April 1995.

[94] N. A. Olsson "Lightwave Systems With Optical Amplifiers," *Journal of Lightwave Technology*, vol. 7, no. 7, pp. 1071-1082, July 1989.

[95] D. Barabash and R. Morris. "SEMICONDUCTOR LASER AMPLIFIER NOISE GENERATION," *TRLabs internal report*, TR-89-15, December 1989.

[96] J. C. Cartledge and A. F. Elrefaie, "Effect of Chirping-Induced Waveform Distortion on the Performance of Direct Detection Receivers Using Traverling-Wave Semiconductor Optical Preamplifiers," *Journal of Lightwave Technology*, vol. 9, no. 2, pp. 209-219, February 1991.

[97] D. M. Pozar, *Microwave Engineering*, Addison-Wesley, 1990.

[98] C. R. Giles and E. Desurvire, "Propagation of Signal and Noise in Concatenated Erbium-Doped Fiber Optical Amplifiers," *Journal of Lightwave Technology*, vol. 9, no. 2, pp. 147-154, February 1991.

[99] E. Parzen, *Stochastic Processes*, San Francisco: Holden-Day, pp. 1-62, 118-144, 1962.

[100] S. Yamamoto et al., "Analysis of Laser Phase Noise to Intensity Noise Conversion by Chromatic Dispersion in Intensity Modulation and Direct Detection Optical-Fiber Transmission," *Journal of Lightwave Technology*, vol. 8, no. 11, pp. 1716-1722, November 1990.

[101] K. Petermann, "FM-AM NOISE CONVERSION IN DISPERSIVE SINGLE-MODE FIBRE TRANSMISSION LINES," *Electronics Letters*, vol. 26, no. 25, pp. 2097-2098, December 1990.

[102] B. P. Lathi, *MODERN DIGITAL AND ANALOG COMMUNICATION SYSTEMS*, Holt, Rinehart and Winston, 1989.

[103] Yongqi He, "Accurate Analysis and Optimisation of Optically Preamplified Receiver for Unrepeatered Long Distance Transmissions at 10 Gb/s," Technical University of Denmark Ph.D. Thesis, October 1996.

[104] A. R. Chraplyvy et al., "PHASE MODULATION TO AMPLITUDE MODULATION CONVERSION OF CW LASER LIGHT IN OPTICAL FIBERS," *Electronics Letters*, vol. 22, no. 8, pp. 409-411, April 1986.

[105] J. Wang and K. Petermann, "Small Signal Analysis for Dispersive Optical Fiber Communications," *Journal of Lightwave Technology*, vol. 10, no. 1, pp. 96-100, January 1992.

[106] R. F. S. Ribeiro et al., "Influence of Laser Phase Noise on Dispersive Optical Fiber Communication Systems," *IEEE Photonics Technology Letters*, vol. 7, no. 12, pp. 1510-1512, December 1995.

[107] A. H. Gnauck et al., "Dispersion Penalty Reduction Using an Optical Modulator with Adjustable Chirp," *IEEE Photonics Technology Letters*, vol. 3, no. 10, pp. 916-918, October 1991.

[108] J. C. Cartledge and R. G. Mckay, "Performance of 10 Gb/s Lightwave Systems Using an Adjustable Chirp Optical Modulator and Linear Equalization," *IEEE Photonics Technology Letters*, vol. 4, no. 12, pp. 1394-1397, December 1992.

[109] H. Chung et al., "Modeling and Optimization of Traveling-Wave $LiNbO_3$ Interferometric Modulators," *IEEE Journal of Quantum Electronics*, vol. 27, no. 3, pp. 608-617, March 1991.

[110] N. Henmi et al., "Prechirp Technique as a Linear Dispersion Compensation for Ultrahigh-Speed Long-Span Intensity Modulation Direct Detection Optical Communication Systems," *Journal of Lightwave Technology*, vol. 12, no. 10, pp. 1706-1719, October 1994.

[111] F. Koyama and K. IGA, "Frequency Chirping in External Modulators," *Journal of Lightwave Technology*, vol. 6, no. 1, pp. 87-93, January 1988.

[112] C. Rolland et al., "10 Gbit/s, 1.56um MULTIQUANTUM WELL InP/InGaAsP MACH-ZEHNDER OPTICAL MODULATOR," *Electronics Letters*, vol. 29, no. 5, pp. 471-472, March 1993.

[113] C. Rolland et al., "Improved Extinction Ratio of Waveguide Electroabsorption Optical Modulators Induced by an InGaAs Absorbing Layer," Journal of Lightwave Technology, vol. 10, no. 12, pp. 1907-1911, December 1992.

[114] J. C. Cartledge et al., "Theoretical Performance of 10 Gb/s Lightwave Systems Using a III-V Semiconductor Mach-Zehnder Modulator," *IEEE Photonics Technology Letters*, vol. 6, no. 2, pp. 282-284, February 1994.

[115] A. F. Elrefaie et al., "Chromatic Dispersion Limitations in Coherent Lightwave Transmission Systems," *Journal of Lightwave Technology*, vol. 6, no. 5, pp. 704-709, May 1988.

[116] H. J. A. da Silva and J. J. O'Reilly, "SYSTEM PERFORMANCE IMPLICATIONS OF LASER CHIRP FOR LONG HAUL HIGH BIT RATE DIRECT DETECTION OPTICAL FIBRE COMMUNICATIONS," ICC'88, pp. 588-592, 1988.

[117] J. Freeman, "THEORY, DESIGN, AND CHARACTERIZATION OF ERBIUM-DOPED FIBER AMPLIFERS," University of Alberta Masters Thesis, Fall 1991.

[118] D. M. Baney and Wayne V. Sorin, "Linewidth and Power Spectral Measurments of Single-Frequency Lasers," *Hewlett Packard Journal*, pp. 92-96, February 1990.

[119] R. S. Tucker, "High-Speed Modulation of Semiconductor Lasers," *Journal of Lightwave Technology*, vol. 3, no. 6, pp. 1180-1192, December 1985.

[120] L. J. Cimini et al., "Optical Equalization to Combat the Effects of Laser Chirp and Fiber Dispersion," *Journal of Lightwave Technology*, vol. 8, no. 5, pp. 649-659, May 1990.

[121] K. Benterud and J. Conradi, "A Novel Photodetector Frequency Response Measurement Technique Using an Electrooptic Modulator," *IEEE Photonics Technology Letters*, vol. 5, no. 9, pp. 1008-1010, September 1993.

[122] K. Bertilsson et al., "Noise Figure of Erbium Doped Fiber Amplifiers in the Saturated Regime," *IEEE Photonics Technology Letters*, vol. 6, no. 2, pp. 199-201, February 1994.

[123] W. B. Jones, Jr., *Introduction to Optical Communication Systems*, Holt, Rinehart and Winston, 1988.

[124] P. S. Henry, "Error-rate performance of optical amplifiers," *OFC'89 Technical Digest*, paper THK3, February 1989.

[125] I. Jacobs, "Effect of Optical Amplifier Bandwidth on Receiver Sensitivity," *IEEE Transactions on Communications*, vol. 38, no. 10, pp. 1863-1864, October 1990.

[126] M. J. O'Mahony, "DUOBINARY TRANSMISSION WITH p-i-n F.E.T. OPTICAL RECEIVERS," *Electronics Letters*, vol. 16, no. 19, pp. 752-753, September 1980.

[127] J. C. Cartledge, "Performance of 10 Gb/s Lightwave Systems Based on Lithium Niobate Mach-Zehnder Modulators with Asymmetric Y-Branch Waveguides," *IEEE Photonics Technology Letters*, vol. 7, no. 9, pp. 1090-1092,September 1995.

[128] D. Penninckx et al., "Relation between spectrum bandwidth and the effects of chromatic dispersion in optical transmissions," *Electronics Letters*, vol. 32, no. 11, pp. 1023-1024, May 1996.

[129] D. Penninckx et al., "The Phase-Shaped Binary Transmission (PSBT): A New Technique to Transmit Far Beyond the Chromatic Dispersion Limit," IEEE *Photonics Technology Letters*, vol. 9, no. 2, pp.259-261, February 1997.

[130] S. Walklin and J. Conradi, "On the Relationship Between Chromatic Dispersion and Transmitter Filter Response in Duobinary Optical Communication Systems," *IEEE Photonics Technology Letters*, vol. 9, no. 7, July 1997.

11 Appendixes

Appendix A: Computer Simulation of Analog Linear Systems

Appendix B: MATLAB Programs Based on a Static Noise Model

Appendix C: Optical Component Data

Appendix D: Electrical Component Data

Appendix E: GaAs IC Power Supply

11.1 Appendix A: Computer Simulation of Analog Linear Systems

In the following, computer simulation of a continuous-time system using a discrete-time representation is explained. The material is presented in the context of a review of important concepts including convolution, the Fourier transform, the fast Fourier transform and related topics.

11.1.1 Discrete Time Records of Continuous-Time Signals

A discrete-time representation must be used when simulating a continuous-time system on a digital computer. This inherently involves sampling the continuous-time signal at equally-spaced points in time and quantizing each sampled value, with a quantization error determined by the word size used to store the result—throughout this discussion the quantization error is assumed to be negligible. A one-dimensional array results, called a signal time record, where each element in the array corresponds to a signal sample at a distinct instant in time. Figure A.1 illustrates the sampling process in which a sensor is used to measure some physical parameter, such as temperature, pressure, sound or light intensity. The signal output from the sensor would be a voltage or current that is sampled at evenly-spaced points in time and encoded in digital form using an A/D (analog-to-digital) converter. A computer could then acquire the data and process it further—possibly in real time, as in a digital control system application—or write it to file, producing a time record (digital stamp) of the signal, as measured over some duration. For the purpose here, the signal time record serves as the input (stimulus) to the system being simulated. Of course, the input signal time record need not come from a real process, but could be computer generated using an appropriate model.

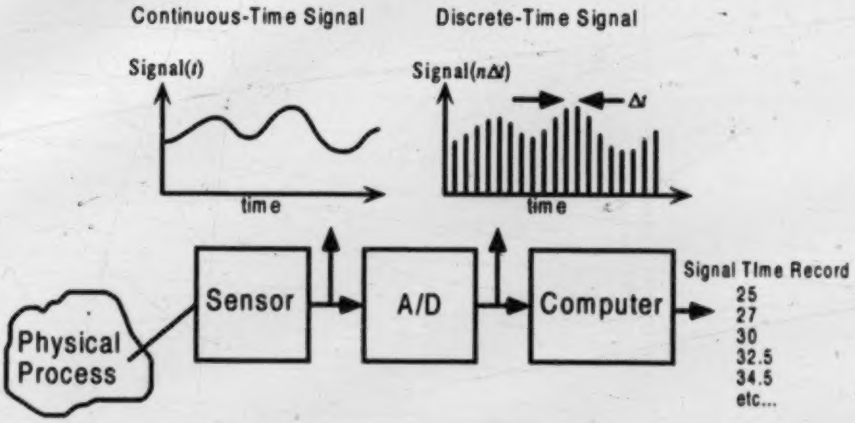

Figure A.1 Sampling an analog signal and constructing a discrete time record.

To ensure the digital signal is a faithful representation of the analog signal, samples must be taken at a rate that is at least twice the highest frequency component in the analog signal (called the Nyquist frequency). A lowpass filter, i.e., anti-aliasing filter, can be placed before the A/D converter to filter out any spurious high-frequency content or noise, thereby preventing spectral aliasing of the sampled signal.

11.1.2 Convolution and the Fourier Transform

Superposition applies to all linear, time-invariant systems. Therefore, the output response $y(t)$ of these systems is given by the convolution of the input signal $s(t)$ with the system impulse response $h(t)$. The operation of convolution is given by

$$y(t) = \int_{-\infty}^{+\infty} s(\tau)h(t-\tau)d\tau \qquad \text{(A.1)}$$

and is often written as $y(t)=s(t)*h(t)$ where '*' denotes convolution. Convolution can be visualized as shown in Figure A.2 where the input signal is partitioned into many segments of equal width. Each segment, at its respective point in time, is applied to the system, resulting in an associated output response. The output responses are then summed to give the overall response. When the width of each input segment is made arbitrarily small (many segments), the output can be viewed as a superposition of impulse responses where each impulse response is initiated at the time of the corresponding input signal segment, and has a weight proportional to the area (or height) of the input segment. The integral in (A.1) represents the limiting case when the segment width in Figure A.2 goes to zero, i.e., the input signal is partitioned into an infinite number of segments.

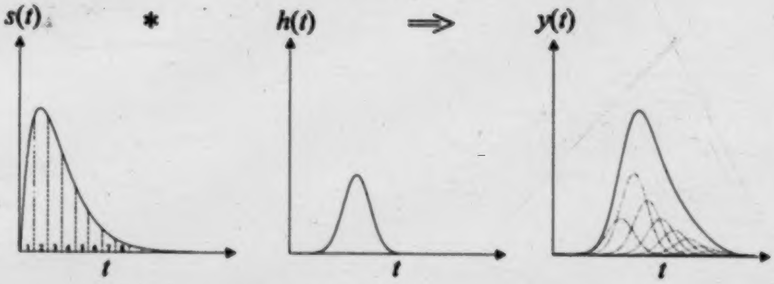

Figure A.2 Visualizing the convolution of an input signal $s(t)$ with the impulse response $h(t)$ of a linear system to produce the output response $y(t)$.

Closed form solutions to (A.1) exist only for certain forms of $s(t)$ and $h(t)$. For arbitrary $s(t)$ and $h(t)$, the operation in (A.1) would have to be done numerically. This is computationally intensive because a numerical integration must be performed for each point in time the output response is desired. If the signals $s(t)$ and $h(t)$ are first mapped into a complex plane using the Fourier transform, the operation in (A.1) can be reduced to multiplication. The frequency spectrum $U(f)$ of a signal $u(t)$ is obtained using the Fourier transform, defined as

$$U(f) = \Im\{u(t)\} = \int_{-\infty}^{\infty} u(t)e^{-j2\pi ft}dt \tag{A.2}$$

and the signal $u(t)$ can be recovered from $U(f)$ using the inverse Fourier transform, defined as

$$u(t) = \Im^{-1}\{U(f)\} = \int_{-\infty}^{\infty} U(f)e^{j2\pi ft}df \tag{A.3}$$

The function $U(f)$ is, generally, complex-valued, and the time signal $u(t)$ can also be complex-valued, such as when modeling bandpass systems with a lowpass equivalent. Letting $S(f)=\Im\{s(t)\}$ and $H(f)=\Im\{h(t)\}$, the convolution in (A.1) can be arrived at from $y(t)=\Im^{-1}\{Y(f)\}$ where $Y(f)=S(f)H(f)$. In other words, convolution in the time domain is equivalent to multiplication in the frequency domain. The Fourier transform of a system's impulse response is called a transfer function. If the system consists of a cascade of linear sub-systems, i.e., the output of one sub-system fed to the input of another, then the entire system can be characterized by a single transfer function, $H(f)$, given by the product of the sub-system transfer functions. Letting $H_1(f)$ be the transfer function for the first sub-system, $H_2(f)$ for the second, etc., the overall transfer function can be obtained from

$$H(f) = H_1(f)H_2(f)\ldots H_{Ns}(f) \tag{A.4}$$

were Ns is the number of linear sub-systems. Therefore, according to (A.4), the output response does not depend on the order of the linear sub-systems because of the commutative property of multiplication.

In order to simulate a linear system using a digital computer, it is necessary to operate on the discrete-time representation of time and frequency-domain signals[9]. The transformation from a discrete-time signal to a discrete-frequency signal can be accomplished using a discrete version of (A.2) known as the discrete Fourier transform.

---

[9] Time and frequency signals are referred to throughout; however, it should be noted that the Fourier transform, and its inverse, can be applied to signals of other dimensions. For example, a probability

11.1.3 The Discrete Fourier Transform

When the time and frequency signals are discrete, the Fourier transform and inverse Fourier transform are appropriately called the discrete Fourier transform (DFT) and inverse discrete Fourier transform (IDFT). An efficient algorithm can be used to perform these transformations, in which case the transforms are said to be *fast*, and the DFT and IDFT are called the fast Fourier transform (FFT) and inverse fast Fourier transform (IFFT), respectively. Shown below are definitions of the FFT and IFFT for three popular computer programs including MATLAB, Mathcad and Mathematica.

$$U = fft(u) \quad \Rightarrow \quad U_m = \sum_{n=1}^{N} u_n e^{-j2\pi(n-1)(m-1)/N} \qquad \text{MATLAB (A.5a)}$$

$$u = ifft(U) \quad \Rightarrow \quad u_n = \frac{1}{N}\sum_{m=1}^{N} U_m e^{j2\pi(n-1)(m-1)/N} \qquad \text{MATLAB (A.5b)}$$

$$U = fft(u) \quad \Rightarrow \quad U_m = \frac{1}{\sqrt{N}}\sum_{n=0}^{N-1} u_n e^{j2\pi nm/N} \qquad \text{Mathcad (A.6a)}$$

$$u = ifft(U) \quad \Rightarrow \quad u_n = \frac{1}{\sqrt{N}}\sum_{m=0}^{N-1} U_m e^{-j2\pi nm/N} \qquad \text{Mathcad (A.6b)}$$

$$U = fft(u) \quad \Rightarrow \quad U_m = \frac{1}{\sqrt{N}}\sum_{n=1}^{N} u_n e^{j2\pi(n-1)(m-1)/N} \qquad \text{Mathematica(A.7a)}$$

$$u = ifft(U) \quad \Rightarrow \quad u_n = \frac{1}{\sqrt{N}}\sum_{m=1}^{N} U_m e^{-j2\pi(n-1)(m-1)/N} \qquad \text{Mathematica(A.7b)}$$

In (A.5)-(A.7), n is an index into the array for the discrete time record where the first element corresponds to $t=0$, the second element to $t=\Delta t$, the third element to $t=2\Delta t$, etc., where Δt is the sampling interval. Similarly, m is an index into the array for the discrete frequency record where the first element corresponds to $f=0$, the second element to $f=\Delta f$, the third element to $f=2\Delta f$, etc., where Δf is the frequency-domain sampling interval. There are three places where the definition of the FFT/IFFT may differ in (A.5)-(A.7). These include a constant scaling factor, the sign of the exponent, and the index of the first array element. For example, MATLAB introduces a scaling

---

density function can be mapped to a characteristic function using the Fourier transform. Time and frequency signals are simply appropriate for the discussion here.

factor of $1/N$ in the IFFT, whereas Mathcad and Mathematica use a scaling factor of $1/\sqrt{N}$ in the FFT and IFFT. Also, in Mathematica and Mathcad the sign of the exponents are reversed. In Mathcad, the index for the first array element is 0, whereas MATLAB and Mathematica start at an index of 1. These differences in the FFT/IFFT are trivial and pose no additional complexity to system analyses. It is, however, important to know how the FFT and IFFT are defined in order to apply appropriate scaling factors for certain analyses, as discussed later on.

11.1.4 Periodicity

When using the FFT and IFFT, it is important to understand the implicit periodic nature of the discrete time and frequency records where the periodicity is determined by the time and frequency sampling intervals. To illustrate, consider a continuous-time function $u(t)$ that exists over the interval $[0\ T]$ and is zero elsewhere. Also, let us specify the transform pair $u(t) \Leftrightarrow U(f)$. If the time function $u(t)$ is sampled at evenly-spaced intervals Δt apart, then the following relationship between $u(t)$ and $U(f)$ will exist

$$\Im\{u(n\Delta t)\} = \frac{1}{\Delta t} rep_{\frac{1}{\Delta t}}[U(f)] \qquad \text{(A.8a)}$$

where the *rep* operator means repetition or replication of the function $U(f)$ every $1/\Delta t$ in the positive and negative sense along the frequency axis. Similarly, if the frequency function $U(f)$ is sampled at evenly-spaced intervals Δf apart, the following relationship will exist

$$\Im^{-1}\{U(m\Delta f)\} = \frac{1}{\Delta f} rep_{\frac{1}{\Delta f}}[u(t)] \qquad \text{(A.8b)}$$

Note that (A.8a) and (A.8b) are mirror images of one another. Therefore, sampling a continuous signal in one domain results in replication of the signal in the other domain. If the signal is discrete in both domains, then combining (A.8a) and (A.8b) gives

$$\Im\{T rep_T[u(k\Delta t)]\} = f_s rep_{f_s}[U(m\Delta f)] \qquad \text{(A.8c)}$$

where $T = 1/\Delta f$ is the period of the replicated time record, and $f_s = 1/\Delta t$ is the period of the replicated frequency record. It should be noted that the FFT and IFFT operate on discrete time and frequency records that are periodic in accordance with (A.8); however, only a single period is stored in the discrete time and frequency record arrays from 0 to T and 0 to f_s, respectively. The time record will consist of signal samples at $\{0, \Delta t, 2\Delta t, ..., T\text{-}\Delta t\}$, whereas the frequency record will consist of samples at $\{0, \Delta f, 2\Delta f, ..., f_s\text{-}\Delta f\}$. Figure A.3 is a visual representation of (A.8c) and illustrates the periodicity of the time and frequency records.

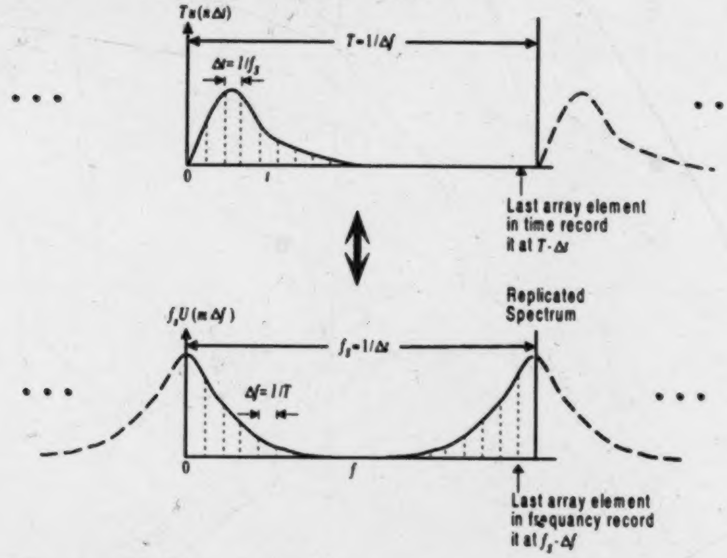
$Tu(n\Delta t)$
$T=1/\Delta f$
$\Delta t=1/f_s$
• • •
• • •
0
t
Last array element
in time record
it at $T\text{-}\Delta t$
Replicated
Spectrum
$f_sU(m\Delta f)$
$f_s=1/\Delta t$
$\Delta f=1/T$
• • •
• • •
0
f
Last array element
in frequancy record
it at $f_s\text{-}\Delta f$

Figure A.3 Relationship between the discrete time record $u(n\Delta t)$ and the discrete frequency record $U(m\Delta f)$.

The periodic nature of the discrete time and frequency records in Figure A.3 is important to remember, especially regarding any impact it may have on system modeling. In some cases, the input to a system is truly periodic, for which the properties in Figure A.3 are desirable. In other cases it may be desired to obtain the system response to a one-time excitation (energy signal), in which case the impact of the periodic properties in Figure A.3 must be understood. Simulation of a system's response to an energy (aperiodic) signal and to a power (periodic) signal is described in the following sections.

11.1.5 System Response to an Energy (aperiodic) Signal

Consider an analog energy signal $s(t)$ that is non-zero only within the interval $[0\ T]$. If $s(t)$ is input to a linear system having an impulse response $h(t)$, then the output can be obtained from $y(t)=s(t)*h(t)$, or from $y(t)=\Im^{-1}\{Y(f)\}$ where $Y(f)=S(f)H(f)$. The objective is to carry out these operations using the FFT and IFFT on a computer. To understand how this can be done, and how to account for scaling factors, first consider the following *intuitive* approach to converting a continuous Fourier transform into a discrete Fourier transform.

If $U(f)$ in (A.2) is evaluated at discrete frequencies, then

$$U((m-1)\Delta f)=U_m=\int_{-\infty}^{\infty}u(t)e^{-j2\pi(m-1)\Delta f t}dt \tag{A.9}$$

where m is an integer index for which $m=1$ corresponds to zero frequency. Assuming that $u(t)$ is non-zero only within the interval $[0\;T]$ and is sampled at $f_s=1/\Delta t$, the time record will have $N=T/\Delta t$ elements, and the integral in (A.9) can be expressed as the following summation

$$U((m-1)\Delta f)=U_m=\Delta t\sum_{n=1}^{N}u((n-1)\Delta t)e^{-j2\pi(m-1)\Delta f(n-1)\Delta t} \tag{A.10}$$

As described previously, sampling a continuous function u(t) at intervals spaced Δt apart results in a replicated spectrum every $f_s=1/\Delta t$ in the frequency domain. Because there are N samples, $\Delta f=f_s/N$. Writing $u_n=u((n-1)\Delta t)$ and using $\Delta f=f_s/N=1/(\Delta t N)$ in (A.10), gives

$$U((m-1)\Delta f)=U_m=\Delta t\sum_{n=1}^{N}u_n e^{-j2\pi(m-1)(n-1)/N} \tag{A.11}$$

which has the same form as the FFT in (A.5a), except for the scaling factor Δt. Therefore, if the function $u(t)$ is sampled to obtain u_n, and then the FFT in (A.5a) is used to obtain the frequency record U_m=FFT(u_n), each element in U_m can be interpreted as a point on the continuous spectrum $U(f)$ if U_m is first multiplied by Δt. Note that each element in U_m is at a frequency $(m\text{-}1)\Delta f$, where $\Delta f=1/T=1/(N\Delta t)$, for frequencies up to the Nyquist frequency, i.e., $(m\text{-}1)\Delta f\leq f_s/2$. For frequencies above the Nyquist frequency, U_m contains samples of $U(f)$ at negative frequencies, given by $(m\text{-}1)\Delta f\text{-}f_s$.

It is also possible to obtain the time function corresponding to a known continuous frequency spectrum by reversing the process described above—for example, the impulse response can be obtained from a system's transfer function using the IFFT. To do this, the continuous transfer function $U(f)$ is first sampled at intervals spaced Δf apart. Recall that the frequency sampling interval determines the length of the time record through $T=1/\Delta f$. Also, the range over which the transfer function $U(f)$ is sampled, from $-f_s/2$ to $+f_s/2$, determines the sampling interval of the time record through $\Delta t=1/f_s$. Once the transfer function is in its sampled from, it should be circular left shifted so that the sample at $f=0$ is the first element of the array. This will shift all samples at negative frequencies up by an amount f_s, after which the sampled transfer function will be compatible with the IFFT, as shown in Figure A.3. If the IFFT function in (A.5b) is used, then the result must be scaled by $1/\Delta t=f_s$ in order to interpret the time record as sampled values of the continuous function $u(t)$, as it would be obtained from (A.3). Note that the corresponding time for each sample of the time record is given by $(n\text{-}1)\Delta t$. If definitions other than (A.5) are used for the FFT and IFFT, such as (A.6) or (A.7), then the appropriate scaling factors should be applied in accordance with the above discussion, i.e., the appropriate scaling factor can be determined by comparing (A.11) with the definition of the FFT.

Now that the relationship between the continuous and discrete Fourier transform is understood, it is possible to carry out the operation $y(t)=s(t)*h(t)$ using the FFT and IFFT. For this discussion, it will be assumed that the definitions in (A.5) apply. First, $s(t)$ and $h(t)$ are sampled to obtain the discrete time records s_n and h_n. Then, the FFT is used to obtain S_m and H_m, which would be scaled by Δt to obtain sampled versions of the circular-left shifted frequency spectrums for $s(t)$ and $h(t)$. Y_m is then computed from $(1/\Delta t)\Delta t S_m \Delta t H_m$ where the multiplication is done element-by-element. Finally, y_n is obtained from $y_n=\mathrm{IFFT}(Y_m)$. In some cases the starting point may be the frequency spectrums $S(f)$ and $H(f)$. In this case, these would first be sampled and circular-left shifted in accordance with the previous discussion, and then multiplied element-by-element. The result would then be scaled by $(1/\Delta t)$ to obtain Y_m, which could then be used to get $y_n=\mathrm{IFFT}(Y_m)$. Each element in y_n could then be interpreted as a sampled value of the continuous function $y(t)$.

It is important to remember that when using the FFT and IFFT to calculate the response of a linear system to a continuous energy signal, what is actually being simulated is the convolution of periodically-extended versions of the input signal and the system's impulse response. Therefore, the duration of the sampled records must be sufficiently long to avoid time aliasing in the result, as shown in Figure A.4a. One way to avoid time aliasing is to add zero-value elements (called zero padding) to s_n and h_n, as shown in Figure A.4b. The number of elements added should be equal to or greater than the number of elements in the original records. Obviously, because of the periodically-extended nature of the sampled signals, it is not, strictly speaking, possible to simulate the convolution of continuous-time signals that are of infinite duration. If the signals are monotonically decreasing, however, or at least have an envelope that is monotonic decreasing, then it is often possible to truncate the signals at an appropriate point, beyond which the signal's amplitude is negligible.

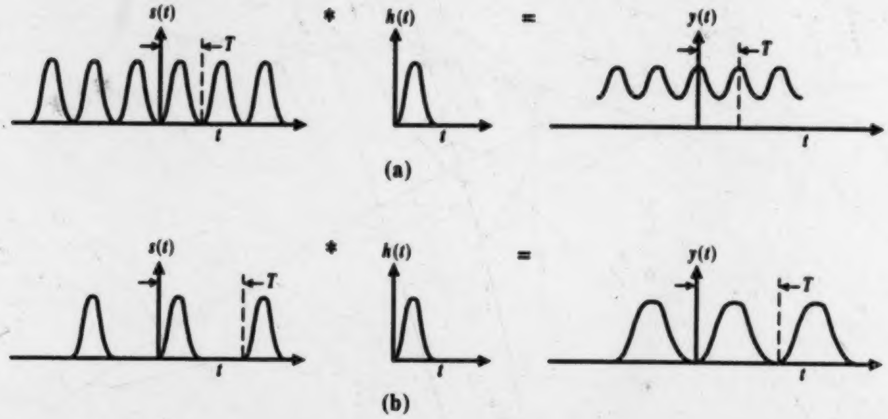

Figure A.4 (a) resulting output $y(t)$ when time record is not extended with zero padding; (b) resulting output $y(t)$ when time record is extended with zero padding.

One way to check a result is to do the simulation with twice the number of points, or more, as a first simulation, and then compare the results. If the results show any significant difference, then points should be added to the time records until the truncation error is within acceptable limits.

11.1.6 System Response to a Power (periodic) Signal

The FFT and IFFT are ideally suited for simulating the response of a linear system to a periodic signal, such as a periodic pseudorandom bit sequence (PRBS). Recall that the spectrum of a periodic signal consists of line spectra spaced $1/T$ apart where T is the period. If the periodic signal is passed through a linear system, then each spectral component will be altered by the magnitude and phase response of the system's transfer function at that frequency. For accurate simulation, the periodic signal should be sampled at a sufficiently high rate to avoid spectral aliasing, and the time record should span one complete period, i.e., samples should be recorded at $\{0, \Delta t, 2\Delta t, \ldots, (T-\Delta t)\}$ to produce a record length with $N=T/\Delta t$ elements. The system's impulse response or transfer function should be put into the form of an FFT/IFFT compatible frequency record, as discussed previously. Note that the system response frequency record will have N elements spaced $\Delta f=1/T$ Hz apart, with the first frequency sample at $f=0$. The time record of the output can then be obtained by computing the FFT of the input time record, multiplying it (element-by-element) with the system response frequency record, and then computing the IFFT of the result.

Note that the frequency record elements of the system's response should truly reflect the magnitude response at a particular frequency, with no additional scaling. For example, if the system has a gain of unity at DC, then the magnitude of the first frequency component should be 1. Similarly, if the system response is down by 20 dB at a particular frequency, then the magnitude of a frequency record element at the corresponding frequency should be 0.1. Any arbitrary scaling introduced by the FFT, as defined by a particular program, is accounted for when the IFFT is computed on the result.

11.1.7 Power Spectral Density and Spectral Resolution

The power spectral density (PSD) of a periodic signal is obtained by squaring the magnitude of each spectral component in its frequency spectrum. For example, letting u_n be the discrete time record of a continuous signal, $u(t)$, the PSD is given by $|U_m|^2$ where $|\cdot|$ denotes absolute value and U_m=FFT(u_n). Furthermore, U_m is usually normalized so that the largest magnitude of any element is unity, and the PSD is often expressed in dB. Therefore, a spectral component with a value of -25 dB implies the power at that frequency is 25 dB lower than the component containing the largest power, which is normalized to zero dB. In some cases, though, it may be desired to express the actual power of each spectral component—for example, as it might be observed on a spectrum analyzer. Of course, to do this, knowledge of the type of signal and load must be known, as well as scaling factors introduced by the FFT in a particular program. For example, assume $u(t)$ is a voltage or current with a corresponding sampled time record u_n, and assume a load normalized to unity. The instantaneous power of this signal is then $P(t) = u^2(t)$, and assuming $u(t)$ is periodic with period T, the average power is

$$P_{avg} = \frac{1}{T} \int_{\langle T \rangle} u^2(t)dt \tag{A.12}$$

where the integration is over one period. Assuming the FFT is defined as in (A.5a), the power in each frequency component is obtained from

$$P_m = \left| \frac{1}{N} U_m \right|^2 \tag{A.13}$$

where N is the number of elements in the time or frequency record. Note that the scaling factor of $1/N$ in (A.13) is arrived at by comparing (A.5a) to (A.8b) and (A.11). For a real-valued signal, recall that the elements in U_m are symmetric about $N/2$.

Therefore, the result in (A.13) can be multiplied by 2 to obtain a single-sided PSD, after which only components up to $N/2$ (i.e., frequencies up to $f_s/2$) are considered. Finally, the actual load and signal type can be accounted for by applying the appropriate scaling factor. For example, if $u(t)$ is a voltage applied across a 50 Ω load resistor, the power in dBm of a spectral component at frequency $f = 3\Delta f = 3/T$ is

$$P_4 = 10\log\left(\frac{1000}{50}\frac{2}{N^2}\left|U_4\right|^2\right) \tag{A.14}$$

If $u(t)$ were a current, then the factor of 50 would be in the numerator in (A.14).

When plotting a PSD, or energy spectral density (ESD) for aperiodic signals, it is often desired to increase the resolution of the spectrum, i.e., decrease the spacing between spectral components. Recall that the spacing between spectral lines is determined by the duration of the time record, through $\Delta f = 1/T$. Therefore, the spectral resolution is increased be simply extending the duration of the time signal. For energy signals this is easily accomplished by padding the time record with zeros—to increase the spectral resolution further, append more zero-valued elements to the time record. When simulating a periodic signal, simply record the time record over integer multiples of a period to increase the spectral resolution.

11.1.8 Summary

Simulating linear, time-invariant analog systems using a discrete-time representation was explained. It was shown that the FFT and IFFT are discrete versions of the Fourier transform and inverse Fourier transform, respectively, and that they can be used to carry out the operation of convolution between continuous-time signals, provided appropriate scaling factors are accounted for. The implicit periodic nature of the FFT and IFFT was illustrated, and the importance of zero padding to achieve a linear convolution was discussed. Simulation of a linear system having a periodic input is a natural process using the FFT and IFFT. Finally, calculating the PSD of a signal can be achieved using the FFT, and the spectral resolution of the PSD can be increased by increasing the duration of the time record.

11.2 Appendix B: MATLAB Programs Based on a Static Noise Model

Analyses based on a static noise model used the following MATLAB programs.

Programs for Binary Signaling

```
% BINARY:       Script that calculates the receiver sensitivity of a binary
%               optical communication system with dependence on essentially
%               any system parameter.
%
% Notes:        This script is intended to generate a receiver sensitivity
%               curve versus a desired system parameter. To do this, one of
%               the system parameters below would be vectorized, while the others
%               would be scalar constants. Then, the "for" loop would be set
%               up to index the vectorized parameter when building up the array
%               representing the receiver's sensitivity. The vectorized parameter
%               should be specified as the abscissa when plotting the result.
%
%               This script makes use of a static noise model and, therefore,
%               assumes ideal levels with zero ISI.

%   Created:    03/8/97         (month/day/year)
%  Modified:    03/10/97
% Author(s):    Sheldon S. Walklin

clear all  % clear MATLAB workspace
clear global

%************************* Define System Parameters *************************

r=0.1;          % optical extinction ratio (P0/P1)
lambda=1557;    % carrier wavelength (nm)
RIN=-140;       % laser source relative intensity noise (dB/Hz)
G=[0:2:40];     % EDFA preamplifier gain (dB)
c1=0.6;         % EDFA preamp input coupling efficiency (pos. dB)
c2=4;           % EDFA preamp output coupling efficiency (pos. dB)
Nsp=2;          % EDFA preamp spontaneous emission factor (>=1)
mt=2;           % number of polarization modes (1 or 2)
Ro=0.6;         % photodetector responsivity (A/W)
Bo=180e9;       % bandwidth of optical bandpass filter (Hz)
Be=7e9;         % one-sided bandwidth of electrical receiver (Hz)
B=10e9;         % bit rate (bits/s)
R=50;           % receiver thermal noise resistance (Ohms)
T=300;          % receiver thermal noise temperature (Kelvins)
F=3;            % electrical receiver noise figure (dB)
BER=1e-9;       % target bit-error ratio

% The following parameters are used to calculate RIN from PM-to-AM
% noise conversion. If a fixed RIN value is desired, specify it above
% and comment out the RIN calculation in the for loop.

lw=10e6;        % source linewidth (Hz)
```

```
D=17;             % fiber dispersion (ps/(km-nm))
L=50;             % fiber length (km)

%************************ End of Parameter Definitions ************************

% physical constants
h=6.626e-34;      % Planck's constant (Joule*sec.)
c=2.998e8;        % free-space speed of light (m/s)

Pavg_vec=[];      % initialize array for receiver's sensitivity

% calculate receiver's sensitivity at each parameter value
for n=1:length(G)
  disp(['Calculating point ' num2str(n) ' of ' num2str(length(G))]);
  %RIN=rininlbe(Be, lw(n), D, L,lambda);
  % get power in MARK state, and total ASE ref. to input of EDFA
  [P1,Pase]=pwrbinry(r,lambda,RIN,G(n),c1,c2,Nsp,mt,Ro,Bo,Be,R,T,F,BER);
  Pavg=0.5*(P1+r*P1);      % calculate average power
  Psig_Pase=10*log10(Pavg/Pase); % ratio of siganl to ASE power
  Pavg_dBm=10*log10(Pavg*1e3); % average received optical power in dBm
  photons=Pavg*lambda*1e-9/(B*h*c);% average number of photons per bit
  % add point to receiver sensitivity array
  Pavg_vec=[Pavg_vec Pavg_dBm];
end;

% plot results
figure                                  % open new figure window
plot(G,Pavg_vec,'w');                   % plot result
xlabel('Preamplifier Gain, dB');        % label abscissa
ylabel('Receiver Sensitivity, dBm');    % label ordinate
grid on;                                % turn on grid in plot


function RIN_dB_Hz=rininlbe(Be, lw, D, L, lambda)
% RININLBE:   Calculates the average RIN in dB/Hz from PM-to-AM noise
%             conversion using the theory of Yamamoto, et al.
%
% Input Parameters:
%
%       Be - noise-equivalent bandwidth of the receiver in Hz.
%            The receiver is assumed to be an ideal, brick-wall
%            lowpass filter.
%       lw - laser source linewidth in Hz
%        D - fiber dispersion in ps/(km-nm)
%        L - fiber length in km
%   lambda - carrier wavelength in nm
%
% Returned Values:
%
%   RIN_dB_Hz - relative intensity noise from PM-to-AM noise
%               conversion in dB/Hz.
%

%   Created:    03/23/97        (month/day/year)
% Modified:
% Author(s):    Sheldon S. Walklin

c=3e5;                    % speed of light (nm/ps)

% Dispersion parameter
F=(1e-24*(lambda^2*D)/(4*pi*c))*L;

%xmax=4*Be*sqrt(pi*F)              % ensure argument is not too large for fresnels.m function

% calculate total RIN in bandwidth Be
RIN=(2*lw/(pi*Be))*(cos(8*pi^2*F*Be^2)-1+...
4*pi^(3/2)*Be*sqrt(F)*fresnels(4*Be*sqrt(pi*F)));

RIN_Hz=RIN/Be;                     % RIN per 1 Hz bandwidth
RIN_dB_Hz=10*log10(RIN_Hz);  % RIN in dB/Hz

return;




function [P1,Pase]=pwrbinry(r,lambda,RIN,G,c1,c2,Nsp,mt,Ro,Bo,Be,R,T,F,BER)
% PWRBINRY: Calculates the required power in a binary MARK for a given BER
%
% Input Parameters:
%
%          r - optical extinction ratio (r=Po/P1)
%     lambda - carrier wavelength (nm)
%        RIN - relative-intensity noise (dB/Hz)
%          G - EDFA gain (dB)
%         c1 - EDFA input coupling efficiency (pos. dB)
%         c2 - EDFA output coupling effieciency (pos. dB)
%        Nsp - EDFA spontaneous emission factor
%         mt - number of polarization modes (1 or 2)
%         Ro - photodetector responsivity (A/W)
%         Bo - optical bandpass filter bandwidth (Hz)
%         Be - one-sided, electrical receiver bandwidth (Hz)
%          R - thermal noise resistance (Ohms, usually 50)
%          T - receiver noise temperature (Kelvins)
%          F - receiver, electrical amplifier noise figure (dB)
%        BER - target bit-error ratio (usually 1E-9)
%
% Returned Values:
%
%         P1 - optical power in a logical ONE (Watts)
%       Pase - total ASE power referenced to input of EDFA (Watts)

%   Created:    03/09/97           (month/day/year)
%  Modified:    03/09/97
% Author(s):    Sheldon S. Walklin

Pmin=-40;                 % min. received optical power to consider (dBm)
Pmax=0;                   % max. received optical power to consider (dBm)
```

```
lambda=lambda*1e-9;        % convert wavelength to meters
G=10^(G/10);               % convert EDFA gain to absolute power gain
c1=10^(-c1/10);            % absolute input coupling efficiency
c2=10^(-c2/10);            % absolute output coupling efficiency
F=10^(F/10);               % electrical receiver amplifier noise factor
Pmin=10^(Pmin/10-3);       % min. power to consider in Watts
Pmax=10^(Pmax/10-3);       % max. power to consider in Watts

% define physical constants
q=1.602e-19;               % electron charge
h=6.626e-34;               % Planck's Constant (Joule-second)
c=2.998e8;                 % free-space speed of light (m/s)
k=1.381e-23;               % Boltzmann's constant (Joule/Kelvin)

Pn=(G-1)*h*c*Nsp*Bo/lambda;      % ASE power in single pol. mode
Pase=mt*Pn/(G*c1);               % total ASE power on photodetector (Watts)
                                 % referenced to EDFA input

% Calculate constants used in expressing noise terms
% All noise currents have units (Amps^2)

% stationary noise

Nth=(4*k*T*F*Be/R);                              % thermal noise
Nase_shot=2*mt*Pn*c2*Ro*q*Be;                    % ASE shot noise
Nsp_sp=(mt*Pn*c2*Ro)^2*Be*(2*Bo-Be)/(Bo^2);      % spont.-spont. beat noise

ks=Nth+Nase_shot+Nsp_sp;                         % total stationary noise

% noise linearly proportional to received power

kshot=2*q*Ro*G*c1*c2*Be;                 % shot noise constant of proportionality
ksig_sp=4*Pn*G*c1*(Ro*c2)^2*Be/Bo;       %sig.-spont. beat noise const. of prop.
k1=kshot+ksig_sp;                        % proportianality constant for noises that are
                                         % linearly proportional to received power

% noise proportional to square of received power

k2=(c1*G*c2*Ro)^2*Be*10^(RIN/10);        % proportionality constant for RIN

Iase=mt*Pn*c2*Ro;          % current from ASE (Amps)
ksig=c1*G*c2*Ro;           % proportionality constant for signal currents

% Solve for received power in MARK state and required number
% of iterations.
[P1 itr]=binsens([Pmin Pmax],ksig,Iase,r,ks,k1,k2,BER);

itr;

return;


function [P1, itr]=binsens(P,ksig,Iase,r,ks,k1,k2,BER)
```

```
% BINSENS:     Calculates the optical power in a MARK state to obtain
%              a specified BER.
%
% Notes:       This function is called from "pwrbinary.m." Details of the
%              parameters passed to this function are provided in the calling
%              function.
%
% Input Parameters:
%
%          P - two-element vector containing the minimum and maximum power to
%              consider in Watts. Vector is of form [Pmin Pmax].
%       ksig - proportionality constant for calculating signal currents (A/W)
%       Iase - total photodetector current due to ASE (Amps)
%          r - optical exticntion ratio (P0/P1)
%         ks - total stationary noise current (A^2)
%         k1 - proportionality constant for calculating noise currents
%              that are linearly proportional to received optical power (A^2/W)
%         k2 - proportionality constant for calculating noise currents
%              that are proportional to the square of received optical power,
%              i.e., RIN (A^2/W^2)
%        BER - target bit-error ratio
%
% Returned Values:
%         P1 - optical power in MARK state that produces the targer BER (Watts)
%        itr - number of iterations required to obtain P1

%    Created:   03/08/97        (month/day/year)
%   Modified:   03/10/97
%  Author(s):   Sheldon S. Walklin

Pmin=P(1);                 % minimum received power to consider (Watts)
Pmax=P(2);                 % maximum received power to consider (Watts)

tol=0.01;                  % error tolerance for BER
ber_max=BER*(1+tol);       % upper limit for BER
ber_min=BER*(1-tol);       % lower limit for BER
max_itr=100;               % maximum number of iterations allowed
itr=1;                     % initialize iterations counter

% check that BER is within optical power limits
P1=Pmax;                   % optical power in mark state (Watts)
I0=ksig*r*P1+Iase;         % photocurrent for logical ZERO (Amps)
I1=ksig*P1+Iase; % photocurrent for logical ONE (Amps)
std0=sqrt(ks+k1*r*P1+k2*(r*P1)^2);% logical ZERO standard deviation (Amps)
std1=sqrt(ks+k1*P1+k2*P1^2);      % logical ONE standard deviation (Amps)
max_BER=Q((I1-I0)/(std0+std1)); % BER at upper optical power limit
P1=Pmin;                   % optical power in mark state (Watts)
I0=ksig*r*P1+Iase;         % photocurrent for logical ZERO (Amps)
I1=ksig*P1+Iase; % photocurrent for logical ONE (Amps)
std0=sqrt(ks+k1*r*P1+k2*(r*P1)^2);% logical ZERO standard deviation (Amps)
std1=sqrt(ks+k1*P1+k2*P1^2);      % logical ONE standard deviation (Amps)
min_BER=Q((I1-I0)/(std0+std1)); % BER at lower optical power limit

% exit if target BER is outside optical power limits
if max_BER>BER
```

```
        disp('max. power passed to function binsens is too low');
        return;
elseif min_BER<BER
        disp('min. power passed to function binsens is too high');
        return;
end;

% solve for optical power in MARK state that gives target BER
while (itr<=max_itr),
  P1=(Pmin+Pmax)/2;% set new received power level to calculate BER at
  I0=ksig*r*P1+Iase;        % photocurrent for logical ZERO (Amps)
  I1=ksig*P1+Iase;          % photocurrent for logical ONE (Amps)
  std0=sqrt(ks+k1*r*P1+k2*(r*P1)^2);% standard deviation for logical ZERO (Amps)
  std1=sqrt(ks+k1*P1+k2*P1^2);   % standard deviation for logical ONE (Amps)
  ber=Q((I1-I0)/(std0+std1));    % bit-error ratio

% check if BER is within tolerance limits
  if (ber>=ber_min)&(ber<=ber_max),
        break;
  end;

  if ber>BER                % narrow difference between optical power limits
        Pmin=P1;
  else,
        Pmax=P1;
  end;

  itr=itr+1;                % increment iterations counter

end;

% issue warning if solution did not converge within max. number of iterations
if itr>max_itr
        disp('max. iterations reached in function binsens');
end;

return;


function y=Q(x)
% Q: calculates 1-CDF for a normal distribution where
% CDF is the cummulative distribution of the normal PDF.
y=0.5*erfc(x/sqrt(2));
return;
```

Programs for 4-ary ASK

```
% FOURARY:   Script that calculates the receiver sensitivity of a 4-level ASK
%            optical communication system with dependence on essentially any
%            system parameter.
%
% Notes:     This script is intended to generate a receiver sensitivity
%            curve versus a desired system parameter. To do this, one of
%            the system parameters below would be vectorized, and the rest
%            would be scalar constants. Then, the "for" loop would be set
%                   up to index the vectorized parameter when building up the array
%                   representing the receiver's sensitivity. The section that plots
%                   the result should also be changed to show the proper parameter
%                   for the abscissa.
%
%                   This script makes use of a static noise model and, therfore,
%                   assumes ideal levels with zero ISI. Levels can be optimized to
%                   produce the lowest BER.

%   Created:        03/8/97         (month/day/year)
% Modified:         03/10/97
% Author(s):        Sheldon S. Walklin

clear all           % clear MATLAB workspace
clear global

%************************ Define System Parameters ************************

r=0.1;              % optical extinction ratio (P0/P1)
lambda=1550;        % carrier wavelength (nm)
RIN=-500;           % laser source relative intensity noise (dB/Hz)
G=15;               % EDFA preamplifier gain (dB)
c1=0;               % EDFA preamp input coupling efficiency (pos. dB)
c2=3;               % EDFA preamp output coupling efficiency (pos. dB)
Nsp=[1:1:4];        % EDFA preamp spontaneous emission factor (>=1)
mt=2;               % number of polarization modes (1 or 2)
Ro=1;               % photodetector responsivity (A/W)
Bo=180e9;           % bandwidth of optical bandpass filter (Hz)
Be=3.5e9;           % one-sided bandwidth of electrical receiver (Hz)
B=10e9;             % bit rate (bits/s)
R=50;               % receiver thermal noise resistance (Ohms)
T=310;              % receiver thermal noise temperature (Kelvins)
F=3;                % electrical receiver noise figure (dB)
BER=1e-9;           % target bit-error ratio

% The following parameters are used to calculate RIN from PM-to-AM
% noise conversion. If a fixed RIN value is desired, specify it above
% and comment out the RIN calculation in the for loop.

lw=4e6;             % source linewidth (Hz)
D=17;               % fiber dispersion (ps/(km-nm))
L=50;               % fiber length (km)

%************************ End of Parameter Definitions ************************

% physical constans
h=6.626e-34;        % Planck's constant (Joule-sec.)
c=2.998e8;          % free-space speed of light (m/s)


Pavg_vec=[];        % initialize array for receiver's sensitivity
e1_vec=[];          % initialize array for normalized weight of logical ONE
e2_vec=[];          % initialize array for normalized weight of logical TWO

% calculate receiver's sensitivity at each parameter value
```

```
for n=1:length(Nsp)
  disp(['Calculating point ' num2str(n) ' of ' num2str(length(Nsp)) '...']);
  % RIN=rininlbe(Be, lw(n), D, L,lambda);
  % get optical power of highest level (logical THREE), and ASE power
  % referenced to input of EDFA. Also, get optimal level spacing
  [P3, e, Pase]=pwr4ary(r,lambda,RIN,G,c1,c2,Nsp(n),mt,Ro,Bo,Be,R,T,F,BER);
  P0=r*P3;                   % optical power in logical ZERO
  P1=P0+e(1)*(P3-P0);        % optical power in logical ONE
  P2=P0+e(2)*(P3-P0);        % optical power in logical TWO
  Pavg=0.25*(P0+P1+P2+P3);        % calculate average received optical power (Watts)
  Psig_Pase=10*log10(Pavg/Pase);               % ratio of optical signal to ASE power
  Pavg_dBm=10*log10(Pavg*1e3);                 % convert average power to dBm
  photons=Pavg*lambda*1e-9/(B*h*c);            % calculate average no. photons/bit
  Pavg_vec=[Pavg_vec Pavg_dBm];                % add point to rec. sens. array
  e1_vec=[e1_vec e(1)];                        % add point to level spacing for logical ONE
  e2_vec=[e2_vec e(2)];                        % add point to level spacing for logical TWO
end;


%plot results
figure                       % open new figure window
plot(Nsp,Pavg_vec,'w');      % plot result
xlabel('Nsp');               % label abscissa
ylabel('Receiver Sensitivity, dBm'); % label ordinate
grid on;                     % turn on grid in plot

figure                       % open new figure window
plot(Nsp,e1_vec,'w',Nsp,e2_vec,'w');          % plot level spacing
xlabel('Nsp');               % label abscissa
ylabel('Normalized Level Weights');% label ordinate
grid on;                     % turn on grid in plot


function [P3,e,Pase]=pwr4ary(r,lambda,RIN,G,c1,c2,Nsp,mt,Ro,Bo,Be,R,T,F,BER)
% PWR4ARY:   Calculates the required power in the highest 4-ary symbol
%            to obtain a given BER
%
% Input Parameters:
%
%        r - optical extinction ratio (r=Po/P1)
%   lambda - carrier wavelength (nm)
%      RIN - source relative-intensity noise (dB/Hz)
%        G - EDFA gain (dB)
%       c1 - EDFA input coupling efficiency (pos. dB)
%       c2 - EDFA output coupling effieciency (pos. dB)
%      Nsp - EDFA spontaneous emission factor
%       mt - number of polarization modes (1 or 2)
%       Ro - photodetector responsivity (A/W)
%       Bo - optical bandpass filter bandwidth (Hz)
%       Be - one-sided, electrical receiver bandwidth (Hz)
%        R - thermal noise resistance (Ohms, usually 50)
%        T - receiver noise temperature (Kelvins)
%        F - electrical receiver amplifier noise figure (dB)
%      BER - target bit-error ratio (usually 1E-9)
```

```
%
% Returned Values:
%        P3 - optical power in a logical THREE (Watts)
%      Pase - total ASE power referenced to input of EDFA (Watts)
%         e - vector containing normalized optimal level spacing
%             [e(1) e(2)] for middle levels. These values are normalized
%             between the maximum and minimum signal power.

%   Created:    03/09/97        (month/day/year)
%  Modified:    03/09/97
% Author(s):    Sheldon S. Walklin

Pmin=-40;                   % min. received optical power to consider (dBm)
Pmax=0;                     % max. received optical power to consider (dBm)

lambda=lambda*1e-9;         % convert wavelength to meters
G=10^(G/10);                % convert EDFA gain to absolute power gain
c1=10^(-c1/10);             % absolute input coupling efficiency
c2=10^(-c2/10);             % absolute output coupling efficiency
F=10^(F/10);                % electrical receiver amplifier noise factor
Pmin=10^(Pmin/10-3);        % min. power to consider in Watts
Pmax=10^(Pmax/10-3);        % max. power to consider in Watts

% define physical constants
q=1.602e-19;                % electron charge
h=6.626e-34;                % Planck's Constant (Joule-second)
c=2.998e8;                  % free-space speed of light (m/s)
k=1.381e-23;                % Boltzmann's constant (Joule/Kelvin)

Pn=(G-1)*h*c*Nsp*Bo/lambda;     % ASE power in single pol. mode
Pase=mt*Pn/(G*c1);              % total ASE power on photodetector (Watts)
                                % referenced to EDFA input

% Calculate constants used in expressing noise terms
% All noise currents have units (Amps^2)

% stationary noise

Nth=(4*k*T*F*Be/R);                 % thermal noise
Nase_shot=2*mt*Pn*c2*Ro*q*Be; % ASE shot noise
Nsp_sp=(mt*Pn*c2*Ro)^2*Be*(2*Bo-Be)/(Bo^2);% spont.-spont. beat noise

ks=Nth+Nase_shot+Nsp_sp;            % total stationary noise

% noise linearly proportional to received power

kshot=2*q*Ro*G*c1*c2*Be;            % shot noise constant of proportionality
ksig_sp=4*Pn*G*c1*(Ro*c2)^2*Be/Bo;%sig.-spont. beat noise const. of prop.
k1=kshot+ksig_sp;                   % proportianality constant for noises that are
                                    % linearly proportional to received power

% noise proportional to square of received power

k2=(c1*G*c2*Ro)^2*Be*10^(RIN/10);% proportionality constant for RIN
```

```
Iase=mt*Pn*c2*Ro;          % current from ASE (Amps)
ksig=c1*G*c2*Ro;           % proportionality constant for signal currents

% Solve for required received power in highest symbol and get optimal level
% spacing. Also, get number of iterations used. Note that to obtain optimal
% level spacings, the function "mult4o" should be called in the line below.
% To use fixed level spacings, the function "mult4e" should be called below,
% and the level spacing should be set within that function.
[P3 e itr]=mult4e([Pmin Pmax],ksig,Iase,r,ks,k1,k2,BER);

itr

return;


function [P3, e, itr]=mult4e(P,ksig,Iase,r,ks,k1,k2,BER)
% MULT4E:      Calculates the optical power in a logical THREE
%              to obtain a specified BER for fixed level spacings.
%
% Notes:       This function is called from "pwr4ary.m." Details of the
%              parameters passed to this function are provided in the calling
%              function. This function is different from mult4o.m in that it
%              does not optimize the level spacing, i.e., it simply uses the
%              level spacing specified in this function.
%
% Input Parameters:
%
%        P - two-element vector containing the minimum and maximum power to
%            consider in Watts. Vector is of form [Pmin Pmax].
%     ksig - proportionality constant for calculating signal currents (A/W)
%     Iase - total photodetector current due to ASE (Amps)
%        r - optical exticntion ratio (P0/P3)
%       ks - total stationary noise current (A^2)
%       k1 - proportionality constant for calculating noise currents
%            that are linearly proportional to received optical power (A^2/W)
%       k2 - proportionality constant for calculating noise currents
%            that are proportional to the square of received optical power,
%            i.e., RIN (A^2/W^2)
%      BER - target bit-error ratio
%
% Returned Values:
%
%       P3 - optical power in logical THREE that produces the targer BER (Watts)
%        e - vector containing the level spacing as specified in this function.
%            e(1) is the normalized optimal level of a logical ONE and e(2) is
%            the normalized optimal level of a logical TWO. Optimal levels are
%            normalized between a logical ZERO and a logical THREE, i.e., a
%            logical ZERO is assigned a normalized value of zero and a logical
%            THREE is assigned a normalized value of one.
%      itr - number of iterations required to obtain P3

%   Created:    03/08/97          (month/day/year)
%  Modified:    05/06/97
% Author(s):    Sheldon S. Walklin
```

```
Pmin=P(1);          % minimum received power to consider (Watts)
Pmax=P(2);          % maximum received power to consider (Watts)

tol=0.01;                   % error tolerance for BER
ber_max=BER*(1+tol);        % upper limit for BER
ber_min=BER*(1-tol);        % lower limit for BER
max_itr=100;                % maximum number of iterations allowed
itr=1;                      % initialize iterations counter

% set level spacing
e1=1/3;e2=2/3;
e=[e1 e2];

% check that target BER is within limits
P3=Pmax;                    % optical power in logical 3 (Watts)
P0=r*P3;                    % optical power in a logical 0 (Watts)
P1=P0+e1*(P3-P0);           % optical power in logical 1 (Watts)
P2=P0+e2*(P3-P0);           % optical power in logical 2 (Watts)
I0=ksig*P0+Iase;            % photocurrent for logical 0
I1=ksig*P1+Iase;            % photocurrent for logical 1
I2=ksig*P2+Iase;            % photocurrent for logical 2
I3=ksig*P3+Iase;            % photocurrent for logical 3
std0=sqrt(ks+k1*P0+k2*P0^2);% logical 0 standard deviation (Amps)
std1=sqrt(ks+k1*P1+k2*P1^2);% logical 1 standard deviation (Amps)
std2=sqrt(ks+k1*P2+k2*P2^2);% logical 2 standard deviation (Amps)
std3=sqrt(ks+k1*P3+k2*P3^2);% logical 3 standard deviation (Amps)
% calculate BER at upper power limit
max_BER=0.5*(Q((I1-I0)/(std0+std1))+Q((I2-I1)/(std1+std2))+...
Q((I3-I2)/(std2+std3)));

P3=Pmin;
P0=r*P3;                    % optical power in a logical 0 (Watts)
P1=P0+e1*(P3-P0);           % optical power in logical 1 (Watts)
P2=P0+e2*(P3-P0);           % optical power in logical 2 (Watts)
I0=ksig*P0+Iase; % photocurrent for logical 0
I1=ksig*P1+Iase; % photocurrent for logical 1
I2=ksig*P2+Iase; % photocurrent for logical 2
I3=ksig*P3+Iase; % photocurrent for logical 3
std0=sqrt(ks+k1*P0+k2*P0^2);% logical 0 standard deviation (Amps)
std1=sqrt(ks+k1*P1+k2*P1^2);% logical 1 standard deviation (Amps)
std2=sqrt(ks+k1*P2+k2*P2^2);% logical 2 standard deviation (Amps)
std3=sqrt(ks+k1*P3+k2*P3^2);% logical 3 standard deviation (Amps)
% calculate BER at lower power limit
min_BER=0.5*(Q((I1-I0)/(std0+std1))+Q((I2-I1)/(std1+std2))+...
Q((I3-I2)/(std2+std3)));

% exit if target BER is outside optical power limits
if max_BER>BER
        disp('max. power passed to mult4e is too low');
        return;
elseif min_BER<BER
        disp('min. power passed to mult4e is too high');
        return;
end;
```

```
%Calculate P3 that gives target BER for specified level spacing
while (itr<=max_itr),
 P3=(Pmin+Pmax)/2;% set new, top-level power level to calculate BER at
 P0=r*P3;                % power in logical 0 (Watts)
 P1=P0+e1*(P3-P0);       % power in logical 1 (Watts)
 P2=P0+e2*(P3-P0);       % power in logical 2 (Watts)
 I0=ksig*P0+Iase;        % photocurrent for logical 0 (Amps)
 I1=ksig*P1+Iase;        % photocurrent for logical 1 (Amps)
 I2=ksig*P2+Iase;        % photocurrent for logical 2 (Amps)
 I3=ksig*P3+Iase;        % photocurrent for logical 3 (Amps)
 std0=sqrt(ks+k1*P0+k2*P0^2);% standard deviation of logical 0 (Amps)
 std1=sqrt(ks+k1*P1+k2*P1^2);% standard deviation of logical 1 (Amps)
 std2=sqrt(ks+k1*P2+k2*P2^2);% standard deviation of logical 2 (Amps)
 std3=sqrt(ks+k1*P3+k2*P3^2);% standard deviation of logical 3 (Amps)
 % calculate BER
 ber=0.5*(Q((I1-I0)/(std0+std1))+Q((I2-I1)/(std1+std2))+...
 Q((I3-I2)/(std2+std3)));

 % check if BER is within tolerance limits
 if (ber>=ber_min)&(ber<=ber_max),
        break;
 end;

 if ber>BER              % narrow difference between optical power limits
        Pmin=P3;
 else,
        Pmax=P3;
 end;

 itr=itr+1;              % increment iterations counter

end;

% issue warning if solution did not converge within max. number of iterations
if itr>max_itr,
        disp('max. iterations reached in function mult4e');
end;

return;


function [P3, e, itr]=mult4o(P,ksig,Iase,r,ks,k1,k2,BER)
% MULT4O:      Calculates the optical power in a logical THREE
%              to obtain a specified BER for optinal level spacings.
%
% Notes:       This function is called from "pwr4ary.m." Details of the
%              parameters passed to this function are provided in the calling
%              function.
%
% Input Parameters:
%
%          P - two-element vector containing the minimum and maximum power to
%              consider in Watts. Vector is of form [Pmin Pmax].
%       ksig - proportionality constant for calculating signal currents (A/W)
%       Iase - total photodetector current due to ASE (Amps)
%          r - optical exticntion ratio (P0/P3)
%         ks - total stationary noise current (A^2)
%         k1 - proportionality constant for calculating noise currents
%              that are linearly proportional to received optical power (A^2/W)
%         k2 - proportionality constant for calculating noise currents
%              that are proportional to the square of received optical power,
%              i.e., RIN (A^2/W^2)
%        BER - target bit-error ratio
%
% Returned Values:
%
%         P3 - optical power in logical THREE that produces the targer BER (Watts)
%          e - vector containing the optimal level spacing that minimizes the BER.
%              e(1) is the normalized optimal level of a logical ONE and e(2) is
%              the normalized optimal level of a logical TWO. Optimal levels are
%              normalized between a logical ZERO and a logical THREE, i.e., a
%              logical ZERO is assigned a normalized value of zero and a logical
%              THREE is assigned a normalized value of one.
%        itr - number of iterations required to obtain P3

%   Created:    03/08/97        (month/day/year)
%  Modified:    05/06/97
% Author(s):    Sheldon S. Walklin

Pmin=P(1);                  % minimum received power to consider (Watts)

tol=0.01;                   % error tolerance for BER
ber_max=BER*(1+tol);        % upper limit for BER
ber_min=BER*(1-tol);        % lower limit for BER
max_itr=100;                % maximum number of iterations allowed
itr=1;                      % initialize iterations counter

% initialize level spacings
e1=0.1;e2=0.5;

% check that target BER is within limits
P3=Pmin;                    % set optical power in highest level
% call function to calculate optimal level spacing (minimizes BER)
[e, options]=fmins('mult4ber',[e1 e2],[],[],P3,ksig,Iase,r,ks,k1,k2);
P0=r*P3;                    % power in logical 0 (Watts)
P1=P0+e(1)*(P3-P0);         % power in logical 1 (Watts)
P2=P0+e(2)*(P3-P0);         % power in logical 2 (Watts)
I0=ksig*P0+Iase;            % photocurrent for logical 0 (Amps)
I1=ksig*P1+Iase;            % photocurrent for logical 1 (Amps)
I2=ksig*P2+Iase;            % photocurrent for logical 2 (Amps)
I3=ksig*P3+Iase;            % photocurrent for logical 3 (Amps)
std0=sqrt(ks+k1*P0+k2*P0^2);% standard deviation of logical 0 (Amps)
std1=sqrt(ks+k1*P1+k2*P1^2);% standard deviation of logical 1 (Amps)
std2=sqrt(ks+k1*P2+k2*P2^2);% standard deviation of logical 2 (Amps)
std3=sqrt(ks+k1*P3+k2*P3^2);% standard deviation of logical 3 (Amps)
% calculate BER at lower power limit
min_BER=0.5*(Q((I1-I0)/(std0+std1))+Q((I2-I1)/(std1+std2))+...
Q((I3-I2)/(std2+std3)));
```

```
Pmax=4*Pmin;

while(Pmax<P(2));
 P3=Pmax;                    % set optical power in highest level
 % call function to calculate optimal level spacing (minimizes BER)
 [e options]=fmins('mult4ber',[e1 e2],[],[],P3,ksig,Iase,r,ks,k1,k2);
 P0=r*P3;                    % power in logical 0 (Watts)
 P1=P0+e(1)*(P3-P0);         % power in logical 1 (Watts)
 P2=P0+e(2)*(P3-P0);         % power in logical 2 (Watts)
 I0=ksig*P0+Iase;            % photocurrent for logical 0 (Amps)
 I1=ksig*P1+Iase;            % photocurrent for logical 1 (Amps)
 I2=ksig*P2+Iase;            % photocurrent for logical 2 (Amps)
 I3=ksig*P3+Iase;            % photocurrent for logical 3 (Amps)
 std0=sqrt(ks+k1*P0+k2*P0^2);% standard deviation of logical 0 (Amps)
 std1=sqrt(ks+k1*P1+k2*P1^2);% standard deviation of logical 1 (Amps)
 std2=sqrt(ks+k1*P2+k2*P2^2);% standard deviation of logical 2 (Amps)
 std3=sqrt(ks+k1*P3+k2*P3^2);% standard deviation of logical 3 (Amps)
 % calculate BER at upper power limit
 max_BER=0.5*(Q((I1-I0)/(std0+std1))+Q((I2-I1)/(std1+std2))+...
 Q((I3-I2)/(std2+std3)));

 if max_BER<BER
        break;
 end;

 Pmin=Pmax;
 Pmax=4*Pmax;

end;

% exit if target BER is outside optical power limits
if max_BER>BER
        disp('max. power passed to mult4o is too low');
        return;
elseif min_BER<BER
        disp('min. power passed to mult4o is too high');
        return;
end;

% Now, adjust power in P3 to obtain target BER using optimal level spacings
while (itr<=max_itr),
 P3=(Pmin+Pmax)/2;% set new, top-level power level to calculate BER at
 % call function to calculate optimal level spacing (minimizes BER)
 [e, options]=fmins('mult4ber',[e1 e2],[],[],P3,ksig,Iase,r,ks,k1,k2);
 P0=r*P3;                    % power in logical 0 (Watts)
 P1=P0+e(1)*(P3-P0);         % power in logical 1 (Watts)
 P2=P0+e(2)*(P3-P0);         % power in logical 2 (Watts)
 I0=ksig*P0+Iase;            % photocurrent for logical 0 (Amps)
 I1=ksig*P1+Iase;            % photocurrent for logical 1 (Amps)
 I2=ksig*P2+Iase;            % photocurrent for logical 2 (Amps)
 I3=ksig*P3+Iase;            % photocurrent for logical 3 (Amps)
 std0=sqrt(ks+k1*P0+k2*P0^2);% standard deviation of logical 0 (Amps)
 std1=sqrt(ks+k1*P1+k2*P1^2);% standard deviation of logical 1 (Amps)
 std2=sqrt(ks+k1*P2+k2*P2^2);% standard deviation of logical 2 (Amps)
```

```
std3=sqrt(ks+k1*P3+k2*P3^2);% standard deviation of logical 3 (Amps)
% calculate BER
ber=0.5*(Q((I1-I0)/(std0+std1))+Q((I2-I1)/(std1+std2))+...
Q((I3-I2)/(std2+std3)));

% check if BER is within tolerance limits
if (ber>=ber_min)&(ber<=ber_max),
        break;
end;

if ber>BER                  % narrow difference between optical power limits
        Pmin=P3;
else,
        Pmax=P3;
end;

itr=itr+1;                  % increment iterations counter

end;

% issue warning if solution did not converge within max. number of iterations
if itr>max_itr,
        disp('max. iterations reached in function mult4o');
end;

return;


function ber=mult4ber(e,P3,ksig,Iase,r,ks,k1,k2)
% MULT4BER:  Function passed as an argument to fmins.m in function
%            mult4o.m to calculate optimal level spacing.
%
% Notes:     This function is called from "mult4o.m." Details of the
%            parameters passed to this function are provided in the
%            calling function.
%
% Input Parameters:
%
%         e - vector containing normalized level spacing for a logical 1 and
%             a logical 2. Vector is of form [e(1) e(2)] and level spacings are
%             normalized between a logical 0 and a logical 3.
%        P3 - optical power in a logical 3 (Watts)
%      ksig - proportionality constant for calculating signal currents (A/W)
%      Iase - total photodetector current due to ASE (Amps)
%         r - optical extinction ratio (P0/P3)
%        ks - total stationary noise current (A^2)
%        k1 - proportionality constant for calculating noise currents
%             that are linearly proportional to received optical power (A^2/W)
%        k2 - proportionality constant for calculating noise currents
%             that are proportional to the square of received optical power,
%             i.e., RIN (A^2/W^2)
%
% Returned Values:
%
```

```
%       ber - bit-error ratio.

% Created:      03/08/97          (month/day/year)
% Modified:     05/06/97
% Author(s):    Sheldon S. Walklin

P0=r*P3;                  % power in a logical 0 (Watts)
P1=P0+e(1)*(P3-P0);       % power in a logical 1 (Watts)
P2=P0+e(2)*(P3-P0);       % power in a logical 2 (Watts)
I0=ksig*P0+Iase;          % photocurrent in logical 0 (Amps)
I1=ksig*P1+Iase;          % photocurrent in logical 1 (Amps)
I2=ksig*P2+Iase;          % photocurrent in logical 2 (Amps)
I3=ksig*P3+Iase;          % photocurrent in logical 3 (Amps)
std0=sqrt(ks+k1*P0+k2*P0^2);% standard deviation of logical 0 (Amps)
std1=sqrt(ks+k1*P1+k2*P1^2);% standard deviation of logical 1 (Amps)
std2=sqrt(ks+k1*P2+k2*P2^2);% standard deviation of logical 2 (Amps)
std3=sqrt(ks+k1*P3+k2*P3^2);% standard deviation of logical 3 (Amps)
% calculate bit-error ratio
ber=0.5*(Q((I1-I0)/(std0+std1))+Q((I2-I1)/(std1+std2))+...
Q((I3-I2)/(std2+std3)));

return;
```

11.3 Appendix C: Optical Component Data

11.3.1 Active Components

11.3.1.1 Lasers

Table C.1 shows measured laser parameters. Linewidths were measured using the Delayed Self-Homodyne (DSH) technique described in section 6.1.2. Figure C.1 shows the spectrum analyzer scans obtained for linewidth measurements. RIN values were measured using the method described in section 6.1.3 and represent an average RIN value over a 5 GHz bandwidth.

Table C.1 Measured laser parameters.

Device	Parameters
OC48 Module 96001	Wavelength: 1532.7 nm Operating Current: 60 mA max. Output Power: +5.5 dBm Adiabatic Chirp: ~2 GHz/mA Linewidth: 6.2 MHz RIN Value: -154 dB/Hz
OC48 Module 96002	Wavelength: 1553.3 nm Operating Current: 75 mA max. Output Power: +3.7 dBm Adiabatic Chirp: ~2 GHz/mA Linewidth: 12.3 MHz RIN Value: -153 dB/Hz
OC48 Module 96003	Wavelength: 1533.0 nm Operating Current: 55 mA max. Output Power: +4.1 dBm Adiabatic Chirp: ~2 GHz/mA Linewidth: 4.0 MHz RIN Value: -160 dB/Hz
Nortel III-V MZ Module	Wavelength: 1557.4 nm Operating Current: 70 mA max. Output Power: -5.0 dBm @ 60 mA (max. out of MZ) Adiabatic Chirp: ~2.5 GHz/mA Linewidth: 35 MHz RIN Value: -142 dB/Hz

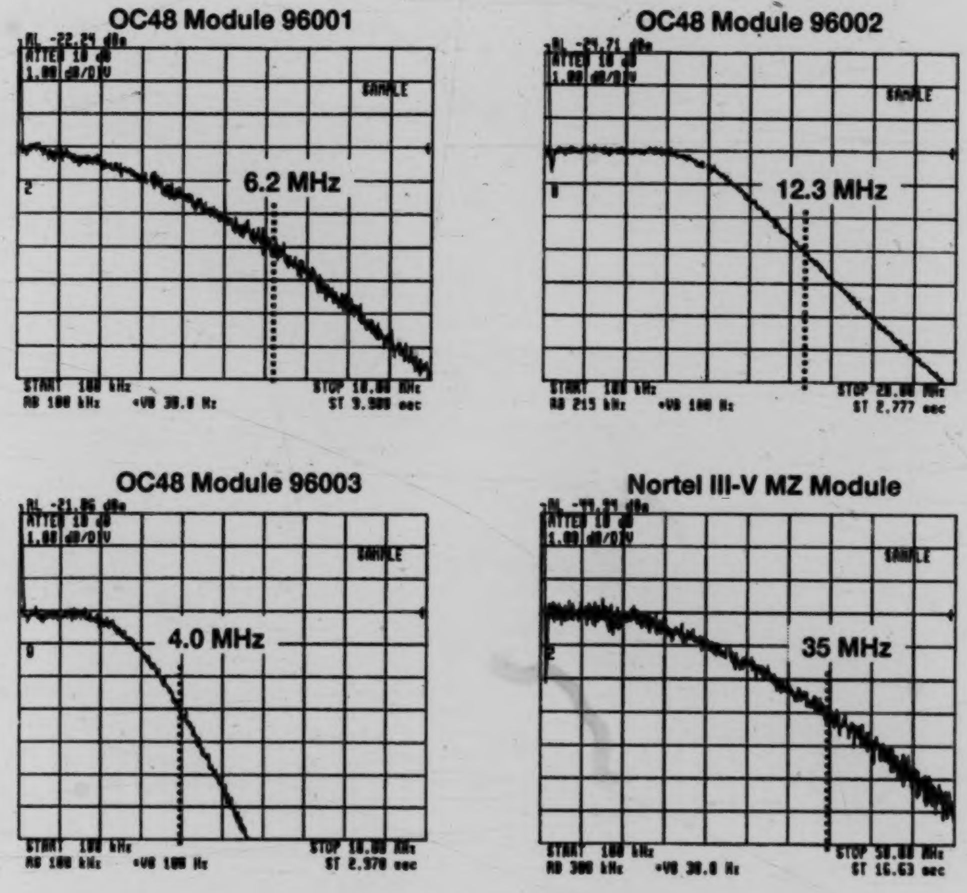
OC48 Module 96001

OC48 Module 96002

OC48 Module 96003

Nortel III-V MZ Module

Figure C.1 Spectrum analyzer scans for laser linewidth measurements using DSH method.

11.3.1.2 Mach-Zehnder Modulators

Table C.2 shows measured and specified parameters for the Nortel MZ module and the Lucent $LiNbO_3$ MZ device.

Table C.2 Parameters for Mach-Zehnder external modulators.

Device	Parameters
Nortel III-V MZ	DC Bias Range*: (0 to –10 V) V_π: 4.2 V at DC DC Optical Extinction Ratio: 28.4 dB (Right Arm=0 V) 19.6 dB (Left Arm=0 V) Bandwidth*: 12.8 GHz. RF Impedance*: 50 Ohms
Lucent $LiNbO_3$ MZ	DC Bias Range*: (-20 V to +20 V) V_π: 3.5 V at DC, 4.2 V at 300 kHz, 4.45 V* at 1 GHz DC Optical Extinction Ratio: ~20 dB with PM fiber at input ~30 dB with polarization rotator at input Bandwidth*: 10.5 GHz Insertion Loss: 3.6 dB RF Impedance*: 43 Ohms

* Specified by manufacturer

Figure C.2 shows the measured power transfer characteristic for each arm of the III-V MZ module, with the remaining arm grounded. Fourth-order polynomial curve fits are also shown for each curve. Figure C.3 shows the measured power transfer characteristic for each arm of the Lucent $LiNbO_3$ MZ, with the remaining arm grounded. Curves are shown for both a positive and negative DC bias. Note the anomalous behavior around the first minimum in the negative-biased transfer characteristic for the left arm of the $LiNbO_3$ MZ. Left and right arms are reference with respect to the output fiber pigtail on MZ devices, as shown below.

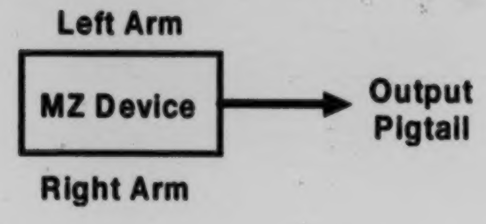

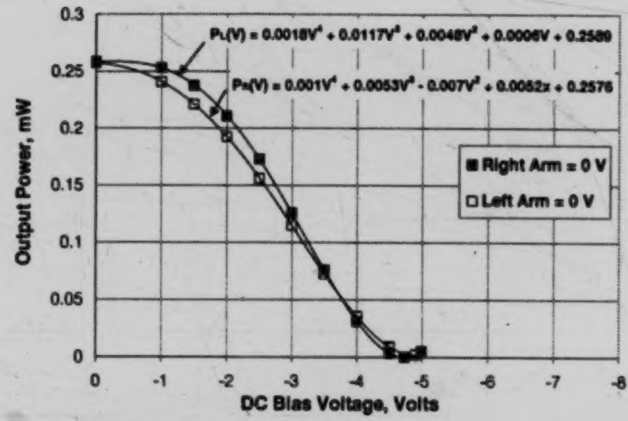

Figure C.2 Power transfer characteristic for left and right arm of III-V MZ.

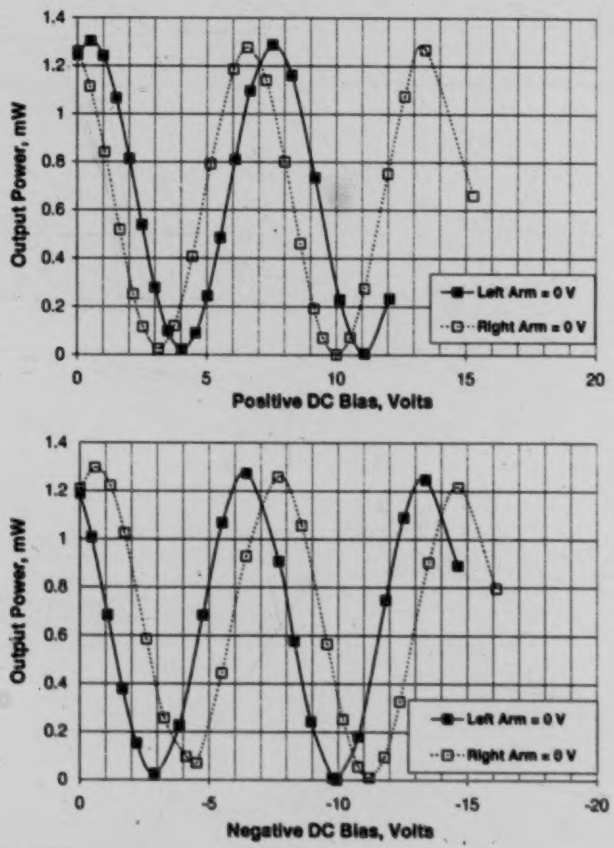

Figure C.3 Power Transfer characteristic for left and right arm of Lucent $LiNbO_3$ MZ for a positive (top) and negative (bottom) DC bias.

11.3.1.3 Erbium-Doped Fiber Amplifiers

Measured gain curves and parameters at various wavelengths for the four EDFAs residing at TRLabs are shown in Figures C.4 through C.8. Note that these are referred to as EDFA 1, 2, 4 and 5, and correspond to EDFAs with the serial numbers TRL9407-BF450-001, TRL9407-BF450-002, TRL-R0302-004 and TRL-R0302-005, respectively. For all measurements, EDFAs 2, 4 and 5 were operated with the pump current set at 155 mA, and EDFA1 was operated at a pump current of 180 mA. All measurements are from optical connector input to optical connector output on each EDFA.

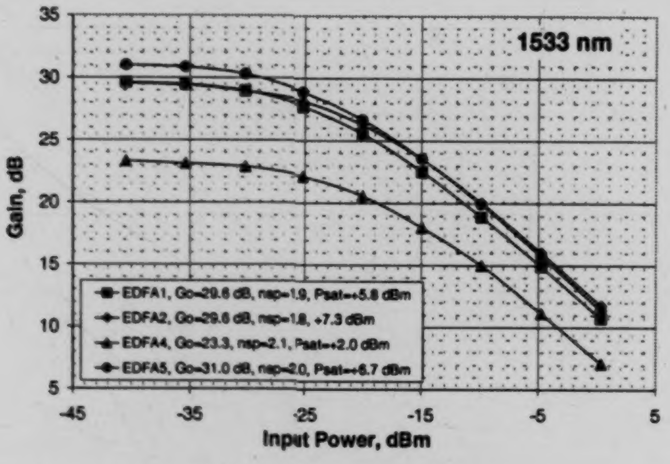

Figure C.4 Meausred gain curves and parameters for EDFAs operating at 1533 nm.

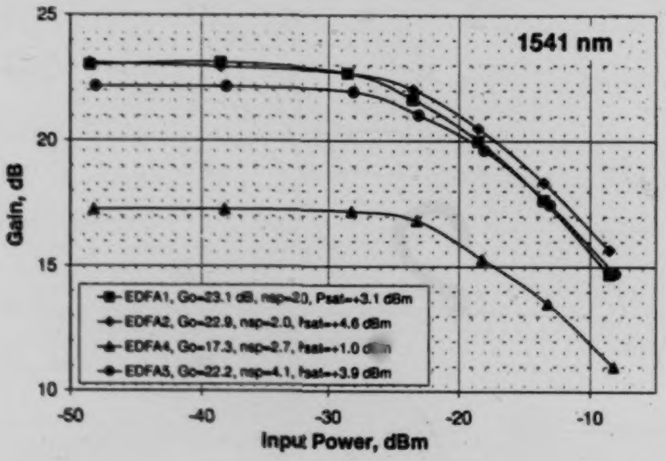

Figure C.5 Meausred gain curves and parameters for EDFAs operating at 1541 nm.

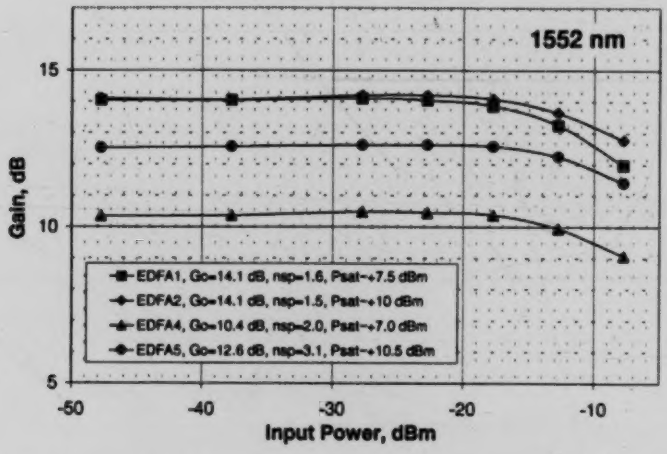

Figure C.6 Meausred gain curves and parameters for EDFAs operating at 1552 nm.

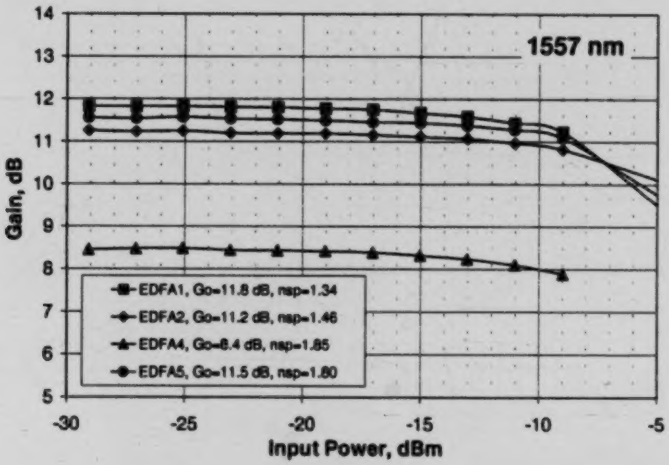

Figure C.7 Meausred gain curves and parameters for EDFAs operating at 1557 nm.

To determine the sensitivity of the spontaneous emission factor and small-signal gain to the pump current, a set of measurements were conducted on EDFA1 for various pump currents, as shown in Figure C.8.

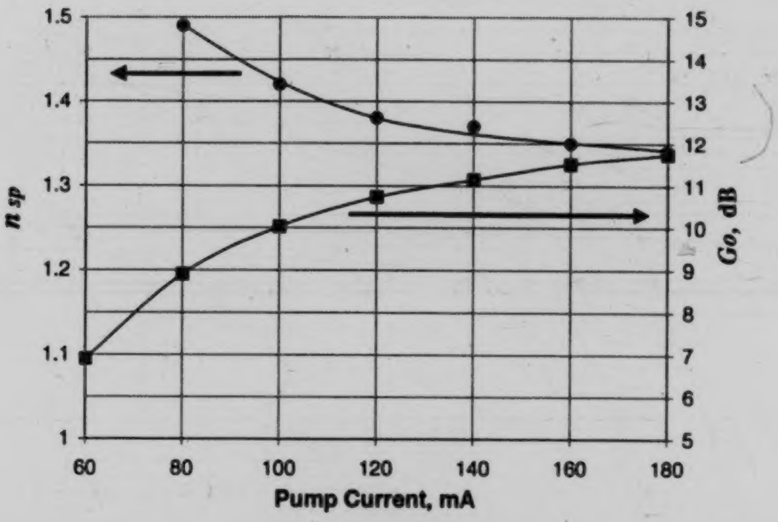

Figure C.8 Spontaneous emission factor and small-signal gain versus pump current for EDFA1.

11.3.1.4 Photodiode Responsivity

Measured values for the DC responsivity of the photodiode in the Nortel PIN-preamp module, and for the BT&D photodiode, are shown in Table C3. The specified maximum average power is also shown.

Table C.3 DC responsivity measurements and maximum average powers for photodiodes.

Device	DC Responsivity, A/W	Maximum Power, dBm
Nortel PIN-preamp	0.69 at 1557 nm 0.71 at 1541 nm	0
BT&D	0.58 at 1557 nm 0.59 at 1541 nm	+5

11.3.2 Passive Components

11.3.2.1 Loss Measurements

Loss measurements for fiber reels, JDS Fabry Perot tunable BPFs, isolators and WDMs are shown in Table C.4. Note that the numbers used in referring to components are marked on the components in the lab.

Table C.4 Loss measurements for passive optical components.

Component	**Loss, dB**	
Fiber Reels:	**1533 nm**	**1557 nm**
Reel 1, 25 km	5.45	5.30
Reel 2, 25 km	6.40	5.80
Reel 3, 25 km	8.05	–
Reel 4, 10 km	2.30	2.10
Reel 5, 10 km	2.70	2.55
Reel 6, 50 km	12.65	12.05
Reel 7, 50 km	12.81	11.90
Reel 8, 50 km	13.60	–
Reel 9, 50 km	14.55	–
Reel 10, 25 km	7.60	–
JDS Tunable BPFs:		
BPF1	2.6	2.3
BPF2	2.4	1.1
BPF3	1.4	0.9
BPF4	2.2	1.6
Optical Isolators:		
ISO1	0.6	0.5
ISO2	2.4	2.3
ISO3	0.7	–
ISO4	0.6	0.7
WDMs (1550/980 nm):		
WDM1	0.9	1.2
VOAs:		
JDS Series 7000 (insertion loss)	3.0	3.3

– Not measured

11.3.2.2 Optical Filter Bandwidths

Bandwidths for the JDS Fabry Perot tunable BPFs are shown in Table C.5. All measurements were at 1557 nm. Both the optical 3 dB bandwidth and noise-equivalent bandwidth are shown in Table C.5, which were measured using the method described in section 6.7. Measurements are also shown for two or more filters in cascade. Figure C.9 shows the transmission response for each of the BPFs. Each response has been adjusted to account for the non-white PSD of the ASE that was used as a source, as described in section 6.7. It should be noted that the monochrometer used had an offset of about 3 nm; hence, the peak transmission is actually about 3 nm higher than that indicated. Finally, it should be noted that BPF3 does not appear to be working properly because it shows a much broader response than the other filters.

Table C.5 Optical filter bandwidth measurements at 1557 nm.

Filter No.	Optical 3 dB Bandwidth, nm	Optical Noise-Equivalent Bandwidth, nm
1	1.34	1.56
2	1.22	1.41
3	2.89	3.33
4	1.20	1.40
1, 2	0.91	0.99
1, 3	1.16	1.31
1, 4	0.92	0.99
2, 3	1.10	1.24
2, 4	0.89	0.96
3, 4	1.06	1.19
1, 2, 3	0.87	0.94
1, 2, 4	0.77	0.82
1, 3, 4	0.85	0.91
2, 3, 4	0.83	0.89
1, 2, 3, 4	0.73	0.77

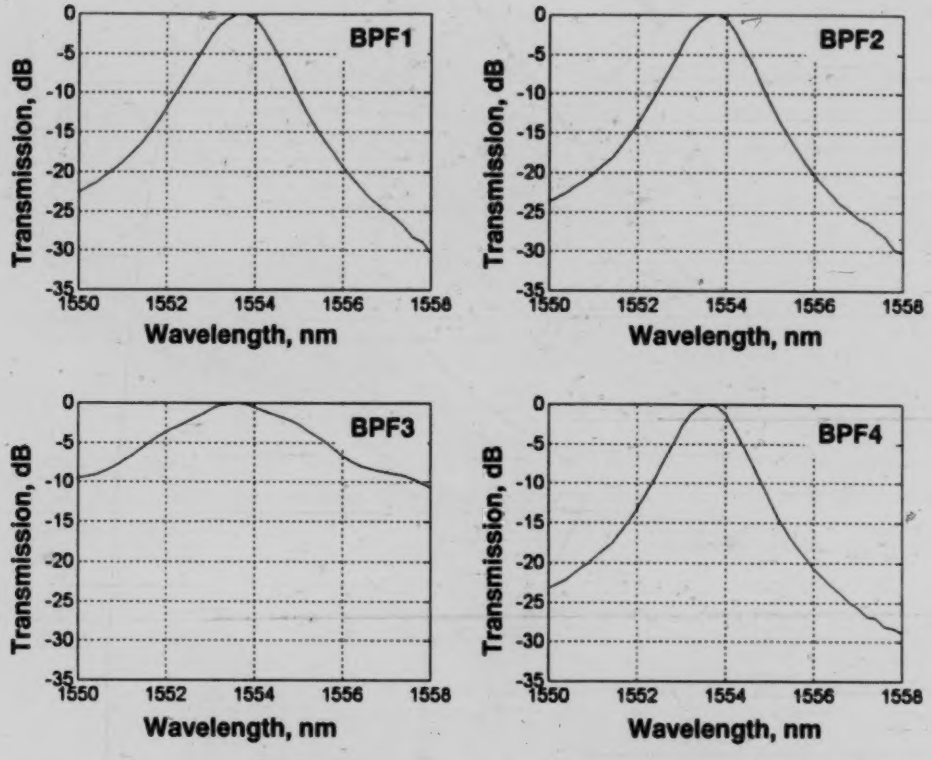

Figure C.9 Transmission response for tunable FFP BPFs.

11.4 Appendix D: Electrical Component Data

11.4.1 Electrical Amplifier Specifications

Important specifications for the electrical amplifiers used in laboratory setups are shown in Table D.1.

Table D.1 Specifications for electrical amplifiers.

Amplifier	Specifications
B&H AC26023H24ELL9P1	Freq. Resp.: 2 MHz – 26 GHz Gain: 23 dB typ. 1 dB Comp. O/P: +24 dBm NF: ~7 dB
SHF90P	Freq. Resp.: 10 kHz – 15 GHz Gain: 23 dB min. 1 dB Comp. O/P: +10 dBm NF: ~7 dB
Mini-Circuits ZHL-1042J	Freq. Resp.: 10 MHz – 4.2 GHz Gain: 25 dB min. 1 dB Comp. O/P: +20 dBm NF: ~7 dB
Veritech VMA3K10C-232	Freq. Resp.: 3 kHz – 10 GHz Gain: 32 dB min. 1 dB Comp. O/P: +17 dBm NF: ~7 dB
Veritech VMPPA-438	Freq. Resp.: 130 kHz – 10 GHz Gain: 38 dB min. 1 dB Comp. O/P: +23 dBm
Veritech VM10LA-155	Freq. Resp.: DC – 10 GHz Gain: 55 dB O/P: ~+15 dBm (limiting mode) NF: < 6 dB
MITEQ JS4-00102600-30	Freq. Resp.: 100 MHz – 26 GHz Gain: 30 dB min. 1 dB Comp. O/P: +5 dBm NF: 3 dB
Aventek LMT12436	Freq. Resp.: 7 GHz – 12.4 GHz Gain: 35 dB min. O/P: +14 to +19 dBm (limiting mode)
CTT APM/080-3036	Freq. Resp.: 2 GHz – 8 GHz Gain: 36 dB 1 dB Comp. O/P: +30 dBm

11.4.2 VM10LA-155 Limiting Amplifier

The Veritech VM10LA-155 limiting amplifier was characterized for its input sensitivity, and for its output swing as a function of the applied control voltage. This amplifier should be useful as a receiver/limiting amplifier in future binary experiments conducted at TRLabs. Measurements were done at 100 Mb/s and 3 Gb/s, which are the minimum and maximum operating speeds of the HP pattern generator, and the results are shown in Figure D.1.

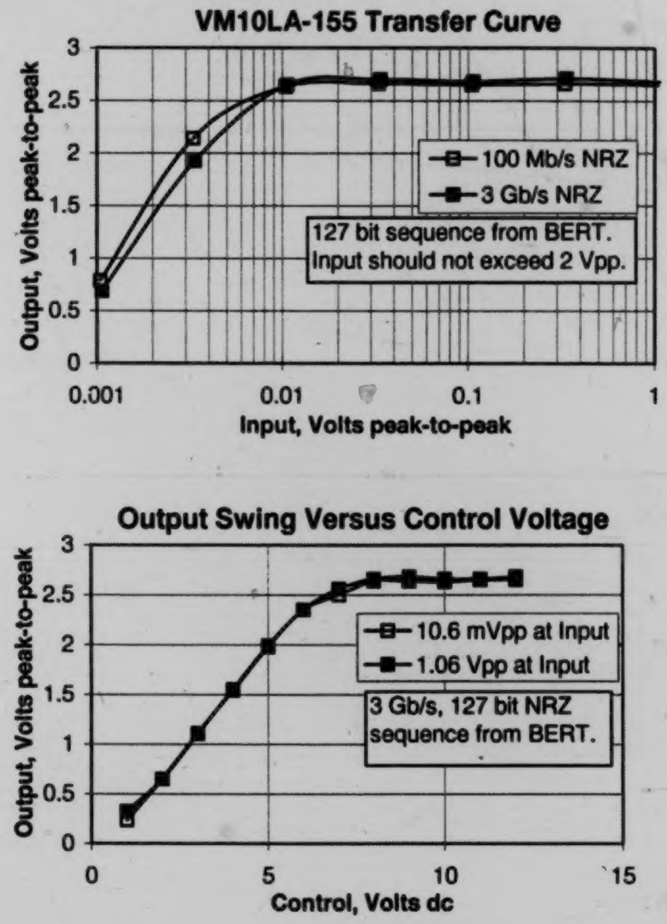

Figure D.1 Input sensiivity (top) and output swing versus control voltage (bottom) for the VM10LA-155 limiting amplifier.

11.4.3 VM10CMD-320 Differential Pulse Amplifier

Characterization of a VM10CMD-320 differential pulse amplifier was also carried out. Although this amplifier was not used in any of the experiments conducted, it should be useful for future experiments at TRLabs. Figure D.2 shows the transfer characteristics from the two inputs to the two outputs for this amplifier. Note that this device is quite linear for input signals up to about 600-700 mV$_{pp}$. Because the intended application for this amplifier is to drive a dual-arm MZ device, it has built in bias circuits to provide a DC offset to the output signal. Unfortunately, the achievable range for the DC offset is only about –0.8V to +0.8V, as shown in Figure D.2. This appears to be an oversight by the designers because it is often necessary to provide a somewhat larger offset than this. Therefore, external bias tees may still be needed.

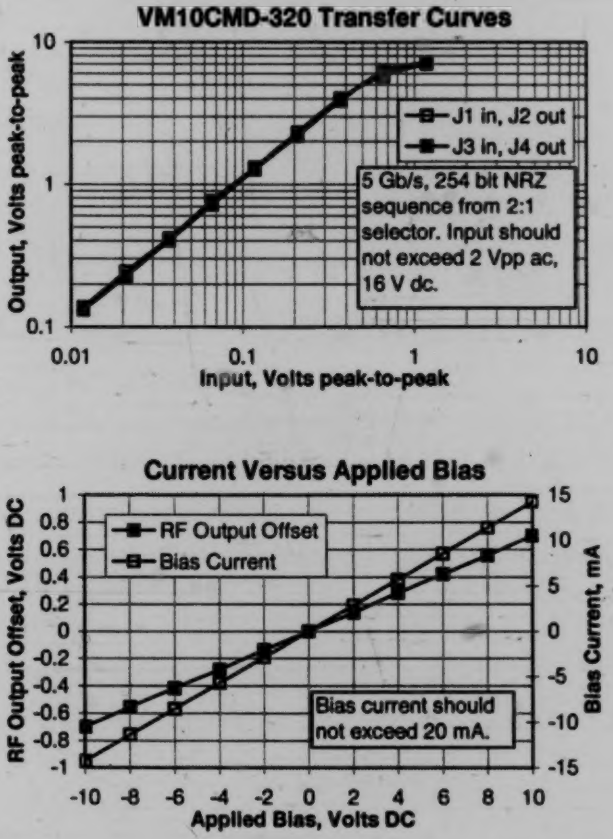
VM10CMD-320 Transfer Curves

5 Gb/s, 254 bit NRZ sequence from 2:1 selector. Input should not exceed 2 Vpp ac, 16 V dc.

Current Versus Applied Bias

Bias current should not exceed 20 mA.

Figure D.2 Transfer curves (top) and output bias offset versus applied voltage (bottom) for the VM10CMD-320 differential pulse amplifier.

11.4.4 Frequency Response Measurements

Frequency response measurements of various electrical components used in experiments are shown in Figures D.3 through D.20. All measurements were made using an HP8510 network analyzer. It should be noted that frequency response records were recorded for many other electrical components residing at TRLabs. A full listing of the filenames, and a description of each component, is included in the FOCSS User's Guide, which is to be filed as a TRLabs internal report. Note that the magnitude response in Figures D.3, D.4 and D.5 is normalized to a maximum transmission of 0 dB. The magnitude response in all other figures truly reflects the gain or insertion loss of the device. Also, much of the linear delay has been removed from phase response plots.

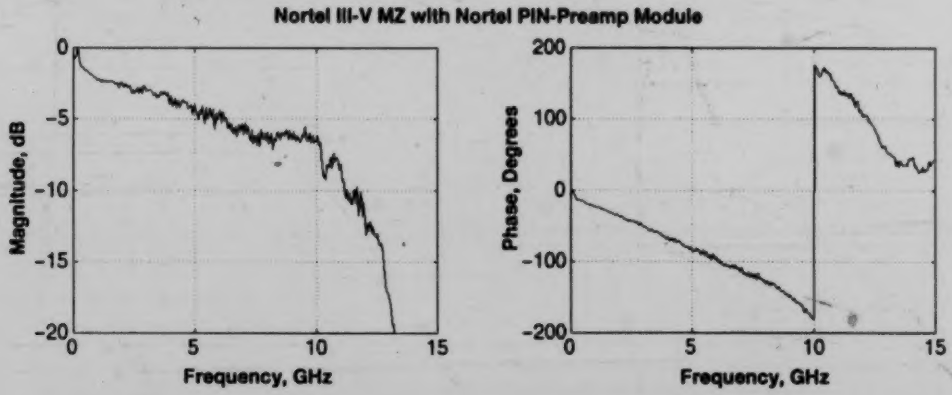

Figure D.3 Small-signal frequency response of Nortel III-V MZ and Nortel PIN-preamp module.

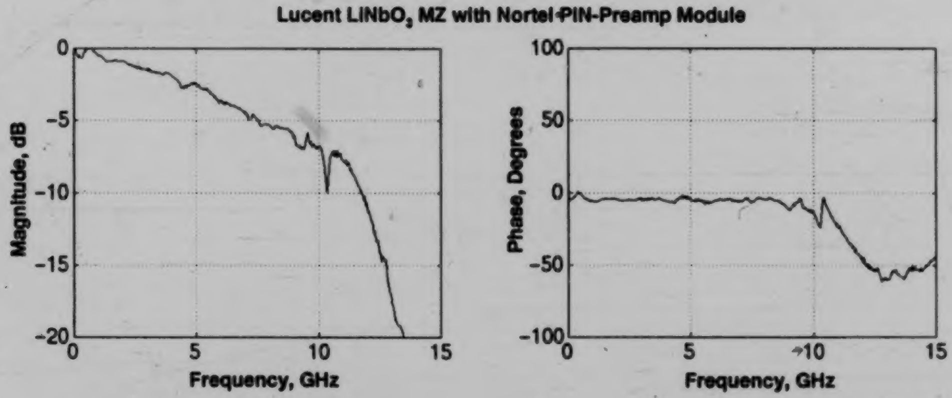

Figure D.4 Small-signal frequency response of Lucent MZ and Nortel PIN-preamp module.

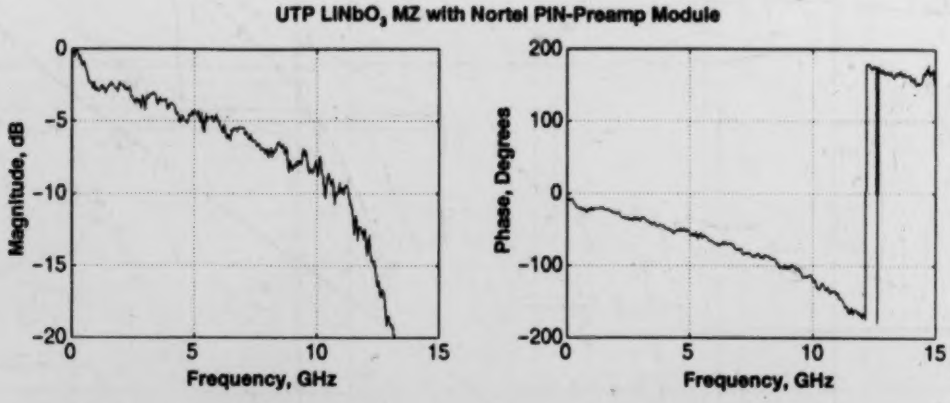

Figure D.5 Small-signal frequency response of UTP MZ and Nortel PIN-preamp module.

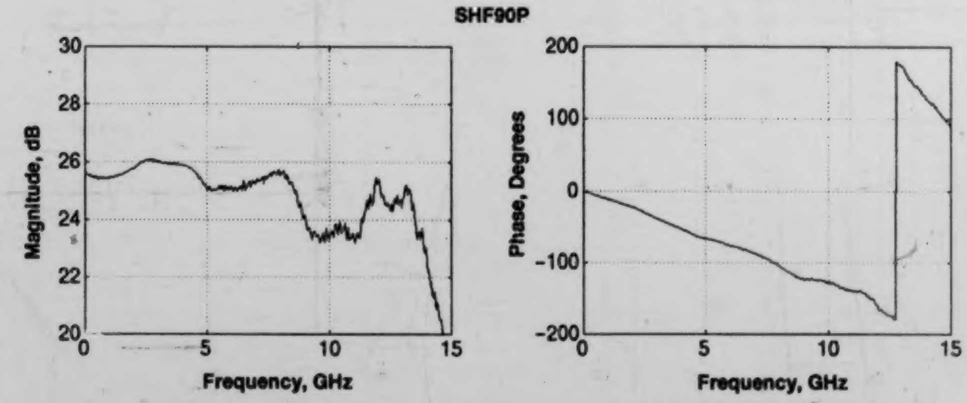

Figure D.6 Frequency response of SHF90P 15 GHz amplifier.

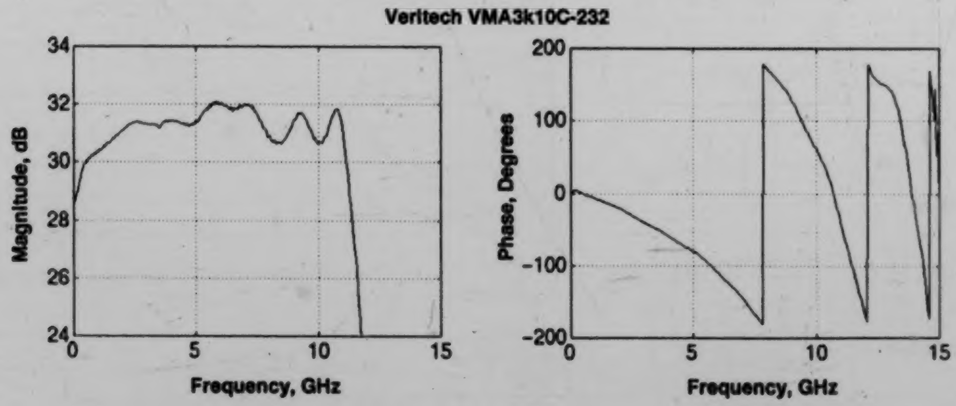

Figure D.7 Frequency response of Veritech VMA3k10C-232 10 GHz amplifier.

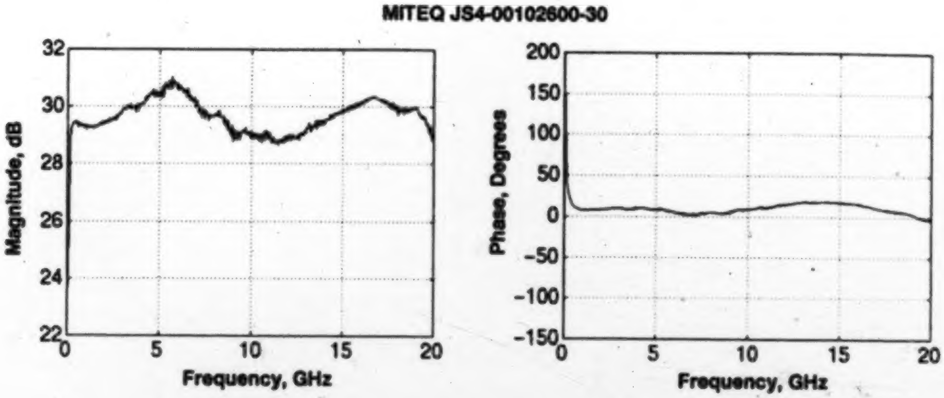

Figure D.8 Frequency response of MITEQ JS4-00102600-30 26 GHz amplifier.

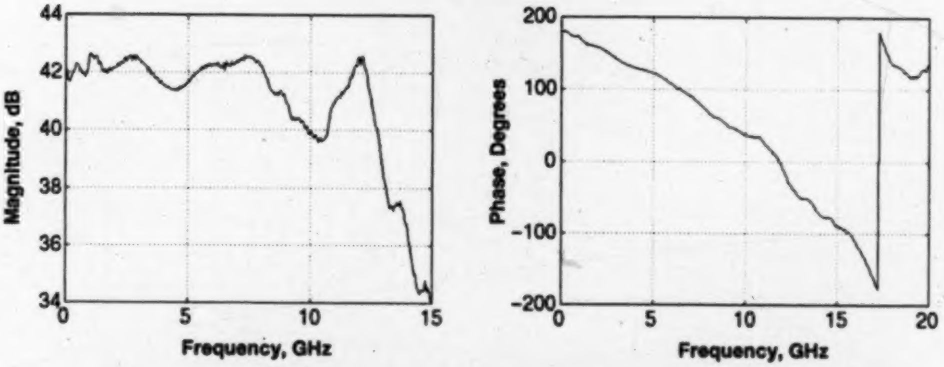

Figure D.9 Frequency response of Veritech VMPPA-438 high-power pulse amplifier.

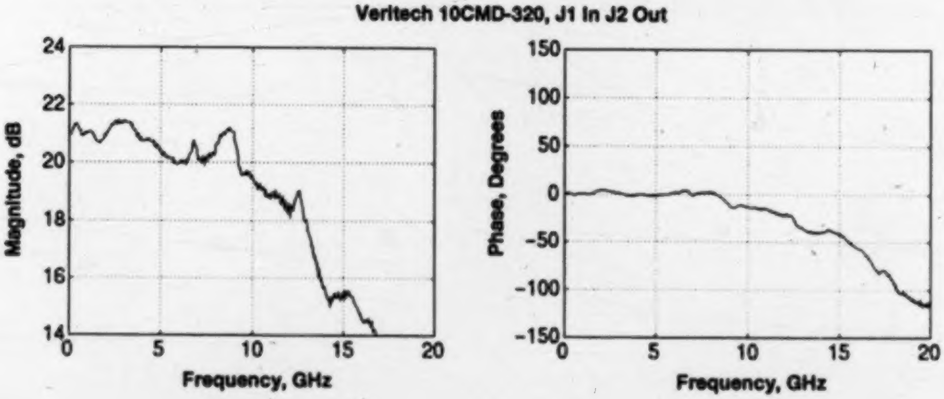

Figure D.10 Frequency response of Veritech 10CMD-320 differential driver amplifier, J1 to J2.

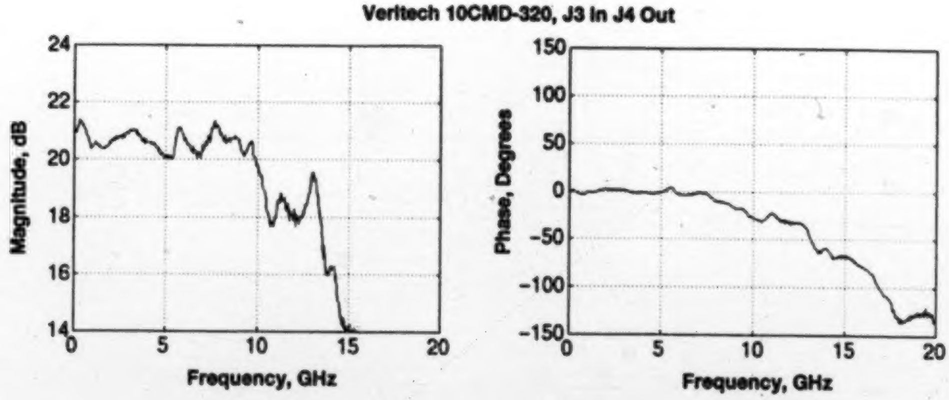

Figure D.11 Frequency response of Veritech 10CMD-320 differential driver amplifier, J2 to J4.

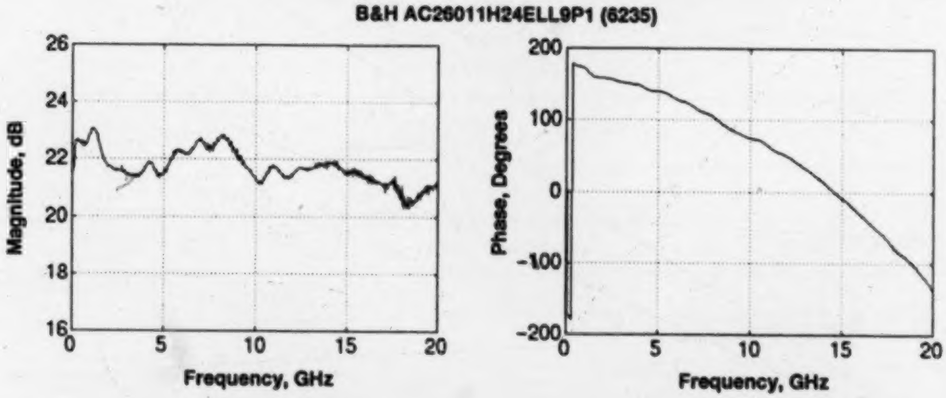

Figure D.12 Frequency response of B&H AC26011H24ELL9P1 (6235) 26 GHz amplifier.

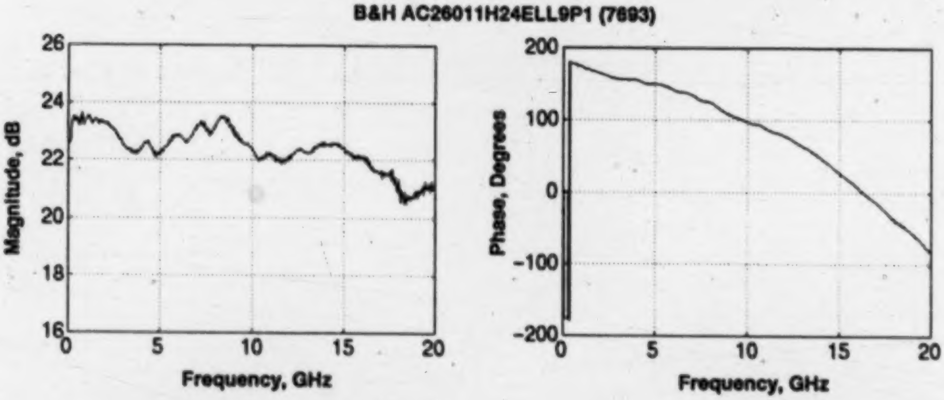

Figure D.13 Frequency response of B&H AC26011H24ELL9P1 (7693) 26 GHz amplifier.

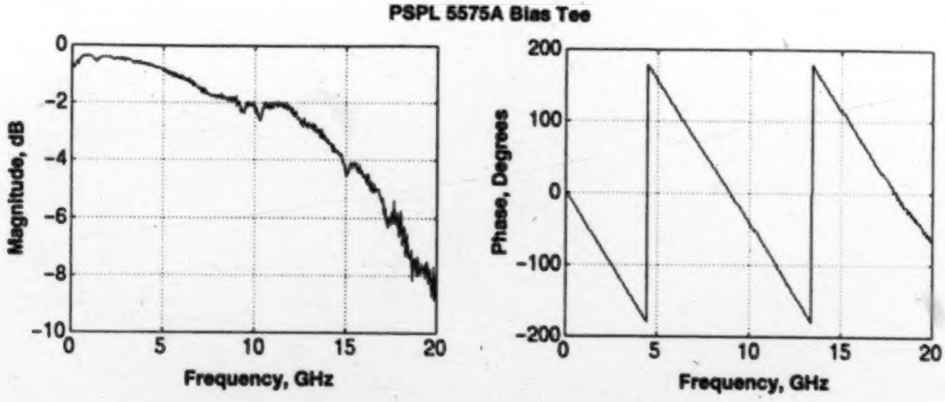
PSPL 5575A Bias Tee

Figure D.14 Frequency response of PSPL 5575A Bias Tee.

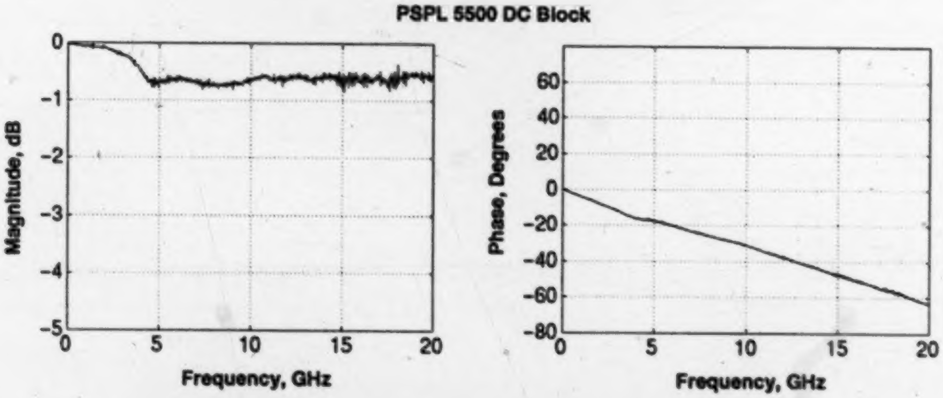
PSPL 5500 DC Block

Figure D.15 Frequency response of PSPL 5500 DC blocking capactior.

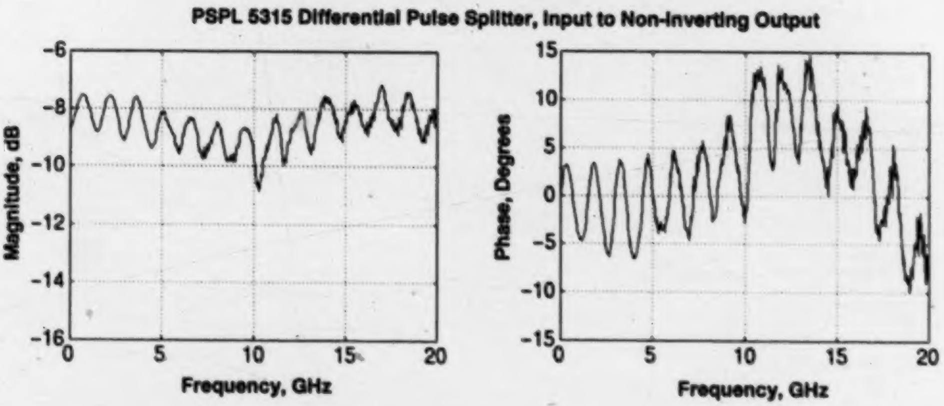
PSPL 5315 Differential Pulse Splitter, Input to Non-Inverting Output

Figure D.16 Frequency response of PSPL 5315 differential pulse splitter, input to non-inverting output.

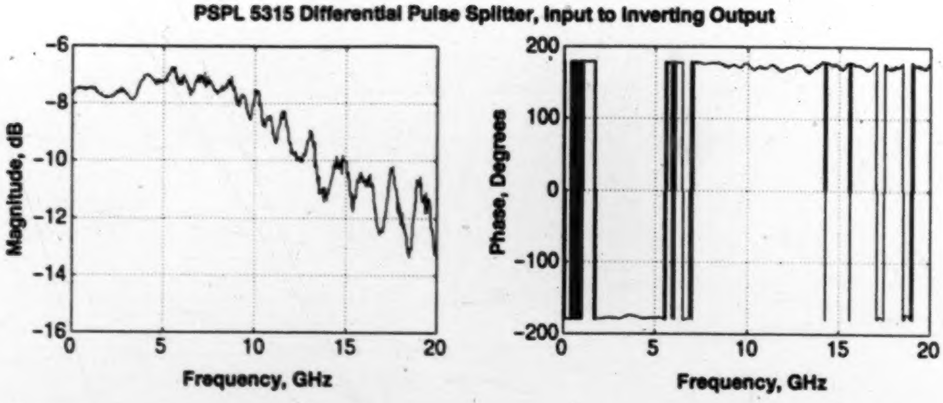

Figure D.17 Frequency response of PSPL 5315 differential pulse splitter, input to inverting output.

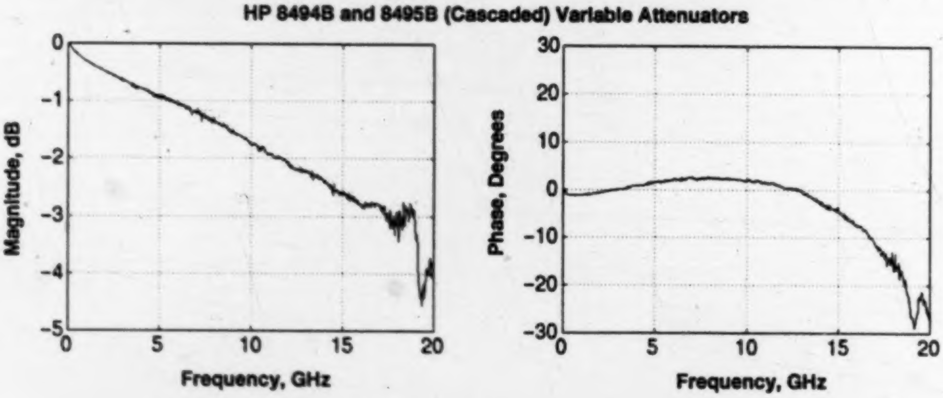

Figure D.18 Frequency response of HP 8494B and 8495B variable attenuators is cascade.

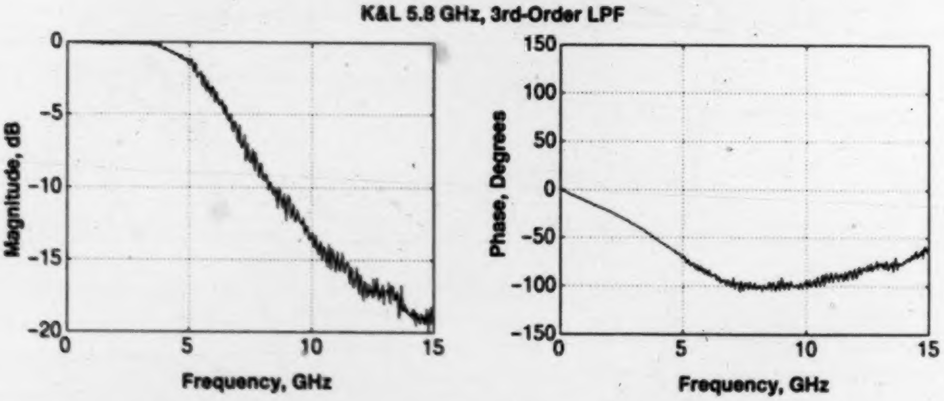

Figure D.19 Frequency response of K&L 5.8 GHz, 3-rd order Butterworth lowpass filter.

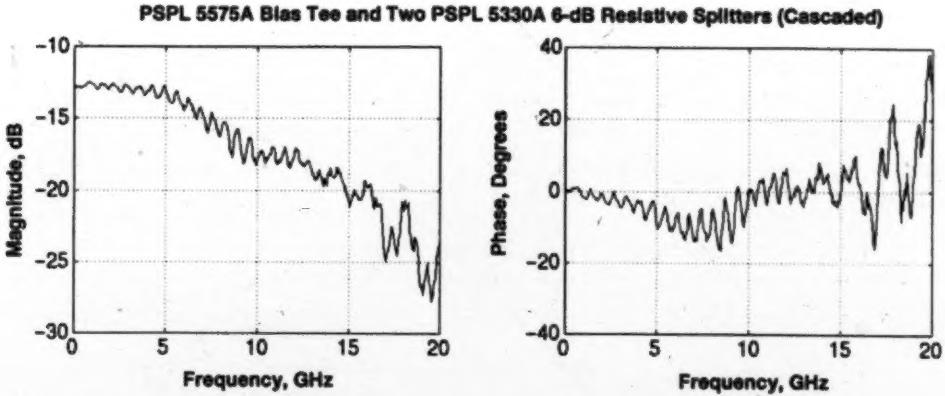

Figure D.20 Frequency response of PSPL 5575A bias tee and two PSPL 5330A 6-dB resistive splitters in cascade. This represents the response of the 1-to-4 power splitter and bias tee used in the multilevel decoder.

11.5 Appendix E: GaAs IC Power Supply

In order to power all the GaAs logic modules and provide the various DC biases, a custom power supply was designed and built. This supply should be very useful for any future experiments at TRLabs that use the GaAs logic modules. The following contains details about the design and operation of the power supply.

11.5.1 Description

The GaAs IC power supply is a custom-built unit for use with NEL's high-speed Galium-Arsenide integrated circuits. It will provide power and adjustable bias levels for up to ten ICs. A built-in voltmeter facilitates the precise setting of bias levels.

NOTE: NEL GaAs logic ICs are extremely static sensitive and are easily damaged if proper operating conditions are not met. Thoroughly read the manufacture's documentation for any given device before attempting to use it. These ICs are negative-voltage devices and must be operated under very stringent conditions. Some general guidelines are provided in a later section of this appendix.

11.5.2 Front Panel Controls and Connectors

Figure E.1 shows the front panel of the GaAs IC power supply

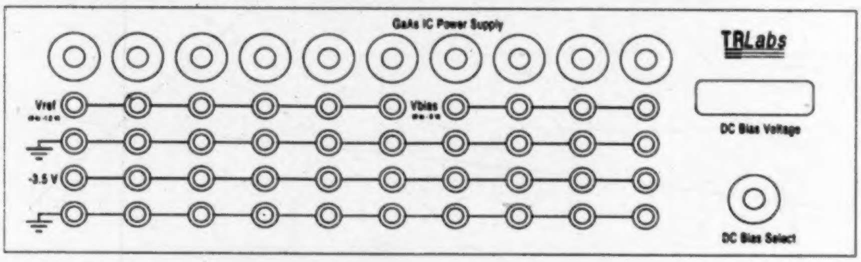

Figure E.1 Front panel of GaAs IC power supply.

11.5.2.1 Supply Voltage Outputs

All ICs require a -3.5 V supply voltage. The GaAs IC power supply provides ten -3.5 V outputs located along the bottom of the front panel, each driven by a separate regulator board contained within the unit. The maximum current provided by any single output is 1500 mA. Therefore, up to 15 Amps of total current can be provided.

11.5.2.2 Variable Voltage Outputs

Located above the supply voltage outputs are ten variable voltage outputs to provide bias levels for the ICs. These are essentially voltage divider circuits so that the voltage generated depends on the resistance of the connected load. The first six variable outputs on the left will provided a voltage from 0 to -1.2 V when connected to a reference voltage pin on any IC. The remaining four outputs will provide a variable voltage from 0 to –5 V and, in conjunction with a bias Tee, are intended to provide the required negative dc bias to RF input signals. They may also be used to bias an external modulator. When using the variable outputs to bias an RF input signal, it is important to ensure that the instantaneous voltage (AC+DC) at any IC input does not exceed the specified limit for the device, to prevent damaging the IC. Variable output voltages are adjusted by a 10-turns dial located above the respective output terminals. Turning the dial completely CCW will set the output terminals to 0 Volts. All ten variable outputs are driven by a single regulator board that can provide up to 1500mA. This is ample current for normal operating conditions.

11.5.2.3 Built-in Voltmeter

An internal voltmeter is provided to facilitate the precise setting of variable output voltages. The rotary selector switch on the bottom-right of the front panel is used to select the variable output to be measured. The measured voltage in Volts is shown in the LED display.

11.5.3 Rear Panel Controls and Connectors

Figure E.2 shows the rear panel of the GaAs IC Power Supply.

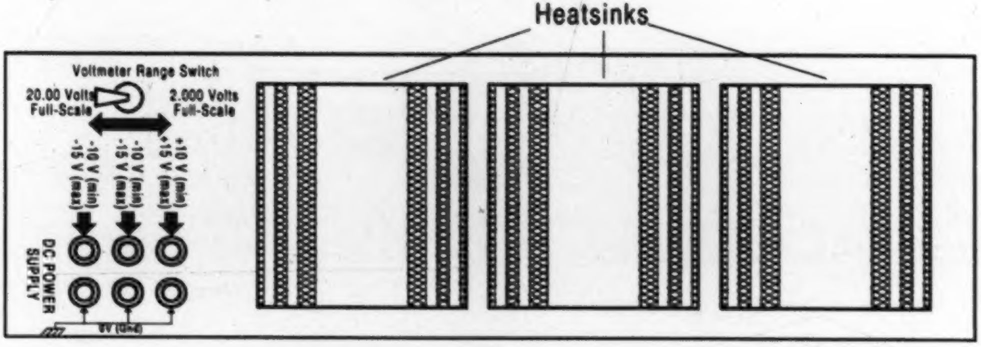

Figure E.2 Rear panel of GaAs IC Power Supply.

11.5.3.1 Power Supply Terminals

The GaAs IC power supply has three sets of terminals for applying power to the unit. One set of terminals requires a positive voltage between +10V and +15V. The positive supply is required to power a positive regulator board, which in turn provides the required positive voltage for the voltmeter control board. Two negative supply voltages are also required in the range -10V to -15V. The left-most negative terminal provides raw DC power to six negative regulator boards inside the unit. One of the regulator boards supplies power to the bias circuitry, as well as a negative voltage for the voltmeter control board. the other five regulator boards are for the first five -3.5 V outputs. The second negative terminal provides power for five additional regulator boards used for the five remaining -3.5 V outputs. The ground terminals are physically connected to each other and to chassis ground. Note that the maximum current required by the unit is determined by the number of components it powers and their total current requirement. For example, if four devices are connected each requiring 500 mA, then the unit must be supplied from a source capable of providing at least 2 Amps. The current requirement of an IC is typically 300-1000 mA. Under full loading, two 5A voltage supplies should be sufficient to drive the negative power supply terminals. Current drawn from the positive supply terminal is about 200 mA.

11.5.3.2 Voltmeter Range Selector

The voltmeter precision and range is set by the toggle switch at the top left on the back panel. The coarse range is from 0 to 20.00V with a resolution of 10mV. The fine range is from 0 to 2.000V with a resolution of 1mV.

11.5.4 Internal Components

The internal components of the GaAs Power Supply Unit are shown in Figure E.3, along with a simple wiring layout. There are fourteen boards in total: one voltmeter display board; one voltmeter control board; one positive regulator board and eleven negative regulator boards. All of these boards were designed by David D. Clegg at TRLabs in Edmonton and are known to be very reliable. The regulator boards provide over-voltage protection, current limiting and reverse-voltage protection for the power supply terminals of the unit. The positive and negative regulator boards make use of the 317 and 337 regulator chips, respectively. These chips provide thermal overload protection and will shut down if the temperature becomes too high. The regulator chips are mounted on the back panel of the unit where adequate heat sinking is provided

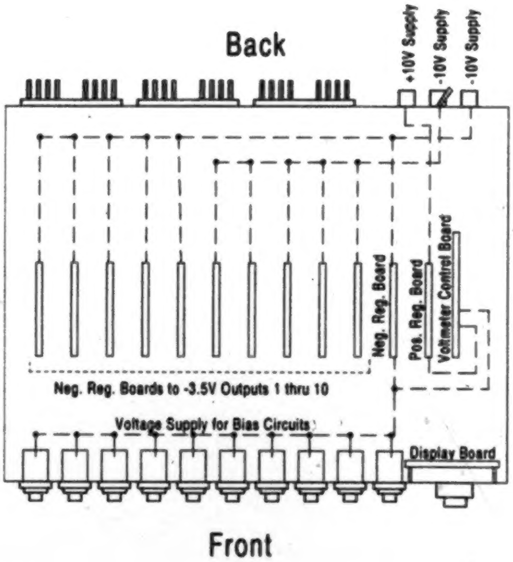
Back
+10V Supply
-10V Supply
-10V Supply
Neg. Reg. Board
Pos. Reg. Board
Voltmeter Control Board
Neg. Reg. Boards to -3.5V Outputs 1 thru 10
Voltage Supply for Bias Circuits
Display Board
Front

Figure E.3 Internal components and wiring of the GaAs IC power supply.

A scanned image of the finished product is shown in Figure E.4.

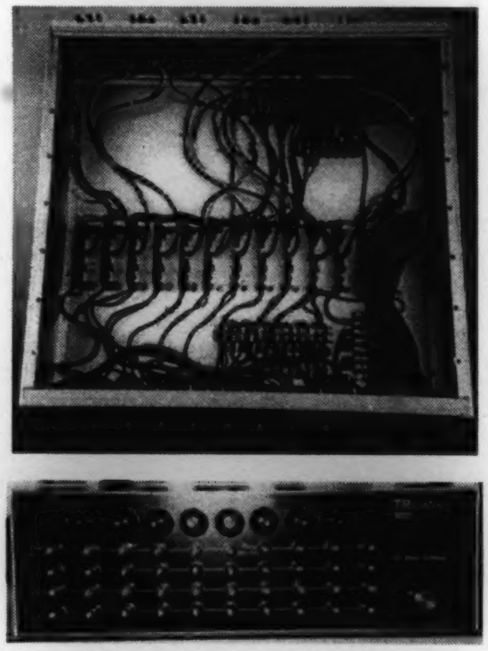

Figure E.4 Scanned image of the finished GaAs IC power supply; (top) internal components; (bottom) front panel.

11.5.5 Bias Circuit for Variable Outputs

The bias circuit used to provide V_{ref} is shown in Figure E.5. The circuit that provides V_{bias} is the same as in Figure E.5, except that resistor R_1 is removed, i.e., replaced by a short.

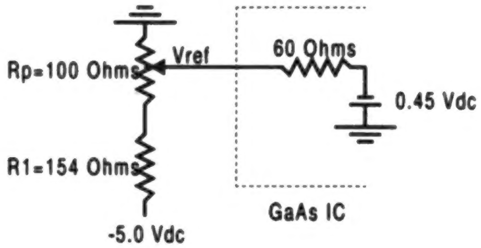

Figure E.5 Bias circuit for reference voltage provided to ICs.

The dial on the front of the unit adjusts the 10-turns pot, R_p, to obtain the desired output voltage, V_{ref}. That portion of the circuit enclosed by a dashed line in Figure E.5 is internal to the IC. R_p is a linear-sweep potentiometer for which the position of R_p can be specified by a linear sweep parameter, L_p, in the range $0 \le L_p \le 1$. $L_p=0$ when the dial is completely CCW, and $L_p=1$ when the dial is completely CW. When V_{ref} is connected to the reference pin of an IC, the value of V_{ref} versus L_p is as shown in Figure E.6 .

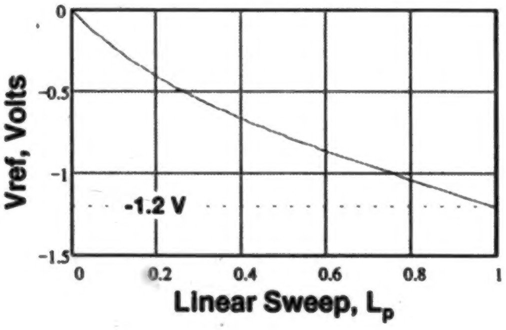

Figure E.6 IC Reference voltage, V_{ref}, versus linear sweep on potentiometer.

For the V_{bias} variable outputs, and assuming a load of 50 Ohms, the output bias voltage versus linear sweep is as shown in Figure E.7.

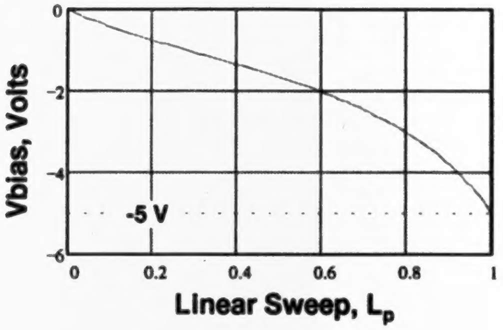

Figure E.7 Bias voltage, V_{bias}, versus linear sweep on potentiometer.

It should be noted that voltage and linearity of V_{ref} and V_{bias} versus L_P is affected by the connected load. It is recommended that V_{bias} not be used to provide a reference voltage for ICs because, unlike V_{ref}, the output is capable of exceeding the maximum specified voltage for the IC.

11.5.6 Handling and Care of GaAs Logic ICs

Always read the documentation provided by the manufacturer before operating these devices. A list of guidelines to follow is shown bellow.

Always wear a grounding wrist strap when handling or operating the ICs; never remove an IC from its anti-static bag unless you are at a well-grounded work area and are wearing a grounded wrist strap.

Positive voltages must never be applied to any part of the IC (the silver-plated aluminum enclosure is at ground potential).

The nominal power supply voltage for Vss is -3.5 V. An acceptable range for operation is -3.4 to -3.7 V. Vss should never fall outside the range 0 to -4.0 V.

The voltage applied to any reference pin must not exceed the range 0 to -1.6 V.

The instantaneous voltage at any RF input must not exceed the range 0 to -1.6 V.

Do not apply a signal to any input before applying power to the chip.

If voltage levels fall outside those stated above, permanent damage will likely result.

Unused outputs MUST be terminated in 50 Ohms